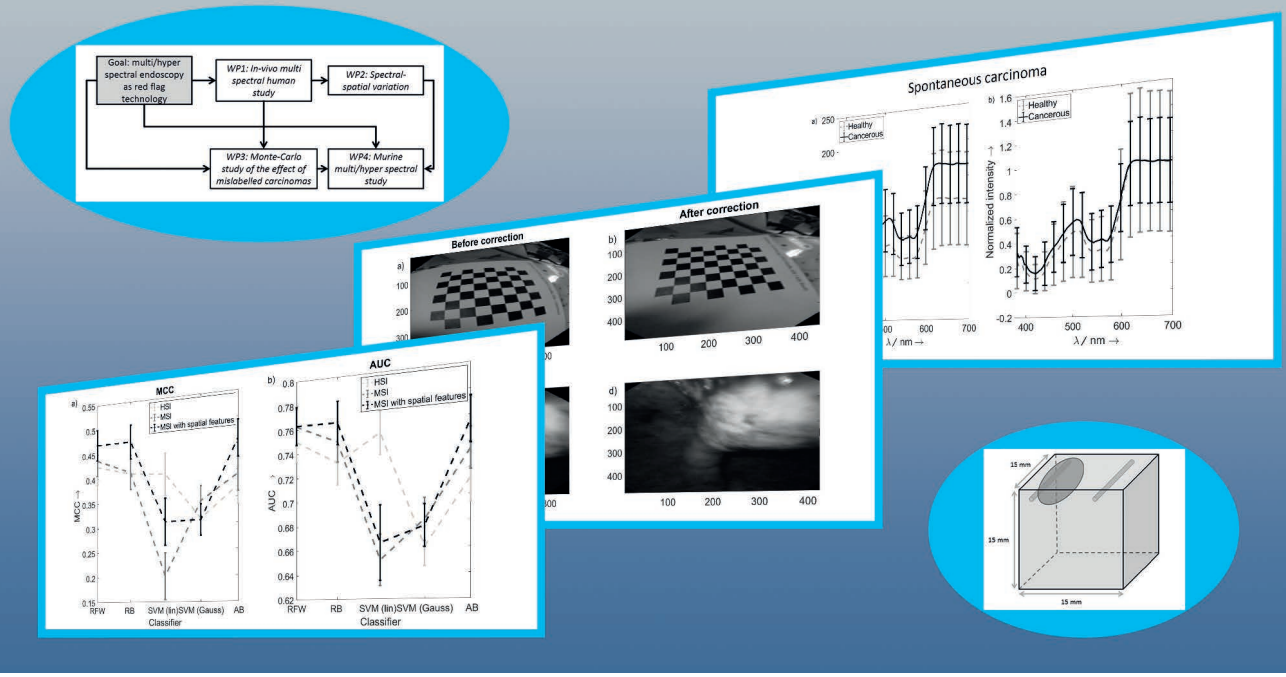

FAU Studien aus dem Maschinenbau 374

Martin Hohmann

Machine learning and hyper spectral imaging: multi spectral endoscopy in the gastro intestinal tract towards hyper spectral endoscopy

FAU UNIVERSITY PRESS

Martin Hohmann

Machine learning and hyper spectral imaging: multi spectral endoscopy in the gastro intestinal tract towards hyper spectral endoscopy

FAU Studien aus dem Maschinenbau

Band 374

Martin Hohmann

Machine learning and hyper spectral imaging: multi spectral endoscopy in the gastro intestinal tract towards hyper spectral endoscopy

Dissertation aus dem Lehrstuhl für Photonische Technologien (LPT)
Prof. Dr.-Ing. Michael Schmidt

Erlangen
FAU University Press
2021

Bibliografische Information der Deutschen Nationalbibliothek:
Die Deutsche Nationalbibliothek verzeichnet diese Publikation in der Deutschen Nationalbibliografie; detaillierte bibliografische Daten sind im Internet über http://dnb.d-nb.de abrufbar.

Bitte zitieren als
Hohmann, Martin. 2021. *Machine learning and hyper spectral imaging: multi spectral endoscopy in the gastro intestinal tract towards hyper spectral endoscopy.* FAU Studien aus dem Maschinenbau Band 374. Erlangen: FAU University Press. DOI: 10.25593/978-3-96147-446-2

Der vollständige Inhalt des Buchs ist als PDF über den OPUS-Server der Friedrich-Alexander-Universität Erlangen-Nürnberg abrufbar:
https://opus4.kobv.de/opus4-fau/home

Verlag und Auslieferung:
FAU University Press, Universitätsstraße 4, 91054 Erlangen

Druck: docupoint GmbH

ISBN: 978-3-96147-445-5 (Druckausgabe)
eISBN: 978-3-96147-446-2 (Online-Ausgabe)
ISSN: 2625-9974
DOI: 10.25593/978-3-96147-446-2

Machine learning and hyper spectral imaging: multi spectral endoscopy in the gastro intestinal tract towards hyper spectral endoscopy
Maschinelles Lernen und hyperspektrale Bildgebung: Multispektrale Endoskopie im Magen-Darm-Trakt als Weg zur hyperspektralen Endoskopie

Der Technischen Fakultät
der Friedrich-Alexander-Universität
Erlangen-Nürnberg

zur
Erlangung des Doktorgrades Dr.-Ing.

vorgelegt von

Dipl.-Phys. Martin Hohmann

aus Quedlinburg

Als Dissertation genehmigt
von der Technischen Fakultät
der Friedrich-Alexander-Universität Erlangen-Nürnberg

Tag der mündlichen Prüfung:	03.05.2021
Vorsitzender des Promotionsorgans:	Prof. Dr.-Ing. habil. Andreas Paul Fröba
Gutachter:	Prof. Dr.-Ing. Michael Schmidt
	Prof. Dr. rer. nat. Robert Huber

Preface

This thesis was written during my work as a research assistant at the Institute of Photonic Technologies at the Friedrich-Alexander Universität Erlangen-Nürnberg. Various opportunities to gain knowledge in thematically related areas of photonics besides my main research area were offered by the courses and events of the Erlangen Graduate School in Advanced Optical Technologies (SAOT), to which I am grateful for the support. During the time when the basic results of this work were achieved, I worked together with several people whom I would like to thank at this point.

My special thanks goes to Prof. Dr.-Ing. Michael Schmidt for the trust he has placed in me and the open and friendly way he has supported me, which has given me a lot of creative freedom to realize my ideas. He gave me the opportunity to work independently in other optical fields such as random lasing, laser surgery, Bayesian inference for diffuse reflectance spectroscopy or the assessment of optical properties of turbid media.

Of course, the support of my office colleagues and their interest in my research topic was also central to the success of this work. I would also like to thank the students, who made an important contribution to this work in the course of their research projects.

Last but not least, I would like to thank my family, who gave me the necessary freedom to create this work. Special thanks go to my wife who was always a great support and to my brother, whose editing has significantly reduced the spelling error rate of this work.

Contents

List of Symbols and Abbreviations

Symbol	*Unit*	*Description*
a/LCI		Angle-resolved low coherence interferometry
AB		Adaboost
AC		Adenoma carcinoma
ACC		Accuracy
$ACC2$		Weighted accuracy
AEG-tumour		Oesophagogastric junctional adeno carcinoma
AFI		Auto fluorescence imaging
ANN		Artificial neural networks
AOTF		Acousto-optic tunable filters
AUC		Area under the curve
B	a.u.	Vectorized hyper spectral data cube
b_c		Dark current noise
BE		Barrett's oesophagus
CLE		Confocal laser endomicroscopy
CRC		Colorectal cancer
DA		Diffusion approximation
DOT		Diffuse optical tomography
EGD		Esophagogastroduodenoscopy
$f_c(\lambda)$	a.u.	Spectral transmission of filter/optics
FP		False positive
FPR		False positive rate
FN		False negative
g		Parameter for describing scattering direction
GI		Gastro-intestinal tract
GIST		Gastrointestinal stromal tumour
GPU		Graphic processing unit
GUI		Graphical user interface
HRME		High resolution microendoscopy

Symbol	*Unit*	*Description*
HSI		Hyper spectral imaging
I	a.u.	Intensity
$\hat{I}$		Reprojected intensity
$I(\lambda)$	a.u.	Spectral distribution of the light source
I_{norm}	a.u.	Normalized intensity
IRB		Institutional review board
KNN		k-nearest neighbours
l		Parameter for $L_p^l(x)$
$L_p^l(x)$	a.u.	Laguerre-Gaussian functions
${}^rLG_l^p(x)$	a.u.	Laguerre-Gaussian functions as used in this thesis
λ	nm	Wavelength
LCTF		Liquid crystal tunable filters
LDA		Linear discriminant analysis
LG		Laguerre-Gaussian functions
LOT		Laminar optical tomography
LVF		Linear variable filters
M		Wavelength dependency matrix of the merged variable $m_c(\lambda)$
$m_c(\lambda)$	a.u.	Spectral response of the optical system
MCC		Matthews correlation coefficient
MCS		Monte-Carlo simulation
MCX		Monte-Carlo extreme
MLP		multiple linear regression
MNF		Minimum noise fraction
mRMR		Minimum-redundancy-maximum-relevance
MRI		Magnetic resonance imaging
MSI		Multi spectral imaging
μ_a	$\frac{1}{cm}$	Absorption coefficient
μ_s	$\frac{1}{cm}$	Scattering coefficient
μ_s'	$\frac{1}{cm}$	Reduced scattering coefficient

Symbol	*Unit*	*Description*
n		Amount
$\hat{n}$		Zero mean imaging noise in vector form
n_c		Zero mean imaging noise
NBI		Narrowband imaging
NCM		Noise covariance matrix
OCT		Optical coherence tomography
OOB		Out-of-bag
OP		Description for μ_a, μ_s or g
P		Sensor response from training samples
p		Parameter for $L_p^l(x)$
$p_{\%}$		Probability
PCA		Principal component analysis
PAT		Photo-acoustic tomography
PET		Positron emission tomography
Φ	a.u.	Transformation matrix
PI		Pseudo inverse
QDA		Quadratic discriminant analysis
r		Rotational constant for ${}^rLG_l^p(x)$
R		Spectral response matrix
R_2	a.u.	Vectorized residuum matrix
$r_{i,j,k}$		Residuum
$r(\lambda)$	a.u.	Spectral reflectance of the sample
RB		Robustboost
RFW		Random forest walk
RGB		Red green blue
ρ		Radial coordinate in cylindrical coordinate system
ROC		Receiver operating characteristic
RMSE		Root mean squared error
rSVM		Regressive support vector machine (SVM)
$s(\lambda)$	a.u.	Spectral sensitivity of the camera

Symbol	*Unit*	*Description*
S	a.u.	Result from SVD
SCC		Squamous cell carcinoma
SEN		Sensitivity
SNR		Signal-to-noise-ratio
SPE		Specificity
SSDC		Spectral and spatial decorrelation
SSV		Spatial-spectral variation
SVD		Singular value decomposition
SVM		Support vector machine
t	s	Time
Θ		Axial coordinate in cylindrical coordinate system
U	a.u.	Left singular vectors
UHR-OCT		Ultra high resolution optical coherence tomography
US		Ultra sound
V	a.u.	Right singular vectors
v	a.u.	Spectral response of the corresponding colour channel in discrete space
v_c	a.u.	Spectral response of the corresponding colour channel
W		Pseudo inverse matrix
W_e		Wheigting maxtrix
W_x	a.u.	Whitend data
WLI		White light imaging
wPI		Weighted pseudo inverse
X	a.u.	Vectorized intensity matrix

1 Introduction

In Germany in 2014, a little bit more than 25 % of the deaths were caused by cancer [1]. From these, more than 25 % were caused by cancer in the gastrointestinal tract (GI) [1]. This high death toll of carcinomas in the GI tract is caused by the difficulty of their detection. The main issue is that patients normally show symptoms in later stages of the tumour development. Thus, the early stage carcinomas cannot be detected as the patients do not visit the doctor. Therefore, the five years survival rate is less than 30 % despite some improvements in the last 40 years [2]. To overcome this issue, regular screening can be used. Currently, the state of the art is using thorough inspection with white light endoscopy and targeted biopsies. However, this still leads to an expected miss of about 20 % of the carcinomas [3].

This happens due to two main reasons. First, the identification of a suspicious area is very difficult with white light imaging. Second, the amount of biopsies is also limited and has a low resolution. Therefore, the difficulty of identifying suspicious areas cannot be completely compensated for by biopsies. To overcome the current limitations, one possible solution would be to develop an optical biopsy technology which would allow to perform many biopsies. This would increase the overall accuracy in a clinical environment. However, a better solution would be a red flag technology with a large field of view to solve both problems at the same time. First, the suspicious area could be detected. Second, the improved red flag technology would be able to pinpoint the right position for the biopsy.

Despite the usage of many optical technologies [4] and advancements of traditional endoscopic technologies [5], most of the methods do not lead to a significant improvement of the detectability of carcinomas in the upper GI [5]. Despite these setbacks, newer meta analyses [5] show a strong tendency in favour of chromoendoscopy or virtual chromoendoscopy. Chromoendoscopy is a normal white light endoscopy procedure with the usage of dyes to enhance certain features whereas virtual chromoendoscopy simulates chromoendoscopy by artificially enhancing the contrast by using a spectral estimation technique of the standard RBG-images [6]. This leads to the conclusion that the next investigation should be done with a method allowing direct access on the spectral information of the upper GI. Also, Swager et al. [7] states in their review about endoscopy in the GI that spectroscopic quantitative measurements of tissue need further investigation to find out if it allows a direct optical diagnosis of early neoplasia for endoscopy applications. This is provided by hyper spectral imaging (HSI).

HSI is an emerging field. It combines machine vision with spectroscopy [8, 9]. It enables the acquisition of two dimensional images with the spectral information for each pixel. Considerable progress has been achieved in many different areas [10]. However for the GI, there is no hyper spectral *in-vivo* study known to the author despite different approaches [8, 11, 12]. So far, hyper spectral imaging is proven to be a solid method for many medical applications [13], including carcinoma detection in the oesophagus [14, 15]. However, most of the studies for endoscopic applications are performed *ex-vivo* despite different approaches for hyper spectral endoscopes [8, 11, 12]. Thus, an additional focus of this work will be on the problems arising from *in-vivo* applications.

Therefore, the main focus will be on the data processing and the statistical analysis of a clinical study and an animal study with a murine inflammation driven tumour model and a murine spontaneous tumour model. A multi-spectral set-up is used due to its easier realisation. By using features corresponding to structural information of the tissue under investigation, typical structures will be identified. Also the conditions of the patients are taken into account such as pretreatment, inflammation and mucus. Moreover, with the help of Monte-Carlo-Simulations (MCS), the theoretical limit of accuracy will be investigated and compared with the results reached by the statistical analysis. From these results, the future steps and the remaining limitations of the set-up will be pointed out and approaches how to address these issues will be presented.. The combination of MCS and set-up limitations should allow to specify how much the accuracy can be improved by technical means to provide an upper limit of the expected accuracy. As last point, spectral estimation techniques are used to provide hyper spectral images from the multi spectral imaging device.

In summary, this leads to the following points to enable a red flag technology:

1. Build and design a multi spectral endoscope for an *in-vivo* clinical study and a multi/hyper spectral endoscope for an *in-vivo* mouse study
2. Develop the right pre-processing for a reliable discrimination between healthy and cancerous tissue
3. Perform classification between healthy and cancerous tissue
4. Simulate multi spectral endoscopy by the means of MCS for understanding the effect of mislabelled data due to *in-vivo* endoscopy

In practice to enable a good discrimination between healthy and cancerous tissue, the barrel distortions of the endoscope are corrected and the minimum noise fraction (MNF) in combination with Gaussian filtering is used for noise reduction. For feature generation, Gauss-Laguerre polynomials are used to detect spatial features. Moreover, a new set of spectral-spatial features (SSV)

is developed and evaluated. For the feature reduction, principle component analysis and Random Forest Walk (RFW) are used and compared. The analysis is done with RFW, AdaBoost (AB), support vector machine (SVM) and RobustBoost (RB). A comparison is also done to quadratic discriminant analysis, naive Bayes and k-nearest neighbours. The data is collected from a clinical study on 14 patients with carcinomas in the stomach. Additionally, a mouse study is performed with 25 mice, in which it is evaluated how spectral estimation might alter the detection of carcinomas. Finally, the effect of the mislabelling is simulated by the means of MCS and it is compared how this influences the classification results.

2 State of the art

In the following, the incidence rates of carcinomas in the GI with focus of carcinomas in the upper GI are discussed. Afterwards, the general technological for carcinoma detection are discussed whereas in the next part this discussion is limited to endoscopic technologies. Finally, hyper spectral imaging and the required statistical tools are discussed together with the application of MCS as simulation tool.

2.1 Tumour incidence rates

In general, cancer related death is the second most common reason of death. In US in 2015, 1.66 million new cancer cases were reported. From these cases, 41,570 were newly found carcinomas in the stomach and oesophagus. At the same time, 589,430 people died from cancer in 2015 leading to 26,310 deaths, caused by carcinomas in the stomach and oesophagus [2].

In comparison in Germany, 223,758 people died from cancer in the year 2014 accounting for 25.8% of the causes of all deaths [1]. After cardiovascular diseases, cancer related deaths are the second most common reason of death [1]. From these 223,758 cancer related deaths, 194,990 were found at specific position at the body. The remaining deaths were associated with tumour types of unspecific location, such as lymphoma or myeloma. From the known cancer sites, the cancer type which causes the highest death toll is cancer in the GI tract with 70,018 cancer related deaths accounting for 32 % of all cancer related deaths. The two most important types of GI cancers are the carcinomas in the oesophagus and stomach [1].

The number of detected oesophageal cancers in the western hemisphere varies from 5 per 100,000 inhabitants in north America to 30 per 100,000 inhabitants in eastern Europe [16]. For gastric cancer, the incidence rate is around 5 per 100,000 inhabitant in whole Europe [16]. Other studies found that in central Europe the highest rates (age normalized) are found in England with 15 per 100,000 inhabitants [17] in the years 2007/2008 or newer. The highest oesophageal cancer rates are found in central Europe (England, Netherlands, France, Germany) while northern and eastern countries (Poland, Sweden, Finland) and Austria have a lower cancer rate [17]. In Germany, the rate of oesophageal cancer related deaths varies from 5 to 15 cases per 100,000 inhabitants. The incident rate is higher in city states (Hamburg, Bremen, Berlin) as well as in the northern areas of Germany [17]. It should be considered that the statistical fluctuation for such fine resolved data is very high. Therefore in many cases, different numbers can be found.

However, the main issue with the oesophageal and gastric carcinomas is the low five years survival rate. In the US, it was less than 30 % between 2004 and 2010 [2]. Due to the low five years survival rate, gastric cancer is the second most frequent cause of cancer related deaths world wide [18]. Despite the common usage of esophagogastroduodenoscopy (EGD) for screening programmes, it is estimated that these tumour entities remain undetected in 20 % of the patients [3].

Carcinomas in the intestines can be grouped into two main types: the diffuse and the intestinal type carcinoma [19]. There are two major types of oesophageal cancer and one major type of carcinoma in the stomach: squamous cell carcinoma (SCC) in the oesophagus and adeno carcinoma (AC) in the oesophagus and stomach. Other rare types are gastrointestinal stromal tumour (GIST) which mainly occurs in the stomach and the oesophagogastric junctional adeno carcinoma (AEG-tumour) which is a carcinoma developing in the oesophagogastric junction.

Both main types of oesophageal cancer have a nearly distinct set of risk factors [20]. While SCC is mainly associated to lifestyle factors such as smoking and alcohol, AC is linked to reflux [16]. Reflux is the main reason for causing Barrett's Oesophagus (BE) [21, 22]. BE is an alteration of the squamous cells mainly of the lower oesophagus. This alteration of the cell increases the chance of developing a carcinoma and it could be found that the AC is mainly developed from BE [23]. In total, the population with BE has a 30-125 times higher risk of developing AC than the remaining or standard population [21, 22]. Depending on the country, the distribution of the two carcinomas types varies. In Germany, 30 % of the oesophagus carcinomas are adeno carcinomas but the number was increasing in the last two decades [17]. In the US, the same trend exists and already more than 50 % of the oesophageal carcinomas are adeno carcinomas [23, 24].

There is a variety of the main types of carcinomas and the early stage carcinomas can only be found by screening due to the fact that early stage carcinomas show only a low amount of symptoms. Moreover, these symptoms are unspecific and can be the cause of many different diseases. Thus, there are three target differentiations which have to be done. In the clinical routine, it is often not possible to differentiate between BE and inflammation [25]. This step would provide the information if the patient is a high risk candidate for AC and, therefore, is required to undergo regular check-ups. Moreover, if the BE is found, it has to be differentiated if the patient has a low-grade dysplasia (normal BE) or high-grade dysplasia (malignant BE, pre-cancer). Last but not least, possible carcinomas have to be found and differentiated from the healthy tissue around them.

At the moment, targeted biopsies performed after a thorough inspection with white light endoscopy contribute most of the diagnosis for all three cases. In the most cases, the patients are examined with high definition white light imaging (HWLI) and afterwards a biopsy is taken from suspicious areas. HWLI normally has a a sensitivity of 79 % - 85 % for the detection of carcinoma and the differentiation between low and high grade dysplasia [26, 27]. Therefore, it is expected that 20% of the tumours remain undetected [3].

For colorectal cancer (CRC) a similar estimation can be done. In general, CRC is one of the cancer types with highest mortality world wide [28]. Colonoscopy using white light endoscopy might be an adequate prophylaxis, as it allows detection of precursor lesions [29]. This approach significantly reduces the CRC mortality [30]. However, still especially smaller and flat lesions are frequently missed in 20-30 % of all cases [31], similar to the miss rate in the upper GI.

Despite complications in carcinoma detection in the oesophagus, it is also difficult to differentiate between BE and inflammation [25]. Despite the usage of the Prague C&M criteria which suggest to use the upper end of the gastric fold as landmark [32], it has the disadvantage that the landmark changes or even disappears during air inflation, respiration and others conditions [25].

On the one hand, cancer remains undetected due to the fact that HWLI does not correctly identify the suspicious area and on the other hand due to the fact that the number of biopsies which can be taken is limited. Therefore, it might happen that a potential lesion is not found because the biopsy is not taken at the right point. One possible solution would be to develop an optical biopsy technology which would allow to perform many biopsies. This would increase the overall accuracy in a clinical environment. Nevertheless, the extensive usage of an optical biopsy might increase the time of examination. This would increase the risk for the patient and also the cost of the procedure might increase. It should also be noted that a better red flag technology with a large field of view would not suffer from the same drawbacks as optical biopsies. The improved red flag technique would ensure that a suspicious area is not overlooked and it would be able to pinpoint the right position for the biopsy.

2.2 Available technologies in preclinical settings

To overcome the issue that a suspicious area is overlooked, there is a vast amount of technologies available for medical imaging. Table 1 shows the most important technologies which are targeting or might target endoscopic applications in the GI. The methods presented in table 1 show current preclin-

ical methods which might be transferred into clinical settings in future. In general, a clinical method should support label free imaging because bringing labels from the lab into clinical usage is a time consuming and expensive procedure. Furthermore, labels often have potential side effects such as allergies. Moreover, their high price often does not allow repeated imaging of the patient.

Due to the usage of labels, positron emission tomography and bioluminescence are not considered further. Moreover, ionized radiation also prevents multiple imaging of the patients because the total radiation dose should be as low as possible. Even if computed tomography (CT) can provide a complete 3D representation of a patient, the dose of one CT scan is within the order of the recommended annual radiation dose. Thus, repeated scanning is unfavourable and not suited for screening programs. In summary, relevant approaches left after these first considerations are laminar optical tomography (LOT), diffuse optical tomography (DOT), optical coherence tomography (OCT), ultra sound (US), magnet resonance imaging (MRI) and photo-acoustic tomography (PAT).

Table 1: Overview of intra-vital imaging approaches in preclinical cancer research [4, 33, 34].

Imaging method	Type of wave	Tissue penetration depth	Resolution	Supports label-free?	Supported labels	Field of view
Optical coherence tomography (OCT)	Near-infrared light	1-2 mm	1-20 μm	Yes	Nano-particles, magnetic particles and near-infra-red dyes	Few mm
Ultrasound (US)	Sound-waves	cm	50 μm	Yes	Micro-bubbles	Few dm
Computed tomography (CT)	X-ray	No limit	50 μm	Yes	Iodine	Few dm
Positron emission tomography (PET)	γ-ray	No limit	1-2 mm	No	Radionuclides (for example, ^{18}F)	Few dm
Magnetic resonance imaging (MRI)	radio waves	No limit	10-100 μm	Yes	Magnetic and paramagnetic	1-2 dm
Bioluminescence	Visible light	cm	60 μm to cm	No	Luciferins	Variable
Photo-acoustic tomography (PAT)	Visible or NIR light and sound	cm	5 μm - 1 mm	Yes	Near-infra-red dyes and nano-particle	Few dm
Diffuse optical tomography (DOT)	Visible or NIR light	cm	5 mm	Yes	near-infra-red dyes	Few dm
Laminar optical tomography (LOT)	Visible or NIR light	Millimetres	100-200 µm	Yes	near-infra-red dyes	Few cm

From these six, both US and MRI allow 3D reconstruction of big areas. Nevertheless, US, MRI and DOT suffer from a low resolution. Additionally, MRI is very expensive and, therefore, also prevents repetitive imaging. US is a cheap tool which is also used for screening. Nevertheless, it is not suited for finding

cancerous and precancerous tissue alteration with a small size. Therefore, all three methods have lacks in major points. The remaining three methods (PAT, OCT, LOT) are optical methods.

Until a few years ago OCT was not suited for differentiation between healthy tissue and malignancies in the oesophagus [35]. However, Aguirre et al. [36] could show that ultra high resolution OCT (UHR-OCT) can significantly help differentiating between normal oesophagus, BE, high grade dysplasia and oesophageal adeno carcinoma. Accuracy values with more than 90 % were reached. However, OCT has two limitations. First, it is more an optical biopsy than a red flag technology. Therefore, it is unlikely that it will be applied widely in the clinical routine for endoscopy as a red flag technology.

PAT is defined as 3D imaging of a material based on the photo-acoustic effect [37]. This approach combines the high optical contrast with scalable ultrasonic resolution with a resolution to depth ratio of around 200 [38]. However, it is computationally very complex and the imaging process takes long. Moreover, the ultra sound detector-array has to be placed very precisely to allow imaging which limits the usage for diagnostics at the moment. Only recently, the first studies on rabbit oesophagus have been done in which it is shown that the images correlate to histology [39]. However, PAT has two limitations: First, the measuring time is normally quite long. E.g. imaging the female breast takes around 3 minutes with an additional reconstruction time of 25 minutes [40]. However, up to 10 Hz imaging speed is possible [41, 42]. Second: similar to UHR-OCT, it is a very complex and expensive technology. Moreover, it is difficult to miniaturize for endoscopic usage and it needs physical contact for its application. Therefore, similar to OCT it is unlikely that it will be applied widely in the clinical routine within the next decades in endoscopy.

LOT is an imaging modality which enables imaging with a resolution of 100-200 μm with a penetration depth of more than 2 mm [34]. It uses a modified confocal microscopic set-up. However, despite confocal microscopy being able to be used in an endoscope [43], LOT is not yet used this way. Due to the same set-up as confocal microscopy it shares the same disadvantages. It can only scan a small section of the area of interest. Therefore, it is not usable as a red flag technology.

In summary, non of the presented imaging methodologies is suitable to be applied in a realistic endoscopic scenario. Either they are not suited as a red flag technology or the complicated and expensive set-up impedes introduction into the clinical routine. Therefore, an approach based on the current available endoscopic technologies should be chosen.

2.3 Endoscopic optical technologies, tested in clinical settings

In the clinical routine, most of the time only high definition white light endoscopy (HD-WLE) is used. Additionally to the HD-WLE, many more methods, particular targeting the oesophagus and the stomach like Narrow Band Imaging (NBI), Autofluorescence Imaging (AFI) or recently chromoendoscopy/virtual chromoendoscopy, have been developed as red flag technologies which are already tested in clinical practice. Furthermore, the following potential biopsy replacement technologies have been tested in a preclinical environment: confocal laser endomicroscopy (CLE) [5], endocytoscopy [5], high resolution microendoscopy (HRME) [5] and angle-resolved low coherence interferometry (a/LCI) [44]. Due to the fact that all the last technologies can probe only a small area, they are not considered further.

NBI is a technology which uses narrow band illumination at the two main absorption peaks of haemoglobin. Due to this, the superficial blood vessel network is highlighted by its increased contrast and can be used for the identification of malignancies. Despite promising early studies, later studies could not yield significantly better results than HD-WLE. Moreover in a systematic review, Curvers et al. [45] could only show a small potential of NBI for detection of high-grade-dysplasia (HGD). Also another review from Subramanian and Ragunath [46] reports that there is little evidence that using NBI might be beneficial in the clinical routine.

Another tested alternative to NBI is AFI. AFI uses the autofluorescence of tissue for the identification of potential diseases. This provides normally a good sensitivity of about 90 %. However, the false positive rate can be up to 81 % [47]. Hence, it is not suited for clinical usage for detection of potential lesions. Moreover, very often the results of AFI and also NBI vary a lot between different endoscopists and, therefore, the interpretation of the results is highly subjective and ,thus, special training and/or experience for the chosen method is essential. However, a new imaging method should ideally do not require extensive training of the operator and the results should be objective and reproducible.

Newer meta analyses show a potential solution by favouring chromoendoscopy or virtual chromoendoscopy rather than random biopsies for the detection of high-grade dysplasia in BE [5]. For chromoendoscopy, the mucosa is dyed. The dye allows either to better see the surface structure or alternatively highlights it by virtually imitating chromoendoscopy. Virtual chromoendoscopy is preferred due to the risk of the dyes. E.g. chromoendoscopy with methylene blue leads to a significant increase of the DNA damage of the

BE [48] which favours the development of carcinomas. Moreover, for many endoscopists chromoendoscopy is a difficult procedure due to the fact that the application of dyes and interpretation of the images depend on the endoscopist [7]. At the same time, a randomised multi-central studie shows that virtual chromoendoscopy has the same accuracy as regular chromoendoscopy [49].

Therefore, the high accuracy of virtual chromoendoscopy provides a hint that extracted fine spectral features allow a better accuracy than normal HD-WLE. Moreover, Swager et al. [7] state in their review about endoscopy in the GI that spectroscopic quantitative measurements of tissue need further studies to investigate if it allows a direct optical diagnosis of early neoplasia for endoscopy applications. Therefore, it should be beneficial to do fine spectral imaging. This fine imaging is provided by hyper spectral imaging (HSI).

2.4 Hyper spectral imaging

HSI is an emerging field. It combines machine vision with spectroscopy [8, 9]. It enables the acquisition of two dimensional images together with the spectral information for each pixel. Considerable progress has been achieved in many different areas of hyper spectral imaging [10] in the last years. HSI became more and more popular in different fields of diagnostic application [13]. At the moment, HSI cancer studies have been performed on four major aspects [13]:

1. analysing biomarkers and genomic alterations of individual tumour cells in vitro
2. classifying the cancer grade of histological specimens
3. identifying precancerous and malignant lesions in vivo
4. deriving the blood volume and blood oxygenation for quantifying the tumour angiogenesis and the tumour metabolism.

HSI is also used for the detection of cancer as one of the main applications of HSI for medical purposes [13]. This method has proven to be successful in identifying cancer in many different parts of the human body: e.g. larynx [50, 51], cervix [52], breast [53, 54], colon [55–59] or oesophagus [12, 14, 15]. However for the GI, there is no hyper spectral *in-vivo* study known to the author despite different endoscope designs [8, 11, 12]. In the GI, studies were performed on *ex-vivo* tissue [12, 14, 15, 55–58] or histological samples [59]. However, the *ex-vivo* classification results are very promising and good classifications could be achieved [15].

Additionally to previously described benefits, HSI allows to relate the measured spectrum to physical parameters. On the one hand, the spectral information allows the reconstruction of the oxygenation state, scattering behaviour and other chromophores of tissue under investigation [60] by an approxi-

mated solution of the diffusion equation [61]. Moreover, the finer spectral resolution increases also the spatial contrast in comparison to RGB-imaging [62]. On the other hand, the ability to do two dimensional spectroscopy allows to gather structural information which might be used for classifications of carcinomas similar to NBI images [63]. For the colon, it could be shown that vascular patterns allow to find carcinomas [64, 65]. Moreover, this approach could also be used for other parts of the GI [66]. Also by combining fine spectral and spatial features, it is possible to derive the spatial changes of different wavelengths, representing different absorbers.

However, the used type of hyper spectral camera has to be considered as different measuring strategies lead to different errors in the final images. Depending on how the hyper spectral image is measured, HSI-devices can be grouped into two main classes by which they generate the hyper spectral image: a scanning or a snapshot approach [67]. The scanning methods are divided into point scanning, line scanning and wavelength scanning methods. Point scanning for HSI can be used for confocal microscopy [68] in which case the image has to be scanned, anyway. The most common hyper spectral cameras are line based cameras for which a two dimensional detector such as a CCD is used to image one line and its spectral components. This design is mainly used due to its simplicity. Even if snapshot devices are preferable due to the fact that the whole images is imaged at once and, therefore, motion artefacts are reduced, their set-up is in general much more complicated.

Moreover, for most devices it is impossible to implement the snapshot camera into an endoscopic system. Wavelength scanning devices can be implemented in two ways: Either the light at the camera is filtered or, alternatively, the illumination light is filtered. Both can be realized by the means of acousto-optic tunable filters (AOTF), liquid crystal tunable filters (LCTF), filter arrays or a linear variable filters (LVF) [69]. However, these devices used in an endoscope have an imaging time of more than 4 s[70] for the whole spectra. Newer approaches take about 0.192 s per complete hyper spectral dataset [11].

Currently, there are two experimental approaches which are not tested extensively, yet. First, the usage of normal black and white CCD or CMOS cameras in combination with the switching of the illumination wavelength. This approach would also work well with endoscopy due to the fact that no external light is present compared to nearly all other situations of hyper spectral imaging. Second, a multi spectral device can be used for simplified design and tested with spectral estimation techniques to allow hyper spectral imaging. The spectral estimation would allow an easier and faster imaging than pure hyper spectral imaging. Moreover, the multi spectral set-up is expected to

be more robust which is especially important during its handling within the daily clinical routine.

By using spectral estimation techniques, a fine wavelength resolution can be reconstructed by calibrating the device with known spectra. Therefore, the robust multi spectral approach might be an alternative for building a complete hyper spectral system. Different spectral estimation techniques were developed in 1976 where the Wiener estimation showed the best results [71]. Most of the time, the spectral estimation is done for RGB-images due to their availability, also for medical application such as the estimation of the haemoglobin and melanin in skin [72].

Newer more advanced methods such as the adaptive Wiener estimation allow a finer reconstruction of the resulting spectra [73]. However, the Wiener and the adaptive Wiener estimation both have the disadvantage that the wavelength dependent effect of all components has to be known. This process is often time consuming, especially for the case of a scientific set-up which is altered regularly. In this case, the pseudo inverse method (PI) offers an alternative. It is calibrated purely by the measured spectra from the multi spectral imaging device and the spectrometer for comparison. However in most cases, the PI does not perform well [74]. By weighting the reconstructed spectra by spectral similarity, more similar spectra can be preferred. The method is called the weighted PI (wPI). It allows an even better spectral reconstruction than the adaptive Wiener estimation [75].

Despite the advantages of hyper spectral images, HSI has to overcome some limitations. The HSI device has to be implemented inside an endoscope and the imaging time should be below 0.5 s or better below 0.2 s for the complete data set to prevent movement artefacts. A possible solution for this is a robust multi spectral set-up. Furthermore, a huge amount of data is collected which cannot be accessed directly and this data has to be processed before presentation of the results. Thus, either physical parameters such as the blood oxygenation state or the vascular pattern have to be reconstructed or an automated statistical data analysis is required. In this thesis, the focus will be on the statistical data analysis.

If HSI is used for endoscopy with the spectral scanning approach, it will have the same resolution as a normal endoscope. Thus, the resolution will be high enough. Compared to normal HD-WLE, only the light source has to be changed, so the robustness of the hyper spectral endoscope is the same as a normal one. Hence, it is suited for the daily routine. The small modifications of the endoscope compared to a normal one will allow a low price for the device which should only be a little bit higher than for regular endoscopes. Finally, the analysis of the hyper spectral images might take some time. However, it

should still be faster than a few minutes. Furthermore, the data analysis can be parallelised so that it can be sped up to a calculation time of less than a few seconds. This is fast enough for the daily routine. In summary, HSI fulfils all necessary requirements for a technique which might be applied in the daily clinical routine.

2.5 Statistical discrimination of healthy and cancerous tissue

The statistical analysis of hyper spectral images is normally done with one of the following methods: Support Vector Machine (SVM), artificial neural networks (ANN) and unsupervised learning strategies [13]. From these methods, SVM [76] and ANN [77] are used as the most common tools to analyse hyper spectral images with clear preference to SVM [13, 78]. SVM is a supervised machine learning tool for data classification and regression. A SVM constructs hyperplanes in a high- or infinite-dimensional space. By choosing the hyperplane with the largest distance to the nearest training data point(s), the margin is maximized. By mapping the problem in a higher dimension, non-linear separable data can be separated by linear functions and, therefore, it can be classified. After training, the model assigns the data points to one of the classes.

In comparison, ANNs are inspired by biological neural networks and compared to rule based learning, a wider range of problems can be solved. Main features for an ANN are: It contains adaptive weights which are changed by a learning algorithm and it is possible to approximate non-linear functions. However, most of the time it is unknown how the solution is derived and thus no underlining pattern can be found. Moreover, ANNs are worse in generalizing the solution in comparison to SVMs. Thus for the case that only a low amount of training data is available especially when the amount of patients is low, ANNs should not be used.

In general, SVM shows good results for different hyper spectral classification problems in the medical field such as cancer detection with infra-red hyper spectral imaging [79], prostate cancer detection [80] or detection of cancer metastasis [81]. ANN normally shows also good results for hyper spectral imaging [13]. However due to the higher amount of required training data, the suitability for *in-vivo* studies is limited. Therefore, ANNs are not suited for the classification of carcinomas in the colon, oesophagus or stomach, given the number of available patients.

For nearly all the classification cases so far, it was expected that the training data was labelled correctly. Nevertheless, this cannot be guaranteed for en-

doscopic *in-vivo* situations. Especially for early cancer or pre cancer lesions, the finding of the exact tumour-margin often remains difficult (stomach [82], oesophagus [83]). Thus, mislabelled data points will be present in the data, acquired by the endoscopic procedure. Therefore, other classification methods should also be considered: AdaBoost (AB) [84], RobustBoost (RB) [85] and Random Forest-walk (RFW) [86] as these approaches show superior classification results over SVM in some cases. All three methods are boosting approaches. Boosting is a strategy, enabling the combination of multiple weak classifiers to a strong classifier. A weak classifier is a classifier which has to provide a better classification accuracy than 50 %. By combining multiple weak classifiers, the boosting approach allows a classification with a similar accuracy than the SVM.

AB is the original boosting approach, combining the weak classifiers by a weighted majority vote [84]. In contrast to SVM, it does not try to maximize the margin between two classes. AB focusses the effort of classification on the misclassified samples of the training data by increasing the weight of the misclassified samples. Due to this behaviour, it is bad at handling outliers due to mislabelled data. However, this can be compensated by ignoring the data points with the highest weight. This variation of AB is RB [85]. Due to this, RB becomes more robust against mislabelled training data [85, 87]. Hence, it is well suited for the classification problem for endoscopic *in-vivo* situations.

Apart from supervised classification also unsupervised classification can be used as it is commonly used for hyper spectral imaging for remote sensing application [88]. Unsupervised classification is a learning method where the classifier does not know the classes. Classification happens by clustering patterns which differ from the structureless noise. This approach was tested by Martin et al. [50] on hyper spectral data. However, unsupervised learning needs in most cases a high amount of data which should also be disjunct. For a comparable simple text recognition, Coates et al. [89] needed 12400 training samples. This is much more than it can be obtained by endoscopy.

Unsupervised and supervised classification can be improved by means of pre-pro-cessing of the data. For the statistical data analysis, the principal component analysis (PCA) is often used [90]. PCA is also often used for data-reduction to speed up the classification or to use less memory of the personal computer (PC). Alternatively, the PCA is applied as noise filtering tool. Noise is normally found in the higher order principal components. Thus by removing the higher order principal components, the noise can be reduced and, therefore, it increases the classification results. The PCA can also be used to enhance the classification result of a specific class by only calculating the PCA for the desired class [91]. E.g. if the PCA is done only for the cancerous

data, the cancerous area will be classified more precisely. This leads to an increase of the sensitivity. For the previously mentioned reasons, the PCA is also widely used for HSI as preprocessing step.

Additional to the PCA, Regeling et al. [92] showed that by minimum noise fraction (MNF) transformation the result of a medical hyper spectral classification can be improved for supervised [93] and unsupervised [94] learning strategies. In all tested variables, the MNF transformation had the largest impact on the final classification results compared to other parameters [93]. The MNF consists of sequential PCAs. The first usage of the PCA scales the white noise with an estimated noise covariance matrix (NCM). The second PCA sorts the data by the decreasing variance from the noise-whitened data. Thereby, principal components with large eigenvalues are linked to eigenimages which mainly contain signal. By doing the back-transformation with the lower order principal components the noise filtering is achieved. Effectively, the data gets sorted by its signal-to-noise ratio (SNR) [92].

For the MNF, the most important point is the correct estimation of the NCM. Regeling et al. [93] proposed to use spatial and spectral information for the estimation compared to only spatial information proposed by the original study [92]. The spectral and spatial decorrelation (SSDC) [95] could be adjusted to MNF due to the fact that SSDC is the best method for estimation of the NCM of hyper spectral data [96]. Afterwards, the noise can be decorrelated with multiple linear regression (MLP).

After noise reduction, the right features as input for the classification have to be selected. Features are single, mostly real values which represent an object or a pixel which should be classified. In the simplest case, features represent the intensity value of a single wavelength of a hyper spectral image. Feature selection can be be done in this case as alternative to PCA to reduce the amount of input parameters by only keeping features with a high Minimum-redundancy-maximum-relevance (mRMR) feature selection [97].

However, also the opposite case should be considered when features are generated from the data to increase the classification accuracy. Compared to the reduction of the used features, there is a vast amount of different approaches for different problems e.g. the usage of world knowledge for text classification [98], the capturing of complex non-linear feature interactions in multi-modal data with help of an ANN [99] and many more. In all cases, more or less attributes are imaged into real numbers. For imaging, this might be the sum of an area around the target pixel which should be classified.

Many different spatial approaches are used for decision support but only a low amount is used for carcinoma detection [100]. However, there is no

analysis done for carcinomas of the upper gastro-intestinal tract (GI) in their review [100]. Nevertheless, new research shows that it is possible to create a computer-aided method to identify images in the upper GI containing lesions with an accuracy of around 90 % for early carcinomas in the upper GI [101].

Despite these very good results generated by Liu et al. [101], they can only identify that there is a lesion in an image but they cannot figure out where it is. Moreover, they need 1500 up to 10000 features for each image to do the analysis. Doing a similar analysis for multi/hyper-spectral images would generate more features as spatial features might change for different spectral bands. Furthermore, the ultimate goal is that the algorithm tells the clinician also where they should look for the carcinoma in an image. For this goal, a pixel by pixel analysis has to be done. A single endoscopic image consists of approximately 90,000 to 1,000,000 pixels. Having this amount of features for every pixel is impossible to handle in terms of memory and calculation time. Thus, it should also be noted that the goal of the accuracy for the pixel by pixel analysis is lower due to the fact that so many feature dimensions are not possible.

One of the most common features are Gabor features as it is used for car detection [102]. It might significantly increase the accuracy for car detection in combination with other pre processing steps and/or classifiers [103]. However, most cars have a similar regular rectangular structure which cannot be found in carcinomas. For carcinomas, the blood vessel pattern as the most important structural information for high magnifications and the gastric pits (GP) for normal endoscopy do not show these kind of geometrical pattern. Moreover, it should allow rotation of the objects, as the carcinomas and the wall of the GI is imaged from different angles. To describe these patterns, better suited features should be chosen.

In summary, a new set of strong features is recommended which contain a maximal amount of information in as few features as possible. Additional to spatial features, combined spatial-spectral features generated from multi/hyper-spectral images might be one solution. Spatial-spectral feature selection is already used in the analysis of remote sensing images [104]. However, they are just added to the selection of features where spectral features are one type of features out of many. Another possibility is to use an adaptive neighbourhood system as Fauvel et al. [105] do. However, these features do not summarize the spectral and spatial information of the spectral and spatial surrounding. One idea by Zhang et al. [106] is the usage of the spatial-spectral surrounding as a tensor as input parameters. While this is feasible for their purpose, for medical multi/hyper-spectral imaging it might lead to a too high dimensionality

of the feature space. Therefore for feature generation, a different approach has to be found for spatial features as well as spectral spatial features.

2.6 Optical modelling of tissue

Finally, the results have to be validated simulatively. Typical simulation approaches for tissue optics use either the diffusion approximation (DA) of the radiative transfer equation or its direct solution with the help of Monte-Carlo-Simulations (MCS). As also wavelengths with a high absorption have to be simulated, the DA cannot be used. MCS are widely used in many kinds of simulation of the light propagation in tissue [107] such as OCT-images [108], fluorescence [109] or blood flow [110]. Thus, their is a wide range of possible applications of the MCS.

A great example of modelling the tissue is done by Hidovic-Rowé et al. [111]. In this study, they model the reflection spectrum of colon by adapting the volume fraction of blood in the mucosa, the haemoglobin saturation in the mucosa, the size of scattering particles in the mucosa, the volume fraction of scattering particles in the mucosa, the thickness of the mucosa, the volume fraction of blood in the sub mucosa, the size of collagen fibres in the sub mucosa, the volume fraction of collagen in the sub mucosa and the thickness of the sub mucosa. Moreover, the influence of all these parameters is investigated. However, there is no MCS done for multi or hyper spectral imaging, known to the author.

It is also possible to analytically describe the reflectance spectra. For example for skin a very good model exists [112]. This model derives similar information as the model from Hidovic-Rowé et al. [111]. It allows also to understand the composition of the tissue under investigation. However, this model cannot be expanded for spatially resolved alterations despite the inherent beauty of having an analytical description. Therefore, the usage of MCS is preferable.

Another way of understanding the tissue is on a more macroscopic scale. One important point to understand the tissue is to understand the inter and intra patient variations. So far, there is nearly no information about the inter and intra patient variations of the optical properties available. Furthermore, it is not clear yet how to simulate inter patient variations properly. However, both of these points are required to evaluate the *in-vivo* endoscopy results for testing the classification as only this allows an understanding of the effects which influence the accuracy of the classification.

3 Objective

In summary, it can be concluded that there is a need for a red flag technology to guide biopsies and ensure that carcinomas are not overlooked as 20 % of the tumours currently remain undetected [3]. It is expected that multi- and hyper spectral imaging might be a tool to allow the finding of carcinomas in the GI. Therefore, the following working hypothesis will guide this study: **Multi- and hyper spectral imaging is a tool to allow detecting carcinomas in the GI as red flag technology**.

The main advantage of HSI with its finer spectral bands compared to multi spectral imaging (MSI) is a higher contrast [62] which should explain the better results for HSI over MSI in various studies [113, 114]. However, it should also be considered that the five main absorbers in tissue (haemoglobin, water, melanin, protein and fat) all show fairly wide spectral features. The spectral width is wider than 50 *nm* most of the time. Therefore, MSI might also deliver similar results than HSI. Moreover, the wide spectral features lead to high correlation between continuous spectral bands [115]. Thus, many hyper spectral bands would not be required. Finally, the curse of dimensionality should also be considered. For high dimensionality problems such as HSI, the volume of the space increases so fast that the available data become sparse. This makes the classification more difficult. Furthermore, a much higher amount of data is required for HSI. However for the human study, it is not expected that this amount of data will be available. Thus, MSI should be used as an alternative. Hence in most of this thesis, MSI is used as a potential substitute for HSI.

To investigate multi/hyper spectral imaging four main research questions have to be answered. Figure 1 shows the overview of the main research questions in this thesis and additionally the guiding hypothesis is the central research question.

WP1: The first point is the identification of arising problems. Often there are too many methods that might by used for clinical issues, but most cannot be transferred into clinical routine. [116]. Therefore, a normal endoscope system was modified and used in a human *in-vivo* study [117]. From these dataset, it is tested how a naïve classification can detect carcinomas and which features are responsible for their detection: Can *in-vivo* MSI endoscopy allow the discrimination between healthy and cancerous tissue and which spatial features are responsible for the classification?

WP2: In general, even if spatial features allow a discrimination between healthy and cancerous tissue, spatial features are normally used in a vast

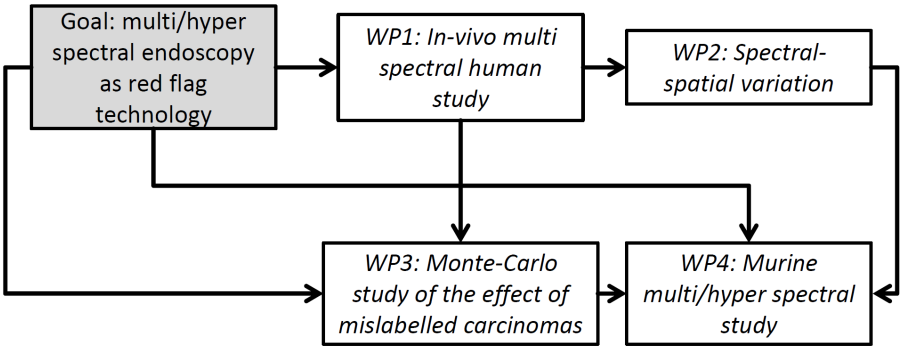

Figure 1: Overview of the main research questions as working package (WP) investigated in this thesis. The grey box symbolizes the generic topic/research question and italic font symbolizes that this part of the flow chart will be shown as generic topic later.

number of features which require a lot of memory and calculation time. As alternative spectral-spatial variation (SSV) is proposed to summarize spatial features and include spectral features at the same time: Can SSV be an alternative or a support for spatial features?

WP3: For an understanding of the reasons of misclassification, a model is required in which the position of the carcinoma is known. Due to the fact that for *in-vivo* endoscopy the margin of the carcinoma is not known [82], the effect of mislabelling cannot be assessed. For this, a simulation is required. Hence, a MCS is developed which allows to image the surface and includes inter patient variations leading to the following research question: Can the MCS be used to study the influence of mislabelling and point to methods for compensation of mislabelling?

WP4: All results culminate in the final murine multi- and hyper spectral study. In this part, the combined results from all other working points are used to generate a robust red flag technology. After the human study, it was recognized that some research question have to be re-evaluated in an animal study: such as, new endoscopy design and it is tested if spectral estimation can improve the classification results, as spectral estimations should not generate new information. For this, the mouse endoscope is calibrated to allow spectral estimation. Due to the fact that most absorbers show wide spectral features spectral estimation should be sufficient. With the previously generated classification scheme it is tested if direct hyper spectral imaging should be investigated or if hyper spectral imaging by means of spectral estimation is enough for the future as one of the hyper spectral system

approaches [118]. Hence, the research question is: Can hyper spectral imaging by means of spectral estimation significantly improve the classification results from multi spectral imaging?

4 Materials and methods

The materials and methods section is grouped according to the WP from the objective. Thereby, WP1 is the longest part in this thesis as most of methods are introduced first in this WP and they will be reused in the other WP.

4.1 In-vivo multi spectral human study

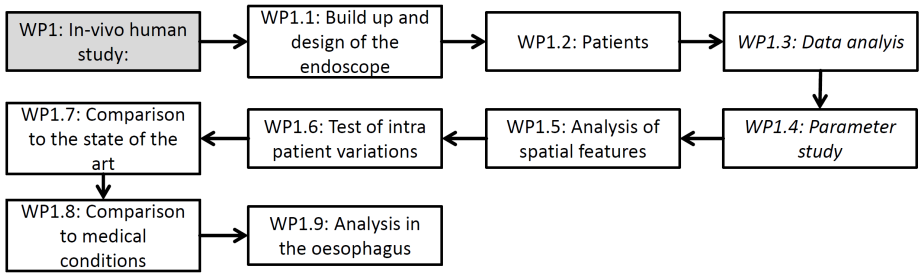

Figure 2: Overview of the first working package. Each box symbolized one sub chapter and corresponds to the headlines. The grey box symbolizes the generic topic/research question and italic font symbolizes that this part of the flow chart will be shown as generic topic later.

This WP is grouped into nine sub groups. First, the design of the endoscope is explained followed by the summary of patients which have undergone an endoscopic procedure by Dr. med. Heinz Albrecht. In the next section, the data analysis is explained including the parameters which are varied in the following parameter studies. With a good parameter set for the classification procedure, it is tested if intra patient variations can be compensated followed by a comparison to the state of the art in which the parameter optimizations were not done. Afterwards, it is investigated how medical conditions such as pre-treatment might influence the classification results. In the last part, the transferability of the analysis scheme to the oesophagus is evaluated.

4.1.1 Build up and design of the endoscope

This section shows the set-up used for the human study. The measurements are done with a modified version of an earlier presented set-up [12], described by Hohmann et al. [117]. It is designed to be robust and stable due to the fact that it is used in a daily routine at the endoscopy unit of the university hospital in Erlangen. For this reason, a very simple set-up design is chosen which can withstand bumps or other shocks, happening during the routine work in the clinics. Furthermore, parts which may come into contact with a patient,

have to be certified. These factors limit the possibility of modifications to the endoscope.

Therefore, the multi-spectral endoscopy set-up is a modified standard endoscopy system, consisting of an Olympus endoscope GIF 100 (Olympus Corporation, Tokyo, Japan), an Olympus video processor CV-140 (Olympus Corporation, Tokyo, Japan), a modified light source Olympus CLV-U40 (Olympus Corporation, Tokyo, Japan) and an external light source (Lumencor spectra 7-LCR-XA, Beaverton, OR, USA). The schematic is shown in figure 3(A). The external light source is coupled into the light source unit CLV-U40. The video signal from the endoscope is used as a master clock for the external light source. The system is controlled by a PC. The data input, data output, graphical user interface (GUI) and the control of the external light source is done by a Matlab (The MathWorks, Inc., Narick, MA, USA) program. Figure 3(B) presents the set-up and how it is used in the clinical environment.

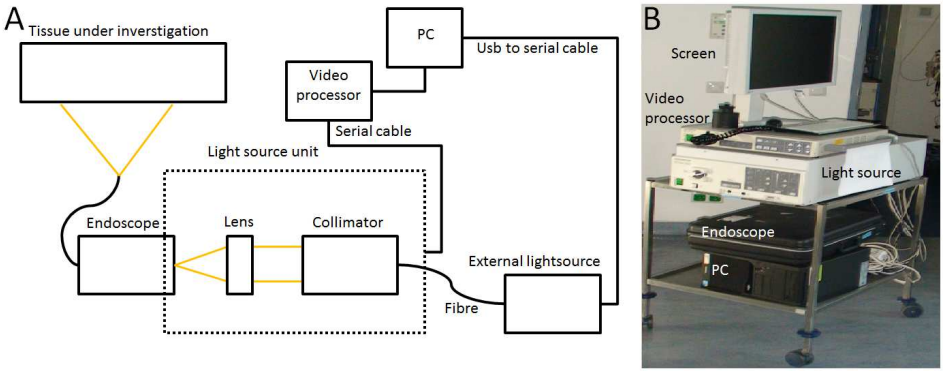

Figure 3: **A:** Schematic set-up of the endoscopic imaging system consisting of a light source unit, an endoscope image processor, an external light source and a PC. **B:** Photo of the set-up: On the upper rack under the screen the video processor can be seen. The modified light source unit is placed below. The light source unit is increased in its size to allow major modifications of the optical path. On the lower rack, the controlling PC and the endoscope (black box) are placed.

The modified light source unit is capable of using seven wavelength bands. However, only six are used, due to the fact the endoscope GIF 100 does not transmit UV-light. The six used wavelength bands range from 400 *nm* to 650 *nm* as shown in table 2. The bandwidth of the colour channels ranges from 12 to 20 *nm* full width half maximum (FWHM).

The multi-spectral imaging mode is implemented as a spectral scanning system where each wavelength is measured consecutively. The system allows

Table 2: Centre wavelength and the half width full maximum of the used wavelength bands for the multi spectral imaging device.

Wavelength in *nm*:	438 ± 12	475 ± 17	512 ± 12	542 ± 13	575 ± 12	628 ± 20

taking a single multi-spectral image and afterwards continues imaging under normal white light illumination. Thus, the standard mode is normal white light imaging. To do so, all six wavelength bands are used at the same time and the multi-spectral imaging can be run during the white light endoscopy.

The final amount of multi spectral images taken varies, depending on how many motion artefacts occurred and how many different angles are possible. The resolution is approximately 350x370 pixels and it is limited due to the normal resolution of the Olympus endoscope. The whole imaging process takes 2 s including pre- and post-processing. Therefrom, 0.45 s are needed to acquire the full multi-spectral image. The rest of time is used for pre-processing and post-processing of the data. This time is measured during the imaging process with the commands ”tic” and ”toc” from Matlab.

The field of view of the endoscope is 120 degrees and the image is sharp with a distance of more than 3 mm between the sample and the tip of the endoscope. The endoscope has a fixed focus within a depth of focus from 3 mm to 100 mm. In realistic images the stomach has a distance of about 0.5 cm to 5 cm. Thus, the pixel size at the image plane varies from 0.05 mm to 0.5 mm.

Despite the different magnification levels due to the distance of the sample and the tip of the endoscope, the main limiting factor is the SNR. The noise level is around ± 5 intensity values from 256 possible intensity values and it is constant and independent of the signal intensity. Thus, in the optimal case with perfect illumination, the SNR is about 20. For realistic cases, it is around 10 but it can also be lower. However, the signal which is measured is a modulation on top of the intensity values. Hence, effectively the SNR is even lower.

Additionally, distortions are taken into account. Depending on the distortion, they have different effects for the later classification. Spectral distortions are minor. Normally, the spectral distortions are described with the keystone and smile. The smile is a centre wavelength shift and the keystone property is a spectral band-to-band misregistration [119]. For this endoscope, there is only a one pixel wide shift between the images for blue and red. Hence, keystone and smile are considered as not being present in the endoscopic set-up.

The typical distortion for endoscopes is the barrel distortion which should be taken into account. The used endoscope shows a dominant barrel distor-

Figure 4: Image taken by the Olympus endoscope of a chess board. The lines of the chess board are bent, demonstrating the present barrel distortion.

tion. Figure 4 shows the effect of the barrel distortion from the Olympus endoscope. It is seen that the lines of the chessboard are bent. For a point wise classification this does not create errors. However, as soon as spatial features are taken into account, the change of the shape of the tissue under investigation might lead to a decrease of the classification accuracy. Therefore, the barrel distortions have to be corrected.

4.1.2 Patients

In total, 58 patient are measured. From these patients, 39 have a histopathologically confirmed carcinoma or BE and could be used for the data analysis. The amount of patients is summarized in table 3. From these 39 patients, 14

Table 3: Patients in each disease class with their age, gender and amount of patients with pre-treatment.

Patients	Disease	Age	Male/female	Pre-treatment
14	Adeno carcinoma, stomach	50-85	11/3	8
13	BE	44-78	10/3	1
12	Carcinoma, oesophagus	52-76	11/1	1

have histopathologically confirmed adeno carcinoma in the stomach. Eight out of these have undergone pretreatment. The youngest patient has an age of 50 years and the oldest has an age of 85 years. From these patients, eleven are male and three are female. For BE, 13 patient can be used for the data analysis. From these, ten patients are male, one has undergone pre-treatment and the youngest patient is 44 years old while the oldest is 78 years old. For

the carcinomas in the oesophagus, all carcinomas are mixed as one entity due to the fact that the amount of patients is fairly low. In total, twelve patients are used for the data analysis with an age ranging from 52 to 76 years. From these patients, eleven are male and one patient has undergone pre-treatment.

For the analysis of the data, the type of disease has to be known. Therefore, the histopathological diagnosis is confirmed for each patient before delineating the margin. The margin is drawn by a medical expert (Dr. med. Heinz Albrecht, Medizin I), according to endoscopic differentiation criteria between dysplasia and normal tissue. For each patient, two to five biopsies at the suspicious areas are performed. The endoscopic procedure is performed by Dr. med. Heinz Albrecht. A certain amount of the tissue is expected to be labelled wrongly due to the fact that even a medical expert cannot be absolutely perfect at finding the correct margin [82]. Also in *in-vivo* situations, biopsies cannot be taken of a sufficient amount for compensation. Hence, there might be areas which are wrongly labelled as cancerous or healthy.

The patients received complete information about this study. Afterwards, the patients attested to informed consent for study participation. The research is carried out in accordance with the Declaration of Helsinki. The study has been approved by the IRB of the Friedrich-Alexander-Universität Erlangen-Nürnberg, Germany.

4.1.3 Data analysis

The section of the data analysis of WP1 consists of the four main steps for the data evaluation as shown in figure 5. First, the required pre-processing is described so that the data can be used for the further steps. Afterwards, the feature generation and the ways to characterize important features or summarize them is explained (feature reduction). The general scheme for this analysis is also used in section 4.3 and 4.4 in this thesis.

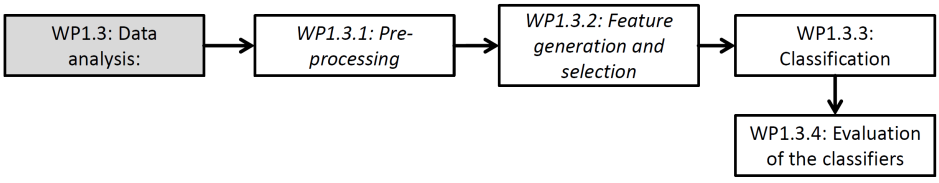

Figure 5: Overview of the data analysis of WP1. The grey box symbolizes the generic topic/research question and italic font symbolizes that this part of the flow chart will be shown as generic topic later.

As reference for the data analysis, the study from Hohmann et al. [117] is used. It is used due to the fact that within the used methods, the results are optimized. Thus, this analysis can be used as standard for comparison. In their study, 14 patients with stomach carcinomas are used for the data analysis. First, the data is smoothed with 7 x 7 pixel wide Gaussian smoothing. A second set of data is created by calculating the derivative image. From both images combined, the coefficient matrix of the Principal Component Analysis (PCA) [90] is calculated from the carcinoma data and applied to the test data. By choosing to calculate the PCA only on one class of the data, the detectability of this class is increased [91]. Hence, the detection rate of malignant tissue should be high in this study. The carcinoma tissue is chosen due to the fact that in the known cases, HSI has a high specificity and a low sensitivity for gastric and oesophageal carcinomas [14]. Therefore, the sensitivity is increased by performing the PCA only on the tumour data. Afterwards, the first principal components accounting for 99 % of the variations are used for the classification. In the study from Hohmann et al. [117], the PCA is used as a further noise reduction tool. For all patients except patient 5, this leads to a usage of nine PCA components. For patient five ten components are used.

Pre-processing Additionally, to the pre-processing done by Hohmann et al. [117], Fourier-filtering, image correction and MNF are introduced to the analysis scheme. Fourier-filtering is implemented to remove line artefacts caused by the endoscope. Further image correction is applied to correct the barrel distortion, originating from the endoscope and MNF is applied as a potential advanced noise reduction tool which takes the similarity of the different spectral components into account. Moreover, the difference of the cause of the errors should be regarded. While the error corrected by the Fourier filtering originated from the camera of the endoscope, the barrel distortion is caused by the optical imaging system of the endoscope and the MNF as well as the Gaussian filter correct the random noise. The pre-processing steps are shown in figure 6 consisting out of eight steps:

1. Annotation of the carcinoma to label the data by Dr. med. Heinz Albrecht
2. Areas with specular reflection are excluded as they would reduce the classification accuracy. Furthermore, they would not include any information about the carcinoma or the healthy tissue.
3. To compensate line errors from the endoscope, Fourier filtering is used.
4. The barrel distortion as shown in figure 4 are corrected to ensure that spatial features are comparable across the whole image.
5. Data normalization, so that the MNF uses all wavelengths equally
6. MNF filter for noise reduction
7. Data de-normalization to generate the correct spectrum again

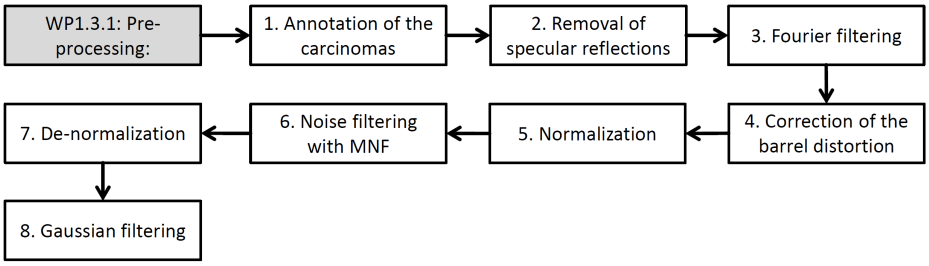

Figure 6: Overview of how the pre-processing is done. The grey box symbolizes the generic topic/research question and italic font symbolizes that this part of the flow chart will be shown as generic topic later.

8. Gaussian filter to reduce further high frequency noise, as MNF only filters this partially

The Fourier filtering has to be done before the removal of the barrel distortion due to the fact that the removal of the barrel distortion would alter the image that a simple Fourier filtering would not be possible any more. Furthermore, the Fourier filtering has to be done before the MNF due to the fact that errors from the endoscope from some wavelengths would mix into images where these errors are not present and they might be interpreted as important features by the derivation of the MNF. Before the noise removal with MNF, the images for every wavelength are normalized to better identify the noise. After the noise removal, the data set is denormalized again. As last step, a Gaussian filter is applied to further reduce the noise.

1. Annotation of the carcinomas The annotation of the carcinoma is done according to endoscopic differentiation criteria between dysplasia and normal tissue by Heinz Albrecht. The margin is drawn in GIMP. Thereby for the same patient, the annotation is done separately for each image to reduce bias. Afterwards, the margins are compared and inconsistencies are decided by a majority vote and plausibility of the drawn margins.

2. Removal of specular reflections After the images are taken, the first step is the pre-processing of the data. First, images with motion artefacts are excluded from the analysis. Also areas of images with over-saturation (e.g. due to specular reflection) are excluded from the analysis. Additionally, a margin of 12 pixels around over saturated areas is also excluded to minimize the effect of partly specular reflective surfaces.

3. Fourier filtering The Fourier-filtering for the removal of the line artefacts is done due to their regular structure. These line artefacts have a

dominating high frequency in all cases and they are parallel to the x-axis. Thus, Fourier-filtering is used. First, a filter is created from the sum of six Gaussian functions with different positions, peak heights and standard deviation. Table 4 shows the values. The filters are selected to filter out the line artefacts but conserve as much other information as possible. The final filter is shown in

Table 4: Position, size and intensity (height) of the Gaussian-functions used for Fourier-filtering.

Number	Coordinates (x,y) [pixel]	Intensity [a.u]	Size [pixel]
1	(60, 0)	5.7	30
2	(60, 0)	2.8	75
3	(60, 55)	7	3
4	(60, 95)	14.1	3
5	(60, 135)	14.8	3
6	(60, 145)	5.6	3

figure 7. There are two large Gaussian functions and four small ones. The big ones are reducing the general high amount of spatial frequencies of sinusoidal functions with high frequency and a directional component $\vec{k}$ parallel to the x-axis. The four small Gaussian filters target the spatial waves with a period

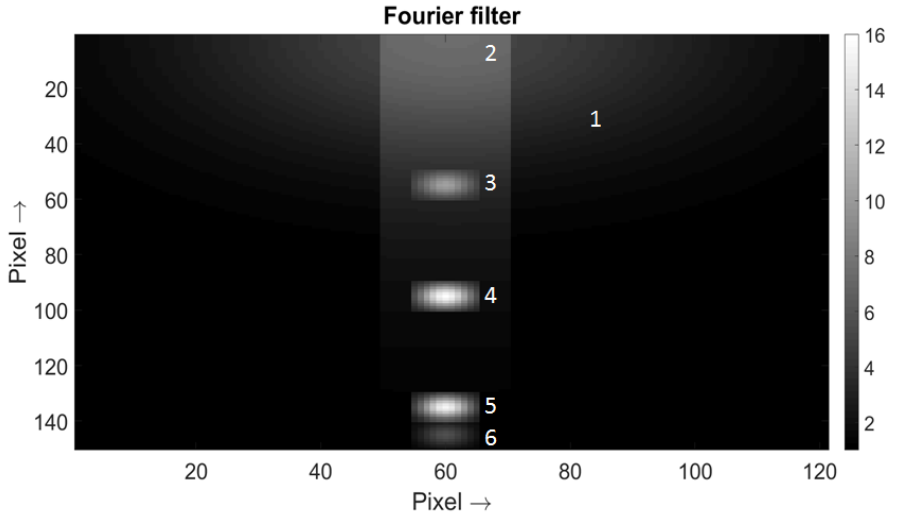

Figure 7: The final Fourier filter which consists of the sum of six Gaussian functions. Filter 1 is the big one. Filter 2 is the narrow one which goes down. Filters 3-6 are small ones, matching to a period of two or multiples of it.

of two, four, six or eight pixels with a $\vec{k}$ parallel to the x-axis. The original period of the distortion is two pixels. The other ones are its harmonics. For the Fourier filtering, the image is Fourier transformed. After the Fourier-transformation, the phase as well as the intensity of the image is divided by the filter function. Afterwards, the filtered image is transformed back to the normal space.

4. Correction of the barrel distortion The image correction of the barrel distortion is done after the Fourier filtering due to the fact that the correction of the barrel distortion would lead to an alteration of the spatial frequencies. The correction of the barrel distortion is done by estimating nine images of chess boards which can be seen in figure 4. The detection is done by detecting the edge points of the chess board with the command "detectCheckerboardPoints" from Matlab. From the detected points, the world coordinate system is calculated with the Matlab command "generateCheckerboardPoints". As last point, the camera parameters are calculated by the command "estimateCameraParameters". For estimation of the precision, the edges of the chess board are re-projected. The resulting error is used to estimate the quality of the correction. From the final camera parameters, a projection is calculated which is applied to all further images.

5. Normalization For the normalization, the multi spectral image of each colour channel is divided by the maximum of the respective colour channel as shown in equation 1:

$$I_{norm}(x, y, \lambda) = \frac{I(x, y, \lambda)}{\max\limits_{x,y} I(x, y, \lambda)} \tag{1}$$

In equation 1, $I(x, y, \lambda)$ is the intensity of the multi spectral image as the function of position and wavelength, $\max_{x,y}$ describes the function to take the maximum over every x and y and $I_{norm}(x, y, \lambda)$ is the normalized multi spectral image. The normalization values ($\max\limits_{x,y} I(x, y, \lambda)$) are saved for the de-normalization.

6. Noise filtering with MNF After the correction of the barrel distortion, the MNF is applied. The MNF is done as proposed by Regeling et al. [93] with one modification which is explained in the next paragraph. To be able to sort the images by their noise fraction, the most important part is the estimation of the NCM. In the original work of the MNF, only spatial information was used. However, Regeling et al. [93] adjusted a spectral and spatial decorrelation (SSDC) to estimate the MNF. This approach is feasible due to the fact

that Gao et al. [96] could show that the SSDC is the best method for NCM estimation for hyper spectral images. To estimate the NCM, the image is divided into disjunct sub-images and MLP is used. For the MLP, the image is divided into disjunct squared sub-images. In the study from Regeling et al. [93], the sub-image size is chosen to be ten times ten pixels. However, there is no reasoning presented for this number. Therefore, this parameter might be varied if it seems necessary. For each sub-image, the MLP is calculated. As in the paper from Regeling et al. [93] the difference between re-projection and the real data is regarded as the noise as shown in equation 2:

$$r_{i,j,k} = I_{i,j,k} - \hat{I}_{i,j,k}, \tag{2}$$

where $\hat{I}_{i,j,k}$ is the re-projected value of $I_{i,j,k}$ and the residuum ($r_{i,j,k}$) is the difference between $I_{i,j,k}$ and $\hat{I}_{i,j,k}$ and it is considered as the noise.

However, this strategy of Regeling et al. [93] leads to strong boundary effects at the boundary of the sub-images as the noise is differently estimated at the boundaries than in the centre of the sub images. For compensation, the MLP is replaced by a regressive SVM (rSVM) in this thesis. This leads to much smaller differences between the centre and the edges of the noise estimation and therefore to less boundary artefacts between the sub-images. At the same time, the size of the sub-images can be increased. This has the advantage that the calculation speed is higher. Moreover, the sub-image size can be seen as input parameter which can be optimized to improve the final classification results. Thus in this study, $\hat{I}$ is the re-projected value from the rSVM. The rSVM is calculated by the "fitrlinear" command in Matlab. The "fitrlinear" command is recommended for high dimensional data. Thus, it is also favourable for HSI with many different wavelengths most likely also for MSI.

After the calculation of the residuum, I and r are reshaped into a matrix of which x-dimension covers all spatial dimensions and the y-dimension covers the amount of wavelengths (x_size · y_size, λ). The resulting matrices are named R_2 and X_2. First, the eigenvector expansion of the vectorized residuum matrix of the noise is calculated by singular value decomposition (SVD) which is shown in equation 3. The following derivation is a modified version from Regeling et al. [93] which is published by Hohmann et al. [120]:

$$S_1 = U_1 \cdot R_2^t \cdot R_2 \cdot V_1 \tag{3}$$

where the columns of V_1 are right-singular vectors and the columns of U_1 are left-singular vectors.

The result from the SVD of the covariance matrix is used to whiten the original data:

$$W_X = X_2 \cdot U_1 \cdot \left(S_1^{0.5}\right)^{-1} \tag{4}$$

where $^{0.5}$ is the element-wise square root and $^{-1}$ is the pseudo inverse of the matrix. The element-wise square root is used due to the fact that the singular values of the Matrix R_2 (the non-zero elements of S_1) are the square root of the positive eigenvalues of $R_2^t \cdot R_2$. From the whitened data the eigenvector expansion is calculated:

$$S_2 = U_2 \cdot W_X^t \cdot W_X \cdot V_2 \tag{5}$$

This can be used now to derive the transformation matrix:

$$\Phi = U_1 \cdot \left(S_1^{0.5}\right)^{-1} \cdot V_2 \tag{6}$$

As last step, the transformation matrix (Φ) has to be applied to the vectorized hyper spectral data-cube:

$$B = X_2 \cdot \Phi \tag{7}$$

The resulting Matrix B are the components of the hyper spectral data-cube sorted by their signal-to-noise-ratio (SNR). Therefore, the higher order components can be set to zero and the noise reduced hyper spectral image can be derived by the following equation:

$$X = B^* \cdot \Phi^{-1} \tag{8}$$

where B^* is the matrix B where the last components are set to zero.

A further important step in using MNF is to choose the right amount of components which are being used and which are set to zero. The amount of used components is selected by a scree plot. For the scree plot, the eigenvalues in S_2 are used. The selection of the right amount of components is important due to the fact that the usage of too many components would lead to an increased noise level while the usage of too less components would lead to a loss of information. In this study from the six components, at least the last two are set to zero.

Furthermore, Regeling et al. showed [93] that the first two components contain 94 % or 98 % of the information. Therefore, the same effect is tested with the data from the endoscope. Moreover, the MNF is applied to a diffuse reflection image provided by Chen Chen similar to published data from Chen et al. [121] for further testing of the filtering algorithm. This step allows to characterize the MNF method for a hyper spectral data set with a low amount of absorbers while for the human *in-vivo* study, a low amount of wavelengths

is used with a high amount of absorbers. Hence, it should be possible to conclude what effects the MNF has.

7. De-normalization For the de-normalization, the normalized multi spectral image of each colour channel is multiplied by the previously stored maximum of the respective colour channel as shown in equation 9:

$$I(x, y, \lambda) = \max_{x,y} I(x, y, \lambda) \cdot I_{norm}(x, y, \lambda) \tag{9}$$

8. Gaussian filtering As last step, a Gaussian filter is applied for every wave-length separately for further noise reduction. The Gaussian filter has a total size of 11 pixel and a standard deviation of 2 pixels. These sizes are chosen as they are good compromise of good noise reduction and not too much blurring of the images. These values are chosen for two reasons: First, it allows a better comparison with the results from Hohmann et al. [117] as in their study, the same values are used. Furthermore, the effect on the classification results is not significant for slight parameter variations. For much weaker filtering, the noise would not be removed effectively, resulting in a worse classification. For much stronger filtering the spectra of the healthy and cancerous areas would be mixed too much. Hence in summary, strong alteration of the values would degrade the results while small alterations would have no significant effect. To have comparison to the results from Hohmann et al. [117], the same values are chosen.

Feature generation and selection Figure 8 shows steps for feature generation and selection. It consists of three points: First, derivative images are generated. Afterwards, the step of generation spatial features is described and how features are selected by RFW and PCA.

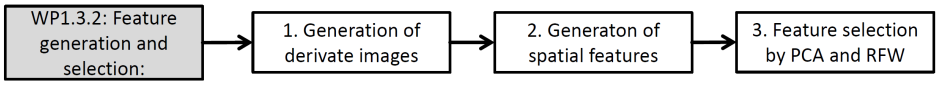

Figure 8: Overview of feature generation and selection. The grey box symbolizes the generic topic/research question and italic font symbolizes that this part of the flow chart will be shown as generic topic later.

1. Derivative images Additionally to the preprocessing, the right selection of the features for the later classification is of great importance [122]. In this study, two main ways of feature selection are realized. First, the intensity and the derivative values are used as features. Second, more features with focus on spatial features are generated by summing up a spatially coded part

of the surrounding of the pixel. A further set of features is used by also using the derivative images. For each wavelength, the derivative is calculated and used as feature. Thus for MSI, this leads to 12 basic features: 6 wavelength intensities and 6 derivatives.

2. Spatial features In this study, Laguerre-Gaussian functions (LG) are used to create spatial features. They are chosen because they allow to sum up a varying surrounding with positive and negative contribution of different elements. Moreover, they can easily be used as rotation invariant features. Furthermore in contrast to Gabor features, the features generated by LGs are expected to be more adapted to the irregular shape of carcinoma. Gabor features are most of the times proved to work for specific objects [123]. However, using Gabor features for every pixel would generate too much data as most of the times hundreds of Gabor features are needed. Moreover, the Gabor features can be seen as similar to Laguerre-Gaussian functions with l=1.

As further advantage, LGs are orthogonal. However, they are not orthonormal as they are used in this study. Due to the orthogonality, there should be no overlap of the information each LG represents. Therefore, it should be possible to generate independent spatial features for each LG.

Laguerre-Gaussian functions are the multiplication of a Gaussian function with the Laguerre polynomials where the Laguerre polynomials are defined as follows:

$$L_p^l(x) = \frac{\mathrm{e}^x\, x^{-l}}{p!}\,\frac{d^p}{dx^p}\left(\mathrm{e}^{-x}\, x^{p+l}\right) \tag{10}$$

where p is the p-th generalized Laguerre polynomial starting with p=0 . In this study, the Laguerre polynomials up to the order of $p = 3$ are used which leads to the following polynomials:

$$L_0^l(x) = 1 \tag{11}$$

$$L_1^l(x) = -x + l + 1 \tag{12}$$

$$L_2^l(x) = \frac{1}{2}\left[x^2 - 2\,(l+2)\,x + (l+1)(l+2)\right] \tag{13}$$

$$L_3^l(x) = \frac{1}{6}\left[-x^3 + 3\,(l+3)\,x^2 - 3\,(l+2)\,(l+3)\,x + (l+1)\,(l+2)\,(l+3)\right] \tag{14}$$

Together with the Gaussian function, the LG is combined in equation 15:

$$
\begin{aligned}
{}^{r}LG_l^p(x) = \exp\left((\rho \cdot s)^{\frac{2}{q}}\right) \cdot (\rho \cdot s)^{\frac{l}{q}} \cdot \\
\left[\cos\left(l \cdot \left[\Theta + \frac{2r\pi}{\max(2l,1)}\right]\right) \cdot L_l^p\left(\rho \cdot s \cdot \arctan[\rho \cdot s)]\right)\right]^{3-q}
\end{aligned}
\tag{15}
$$

where q and s are constants, ρ and Θ are the cylindrical coordinates and r is a parameter, describing image rotation with $(\{r \in \mathbb{R} \mid 0 \leq r \leq 1\})$. Thereby, $r = 0$ means no rotation and $r = 1$ means half of the rotation which would be needed for an identity projection. This is done due to the fact that ${}^{0}LG_l^p(x) = -{}^{1}LG_l^p(x)$. Combined with the fact that just the absolute values are used, the amount of rotation can be halved with this ansatz and therefore speed up the calculation time. Moreover to measure the surrounding, only the highest absolute value is of importance due to the fact that different images might be rotated towards each other. Furthermore, one point of tissue under investigation might be imaged from different angles and, thus, only the feature with the best matching direction will be the one used as a feature. Therefore, the features generated with LGs are rotation invariant. This ansatz also reduced the amount of features significantly and, thus, speeds up the analysis process.

The constant q can be set to one or two and determines if the amplitude or the intensity of the function is plotted. Due to the fact that negative numbers are needed for the feature detection q is set to 2[1]. The parameter p describes the radial behaviour and can be seen as a number which counts the amounts of zero crossings along the radial coordinate. The parameter l describes the azimuthal behaviour. It can be seen as the spin[2] of the LG function. The constant s is a constant to derive the right function for the LG-filter. The parameter s is chosen in a way, that the main features of the LGs are present without being bigger than the filter size. In the study, s is set to 18, p is used from 0 to 3, r is varied from 0 to 1 in steps of 0.25 and l is used from 0 to 4. The resulting LGs $L_p^l(x, y)$ are shown in figure 9. However by the free altering of s, the LG cannot be orthonormal but it might be orthogonal in practice. Due to the fact that the filters are restricted in size, orthogonality cannot be guaranteed and has to be tested.

[1] The exponent is defined as $3 - q$. Thus, $q = 2$ is required for negative values

[2] The spin describes the amount/angle of spinning which has to be done to reach an identical state: $\alpha = \frac{2\pi}{l}$ where l is the spin

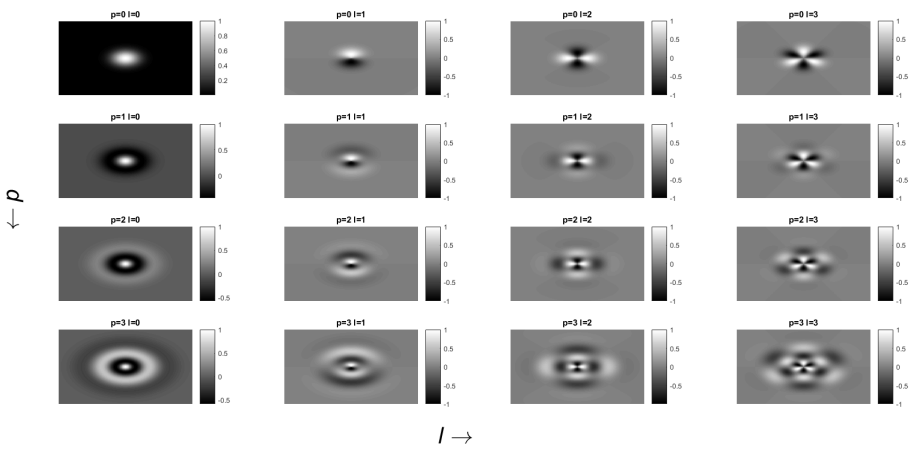

Figure 9: Laguerre Gaussian functions as used in this study for $q = 2$, $r = 0$, $s = 18$. On the upper left p and l are zero. Towards the right l is increased and towards the bottom p is increased. It should be noted that for $l \geq 1$ the outer change is very small and therefore barely visible.

The orthogonality can be calculated by the following integral:

$$\int_{x-k}^{x+k} \int_{y-k}^{y+k} {}^{r}LG_{p}^{l}(\hat{x},\hat{y}) \cdot {}^{r'}LG_{p'}^{l'}(\hat{x},\hat{y}) d\hat{y} d\hat{x} \tag{16}$$

where orthogonality is present if the integral from equation 16 is zero for $r \neq r'$, $l \neq l'$ and $p \neq p'$. This is tested for the l and p values used in this study ($l \leq 4, p \leq 3$). The results are shown in figure 10. For one block of four times four pixels, l is constant and p varies from 0 to 3. Thus, the diagonal four times four pixel sized boxes represent the variation of p for a constant l. It can be seen that the features with varying p are not orthogonal if l is the same. The bigger l gets the lower the orthogonality becomes. The reason of this behaviour can be seen in figure 9. Features with the same l probe in their centre similar information even if p is varying. The more outer parts of the function are different. Therefore, these features show informational overlap. However for varying l, the features are orthogonal even if p is varied. Thus, it can be concluded that most of the generated feature are orthogonal and, therefore, they probe a distinct or even disjunct set of information.

From these two points, two contradicting conclusions can be done: First, it might be that the PCA for feature reduction might group features with different p together in more important principal components than features with different l as features with different p probe similar information. Moreover, a

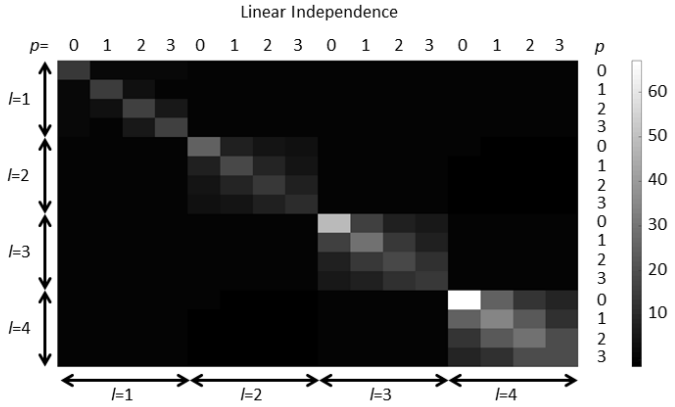

Figure 10: Equation 16 applied on all used Laguerre Gaussian functions. For one block of four times four pixels, l is constant and p varying. It can be seen that for all cases with different l, the features are independent.

varying p can also be seen as a feature which is dependent on the distance between endoscope and tissue. Therefore, if images are taken with different distances, a varying p might show the same spatial surrounding. Thus, p is expected to be dependent on the imaging during the endoscopy. Therefore, the features with same l and different p should also be more likely grouped together to more important principle components. As both conclusions are contradicting, it has to be tested which effect is more dominant in the final image analysis. One potential outcome would be that one principle component groups different p and a different one groups features with different l together.

The final features, used in this study, are calculated by integrating the multiplication of a single pixel and its surrounding with the Laguerre Gaussian functions which is seen in equation 17:

$$Feature(\hat{x},\hat{y}) = \int_{x-k}^{x+k}\int_{y-k}^{y+k} {}^{r}LG_p^l(\hat{x},\hat{y}) \cdot I(\hat{x},\hat{y}) d\hat{y} d\hat{x} \tag{17}$$

where k is half of the size of L_p^l. If this is done for the whole image, this process becomes a convolution. Therefore, equation 17 can be rewritten to the standard convolution if equation 17 is done for all values:

$$Feature(x,y) = \int_{\tau}\int_{\xi} I(\tau,\xi) \cdot {}^{r}LG_p^l(x-\tau, y-\xi) d\xi d\tau \tag{18}$$

Additionally, it should be noted that the calculations have to be done in a discrete space. Thus, the integrals in equation 17 has to be changed to sums:

$$Feature(x,y) = \sum_{\tau}\sum_{\xi} I(\tau,\xi) \cdot {}^{r}LG_{p}^{l}(x-\tau, y-\xi) \tag{19}$$

In this study, the "conv2" command from Matlab is used to do the complete convolution. After the convolution, the maximal absolute value for each set of l and p for varying r is taken for further processing. As mentioned before, this step ensures that only certain spatial features are probed and not their orientation. Another point to ensure better spatial variations and less sensitive behaviour to fluctuations is to test if

$$\int_{x-k}^{x+k}\int_{y-k}^{y+k} {}^{r}LG_{p}^{l}(\hat{x},\hat{y})d\hat{y}d\hat{x} = 0 \tag{20}$$

due to the fact that positive and negative parts should have the same impact on the final feature. This cannot be true for $p = 0$ and $l = 1$ because the function L_0^1 is always positive. However, this is no problem due to the fact that this term only probes a similar effect as Gaussian filtering. Moreover, testing shows that for all terms with $l \geq 1$ this condition is fulfilled as seen in figure 11 due to the symmetry of the resulting function.

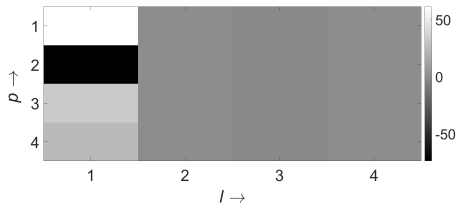

Figure 11: Equation 20 applied on all used Laguerre Gaussian functions. It can be seen that for all cases with $l \geq 2$ the integral is zero.

The LGs are generated with a resolution of 40 times 40 pixels and they are rotated in five steps for $\frac{180}{l}$ degree. The size of forty pixels is chosen as it is a compromise from not using to much of the surrounding and having enough pixels to represent the features well enough. Afterwards for every rotation, the convolution is calculated for each wavelength of the multi-spectral image. For each wavelength, the maximum of the absolute values for the different rotations is used as feature. This step is done to reduce the dimensionality of the data and to take into account that the same carcinoma might be imaged from different directions and/or distances.

3. Feature selection by PCA and RFW After feature generation, the features are used as input parameter for the classifiers and the best features are selected for the analysis. This is done to reduce the amount of features and, therefore, the calculation time and to correlate the best features with the morphology. For this reason, two main ways are done to select the features. First, like in the study from Hohmann et al. [117], the PCA is used for feature reduction. Additionally, the PCA allows to test which variance is required. Thus, the analysis will be done for using 90 %, 95 % and 99 % of the variance.

As second way of feature reduction, the RFW can be used. Due to the fact that RFW uses out-of-bag (OOB) information, the OOB-error can be tested for each feature separately. Therefore, the OOB-error can be defined as a measure for feature importance. The better the OOB-data is described by a single feature, the higher is the feature importance. By calculating the feature importance for the training data set, the most important features can be selected. These features are used directly for the classification. The RFW-method has the advantage to tell directly the most important features. As the RFW selects the n most important features, all the information from the other features are discarded. Therefore, information might be lost and furthermore the noise will be higher due to the lack of combination of features.

For the final analysis, four to ten features are selected and used for classification. For the leave-one-out analysis, for each case the most important features are stored. From these stored features, the histogram is calculated to identify the used features and to derive their importance.

Classifiers The most essential part of the analysis is the classification of the data. After the pre-processing of the data and the generation of the features, the data has to be classified. The classification is done for each pixel separately. By using spatial features, many of the features use information about the close surrounding. For classification, a SVM is used with a Gaussian Kernel and another one with a linear kernel. SVM is chosen because it proved to be a good classifier for HSI classification [79–81]. Moreover, AB is used with a tree learner due to the fact that it shows normally similar results as SVM. Additionally, RB is used as it is more robust against mislabelled training data [85, 87]. Hence, it is well suited for the classification problem in this study. RFW is used because it is an advanced version of AB which is also robust against labelling noise [86]. Furthermore in some cases, RFW shows superior classification performance for cancer classification [124] or for the analysis of hyper spectral images [125] when compared to SVM.

The test data is generated by cross validation with a leave-one-out strategy. Therefore, one patient is chosen as test data and all the rest are used as the

training data. The leave-one-out strategy is chosen due to the fact that it is the only one which can be tested exhaustively because it minimizes the amount of potential combinations which have to be tested and, therefore, it reduces also the computation time. At the same time, there is no bias towards good results due to manual selection of patients. For the case that a leave p out analysis would be done and n is the amount of patients and p the amount of patients used for the leave out there will be $\binom{n}{p}$ combinations. For example, for 20 patients the leave-one-out strategy would lead to 20 combinations. A potential leave-two-out strategy would already have 190 combinations. This would increase the calculation time by nearly a factor of ten. A ten times longer calculation time would decrease the possibility for a feasible data analysis significantly. Furthermore, the leave-one-out strategy provides more information about a specific patient due the fact that there is only one left out at the same time. Therefore, the leave-one-out analysis is preferred.

Moreover, the dataset can be separated into training data, test data and OOB data. For example if the leave-one-out analysis with 20 patients is done with OOB data, one patient would be removed from the data set as out of the bag data. For the rest of the 19 patients the normal leave-one-out analysis would be done and the best classifier would be tested with the out of the bag data. Due to the increase of required training and test procedures the calculation time would increase by a factor of n-1. To prevent the long calculation time, the OOB strategy is not performed.

For the training procedure, only a certain percentage of the actual training data is used for training to speed up the training process. However for the feature reduction by the PCA, the full dataset is used. By performing the PCA with the reduced dataset, the classification results would worsen significantly. Furthermore, the extra calculation time is less than a minute and, therefore, acceptable. For the parameter study, 0.25 % of each patient's data is chosen randomly for the training step to reduce the calculation time for the parameter study. For the comparison with the state of the art, 1 % of each patient's data is chosen randomly for the training. For the analysis of the mice experiments, 1 % of each patient's data is chosen randomly for the training. The parameter study uses less training data than the comparison to the state of the art to speed up the calculation time. It should be noted that multiple random selections of different data sets for the classification do not show a significant influence on the final classification result. This happens due to the fact that 1 % of a few million data points are chosen. Hence, a realistic sample is selected. Furthermore for the usage of the PCA, it is done on whole data set.

The data analysis for all classifiers is done with Matlab 2017b. For the complete analysis, the same Matlab version is used to prevent alteration of the classification results as the implemented methods are used:

- *fitensemble* for AB, RB
- *fitcsvm* for SVM
- *treebagger* for RFW
- *predict* for all

These methods have the disadvantage of a long calculation time. One leave-one-out analysis takes approximately a week for all classifiers despite the reduction of the training data to one per cent. Thus, all schemes for reduction of the calculation time are done.

After the training data is prepared, all classifiers get the same training data. AB and RB are used with a decision stump tree classifier. The maximum number of splits is set to one, the minimal parent size (minimal amount of observations for nodes) is set to two and the minimal leaf size (minimal size of observations for leafs) is set to one. AB stops after training of 500 weak learners and RB latest after 300 weak learners. This number can be chosen high due to the fact that both classifiers are resistant against over-classification. For RFW a deep tree learner is used. The maximum number of splits is set to the amount of predictors minus one, the minimal parent size is set to two and the minimal leaf size is set to one. RFW stops after training of 500 weak learners. For both cases of the SVM, the settings for *fitcsvm* are on auto and the classifier centres and scales each column of the predictor.

Due to the fact that a certain amount of the data is mislabelled, an additional step is introduced to find outliers. For the SVM with a linear kernel and the SVM with the Gaussian kernel a second step is introduced which selects 0 % to 10 % of the training data as outlier. With this, the effect of the outliers in the PCA-space is probed. The training of a SVM with the training data is done with a Gaussian kernel for a single class. The training is done in a way that everything except the outlier rate is seen as belonging to one single class. For the final classification, the best set is chosen. The found outliers are discarded for the training process.

In contrast to SVM, for RB an expected outlier rate has to be selected. The outlier rates of RB within the range of 5 % to 35 % are tested. The training of the data is done like for Adaboost. However, the percentage of the data with the highest margin is considered as outlier. These data points are not used for the training of the classifier. The data points considered as outliers may change during the training process. In the final classifications, the best suited

outlier rates are used. It should be noted that the different ways of finding the outliers leads to a different optimal outlier rate for both methods.

Furthermore in comparison to the outlier finding of the SVM, the outlier rate of RB should give an estimation of the upper limit of the outliers present in the data. It is expected to be an upper limit due to the fact that with too high outlier rates the results degrade again. Thus, if the chance of wrongly been seen as an outlier or correctly labelled data is similar, more data will be wrongly seen as outlier than the other way around. Such an effect can be seen with dummy data. If 10 % of the data is wrongly labelled, the classification with an outlier rate around 12-14 % will lead to the best classification results of the test data set.

Moreover, the analysis of the data is done for three further different entities: adeno carcinomas in the oesophagus, squamous cell carcinomas in the oesophagus and BE. The analysis is done with the final parameter sets where a transfer of the classification schemes is tested. Therefore, the analysis is not done with extensive parameter optimization. Due to the low amount of GIST present, it is considered as adeno carcinoma of the stomach. Moreover from the histological view, it is very similar to adeno carcinomas from the stomach. The main focus of this study is the analysis of adeno carcinomas in stomach due to the fact that the most data is available from this class and moreover it is the easiest entity and, therefore, the best to test the new method of *in-vivo* MSI.

Evaluation of the classifiers Even if the most essential part of the data analysis is the classification, there has to be a measure for the evaluation of the classifiers. The evaluation is normally done by the calculation of the sensitivity (SEN), specificity (SPE) and accuracy (ACC). Equations 21 to 23 show the calculation of SEN, SPE and ACC:

$$SEN = \frac{TP}{TP+FN} \tag{21}$$

$$SPE = \frac{TN}{TN+FP} \tag{22}$$

$$ACC = \frac{TP+TN}{TP+TN+FP+FN} \tag{23}$$

where TP is the amount of true positive results, TN is the amount of true negative results, FP is the amount of false positive results and FN is the amount of false negative results. Equations 21 to 23 present the standard way of characterizing a two class problem. However, the usage of the ACC might lead to wrong results if one class is dominant. For example if 90 % of the data represents the healthy part, classifying everything as healthy would lead to an accuracy of 90 %. However, the classification results would be useless.

To compensate this effect for asymmetric datasets, another metric is defined in equation 24. It should be noted that the classical definition of a metric does not apply however the term will be used nevertheless due to the fact that the behaviour is very similar.[3]

$$ACC2 = \frac{SEN + SPE}{2}. \tag{24}$$

Equation 24 defines the ACC2 as the mean of the sensitivity and specificity. In the previous example in which the ACC failed, the ACC2 would be 0.5 and, therefore, would correctly predict the bad classification result. However, the ACC will still be shown because it shows the overall percentage of correct classified samples and it is a standard method in the literature.

Additionally to ACC2, the Matthews correlation coefficient (MCC) can be calculated [126]:

$$MCC = \frac{TP \cdot TN - FP \cdot FN}{\sqrt{(TP + FP)(TP + FN)(TN + FP)(TN + FN)}}. \tag{25}$$

Similar to the ACC2 it is a balanced measure of an accuracy-like metric. Its main advantage is that it can be used also for problems with very different class sizes. In one report, it is stated to be the best available single value to characterize the classification in a single number [127]. However, it should be noted that in contrast to all other previously mentioned metrics, it scales from -1 to +1 where the value 0 corresponds to an ACC2 of 0.5.

Despite the high quality of these metrics, they all rely on a specific operation point of the classifier of a specific subset of SEN and SPE. In general, classification works in a way that the input data set is imaged into a set of real numbers: $f(\text{dataset}) : \mathbb{R}^f \rightarrow \mathbb{R}$. This behaviour is true for SVM, AB, RB and RFW which also image the f features into a real score value. For the two class case, everything below zero is one class and everything above zero is the other class. Moreover, it can also be said that the score value describes the confidence of the classifier. For SVM, this value can even be used to derive a posteriori probabilities if calibrated accordingly.

By altering at which score the data is sort into the classes, the weight towards one class can be changed in such a way that only classes are sorted into a specific class if the classifier is "sure". By varying the threshold for the class selection, a receiver operating characteristic (ROC) curve can be generated. This allows to derive the sensitivity as the function of the specificity or the

[3] definition pseudo metric: $d(x,x) = 0$, $d(x,y) = d(y,x)$ and $d(x,y) \leq d(x,z) + d(z,y)$. for a metric additionally: $d(x,y) = 0 \Leftrightarrow x = y$

other way around. However most of the time, the false positive rate (FPR), shown in equation 26, is used instead of the specificity. Therefore, the FPR is also used in this study.

$$FPR = \frac{FP}{FP + TN} \tag{26}$$

The ROC allows to define a new metric for measuring the quality of the classifier: the area under the curve (AUC) of the sensitivity as function of the false positive rate. In comparison to the ACC, ACC2 and the MCC, the AUC takes the whole score of the classifier into account. Thus, the overall quality of the classifier is evaluated.

To reduce the calculation time, a single metric will be chosen as main metric on which the classificator gets optimized due to the fact that the four metrics might find the best result for different input parameters. In this case, the best result would have to be found for each metric separately. To decide for the best metric, the optimisation of the mislabelled data amount of SVM and RB is done for ACC, ACC2, MCC and AUC. Based on the results, a final metric is chosen on which the results are optimised on. For the final results however, the values of all metrics will be presented. For the whole analysis, the evaluation of the classifiers is done on a pixel basis. Hence, for every pixel it is checked if it is correctly labelled. Doing this for all images provides the previously described values of ACC, ACC2, AUC and MCC. The comparison if a pixel is classified correctly is done using the tumour margins drawn by the medical expert.

4.1.4 Parameter studies

Before a comparison to the state of the art from Hohmann et al. [117] can be done, the new sets of parameters are tested. Thus, all parameter studies are done with adeno carcinomas in the stomach. Figure 12 shows an overview about all tested parameters. Six main parameters are tested:

- The number of features used for the classification
- Feature delocalization
- Outlier rate
- Kind of feature selection
- MNF cut
- Comparison to the basic classifiers

These features require sometimes multiple specific parameter changes. Table 5 summarizes all tested parameters of the parameter study. Due to the amount of parameters only one parameter is tested at the same time while the others remain constant.

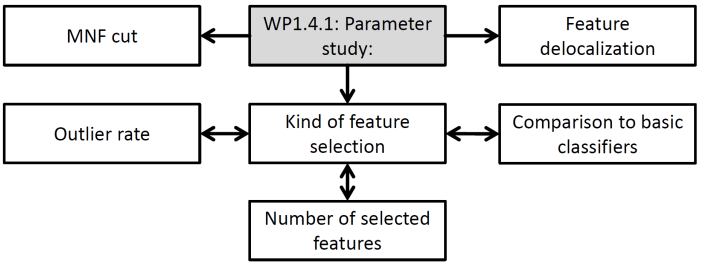

Figure 12: Overview of the parameter study. The grey box symbolizes the generic topic/research question and italic font symbolizes that this part of the flow chart will be shown as generic topic later. The two sided arrows symbolize parameters which are studied in full dependency from each other in which all combinations are tested.

Table 5: Summary of the parameters varied for the parameter study.

Number	Parameter	Range
1	Kind of feature selection	PCA, RFW
2	Selected variance in PCA	90 %, 95 %, 99 %
3	Features selected by RFW	4, 8
4	PCA features selected by RFW	4, 8
5	First n features selected by RFW	8, all
6	Feature delocalization	yes, no
7	MNF cut	2, 4
8	Outlier rate SVM	0.02- 0.26
9	Outlier rate RB	0.05- 0.45
10	Comparison to basic classifiers	QDA, KNN, naive Bayes

To speed up the calculation time, only LG-components up to $p = l = 2$ are used. Table 6 shows the resulting naming/numbering of the features. For each wavelength, first p and then l is varied. The wavelengths are sorted according to table 2. For each feature, five steps of rotation are used, being equal to the r parameter of 0, 0.2, 0.4, 0.6 and 0.8. This leads to a maximal rotation of 36 degree (for $l = 1$) which is resolved. The sub-image size for the MNF is ten as chosen by Regeling et al. [93] for the first parameter study. The PCA is only calculated for the data labelled as carcinoma to increase the sensitivity of the results [128] because most of the time the sensitivity is lower than the specificity. Furthermore, for the carcinoma labelling a save margin is introduced. From the final labels from the medical expert, the healthy area

Table 6: Sorting of the feature number for one wavelength. For each wavelength, first the intensity is used, then the derivative is used and afterwards the spatial features are taken. For the spatial features, first l is varied and than p.

Feature	**1**	**7**	**13**	**14**	**15**	**16**	**17**	**18**
λ in nm	438	438	438	438	438	438	438	438
p	-	-	0	0	1	1	2	2
l	-	-	1	2	1	2	1	2
intensity	yes	no	no	no	no	no	no	no
derivative	no	yes	no	no	no	no	no	no

as well as the cancerous area is reduced by a five pixel wide save margin. This effects should reduce the amount of mislabelled data points.

The first tested parameter is the kind of feature selection (table 5, number 1). For this, it will be tested if the PCA or the RFW is the better way to select features. Nevertheless for both ways of feature selection, a different parameter has to be optimized: Data with which percentage of the variance is used (table 5, number 2) for the PCA method and how many features are selected by RFW (table 5, number 3). For RFW, the best 4 and 8 features are tested and compared and for the PCA the first principal components with a total variance of 90 %, 95 % and 99 % is used for testing. As both methods are independent from each other, also the combination of both of them is evaluated. First, the PCA is calculated and instead of using the first n features which account for a certain variance, RFW is used to select the best 4 or 8 best principal components (table 5, number 4). It is also tested if the feature reduction by the RFW does worsen the results in comparison of using all features (table 5, number 5).

The next parameter taken into account is the delocalization of the spatial features (table 5, number 6). By a strong filtering of the spatial features with a Gaussian filter, irregular feature areas are homogenized and, therefore, the effect of the features is delocalized. Due to the fact that the spatial features can appear only locally but very strong, they might only provide a good classification at these specific points. By using a Gaussian filter, the effect also applies to the surrounding of which the features has been generated from. This parameter is tested in combination with both methods of feature selection.

Afterwards, the amount of features which are used for the MNF, are tested (table 5, number 7). One time, only the first two features are used

and the second time the first four features are used. These two numbers are chosen due to the fact that the scree plot shows after 2 and 4 features a strong decay of the importance of the components for noise reduction. This parameter is called MNF cut.

For RB and SVM, the effect of the outlier rate is tested due to the fact that the introduction of the MNF and the additional spatial features might change the optimal outlier rate used in the study from Hohmann et al. [117] (table 5, number 8,9). For the SVM, the outlier rate is varied from 0.02 to 0.26 and for RB, the outlier rate is varied from 0.05 to 0.45.

As further step, a comparison of the results should be done to basic classifiers (table 5, number 10). This comparison allows to quantify the benefit from the advanced classifiers. The bigger the difference between the results, the bigger the fragmentation of the classes. For this reason, quadratic discriminant analysis (QDA), naive Bayes with and with out a kernel smoothing density estimation and k-nearest neighbours (KNN) are tested. The classifiers are chosen because they are very resistant to over-fitting and only a few parameters have to be adjusted. Moreover, QDA and KNN are comparable fast.

QDA is not dependent on any further parameters. Naive Bayes mainly depends on the kernel smoothing width, while KNN mainly depends on the amount of neighbours used for classification and the kind of the metric for calculating the distance. For each of these classifiers, an optimization of the parameters is done with cross-validation of the training data before the training.

For the results, AUC and MCC are mainly used for the parameter study. All parameters (ACC, ACC2, AUC, MCC) are shown, however, the AUC and MCC are highlighted. An ANOVA is not done for each parameter separately due to the fact that only 0.25 % of the data is used for training and, therefore, a single feature will not provide a statistical significant effect. Nevertheless, the total amount of improvements is tested in chapter 4.1.6 (Comparison to the state of the art).

4.1.5 Analysis of spatial features

After the parameter study, it is studied which features are relevant. For this, both previously used feature selection methods are used: RFW and PCA. As RFW splits the training data into training, test and OOB data, the important features for a reliable classification of the OOB-data can be used as a measure for the feature importance. For the PCA, the loadings of the principle components can be analysed. By investigating patterns, the principle components are characterized. Furthermore, the combination of both is analysed. Thereby,

the principle components are selected by RFW. The analysis is done for data sets from the parameter study. The focus is on the feature de-localization, as this might alter the selection of the features. Moreover, this newly introduced parameter can be characterized.

4.1.6 Test of intra patient variations

After the parameter study is done for inter patient variations, the analysis with the best parameters is tested for intra patient variations. This is done to ensure that it might be possible with enough training data sets to reach a reliable classification. The intra patient analysis is done using 1 % of data from all the patients as the training data. Afterwards, the complete data set is used for testing of the classifiers. As in the parameter study, a save margin of five pixels is used to compensate labelling errors.

4.1.7 Comparison to the state of the art

The comparison of the results to the state of the art is done to the results from Hohmann et al. [117], shown in table 7. Doing this comparison, the importance of the feature generation can be tested.

For the analysis, 1 % of the data is used for the analysis as it is the same amount used in the study from from Hohmann et al. [117]. Spatial features are used for $p \leq 2$ and $l \leq 4$. The rest of the parameters are unchanged in comparison to the best results from the parameter study.

Table 7: Classification results of the tested classifiers for 14 patients with leave one out strategy from Hohmann et al. [117].

Method	SEN	SPE	ACC	ACC2
Random Forest Walk	0.56	0.62	0.55	0.59±0.08
RobustBoost	0.63	0.65	0.64	0.64±0.09
SVM linear kernel	0.57	0.62	0.61	0.60±0.11
SVM Gaussian kernel	0.66	0.52	0.56	0.59±0.09
AdaBoost	0.56	0.63	0.55	0.59±0.08

Hohmann et al. [117] were able to reach a maximal ACC2 of 0.64 for RB. SVM with a linear kernel has a ACC2 of 0.60 while RFW, AB and SVM with Gaussian kernel show worse classification results. For the later comparison, the accuracy and accuracy2 are used and provide the benchmark for the following analysis. The comparison is done according to the best results from section 4.1.4. The

comparison to the state of the art is evaluated with a two-way ANOVA where one dimension is the classifier and the other one the dependence on the new features. It should be noted that the expected significance is rather low due to the fact that only 13 patients are available in total. Thus, the results only provide hints.

4.1.8 Comparison to medical conditions

The results of the classifications are compared to medical conditions of the patients. For this, the amount of present mucus, the strength of the inflammation and the fact if the patient underwent therapy before will be considered. It is tested how these three parameters effect the classification results. A strong inflammation might disguise the carcinoma and a high amount of mucus will most likely disguise the carcinoma. As a second step, the effect of pre-treatment is tested for the patients and if the pre-treatment will worsen the classification results due to its removal of the carcinoma. This comparison is also done for patients without strong mucus and/or inflammation. This is done to ensure that the effect of pre-treatment is not overlaid with the effect of mucus and inflammation.

4.1.9 Analysis in the oesophagus

After the classifiers are optimized and tested for adeno carcinomas in the stomach, the analysis is done for carcinomas and pre-carcinomas in the oesophagus. First, the analysis is done for BE. Afterwards, the analysis is done for patients with adeno and squamous cell carcinomas in the oesophagus. Both carcinomas in the oesophagus are mixed due to the fact that not enough patients are available for an independent analysis.

For the analysis, the same parameters as in the analysis of the carcinomas of the stomach are used. The effect of the PCA and the effect of the spatial-spectral features are tested. All other parameters remain constant. The amount of the data used for training is 0.25 %. Also the leave-one-out analysis is done for all disease types.

For the analysis of BE, 13 patients are tested. All of these 13 patients were suspected to have BE. However, for four of them the histology showed that no BE is present. These four patients are seen as healthy for the training and testing as the presence of BE should be tested. Therefore, additional to the pixel based accuracy, it is tested if the patients with or without BE can be identified. The analysis if BE is present is done, by visual inspection of the results of the best classifier. If only a small area shows BE or many small areas show BE from the classification, it will be assumed that the classification

shows no BE. This is done as BE does not appear in these shapes. If a wide area shows BE with a few exception, it will be interpreted as BE is present.

This leads to the following rules used for classification. If in a certain area healthy and sick tissues are mixed, it will be seen as healthy if more tissue is classified healthy and the other way around. The shape of the found BE has to match that of a typical shape for BE by visual inspection. Due to the fact that for each patient more than one image is taken, the decision is done for each image separately and the final decision if a patient has BE is done by majority of images (majority vote)[4].

4.2 Spectral spatial variation

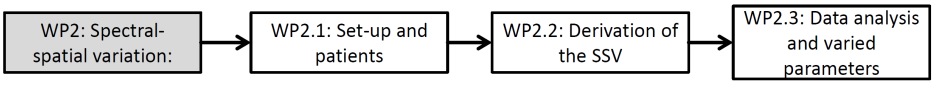

Figure 13: Overview of the second working package. Each box symbolized one sub chapter and corresponds to the headlines. The grey box symbolizes the generic topic/research question and italic font symbolizes that this part of the flow chart will be shown as generic topic later.

In this WP2, the SSV is introduced. Figure 13 provides an overview over all sub chapters for WP2. In general, the most part of the methods are the same as in WP1 in chapter 4.1 (In-vivo multi spectral human study). Nevertheless for a better overview, a small summary of the important points is provided.

4.2.1 Set-up and patients

For WP exactly the same endoscope as well as the same data set as in WP1 is used. The data analysis is done for the 13 patients with carcinoma in the stomach.

4.2.2 Derivation of the SSV

The residuum is calculated with equation 2 ($r_{i,j,k} = I_{i,j,k} - \hat{I}_{i,j,k}$). Thereby $\hat{I}_{i,j,k}$ is the re-projected value of $I_{i,j,k}$ and as before is calculate by a regressive SVM. The residuum $r_{i,j,k}$ is seen as the SSV as it contains spectral and spatial information about the surrounding of a pixel. This combination is the essential idea of this chapter. With a comparable simple step, a new spectral spatial feature can be introduced. As the MNF of noise reduction is a recommended pre-processing step, the SSV does require only little additional calculation time. In comparison to the usage of spatial features and other spectral spatial

[4] E.g.: If in more than half of the images BE is found, the final decision will be BE.

methods, the SSV combines the spatial and spectral fluctuations to a single noise term. Therefore, it might lead to improved results as well as a reduced feature number.

4.2.3 Data analysis and varied parameters

The pre-processing as well as the classification is done the same way as in WP1. To ensure the usability of the SSV, three parameters are varied: MNF cut, the sub image size and if spatial features are used. The sub image size is the size of the sub image in equation 2 for which the regressive SVM is done. Afterwards, it is tested if the improvement is statistically significant. The comparison is done between all parameters. The statistical significance is tested with a five way ANOVA test for repeated measurements with the dimensions: classifiers, effect of the subimage size, effect of the filtering by the MNF, usage of spatial features and usage of the SSV. The ANOVA test is used as it allows to use all five dimensions at the same time to provide a more significant result. However due to the extended calculation time, not all parameters are varied to the full extend. This is done due to the fact that one complete analysis for one feature combination would take approximately one week.

4.3 Monte-Carlo study of the effect of mislabelled carcinomas

The precise evaluation of the classifiers might allow to pinpoint the different spatial features which are visible with only certain wavelength bands. However, it is not known what causes the features or wavelength bands to be the most important ones. Also it is not possible to derive this information from the patients due to the fact that from the patients only the multi spectral pictures and a few points of the biopsies are known for each carcinoma. The exact margin of the carcinoma is not known for the clinical data set as the biopsy cannot be done on all parts of the image. Furthermore, potential measurements on the patient would be done in a complicated system which does not provide a controlled environment. To overcome this issue, MCS of multi spectral images can be used.

Figure 14 shows an overview of the Monte-Carlo study. In the first point, the simulation itself is shortly explained and how it is validated. In the second part, it is described how the inter patient variations are modelled. In the third part, the model for the MCS is explained followed by how the mislabelled data set of the carcinoma is generated. In the last section of WP3, the study of the effect of mislabelled carcinomas is presented.

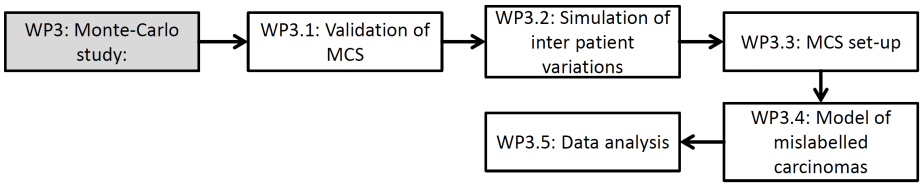

Figure 14: Overview of the third working package. Each box symbolized one sub chapter and corresponds to the headlines. The grey box symbolizes the generic topic/research question and italic font symbolizes that this part of the flow chart will be shown as generic topic later.

4.3.1 Validation of MCS

For the simulation, an own graphic processing unit (GPU) based MCS is used to reach the necessary speed. To allow a reliable usage of the MCS, it has to be validated first. For this reason, it is validated against Monte-Carlo Extreme (MCX) [129] and against the diffusion theory. For the comparison, a three dimensional volume is simulated as shown in figure 15. The simulation

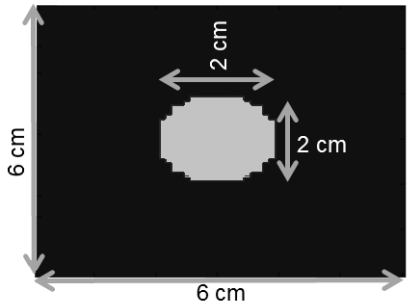

Figure 15: Cut through the set-up for the validation of the MCS: The light comes from the bottom and hits the sample in the centre.

parameters are the same as in the paper from Fang et al. [129]. The simulation volume is a cube with an edge length of 6 cm. In the centre of the simulation volume is a spherical structure with a diameter of 2 cm. The outer part of the sample has an absorption coefficient of 0.002 mm^{-1}, a scattering coefficient of 1 mm^{-1} and a g-factor of 0.01. The inner part has an absorption coefficient of 0.005 mm^{-1}, a scattering coefficient of 5 mm^{-1} and a g-factor of 0.9. The total amount of simulated photons is set to 67 millions. For comparison with diffusion theory and MCX, a cut in the centre is compared. To enable a precise comparison, MCX as well as the MCS from this study are normalized and used for comparison.

4.3.2 Simulation of inter patient variations

After the simulation is validated, the multi spectral images are simulated. For the simulation, a carcinoma in oesophageal tissue is simulated due to the fact that the optical properties (μ_a, μ_s or g) of these tissue types is known. The optical properties are taken from the study from Holmer et al. [130] instead of the own optical properties which were published before [131] due to the fact that Holmer et al. [130] measured the optical properties from carcinoma and from healthy oesophagus. However, there is a high chance that the measurements from Holmer et al. [130] have a systematic error as shown by Hohmann et al. [131]. Despite the fact that they use cryo-homogenisation, this should not influence the optical properties [132]. Thus, the source of the potential error cannot be explained. Moreover, the reconstructed optical properties often differ from group to group [133]. Therefore, it is better to use the data for two tissue types from one group. Thus, it can be expected that healthy tissue and the carcinoma tissue should have a similar systematic error and, therefore, it makes more sense to use the dataset from Holmer et al. [130] since the difference between both tissue types is likely realistic.

To derive the optical properties and include inter patient variations, the following strategy is chosen: First, a centre value is calculated and, second, the variations are derived. The centre value of the optical properties is derived by averaging the optical properties for each spectral bandwidth using the spectra of the illumination source as weight from the spectra of the light source for the endoscope. By integrating the optical properties (μ_a, μ_s or g), abbreviated with OP, times the normalized intensity (I) of the light source, the final optical properties are calculated as weighted mean, shown in equation 27:

$$OP_{average} = \frac{\int_{\lambda_a}^{\lambda_b} I(\hat{\lambda}) \cdot OP(\hat{\lambda}) d\hat{\lambda}}{\lambda_b - \lambda_a} \tag{27}$$

where λ is the wavelength and λ_b and λ_a are the boundaries at which the intensity (I) becomes zero. In total, the following seven centre wavelengths are simulated: 396, 437, 474, 511, 549, 574 and 637 nm.

In a realistic tissue, every patient has slightly different optical properties for all organs. This effect can be seen for example at the varying skin colour of different people. These inter patient variations of the optical properties is taken from the standard deviations from Holmer et al. [130] as it is the only data available. Due to the fact that Holmer et al. [130] show only three values for the standard deviation, the missing data points of the standard deviation are interpolated. First, the relative standard deviation is calculated. A linear fit is used to generate the data for the wavelengths used in this study. This step is

done as the data is required. An optimal solution for later applications would be to switch to Bayesian statistics to generate a-posteriori information as shown by Kreiß and Hohmann et al. [134] for diffuse reflectance spectroscopy.

For the simulation, it is assumed that most of the standard deviation of the optical properties is caused by the inter patient variations from the study from Holmer et al. [130] and not from random variations of the measuring procedure. Due to the fact that they dissociated the oesophagus, the intra patient variations should be much lower compared to physological conditions.

The inter patient variations are derived by using a relative standard deviation from the mean values and varying it with a Gaussian distribution with the same full width at half maximium (FWHM) as the relative standard deviation. It should be noted that this assumption might not be true because most likely the distribution of the optical properties is not Gaussian. However due to the fact that Holmer et al. [130] assumed a Gaussian distribution, the same assumption has to be done in this study. Furthermore, it is expected that the variation of μ_a, μ_s and g might not be independent from each other. However to date, there is no information on any dependencies and, therefore, this effect has to be neglected.

For the simulation, the variations of the optical properties cannot be seen as wavelength independent. For example, a variation of the scattering for blue light is not independent of a variation of the scattering for red light. Normally, a change of scattering in one wavelength range implies a change of the scattering in another wavelength range. However, as the functional dependence between different wavelengths is not known, an additional random fluctuation should be considered to allow wavelength dependencies. For the scattering, this might be caused by different sizes of the scatterers.

As the functional dependencies are not known, a more practical approach is chosen. The effect of the same relative variations across all wavelengths and a completely random fluctuation is considered. The same relative variation of the scattering coefficient and/or the g-factor would lead to a different penetration depths and the tissue would appear brighter or darker without major changes of the tissue colour. The same relative variation of the absorption coefficient across all wavelengths would have a similar effect compared to the scattering. However, the largest difference would be for the wavelengths with a high absorption coefficient. As in the tissue, blood as red absorber is present, the tissue would appear more or less reddish and, therefore, the amount of blood in the tissue would be varied with this. Both variations are realistic and definitely play a major role in the inter patient variations.

In contrast, if the optical properties are varied randomly for each wavelength, the colour of the tissue would change independent from the three optical properties. This effect is present only weakly in healthy tissue as for most healthy tissue the colours are similar but they are not identical. However for cancerous tissue, this effect might play a bigger role due to the fact that in the upper GI, carcinomas might appear reddish to discoloured [14].

To simulate both effects, for healthy tissue 80 % of the variation is assumed to occur due to the same relative variations across all wavelengths. This effect should not alter the colour significantly nevertheless it should allow small fluctuations between the patients. For the cancerous tissue only half of the variations is assumed to occur due to the same relative variations across all wavelengths to allow discoloured carcinomas. However, it should be noted that there is no way available currently to derive these numbers with a higher precision than with educated guessing. Nevertheless, this effect should be considered as carcinomas might appear reddish to discoloured [14] and healthy tissue appears more similar between patients.

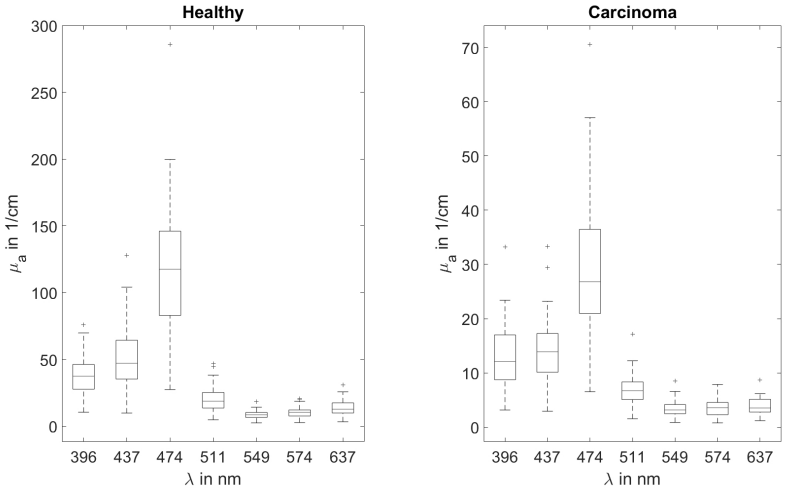

Figure 16: Boxplot of the random values used for the simulation of the absorption coefficient for the healthy and cancerous tissue.

Taking all the previous effects into account leads to the following optical properties which are shown in figure 16, 17 and 18. Figure 16 shows a boxplot of the absorption coefficient. Figure 17 shows a boxplot of the scattering coefficient. Figure 18 shows a boxplot of the g-factor. It can be seen that the scattering coefficient as well as the absorption coefficient varies more than a factor of two. The g-factor varies less, however, its effect on the back scattering

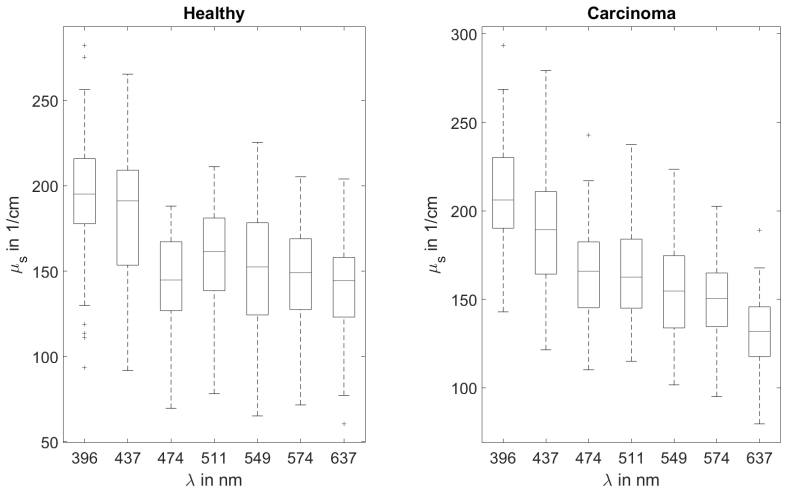

Figure 17: Boxplot of the random values used for the simulation of the scattering coefficient for the healthy and cancerous tissue.

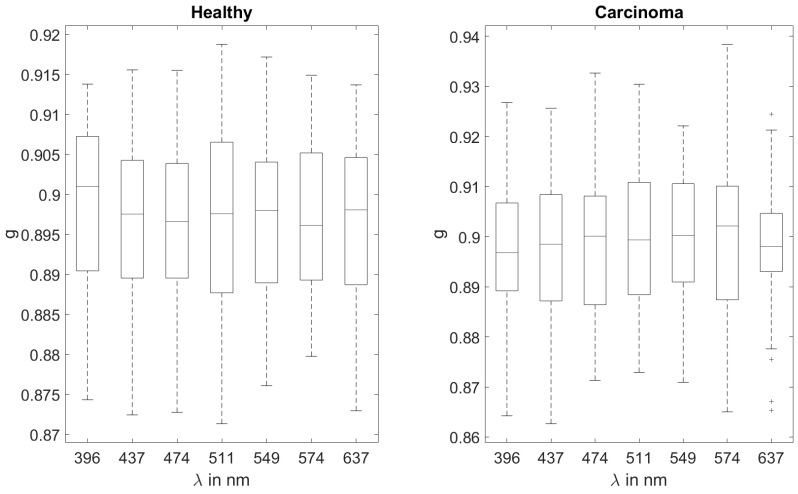

Figure 18: Boxplot of the random values used for the simulation of the g-factor for the healthy and cancerous tissue.

is fairly high due to the strong effect on the effective scattering coefficient $\mu_s' = \mu_s \cdot (1 - g)$.

4.3.3 MCS set-up

After the optical properties and the inter patient variations are set, the geometric set-up is the next thing to consider. The set-up for the MCS is illustrated in figure 19. The upper surface is divided into nine equally sized squares. This is done as only photons from the inner square are considered for detection. Furthermore, only in the centre square the carcinoma is placed. Thus, the sketch in figure 19 shows the inner square. The whole set-up has a volume of 15 x 15 x 15 mm^3 as bulk tissue. The simulation volume is chosen to be small for two reasons: First to speed up the simulation process. Second, there is an overlap area at boundary at the carcinoma where its effect on the back reflection fades out more the further away you are from boundary. For bigger carcinomas, the optical overlap area between healthy and cancerous area would be relatively smaller. Therefore, the effect of mislabelling would be much stronger. Thus, smaller carcinomas are chosen. Moreover, for small carcinomas mislabelling is more likely. in contrast to the real stomach, only a single layer structure is simulated due to the fact that Holmer et al. [130] dissociated the oesophagus before performing their measurement.

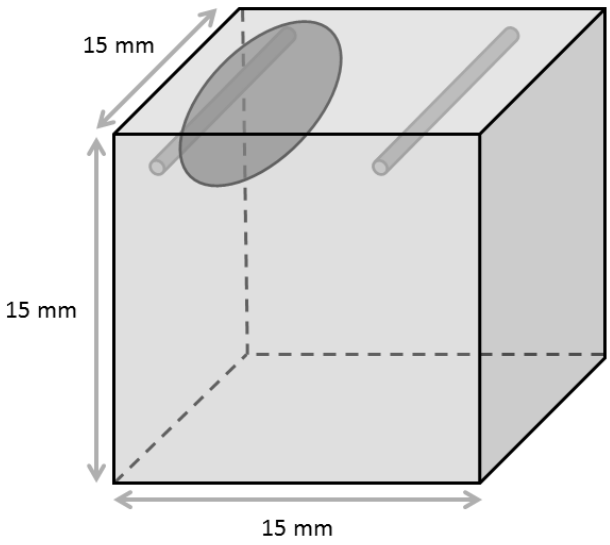

Figure 19: Set-up for the simulation: The set-up is a cubic volume of a size of 15 x 15 x 15 mm^3. Two blood vessels (cylindrical) and a carcinoma (elliptical) are placed in to the simulation volume. The carcinoma has a size of 1.5, 2.0 and 0.1 mm. The two blood vessels have a diameter of 10 μm.

The simulation volume includes two blood vessels as cylinders and the cancerous tissue as ellipsoid. Two blood vessels are added to introduce small

inhomogeneities in the tissue. The two blood vessels have a diameter of 10 microns. One vessel is 0.25 mm below the centre of the carcinoma and the second one is placed 0.3 mm below the surface. The carcinoma has a diameter of 1.5, 2.0 and 0.1 mm in x,y and z-direction. The position of the centre is 6.5, 7.5 and 0.4 mm from the left upper edge. The tissue is simulated with semi-infinite boundary conditions. Hence, Fresnel reflection is only taken into account on the top surface. The simulation stops when 131'072'000 photons reach the detector. Less than 5 % of the photons reach the detector and, therefore, at least 3 billion photons have to be simulated.

For the simulation, close imaging is simulated. Even if in *in-vivo* situations the imaging is often not perpendicular, this set-up is chosen for three reasons: First, it is easier to simulate. Second, if a tilted simulation is chosen, there are too many possible ways to choose from. This would make it difficult to compare if different people show different angles. Third, the imaging is done with a small distance between endoscope and surface. In this case, it is also in *in-vivo* situations possible to have nearly perpendicular imaging.

The light source emulates an endoscopic light source with homogeneous intensity distribution on the surface. The light in the centre hits the surface perpendicular and the light in the outer part with an angle of 30 degrees. Hence, the light source is a point source with a distance of about 1.7 mm to the surface. For the detection the surface is divided into nine squares with equal size. The photons are only taken from the central square to minimize boundary effects from the finite simulation volume. There are no other photons which stray in the detector due to the fact that only the photons from this central square are checked if they can reach the detector. All others are immediately terminated. The surface of the central square is divided into 301 times 301 pixels which is imaged on the detector.

Due to fact that MCS is a statistical method in which random events take place, the noise of the simulation has to be considered. If the probability of hitting one pixel is assumed to be the same for every pixel, the average amount of photons per pixel can be calculated by dividing the sum of all pixels by the total sum of the photons reaching the detector. Thus, in average 1446 photons arrive at each pixel. Hence, the noise by the simulation is expected to be high. If the Binomial distribution is assumed for hitting a single pixel and furthermore it is assumed that the probability of the light to hit a single pixel is the same for all detectors then the standard deviation can be calculated with the following equation 28:

$$std = \sqrt{n \cdot p_{\%} \cdot (1 - p_{\%})}, \tag{28}$$

where n is the total amount of photons ($n = 131,072,000$) and p is the probability for hitting a single detector which is $p_{\%} = 1.1037 \cdot 10^{-5}$. Thus, the resulting standard deviation is 38 intensity values for each detector, resulting in an average noise of about 3 % of the signal. Therefore, a further noise reduction step is required. For the noise reduction, a seven times seven pixel wide Gaussian filter with a FWHM of 2 pixel is used. The noise can be estimated in the same way as before but with 49 times less pixels. This results in an average signal of $signal = (70890 \pm 270)$ photons, reducing the noise to around 0.4 %. However due the usage of the Gaussian filter, the noise is expected to be higher. Stronger noise reduction or more photons are not needed due to the fact that the noise level is similar or even better than the results from WP1. Using the Gaussian filtering instead of decreasing the spatial resolution of the detector has two advantages: First, the resolution is similar to at least older endoscopes. Second, the later introduced shifts of the carcinoma can be done with the necessary precision. Reducing the resolution by the same factor would lead to a pixel size of 43 times 43 pixels. This is too less to adequately do the later calculations.

With the finalized set-up of the Monte-Carlo simulation 40 patients are simulated and for each patient one endoscopic image is generated. Each patient has a randomly selected different set of optical properties for the carcinoma and the healthy tissue.

4.3.4 Model of mislabelled carcinomas

The effect of the mismatch between the real carcinoma and the carcinoma used for training is calculated for three different kinds of mismatch. Figure 20 shows an example of the three kinds of mismatch that are investigated in this study. The white ellipse shows the margin of the carcinoma and the grey

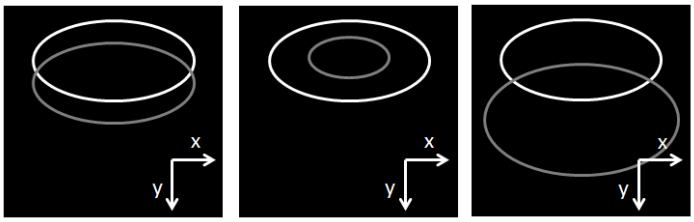

Figure 20: Different models of how to vary the carcinoma data which is used for training. The images represent the final generated image (topview). The white ellipse shows the margin of the carcinoma and the grey ellipse shows the margin of the carcinoma which is used for the training of the classifier. Left: Variation of the position, Middle: Variation of the size, Right: Random variation of size and position.

ellipse shows the margin of the carcinoma which is used for the training of the classifier. Furthermore table 8 shows an overview of the variations between the carcinoma used for training and the real one.

Table 8: Used variations between the real carcinoma and the carcinoma used for training. For the last line, both parameters are varied randomly at the same time.

Varied Parameter	Minimum	Maximum	Step size
Position	0 %	50 %	5 %
Size	25 %	175 %	25 %
Both (size)	25 %	175 %	
Both (position in radius of carcinoma)	0	1.25	

First, the effect of the shift between the real carcinoma and the one used for training is tested as symbolized in figure 20 left. The carcinomas are shifted in y-direction in a way that the overlapping area between the real carcinoma and the one used for the training of the classifiers is varied from 100 to 50 % in steps of five per cent points. This simulates the situation when that part of the carcinoma is found while part of the healthy tissue is seen as carcinoma.

Second, the effect of the relative size of the carcinoma used for training and the real carcinoma is tested as symbolized in figure 20 middle. The size of the carcinoma used for training is varied from 0.25 times the area of the real carcinoma to 1.75 times the size of the real carcinoma in steps of 0.25. This simulates that too much of healthy tissue is seen as cancerous or if not the whole cancerous area can be detected.

Third, the random combination of both previous effects is studied as symbolized in figure 20 right. In this part, a maximal variation is set. This maximal difference of the area is 0.25 or 1.75 times the area of the real carcinoma. The maximal shift of the carcinoma is 1.25 times the radius of the original carcinoma. For selecting a value, a uniform random number is chosen between the minimum and the maximum difference from the real carcinoma. Before the random number determines the position the maximal shift and size variations are limited from 0 to 100 % of the maximal variation in steps of 10 per cent points. Hence, the strength of the random overlap can be varied. For the random combination every patient has a different position of the carcinoma used for training.

The last studied effect is expected to be the most realistic, as sometimes only random parts of the carcinoma can be labelled correctly or way too much of the tissue might be labelled as cancerous. Moreover, for this study

it is the most realistic setting due to the fact that not all patients have the same mislabelling. The labelling differs from patient to patient. Sometimes the margin of the carcinoma is pretty good, sometimes only a part of the carcinoma is found and sometimes a big chunk of healthy tissue is seen as cancerous.

However for the third mismatch effect, the real overlap is unknown compared to the other two effects. To estimate the overlap, an average overlap area is calculated by choosing 1000 times a random combination of size and position. However, two different kinds of overlap have to be considered. First, the amount of the original carcinoma which is covered by the one used for training and second the amount of the carcinoma used for training which contains the actual carcinoma. Both parameter describe the same area. Nevertheless, they describe it from a different perspective. The parameters differ when the size of the carcinoma used for training differs. The effect can be seen in figure 20 middle and right. For example in figure 20 middle the amount of the original carcinoma which is covered by the one used for training is around 30 % while the amount of the carcinoma used for training which contains the actual carcinoma is 100 %.

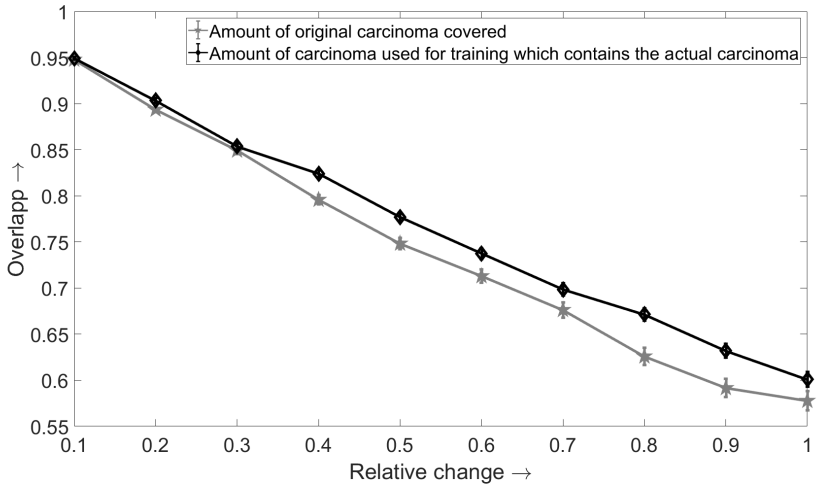

Figure 21: Overlap and the standard error between the real carcinoma and the one used for training. The black graph shows the amount of carcinoma used for training which is actually real carcinoma and the grey graph shows the amount of real carcinoma covered by the one used for training.

Figure 21 shows both overlaps for different percentage of the maximal variation. It can be seen that both variations differ and, therefore, only the relative maximal variation will be used as variable. On average, the amount of real

carcinoma that is covered is higher than the amount of carcinoma used for training which is actually the real carcinoma. Both graphs drop from 95 % overlap to 60-65 % overlap. This means even in the worst case, in average around 60-65 % of the carcinomas are correctly used for the training. This number seems to be realistic or even underestimates the error as even in the case of correct markings there might be a more than 60 % mislabelled area (figure 3 from Yoshinaga et al. [82]).

4.3.5 Data analysis

The statistical analysis is done the same way as in WP1 with a few modifications. First, there is no Fourier filtering and no removal of the barrel distortions due to the fact that both of them are not needed. Instead of MNF, just Gaussian filtering is used. The filter size of the Gaussian filter is set to seven pixel and the FWHM is two pixel. The chosen filter size is used, as it reduces the noise to realistic level. In contrast to the human study, seven wavelengths are used as for the mice experiments in WP4. For each wavelength band, the derivative is calculated and used as feature. The analysis is done with AB, RB, SVM with linear and Gaussian kernel and RFW. The accuracy measures are calculated for the shifted and the real carcinoma, separately as there might be a difference.

4.4 Murine multi/hyper spectral study

Figure 22 shows an overview of the murine multi/hyper spectral study. In the first point, the spectral estimation techniques are explained. In the following point, the evaluation is described, followed by the endoscopic set-up and the data analysis.

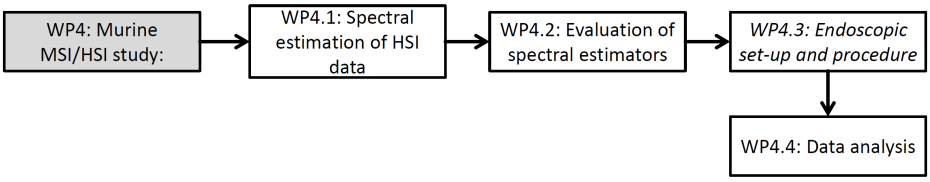

Figure 22: Overview of the forth working package. Each box symbolized one sub chapter and corresponds to the headlines. The grey box symbolizes the generic topic/research question and italic font symbolizes that this part of the flow chart will be shown as generic topic later.

4.4.1 Spectral estimation of HSI data

In general, the goal is to collect hyper spectral images. However so far, only multi spectral imaging is presented. Despite the conclusion from Swager et al. [7] that real hyper spectral imaging should be used, the effect of the spectral estimation has to be tested: Does the estimated hyper spectral imaging provides better results than the multi spectral imaging?

In general, the spectral response of a device for the c-th colour channel can be described by the following formula:

$$v_c = \int_{\lambda_a}^{\lambda_b} I(\lambda) r(\lambda) f_c(\lambda) s(\lambda) d\lambda + b_c + n_c \tag{29}$$

where $I(\lambda)$ is the spectral power distribution of the light source, $r(\lambda)$ the spectral reflectance of the sample, $f_c(\lambda)$ the spectral transmission of the filter for the camera (e.g. spectral transmission of colour filter from an RGB-camera), $s(\lambda)$ is the spectral sensitivity of the camera, b_c is the bias response caused by the dark current and n_c is the zero mean imaging noise. Normally, the three variables $I(\lambda)$, $f_c(\lambda)$ and $s(\lambda)$ are merged to a single variable $m_c(\lambda)$ due to the fact that they are fixed for a given imaging system.

In a realistic system, the measured spectra are discrete. Thus, the formula (29) is changed to the vector and matrix notation:

$$v = M \cdot r + b + \hat{n} \tag{30}$$

where v is the response vector for the colour channels, r is the reflectance spectra, M is the wavelength dependency matrix of the merged variable $m_c(\lambda)$, b is the dark current in vector form and $\hat{n}$ is the zero mean noise in vector form. The effect of the dark current can be considered in a new variable $u = v - b$ which leads to the following:

$$u = M \cdot r + \hat{n}. \tag{31}$$

This problem can either be solved by inverting the wavelength dependency matrix or by finding another matrix fulfilling the following equation [74]:

$$r_{reconstructed} = W \cdot u \tag{32}$$

where $r_{reconstructed}$ is the reconstructed reflection spectra and W is the reconstruction matrix from the measured multi spectral spectra.

The PI method, does not require a priori knowledge of the spectral sensitivities of the system components. By creating a direct reconstruction matrix W from a known training set, the spectral behaviour can be retrieved by minimizing the associated error values. In this case in equation 32, W becomes the pseudo inverse matrix of M. For k training samples, e spectral bands acquired by the multi spectral camera and s spectral bands from the reference spectrometer, the reconstruction matrix with a dimension of $s \cdot e$ allows the following calculation:

$$W = R \cdot P^{-1} \tag{33}$$

where P^{-1} represents the pseudo inverse matrix of P. The reconstruction matrix W can be achieved by minimizing the following:

$$||R - W \cdot P|| \tag{34}$$

where the matrix P contains the sensor response from the training samples and the matrix R contains the corresponding spectral reflectance.

Even though equation (33) is a simple optimization problem, the similarity and generalizability are not achievable at the same time. This effect can be seen in the study from Shimano et al. [74] in which the pseudo inverse method provides excellent results if the reconstruction is tested with the training data but mediocre results if other spectra are used for testing. This happens due to the fact that the same matrix is used for all measured data, even if the pseudo inverse matrix does not match.

To overcome this problem, the training spectra can be weighted according to the similarity of them to the measured data [75]. For this approach, equation (33) is altered by adding a weight matrix W_e which is described by $W_e = \mathrm{diag}(w_1, w_2, ..., w_n)$ [75]. The weight factors w_i are the inverse of colour difference values between the i^{th} sample in the training database and the current sample which is reconstructed. However in this study, the distance is derived by the Frobenius norm of the current analysed sample minus the values of the i^{th} training sample. The calculation of the pseudo inverse is altered to the following [75]:

$$W = R \cdot W_e \cdot (P \cdot W_e)^{-1} \tag{35}$$

By inserting equation (33) or equation (35) in equation (32) the reflection can be calculated as follows [75]:

$$r_{reconstructed} = R \cdot P^{-1} \cdot u \tag{36}$$

$$r_{reconstructed} = R \cdot W_e \cdot (P \cdot W_e)^{-1} \cdot u \tag{37}$$

The first equation describes the pseudo inverse method and the second equation the weighted pseudo inverse (wPI) method.

In general, the wPI method is expected to provide better results than the PI method. However, the wPI method is much more computational expensive, due to the fact the weight and the pseudo inverse have to be calculated for each pixel while the PI method just requires a simple matrix multiplication. Therefore, both methods are tested.

As calibration sample, a MacBeth colour chart with 24 coloured Lambertian reflectors is used. Furthermore, a blood sample from a healthy volunteer is measured in a technical triplicate and four measurements of human skin are performed. As shown by Shimano et al. [74] the spectral estimation gets better, the closer the calibration samples are compared to later samples from which the spectrum is estimated. Hence, these additional biological samples are added as calibration data as human skin allows the characterization of melanin and blood with realistic scattering. Additionally, as mice only have 1 to 1.5 ml of blood in total, human blood samples are used for calibration which are performed with several ml per sample in accordance with the 3R concept (refine, reduce, replace).

The spectral estimation techniques are implemented and tested for the mouse endoscopy system due to the fact that the image noise is much weaker and, therefore, a reconstruction is expected to provide better results. The calibration of the mouse endoscope is done with help of an Ocean optics QE65000 spectrometer (Ocean optics, US) which is shown in figure 23. The distance between the sample and fibre of the spectrometer is kept constant for all samples. It is chosen in such way that for the white reflector a reflection of 95 % is measured.

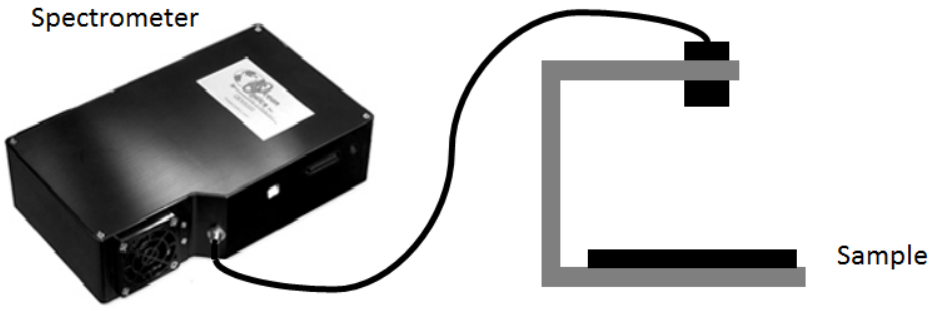

Figure 23: Set-up for the calibration of the mouse endoscope for estimation of the hyper spectral images. The distance between the sample and fibre of the spectrometer is kept constant for all samples.

The illumination of the samples is done with day light. It was not tried to achieve a standard D65 norm light scenario[5] as reference light. However, daylight with clouds was preferred due to the lower effect of the direct sunlight on the measured spectra. It is expected that the spectrum of the diffuse light also changes less during the measuring procedure and, therefore, it is preferred. Both the measured day light spectrum as well as the measured reflectance spectra are smoothed to reduce the noise. The same samples are later measured with the mouse endoscope in a dark room without without external lighting. The distance between the sample and the endoscope as well as the intensity of the illumination are chosen in a way that for the green channel with a central wavelength of 547 *nm*, the relative saturation is the same as for the spectrometer at 547 *nm*. The intensity of the endoscope is measured by the mean of the centre area with a size of 100 times 100 pixels to minimize potential noise.

4.4.2 Evaluation of spectral estimators

To test the quality of the estimation, the pseudo inverse and the weighted pseudo inverse are calculated with the leave one out strategy. As it is done in the classification, one sample is excluded and the other ones are used for estimating the pseudo inverse or the weighted pseudo inverse. Afterwards from each sample, the error is calculated with the root mean squared error (RMSE).

4.4.3 Endoscopic set-up and procedure

Figure 24 shows an overview of the endoscopic set-up and procedure section. In the first point, the set-up is presented while in the second point the mouse model including the endoscopic procedure is explained.

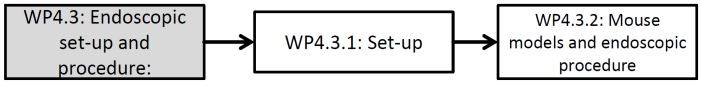

Figure 24: Overview of Endoscopic Set-up and procedure. Each box symbolized one sub chapter and corresponds to the headlines. The grey box symbolizes the generic topic/research question and italic font symbolizes that this part of the flow chart will be shown as generic topic later.

Set-up The mouse endoscope is a modified system of the COLOVIEW System Mainz from Karl Storz, Germany. In comparison to the modifications done by Hohmann et al. [117], for this modification only the head of the endoscope is used. This is possible due to the fact that the endoscopy system

[5] averaged mid day light in northern and western Europe without clouds

is not a video endoscopy system[6]. The endoscope consists of the lens based head which is connected to the optics and an external light source (Lumencor spectra 7-LCR-XA, Beaverton, OR, USA) with a liquid light guide. The optics images the light onto the camera. The schematic of the complete set-up is shown in figure 25. The video signal from the camera is used as master clock for the system especially the external light source. The system is controlled by a PC. The data input, data output, GUI and the control of the external light source is done by a Matlab program.

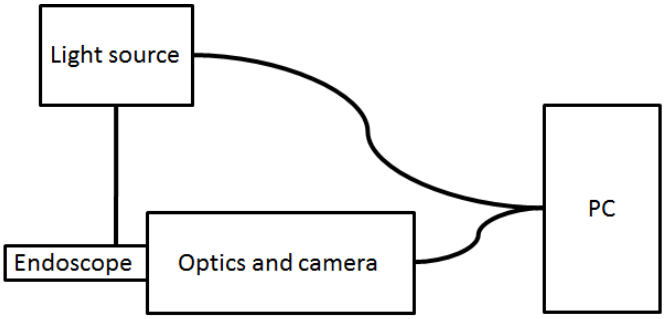

Figure 25: Set-up of the mouse endoscope: The external light source is coupled into the endoscope head with a liquid light guide. The video signal from the camera is read by a PC and the PC controls the light source.

The optics is shown in figure 26 and consists of two lenses and a 10X infinity corrected plan apochromat objective (Mitutoyo, Japan) with an NA of 0.28 and a working distance of 34 mm. The first lens is an achromatic lens with a focal length of 35 mm and it images the intestines from the endoscope head as intermediate image. This intermediate image is imaged by the objective to infinity. The second lens is a 100 mm achromatic lens and brings the image from infinity onto the camera (DCC1240M, Thorlabs). Out of the full resolution of 1280x1024 pixels, 520x496 pixels are acquired to speed up the imaging process of the whole multi spectral image below 0.5 s. The sensor boost is set to 50 % and the gain boost is turned off. The objective is mainly used for two reasons. First, it is used to prevent chromatic aberrations which would worsen the quality of the multi spectral images strongly. For this reason, the other lenses are also achromatic. The usage of an infinity corrected objective allows an easy modification of the optical system if a second camera is added. In this case, a chromatic beam-splitter can be placed between the objective and the second lens without alteration of the beam

[6] A video endoscopy system is an endoscopy system in which the CMOS or CCD chip is placed in the tip of the endoscope.

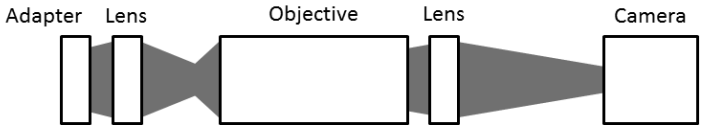

Figure 26: Set-up of optics of the mouse endoscope: The endoscope head is connected to the adapter and an intermediate image is generated by the first achromatic lens. This intermediate image is imaged again with the objective to infinity. The infinity corrected images is later imaged on the camera by the achromatic second lens.

path. The total set-up has only small distortions. Smile as well as keystone are not present. Also, there is no barrel distortion. However, a small chromatic aberration is found for the outer parts of the image.

Mouse models and endoscopic procedure Animal studies are approved by the Institutional Animal Care and Use Committee of the University of Erlangen-Nürnberg and the government of Lower Franconia.

Inflammatory carcinogenesis is induced using the AOM/DSS model as described by Neufert et al. [135] and spontaneous tumours were based either on the genetic APCmin or TP53 model. Endoscopy is performed as described by Becker et al. [136] and Neurath et al.[137]. The anaesthesia of the mice is done with isoflurane due to its reliability for long term anaesthesia [138]. As recommended by the current guide lines, it is used with a dose of 4-5 % for induction and 1-2 % for maintaining the anaesthesia [139]. However, with a dosis of 1-2 % of isoflurane, the breathing cycle happens between 0.5 s. To compensate this the dosages are increased to 3-3,5 % during a short period of time for the multi-spectral imaging. In general, the bowel is carefully flushed with tap water to remove stool and the bowel is distended by means of careful air insufflation via the working channel. The colon is investigated with white light imaging and lesions that are deemed “definitive” neoplasms based on the assessment of their macroscopic appearance by the experienced endoscopists were additionally evaluated with multi- and hyper spectral imaging.

4.4.4 Data analysis

The data analysis from this mouse study is performed the same way as it is done in WP1 with the exception that the correction of the aberrations and the Fourier filtering are not done due to the fact the effect of the aberrations is negligible small and there are no artefacts from the camera, needing to be corrected. However, a further noise reduction step is introduced.

In summary, the analysis is done with a pixel per pixel classification process. For the pre-processing of the data, specular reflections are removed, the MNF is used for de-noising, followed by a smoothing with a Gaussian filter. Furthermore from the MNF, the spectral spatial variation is derived, used as feature and combined into a single data set. Moreover, the derivative images are used as input features. After the feature generation, the PCA is used for feature reduction and the features accounting for 99 % of the variance are used for classification. As in the previous working packages, RB, AB, SVM with linear and Gaussian kernel as well as RFW are used for classification. To speed up the classification process, a random selection of 1 % of the data is used for training. For the evaluation of the classifiers, the four measures ACC, ACC2, AUC and MCC are used. The data evaluation is done with a leave-one-out strategy in which 24 mice are used for training and one for testing. The final accuracy measures are the mean of all 25 permutations.

Lesions for spectral analysis are identified by two medical experts by classification as a "definitively neoplastic lesion" based on macroscopic appearance. For labelling of the training and test data, one of the medical expert drew the lesion margin. To minimize the errors, the inspection for the unknown cases is done by two doctors from which only one has performed the endoscopic procedure. This is done to minimize observer bias.

Furthermore, the analysis is done for the multi spectral data set with and without spatial features as well as the hyper spectral data set generated by the spectral estimation by the wPI method. The hyper spectral data set is not used with spatial features, as the memory requirement would be too high. Moreover, too dark areas are excluded due to the fact that in these areas the noise is too strong and this would result in a wrong spectral estimation. If the intensity of a pixel in the red or yellow region is less than 5 % of the maximal intensity, the pixel is excluded. The data is excluded in all data sets.

5 Results and discussion

This part is divided into four sections for the four WPs as shown in figure 1. Not all section such as ”patients” will appear in the respective WPs. The sub-WPs will be named WPR for working package result section. In all tables, the AUC and the MCC are the important values. Hence, they are marked in grey. The ACC and the ACC2 are also presented due to the fact that they are the most common parameter and that they can be interpreted easily.

5.1 In-vivo multi spectral human study

Figure 27 provides an overview about the presented results of WP1. First, the effect of the pre-processing and the image correction is presented. The corrected images are used for the parameter study which results are used to analyse the usage of the spatial features. Afterwards, it is tested if intra patient variations can be compensated followed by the test of the inter patient variations combined with the comparison of the state of the art. These results are used to compare the classification to medical conditions. As last point, the same classification scheme is applied to carcinomas and pre-carcinomas in the oesophagus.

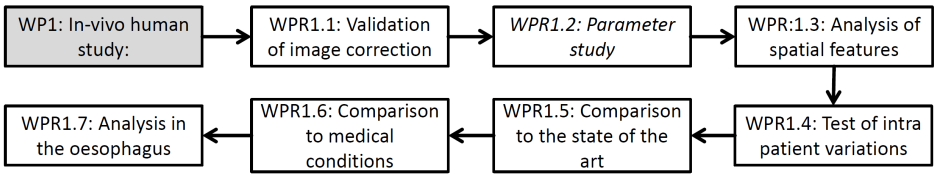

Figure 27: Overview of the first working package for the result section. Each box symbolized one sub chapter and corresponds to the headlines. The grey box symbolizes the generic topic/research question and italic font symbolizes that this part of the flow chart will be shown as generic topic later.

5.1.1 Validation of image correction

For the correction of the images, the change in the Fourier-space is only found on a small part of the image which is shown in figure 28. However, the effect on the image in the real space is huge. The artefact lines are removed and the underlying structure of the tissue can be seen better as shown in figure 28. The presented example has a high amount of artefacts. Images with lower amount of artefacts are also tested. With the same amount of filtering, there are no artefacts introduced due to the Fourier filtering.

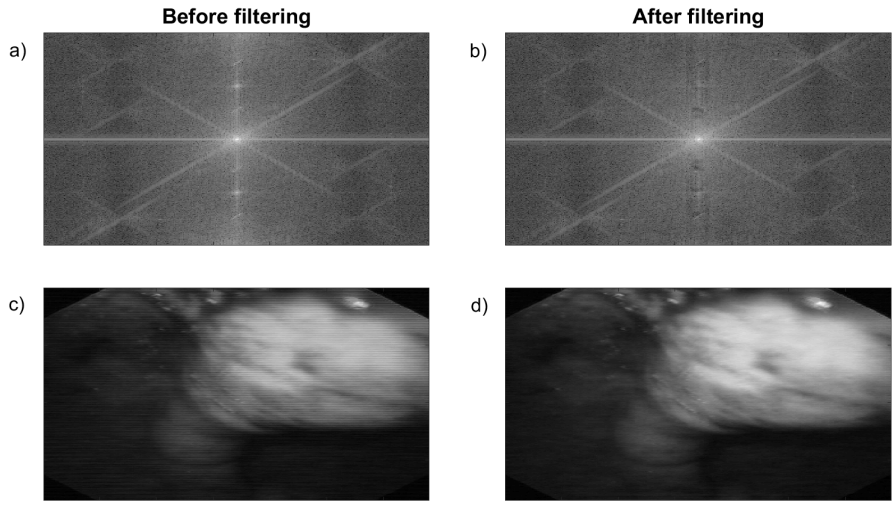

Figure 28: The effect of the Fourier filtering in the Fourier (a,b) and real space (c,d). The top row images show the Fourier space and the bottom row the real space. The images in the Fourier space are shown with a logarithmic scale. On the left side the images are shown before filtering (a,c) and on the right side they are shown after filtering (b,d).

After the Fourier filtering, the barrel distortion is corrected. First, the detection of the chess board pattern should be tested. Therefore, the precision of the re-projection shows the correct finding of the chess board pattern. The result is shown in figure 29. From the nine images used for the detection of the barrel distortion, the mean re-projection error is 0.18 pixels and the maximum error is 0.34 pixels. Therefore, it can be concluded that the chess board pattern is found correctly and, therefore, it can be used for the correction of the barrel distortion.

With the correct detection of the chess board pattern, the image from the endoscope can be corrected for the barrel distortion. Figure 30 shows the comparison of an image of a chess board pattern and a single wavelengths of a multi spectral image before and after the correction. The chess board pattern is shown to demonstrate the correction due to the fact it is more easy to see it in comparison to the multi spectral image. While in the uncorrected image, the lines of the chess board are not straight, in the corrected image all lines in the image are straight. Therefore, the distortion of the endoscope due to the imaging optics is corrected and the spatial structure of features can be seen independently of the position in the image. For the multi spectral image, the difference before and after the correction seems to be smaller. However, a close comparison reveals the difference. The specular reflection

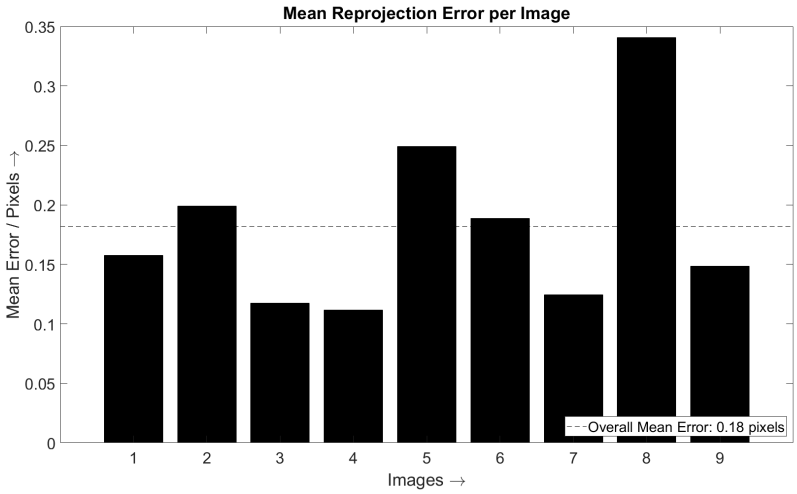

Figure 29: Re-projection error from the detection of the chess board pattern. The mean re-projection error is 0.18 pixels.

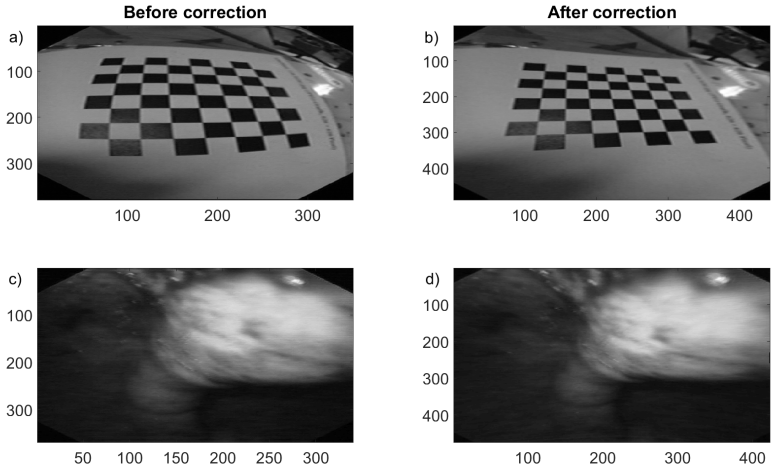

Figure 30: Corrected image of the chess board pattern (a,b) and a multi spectral image (c,d). On the left side, the images are shown without correction of the barrel distortion (a,c) and on the right side after the correction (b,d).

on the top right part changes its shape from elliptical to a more spherical one. It should also be noted that the usage of the correction of the barrel distortion increases the image size from 370 times 340 pixels to 475 times 423 pixels due to the interpolation required for the correction of the barrel

distortion. Moreover, a small part of the edges of the images is cut to prevent blank space in the image.

The final pre-processing step is the MNF. First, the residuum has to be calculated. The most clear result is that the residuum of the MNF seems to correspond with the intensity of image (figure 31 left). In the bright parts, the absolute value of the residuum is very high. However, for most of the image the residuum is constant and independent of the intensity value. Therefore, the residuum should be also looked at a normalized version. The normalization is done by dividing the residuum pixel-wise by the image before the MNF is done. This is shown in figure 31 on the right side.

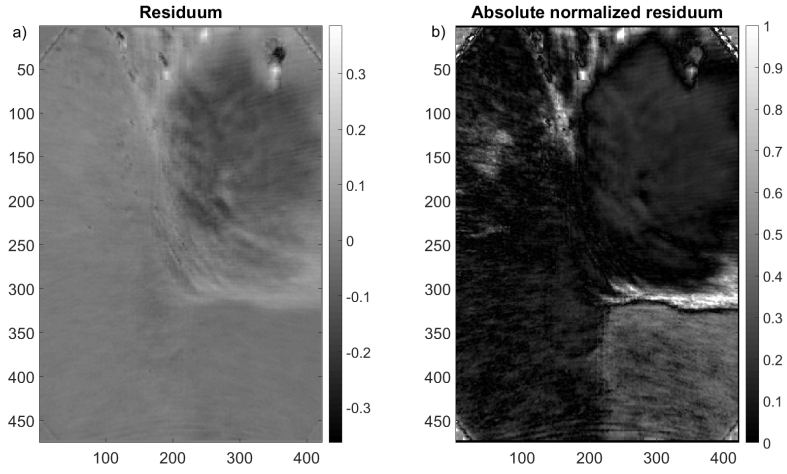

Figure 31: Residuum (a) and absolute value of the normalized residuum (b). The ellipse shows the position of the carcinoma.

It can be seen, that the normalized residuum is high for areas where the spatial change of the image is high and for areas where the signal is very weak (dark parts of the image) like the area on the left bottom side (figure 31 right). For the first case, it is expected that small movement artefacts are present in the images. These would be seen especially strong on the boundaries of contrast rich areas. Therefore, the residuum has to be high there. The second case happens in areas where the overall signal strength is low. Due to the fact that the endoscope has a constant noise value added to the signal in the areas with low signal, the relative noise is expected to be higher and dominated by the intrinsic noise from the endoscope. This effect is seen in the whole image except the upper right part. However, the relative noise is different which can be seen in the lower right area. Nevertheless, in figure 30 it can be seen that

that the image intensity varies over the whole image. Thus, the MNF finds the noise from the endoscope.

Moreover, the area on the right upper side should also be considered. In this area, the normalized residuum as well as the unnormalized residuum are a little bit elevated. However, not much noise is expected to be present there. There are three potential reasons: First, this part of the image is closer to the endoscope and, therefore, blood vessels are visible. Thus, movement artefacts might play a small role. Second, the difference of the reflected light for different wavelengths is most pronounced when the signal is high. This might get interpreted as a noise like structure. Third, the area where this happens is the cancerous area. Therefore, a higher spatial and spectral variation is expected [14]. Thus, it might indicate the presence of cancerous tissue. For this reason, the residuum will be tested as separate feature: the spatial-spectral variance (SSV).

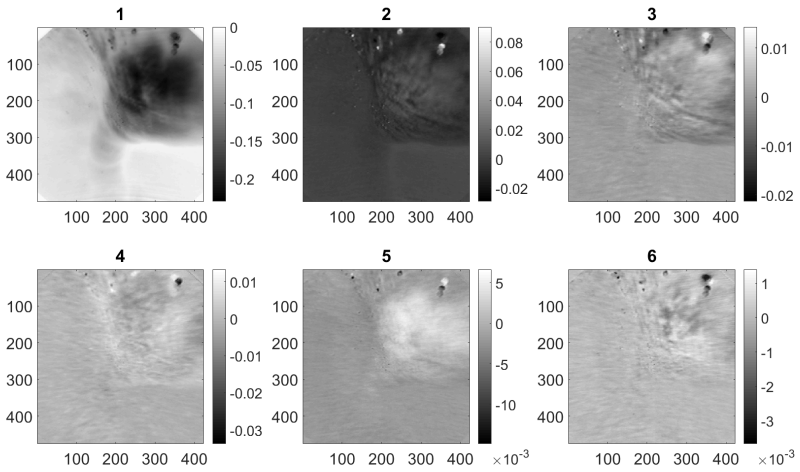

Figure 32: The six MNF components which are sorted by increasing SNR from left top to right bottom.

Moreover in figure 32, it can be seen that in the last components, a part of the line error could not be removed by Fourier filtering. However, the MNF removes these components due to the fact they are weak and therefore found in the image with the highest SNR.

Furthermore, the effect of the MNF can be seen in figure 33. The first effect is that the noise is a little bit lower. Furthermore in some places, strong features are more pronounced and, therefore, easier to detect (figure 33 middle). This is in agreement with results of Regeling et al. [93]. In comparison to Gaussian

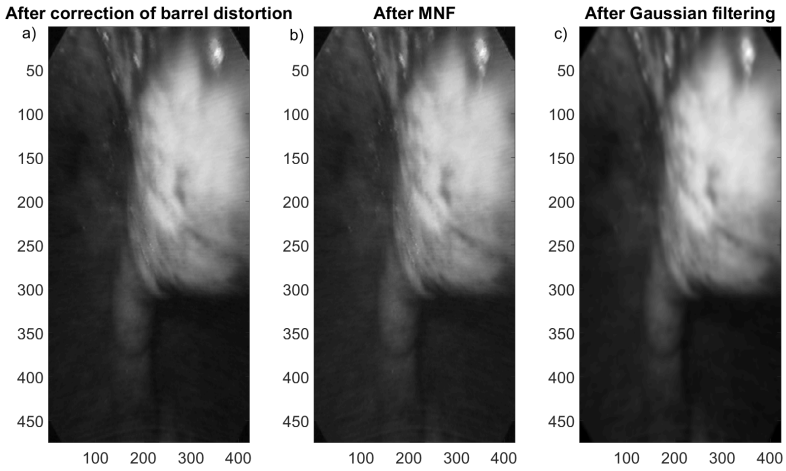

Figure 33: The effect of the different noise removal techniques. The left image shows the image after correction of the barrel distortion (a), the middle one after MNF (b) and the right one after Gaussian filtering (c).

filtering shown in figure 33 right, this is a huge advantage. While the Gaussian filter removes more noise, it also blurs the image.

The most important information to be considered is the amount of required components. With the help of the residuum, the components sorted by SNR are calculated as shown for an example in figure 32. From these components, it can be seen that the last two or perhaps even the last four are noise. A more clear view of the noise is seen in in the scree plot in figure 34. In nearly all cases, around 97 % of the information are present in the first two components. For this reason, the first two components should at least be used for further analysis.

If the fact is taken into account that the original data has only 256 intensity values, everything below 0.1 % variance can be seen as noise. This effect provides a second hint for the fact that the sole usage of the two first components might be enough, similar to the results obtained by Regeling at al. [93]. Consequently, only two components are required. However, in comparison to figure 32, it can be seen that the components three and more still seem to represent some relevant features as the shape of carcinoma can be seen. It should also be noted that for Regeling at al. [93] also the first five to seven components still might have useful information despite having a low importance.

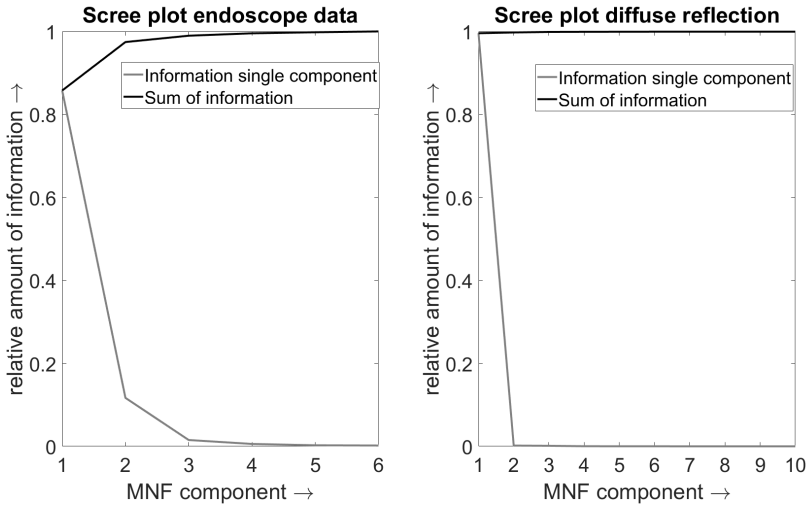

Figure 34: Scree plot for a typical example hyper spectral images (left). Scree plot for diffuse reflectance imaging (right).

This data suggests that only the first 2 to 4 MNF components need to be used for near infra red and visible light. Thus, diffuse optical imaging is tested with only two main absorbers. In this case a phantom with deoxyhaemoglobin is used. The two absorbers are deoxyhaemoglobin and the matrix material. The scree plot in figure 34 shows that only one or two components might be required. A closer look at the components is shown in figure 35.

Figure 35 shows that all components higher than two show only noise. Testing shows that for reconstruction of the data, the second component is still important despite the fact that the scree plot shows a very low importance. Without it, the spectral change of the image would be lost. Therefore, a component with a very low amount of information (figure 34 right) is still relevant. Hence, it can be concluded that the components three and four from the MSI still might contain relevant information as their amount of information is even higher than suggested by the scree plot (figure 34 left).

In general, it seems that the MNF might have relationship to the amount of absorbers present. As tissue has many absorbers, most of the components might be relevant. For the diffuse reflection spectroscopy only two components are relevant. This matches to the number of absorbers. Moreover, it should be considered that absorbers which have a low effect are also more degraded by noise and, therefore, they are sorted in higher components. Hence, the removal of all components bigger than two might eliminate important information of other then the two main absorbers. Therefore, higher orders

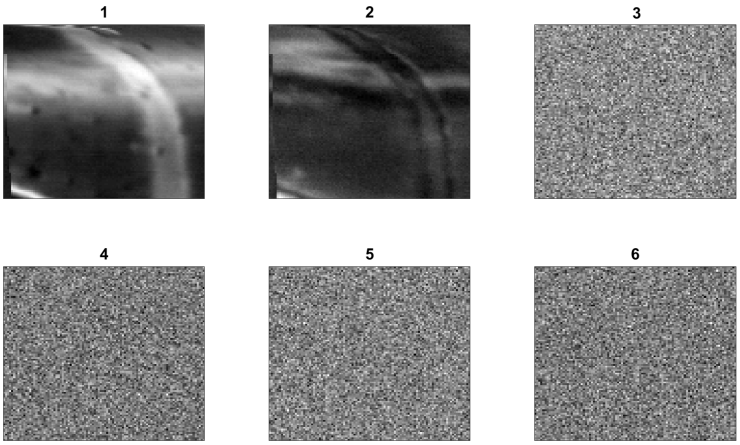

Figure 35: First six components of the MNF for a diffuse reflection image of a haemoglobin filled channel in a solid tissue phantom. (Rawdata provided by Chen et al. [121]).

should not be ignored for the further analysis. In summary, the first four or two MNF components seem to be the optimal choice. Therefore, to use two or four components as planned in the method section seems to be a good number for testing.

Another conclusion is that six wavelengths might not be enough for a good analysis. Most likely, more then six absorbers are present. This can be seen by the paper from Regeling at al. [93]. At least, the first seven components still show reasonable information. If six wavelengths are present and there are seven absorbers, there will be too less information to gather all the information about the absorbers. Moreover, a higher spectral resolution would help to reduce the noise when using the MNF.

5.1.2 Parameter study

Figure 36 shows the overview of the parameter study. It is grouped into seven parts. At first, the required variance by pre-processing with PCA is tested. Afterwards, the effect of the feature delocalization is studied, followed by a study where RFW is used for feature selection: once as feature selection method and once after the PCA. In the next point, the effect of the parameter MNF cut is studied. The last points are the outlier rate, the effect of feature reduction by RFW and the comparison to basic classifiers. As this section contains many different points to consider a summary is added in the end.

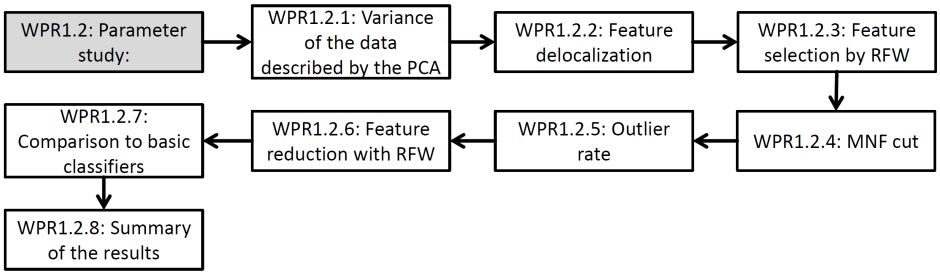

Figure 36: Overview of the parameter study of WP1 in the result section. Each box symbolized one sub chapter and corresponds to the headlines. The grey box symbolizes the generic topic/research question and italic font symbolizes that this part of the flow chart will be shown as generic topic later.

Variance of the data described by the PCA First, the effect of the amount of principal components is shown in table 9. In average, it seems that for 95 % of the variance explained by the PCA components, the best results can be reached. For 99 % used variance, the results get a little bit worse. For 90 % used variance, the results are the worst in the test. In summary, 95 % or 99 % of the variance should be used for classification after the PCA. Higher orders seem to be noisy and if too less orders are used, information is lost.

Moreover, this information allows a comparison with the variance the endoscope camera has to be able to detect. The endoscope camera provides an eight bit colour depth (256 intensity values). In the optimal cases for a variance of 95 %, it corresponds to 13 intensity values for the case the image is perfectly illuminated. However, most of the time the image is illuminated with an intensity of 100 out of 256 intensity values.

Therefore, the unused variance has the same order of magnitude as the noise level of the endoscope. The noise level of the endoscope is about five intensity values and it is independent of the brightness of the image. Thus, an effective noise reduction is essential to prevent the training of the classifiers to noise instead of the signal and, therefore, minimize over-fitting of the classifiers. Therefore, the usage of MNF as well as most advanced noise reduction method as the Gaussian filter seems to be of high importance. It reduces the noise level below the five intensity values. Hence, the 99 % used variance also provides good results. However despite the noise filtering, a significant noise level still seems to be present in the data.

Feature delocalization The next parameter taken into account is the delocalization of the spatial features. By a strong Gaussian filter, the features are blurred with the surrounding. The effect of the delocalization of the spatial

Table 9: Classification results of the tested classifiers for 13 patients with leave one out strategy after pre-processing with MNF and correction of the barrel distortion and usage of spatial features for 0.25 % of the data being used as training data. The results are shown for a used variance of 90 %, 95 % and 99 %.

Method	ACC	ACC2	AUC	MCC	Used variance
RFW	0.54	0.61	0.61	0.19	0.90
RFW	0.54	0.60	0.62	0.18	0.95
RFW	0.51	0.59	0.58	0.16	0.99
RB	0.49	0.56	0.56	0.10	0.90
RB	0.48	0.58	0.59	0.13	0.95
RB	0.47	0.58	0.58	0.14	0.99
SVM (lin)	0.50	0.52	0.54	0.03	0.90
SVM (lin)	0.55	0.63	0.49	0.21	0.95
SVM (lin)	0.47	0.58	0.47	0.12	0.99
SVM (Gauss)	0.47	0.55	0.55	0.10	0.90
SVM (Gauss)	0.47	0.57	0.56	0.12	0.95
SVM (Gauss)	0.45	0.56	0.56	0.10	0.99
AB	0.49	0.57	0.57	0.12	0.90
AB	0.48	0.58	0.60	0.14	0.95
AB	0.47	0.58	0.59	0.14	0.99

features can be seen in table 10. The left side shows the classification without delocalization and the right side with delocalization. The feature delocalization seems to have a small positive net gain on the classification results for nearly all cases. Only the maximal value decreases slightly. Therefore, the feature delocalization is expected to be beneficial.

Feature selection by RFW A further parameter taken into account is the effect of the combination of PCA and RFW and the sole usage of the RFW for feature reduction. Table 11 shows the effect of RFW for both cases and the effect of the feature delocalization.

For the case of using RFW, the feature delocalization increases the classification results for nearly all cases and all measures as found for the sole usage of the PCA (figure 10). However, the comparison of table 10 and table 11 shows

Table 10: Classification results of the tested classifiers for 13 patients with leave one out strategy after pre-processing with MNF and correction of the barrel distortion and usage of spatial features for 0.25 % of the data being used as training data and the PCA is done and 95 % of the variance of the PCA is used. On the left side, the results are shown without and on the right side with feature delocalization.

Method	ACC	ACC2	AUC	MCC	ACC	ACC2	AUC	MCC
Feature delocalization	No				Yes			
RFW	0.54	0.60	0.62	0.18	0.54	0.62	0.61	0.19
RB	0.48	0.58	0.59	0.13	0.51	0.59	0.58	0.16
SVM (lin)	0.55	0.63	0.49	0.21	0.54	0.63	0.49	0.20
SVM (Gauss)	0.47	0.57	0.56	0.12	0.49	0.59	0.56	0.16
AB	0.48	0.58	0.60	0.14	0.51	0.59	0.58	0.16

Table 11: Classification results of the tested classifiers for 13 patients with leave one out strategy after pre-processing with MNF and correction of the barrel distortion and usage of spatial features for 0.25 % of the data being used as training data. On the left side RFW is used for feature selection with eight features and on the right side RFW for feature selection is used after the PCA. The top rows represent analysis without and bottom rows with feature delocalization.

Method	ACC	ACC2	AUC	MCC	ACC	ACC2	AUC	MCC
Feature selection	RFW				PCA+RFW			
RFW	0.45	0.55	0.58	0.08	0.46	0.56	0.51	0.10
RB	0.44	0.54	0.59	0.09	0.43	0.56	0.53	0.10
SVM (lin)	0.42	0.55	0.45	0.07	0.50	0.61	0.47	0.18
SVM (Gauss)	0.44	0.54	0.56	0.07	0.48	0.56	0.55	0.11
AB	0.43	0.55	0.61	0.10	0.43	0.53	0.52	0.05
RFW	0.47	0.59	0.61	0.15	0.50	0.57	0.55	0.14
RB	0.46	0.58	0.59	0.14	0.45	0.54	0.55	0.08
SVM (lin)	0.49	0.59	0.49	0.14	0.52	0.57	0.47	0.13
SVM (Gauss)	0.45	0.58	0.55	0.09	0.49	0.57	0.58	0.15
AB	0.45	0.56	0.61	0.12	0.47	0.58	0.57	0.10

that the usage of RFW for feature selection does not provide advantages. Therefore, it should not be considered for the final analysis.

Furthermore, it is tested how the amount of features selected by the RFW influences the results after the PCA. Table 12 shows the results for the four respectively eight most important features. The quality drops only for both

Table 12: Classification results of the tested classifiers for 13 patients with leave one out strategy after pre-processing with MNF and correction of the barrel distortion and usage of spatial features for 0.25 % of the data being used as training data. On the left side the results are shown with the four and on the right side with the eight main features after PCA.

Method	ACC	ACC2	AUC	MCC	ACC	ACC2	AUC	MCC
Number features	4				8			
RFW	0.50	0.60	0.54	0.14	0.50	0.57	0.55	0.14
RB	0.45	0.54	0.55	0.08	0.45	0.54	0.55	0.08
SVM (lin)	0.56	0.55	0.51	0.07	0.52	0.57	0.47	0.13
SVM (Gauss)	0.46	0.57	0.55	0.12	0.49	0.57	0.58	0.15
AB	0.45	0.55	0.54	0.08	0.47	0.58	0.57	0.10

SVMs when using four features a little bit. Hence, the results for eight features are favourable.

MNF cut The next point to probe is the optimal amount of features used from the MNF. Table 13 shows the difference of the classification results.

Table 13: Classification results of the tested classifiers for 13 patients with leave one out strategy after pre-processing with MNF and correction of the barrel distortion and usage of spatial features for 0.25 % of the data being used as training data. In both cases the PCA was done and 95 % of the variance of the PCA is used. On the left side the results are shown with the first two components of the MNF and on the right side the results with the first four components of the MNF are shown.

Method	ACC	ACC2	AUC	MCC	ACC	ACC2	AUC	MCC
MNF cut	2				4			
RFW	0.54	0.61	0.61	0.17	0.54	0.62	0.61	0.19
RB	0.49	0.58	0.58	0.14	0.51	0.59	0.58	0.16
SVM (lin)	0.55	0.64	0.49	0.22	0.54	0.63	0.49	0.20
SVM (Gauss)	0.49	0.59	0.57	0.15	0.49	0.59	0.56	0.16
AB	0.49	0.58	0.59	0.14	0.51	0.59	0.58	0.16

While the linear SVM benefits from using only two MNF components, all the other classifiers show slightly worse results. Therefore, for the final analysis the reduction of the MNF components to two can be tried. There is no clear information which value is preferable. Due to the average over all increase of the results, the first four components will be used for classification. Furthermore, if the hint is correct that the amount of components corresponds to

the amount of absorbers, it makes sense to use four components due to the fact that more than two absorbers are present.

Outlier rate For SVM and RB, the effect of the outlier rate is shown in figure 37 and figure 38. Figure 37 shows the AUC and ACC2 for RB and SVM separately with the effect of the PCA. Figure 38 shows the MCC value for SVM and RB together with the effect of the PCA. From figure 37, it can be seen that for SVM, the outlier rate has nearly no effect. For RB, an outlier rate less than 0.23 seems to be beneficial with a small increase at 0.23 for the most cases. If RFW is used for feature selection, AUC increases with higher outlier rates. Furthermore, if the PCA is used a high outlier rate of more than 0.4 seems to be beneficial. However due to the fact that it is only shown for a single value, it might be an artefact. Hence, the final outlier rate is set to 0.23.

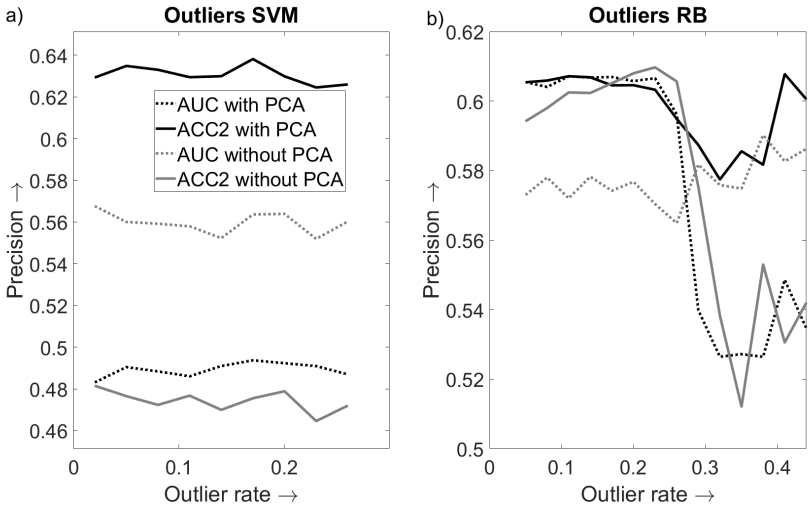

Figure 37: AUC and ACC2 as a function of the outlier rate for SVM (a) and RB (b).

In comparison to the AUC and ACC2, the MCC provides more smooth results with less outliers, as shown in figure 38. In general, the same trends can be found for MCC as found for ACC2 and AUC (figure 37). The SVM is not very dependent on the outlier rate with a small peak at an outlier rate at an outlier rate of 0.17. For RB without PCA, the ideal outlier rate should be higher than 0.3 while with PCA, no influence of the outlier rate on the MCC can be found. This behaviour pinpoints that by the feature selection with RFW, more noise seems to be present because in most cases, the higher principle components contain mainly noise and these components are not used for the classification. However, the PCA seems to smooth the results due to the fact that a weighted

sum of all the other features is used for every principle component. Due to the higher noise without the PCA, some data points might be strongly influenced by noise. This noise might be reduced by RB by ignoring these points. This seems to allow RB to reach a similar MCC as with the usage of the PCA.

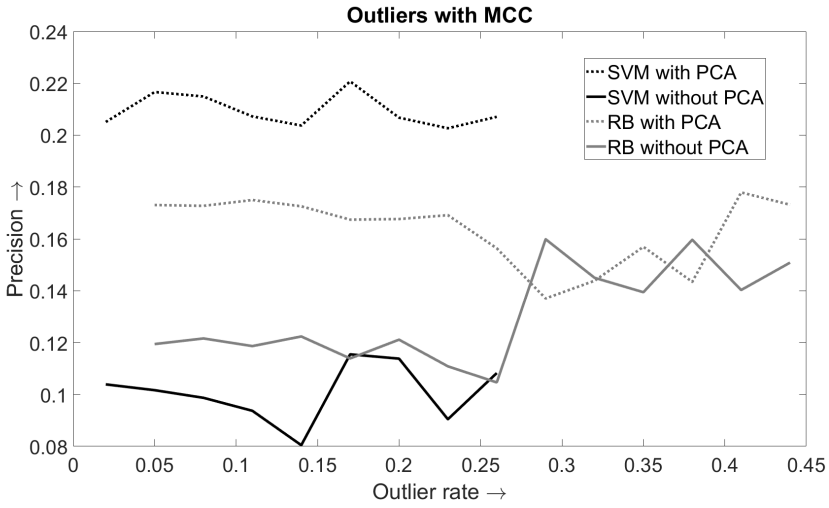

Figure 38: MCC as a function of the outlyer rate for SVM and RB.

Feature reduction with RFW As one of the last parts, it is tested how the feature reduction using RFW would affect the results. Table 14 shows the comparison for the usage of the eight most important features in comparison with the usage of all features.

On the right side, there are the classification results for the case that all features are used and on the left side there are the classification results for the case that the eight most important features are used with PCA (top) or without PCA (bottom). In all cases, the usage of all features does not significantly increase the precision of the classification. Therefore, the feature reduction method of RFW is valid. Furthermore, for the case that all features are used for classification, the usage of the PCA for preprocessing increases the accuracy with all four measures. Therefore, the classification independent pre-processing seems to be an important point for further increase of the classification accuracy. Moreover, the feature reduction is successful: More features do not improve the results.

Comparison to basic classifiers As last step for the usage of the features, the improvement in comparison to simple classifiers is tested. Table 15 com-

Table 14: Classification results of the tested classifiers for 13 patients with leave one out strategy after pre-processing with MNF and correction of the barrel distortion and usage of spatial features for 0.25 % of the data being used as training data. On the left side, only the eight most important features are used and on the right side all features are used. Furthermore, on top the PCA was applied before feature selection and on the botton it was not applied.

Method	ACC	ACC2	AUC	MCC	ACC	ACC2	AUC	MCC
RFW features	8				all			
RFW	0.54	0.62	0.61	0.19	0.54	0.62	0.61	0.19
RB	0.51	0.59	0.58	0.16	0.51	0.59	0.58	0.16
SVM (lin)	0.54	0.63	0.49	0.20	0.54	0.63	0.49	0.20
SVM (Gauss)	0.49	0.59	0.56	0.16	0.49	0.59	0.56	0.16
AB	0.51	0.59	0.58	0.16	0.51	0.59	0.58	0.16
RFW	0.47	0.59	0.61	0.15	0.47	0.58	0.61	0.13
RB	0.46	0.58	0.59	0.14	0.45	0.58	0.61	0.14
SVM (lin)	0.49	0.59	0.49	0.14	0.46	0.58	0.49	0.15
SVM (Gauss)	0.45	0.55	0.55	0.09	0.44	0.58	0.57	0.14
AB	0.45	0.56	0.61	0.12	0.46	0.58	0.62	0.14

Table 15: Classification results of the tested classifiers for 13 patients with leave one out strategy after pre-processing with MNF and correction of the barrel distortion and usage of spatial features for 0.25 % of the data being used as training data. On the left side, the PCA is done and 95 % of the variance of the PCA is used and on the right, side RFW is used for feature selection and the eight best features are used.

Method	ACC	ACC2	AUC	MCC	ACC	ACC2	AUC	MCC
Feature selection	PCA				RFW			
RFW	0.54	0.62	0.61	0.19	0.47	0.58	0.61	0.15
RB	0.51	0.59	0.58	0.16	0.46	0.58	0.59	0.14
SVM (lin)	0.54	0.63	0.49	0.20	0.49	0.59	0.49	0.14
SVM (Gauss)	0.49	0.59	0.56	0.16	0.45	0.55	0.55	0.09
AB	0.51	0.59	0.58	0.16	0.45	0.56	0.61	0.12
QDA	0.55	0.61	0.51	0.18	0.46	0.58	0.52	0.13
Naive Bayes	0.56	0.61	0.56	0.19	0.53	0.61	0.59	0.17
KNN	0.51	0.58	0.54	0.12	0.44	0.51	0.51	0.02

pares the results for QDA, naive Bayes and KNN with AB, RB, SVM and RFW. QDA and Naive Bayes have a higher ACC than the advanced classfiers. How-

ever, ACC2 and MCC show a lower classification accuracy than for the main classifiers. Furthermore, the AUC values are much lower. KNN shows the worst results for all measures. This is partly contradicting to the expectation due to the fact that adaptive KNN can be seen as a similar method as RFW [140]. However, this shows the improvement of RFW compared to KNN. If RFW is used for feature reduction, the results of naive Bayes will be better than for all the advanced classifiers. However, the results are worse if PCA is used for feature reduction. In general, the advanced classifiers show a better classification accuracy in most of the measures. However, naive Bayes might be considered further if it wouldn't be the slowest classifiers for training and testing even in comparison to SVM for the used Maltab implementation.

Summary In summary, different features gradually improve the classification results. PCA for feature selection provides better results than using RFW and a high amount of used variance of 99 %. Feature delocalization seems to be preferable and MNF cut of four provides better results. The outlier rate for SVM has nearly no effect while for RB 0.25 and 0.4 deliver the best results. Moreover, the usage of feature reduction does not decrease the results in comparison to all features. For the usage of PCA, the results even improve. Naive Bayes is a further possible classificator which provides good results.

5.1.3 Analysis of spatial features

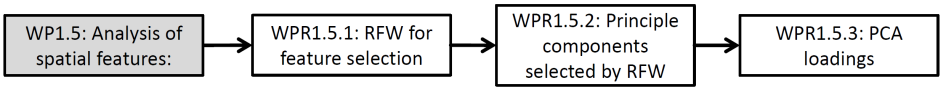

Figure 39: Overview of the analysis of the spatial features of WP1 in the result section. Each box symbolized one sub chapter and corresponds to the headlines. The grey box symbolizes the generic topic/research question and italic font symbolizes that this part of the flow chart will be shown as generic topic later.

Figure 39 shows the overview of the analysis of the spatial features. In this section first, it is shown which features are picked by RFW as feature selection tool for all cases of the leave-one-out analysis from the parameter study. Afterwards, the loadings of the PCA are studied. Finally, it is looked which principle components of the PCA are selected by the RFW. Additionally to the parameter study, the feature reduction process is studied in this section. From the parameters, especially the feature delocalization is expected to have an influence on feature selection. The interpretation of the features is done only qualitatively as does not provide any insights for the goal of having MSI/HSI as red flag technology. However, it provide some interesting insights.

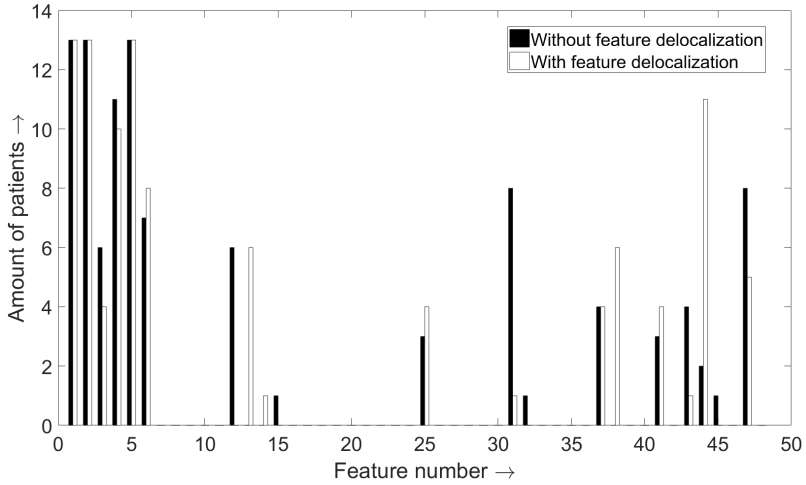

Figure 40: Most important features selected by RFW used for classification with and without feature delocalization.

RFW for feature selection Figure 40 shows the most frequently selected components for the case that RFW is used for feature selection. In total, the effect of feature delocalization is small. However, higher order features become slightly more important if feature delocalization is used. Hence, longer wavelengths get more important (compare to table 6). This is most likely caused due to the fact that the fine features from shorter wavelengths are averaged out due to feature delocalization. This effect might explain the improved results by the feature delocalization as longer wavelength show better results for carcinomas in the upper GI [14]. Furthermore, if a feature is relevant on a single place, the surrounding is in most cases of the same class where the feature occurred. Thus by this averaging process, the noise is reduced.

Principle components selected by RFW For the case that a PCA is used before feature selection by RFW, figure 41 shows the results. In this case, there is a shift to higher order principle components (features), especially feature number 42 and 47. However, the shift is small and does not seem to be beneficial. Despite the fact that higher order principal components seem to be used repeatedly, other components seems to bear relevant information. A test with the usage of the four best principal components selected by RFW prefers still the first principal component and to a high degree some higher principal components. Thus, the higher principle components do seem to contain relevant amounts of information.

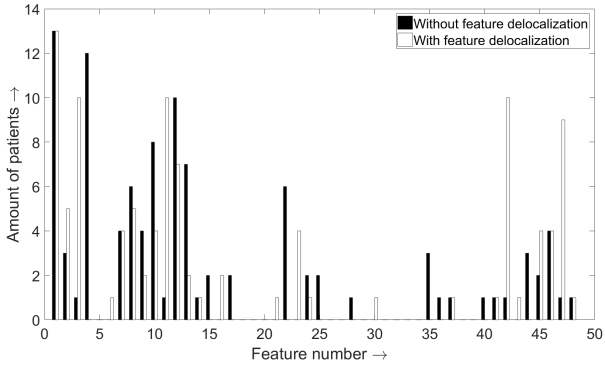

Figure 41: Most important principle components for classification selected by RFW.

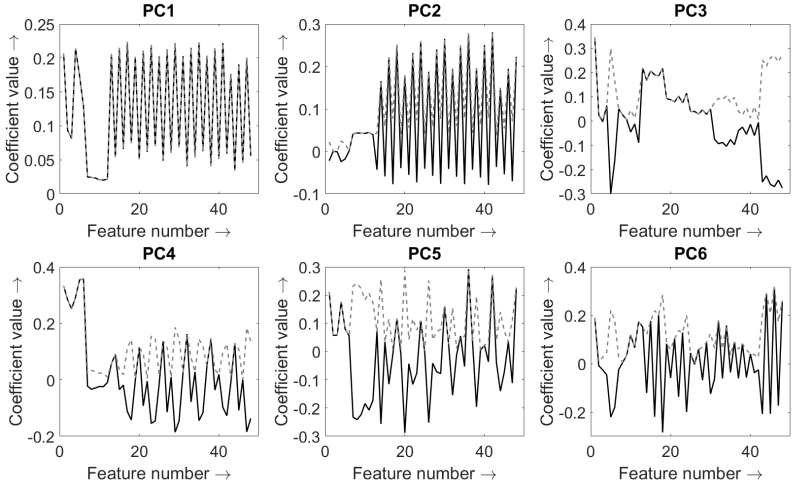

Figure 42: Principle components for the six main features of the PCA. The components (black line) and its absolute value are shown (grey dotted line).

PCA loadings Another way to analyse the importance of the features is to use the coefficient matrix of the PCA. Figure 42 shows the first six principle components and its absolute values. The absolute values are shown to present the feature importance while the normal values show the relative effect of the features. Hence, it can be seen which features have a similar and which features have an opposing effect. The first principle component is the most important one. It describes 56 % of the variance if the PCA is done for all 13 patients. Furthermore using RFW for feature selection, it is also the most important feature. It seems to describe the basic offset due to the fact that all features have a positive impact.

For the first principle component, the blue as well as the yellow light is very important (feature number 1 and 4). However, the derivative features (feature numbers 7-12) have nearly no influence. In total, the spatial features dominate the first principle component. For each wavelength, every second spatial feature is of high importance. There is no dependency of the wavelength found. All features with $l = 1$ are important independent of the p as seen in figure 42 for PC1. However, for rising p their importance increases. Thus, all the features with $l = 1$ are grouped together. Therefore, it seems to be more beneficial to increase l instead of p to describe the tissue more precisely.

The second principle component shows an opposing behaviour to the first principle component. It describes 31 % of the variance if the PCA is done for all patients. The normal intensity values have no influence while the main variance is generated by features with $l = 2$ while features with $l = 1$ have a small negative effect on the second principle component as seen in figure 42 for PC2. Again features with increasing p generate a stronger effect on the second principle component. Therefore, features with $l = 2$ also seem to be important and seem to show different effects than features with $l = 1$. Moreover, it appears that the usage of the features is nearly disjunct to the first principle component. This might be caused by the fact that features with $l = 1$ and $l = 2$ are completely linear independent as shown in figure 10. Thus, probing with different l values seem to provide different data and, therefore, more different important principle components. Hence, the usage of more features with higher l might increase the classification results. Moreover, this feature describes a high amount of the variance of the data. As conclusion, it can be said the l is the more relevant parameter than p as different l are sorted in different principle components.

The third principle component is dominated by the positive blue (feature number 1) and the negative green (feature number 5) single pixel intensities and with the negative spatial features of the red light. In general, shorter wavelengths have a positive impact on this feature and longer wavelengths a negative impact. The spatial components of this feature are sorted by their spectral band. Due to the different penetration depth of short and long wavelengths, this principle component seems to test if spatial features are caused by shallow or deep effects. Thus, this principle component will become smaller if any deep features are present and it will become bigger if shallow features are present. Therefore, this principle component seems to probe the average depth of the present spatial features. Additionally, this feature has similarities with the inverse penetration depths. Thus, it can also be seen as spectral feature.

The fourth principle component is dominated by all six single pixel intensities and with opposing sign most of the features which show the presence of spatial features. Thus, this principle component seems to probe how strong the general strength of spatial features is.

The fifth principle component is dominated by the intensities of the derivative images and the spatial features with $p = 0$ and $l = 2$ for all wavelengths which are all counted negative. Features with $p = 2$ and $l = 2$ are considered positive. Therefore, this principle component seems to probe the difference between spatial features with a high spatial frequency and a low spatial frequency. The higher the spatial frequency, the higher is the value of this principle component. In contrast to the second principle component, it seems to probe the presence of spatial features with a high spatial frequency.

The sixth principle component is dominated by many effects. For shorter wavelengths spatial features with $l = 2$ are negative and for longer wavelength spatial features with $l = 1$ are negative. In both cases the others are positive. Furthermore, the derivative has a positive impact as well as the blue single pixel feature. The green and red single pixel feature has a positive impact. Hence, it seems that this principle component probes the change of the feature size from shallow to deep features.

The interpretation of the principle components is done only qualitatively as it does not provide any insights for the goal of having MSI/HSI as red flag technology. Nevertheless, the qualitative interpretation allows already an understanding why the PCA provides better results than RFW for feature selection:

The first interesting result is that the PCA groups automatically the features by wavelength, depth and similar spatial information. Therefore, it is convincing that the PCA improves the overall classification results as it corresponds to physical parameters. As the PCA is a linear method, the grouping is a weighted sum of the features and, therefore, the PCA is a method for further noise reduction. The second interesting result is that the feature delocalization makes the fourth principle component less important as seen in figure 41. It is logical that the smoothing decreases the importance of spatial features. Thus, the classifier has to use different features for collecting spatial information. The third principle component will be used as a substitute which also provides combined spatial information. As the overall results improve with feature delocalization, it should also be noted that the information if spatial features have a significant amount of variance does not seem to provide relevant information for the detection of carcinomas in the stomach.

Furthermore, RFW consequently uses the non-spatial features with high priority while for the feature selection by PCA, the spatial features are much more important. At the same time, the results with PCA instead of RFW for feature selection are better. Thus, it can be concluded that the spatial features are important.

5.1.4 Test of intra patient variations

Table 16: Classification results for the intra patient analysis. Only spatial features with a maximal $p = 2$ and $l = 4$ are used. The PCA is done for feature reduction and 99.5 % of the variance is used for the training.

Method	ACC	ACC2	AUC	MCC
RFW	0.93	0.93	0.88	0.83
RB	0.74	0.74	0.74	0.45
SVM (lin)	0.72	0.74	0.72	0.43
SVM (Gauss)	0.96	0.96	0.89	0.89
AB	0.96	0.96	0.89	0.89

Table 16 shows the final results for the intra patient analysis. In general, the classification results are excellent with an MCC of more than 0.8. Furthermore, the maximal ACC2 as well as the ACC are larger than 0.95. Thus, the carcinomas can be correctly identified. However, only RFW, SVM with a Gaussian kernel and AB are able to identify the carcinomas correctly. This result is contradicting to the analysis of inter patient variations where SVM with Gaussian kernel normally shows the worst results and SVM with linear kernel, RFW and RB show the best results as shown in chapter 5.1.5. Most likely, SVM with Gaussian kernel over-fits the training data so that a generalization of the results becomes difficult. RB has likely worse results due to the fact that the outlier rate is too high for intra patient variations. With an adequately chosen outlier rate, its result would be the same as for AB. In conclusion, the intra patient variations allow a reliable classification and, therefore, multi/hyper spectral imaging might be used to find carcinomas in the future.

5.1.5 Comparison to the state of the art

After full optimization, the results in section 5.1.2 show the same final accuracy as the results from Hohmann et al. [117]. However due to the fact that only a fraction of the training data compared to Hohmann et al. [117] is used, there is an expected improvement when the same amount of training data is

used. The results for the same amount of training data is shown in table 17. Compared to the parameter study in section 5.1.2, the value for l is 3 instead of 2.

Table 17: Classification results of the tested classifiers for 13 patients with leave one out strategy after pre-processing with MNF and correction of the barrel distortion and usage of the MNF features and the spatial features for 0.5 % of the data being used as training data. The PCA is done and 99 % of the variance of the PCA is used. On the left side, the results with spatial are shown and on the right side the results are shown from the study of Hohmann et al. [117].

Method	ACC	ACC2	AUC	MCC	ACC	ACC2
Study	This thesis				Hohmann et al. [117]	
RFW	0.66	0.68	0.69	0.32	0.55	0.59
RB	0.59	0.64	0.64	0.25	0.64	0.64
SVM (lin)	0.66	0.68	0.66	0.31	0.62	0.62
SVM (Gauss)	0.54	0.61	0.60	0.20	0.55	0.59
AB	0.59	0.65	0.64	0.27	0.55	0.59

For the ACC2, there is an increase of 0.04 per cent points from 0.64 to 0.68 of the maximal ACC2 in comparison to the results from Hohmann et al. [117]. The ACC2 is significantly different for the improved version with an p-value of 0.0034 (as shown in table 18) compared to the previously published ones by Hohmann et al. [117]. At the same time, neither the classification method nor the interaction is significant. In summary, the usage of advanced noise filtering and spatial feature provides a robust way for improving the overall classification results. However, it should be noted that the accuracy measures are still fairly low, despite the improvement.

Table 18: Anova for the ACC2 with the interaction for the classifiers and the advantaged noise removal and spatial features. The new pre-processing shows a significant difference of the results compared to the previously published ones by Hohmann et al. [117].

Source	Sum Sq.	d.f.	Mean Sq.	F	p
Classifier	0.028	4	0.0069	0.62	0.65
MNF and spatial features	0.10	1	0.10	8.9	0.0034
Interaction	0.019	4	0.0048	0.43	0.79

5.1.6 Comparison to medical conditions

In general, it should be noted in this section that all results are fairly speculative. This is due to the fact that the amount of patients is too low for a statistical analysis. Hence, all results should be seen as hints towards a certain direction. First in table 19, the effect of pre-treatment is shown. On the left side, the effect of the pre-treatment is assessed for all patients and on the right side, the patients with strong inflammation and mucus are excluded due to the fact that inflammation and mucus might overshadow the effect of the pretreatment. In contrast to the study from Hohmann et al. [117], the pre-treatment does not seem to have an effect on the final accuracy. The usage of the new noise filtering, the spatial and spectral-spatial features seem to negate the effect of the pretreatment.

Table 19: Effect if pre-treatment was done or not. The left side shows the effect of treatment for all patients and the right side shows the effect of treatment for the patients with no or low amount of mucus and/or inflammation.

Method	ACC2	MCC	ACC2	MCC	ACC2	MCC	ACC2	MCC
Patients	All				No/weak mucus + inflammation			
Pre-treatment	yes		no		yes		no	
Patients	6		8		4		7	
RFW	0.70	0.32	0.69	0.37	0.68	0.37	0.71	0.40
RB	0.70	0.34	0.68	0.34	0.68	0.39	0.70	0.38
SVM (lin)	0.71	0.34	0.69	0.34	0.69	0.37	0.72	0.40
SVM (Gauss)	0.66	0.29	0.65	0.31	0.66	0.33	0.66	0.32
AB	0.68	0.32	0.66	0.31	0.67	0.37	0.67	0.33

Table 20 shows the effect of inflammation. Except for the case of strong inflammation, there is no significant effect of the classification ACC2 and MCC based on the inflammation. However, the results seem to pinpoint that a weak to medium inflammation might increase the classification performance as the classifiers might learn that the presence of inflammation is a sign for carcinomas. This might be a clever Hans-effect [141] in which the classifier does not learn to find the carcinoma, it only finds correlations. In this case, the inflammation is associated with carcinomas which is true. However, the rate of incidence is much higher in normal endoscopy procedures. Moreover, inflammation appears most of the time without carcinomas. Hence, this correlation is not useful. However, for strong inflammation the classification is barely possible. This might have two major reasons. First, there is no other patient with strong inflammation where the classifier might be trained on.

Table 20: Effect of inflammation on the classification results.

Method	ACC2	MCC	ACC2	MCC	ACC2	MCC	ACC2	MCC
Inflammation	no		weak		medium		strong	
Patients	6		4		3		1	
RFW	0.67	0.35	0.75	0.41	0.69	0.31	0.55	0.12
RB	0.67	0.34	0.71	0.39	0.72	0.36	0.54	0.09
SVM (lin)	0.67	0.34	0.76	0.41	0.73	0.35	0.48	-0.05
SVM (Gauss)	0.65	0.31	0.68	0.32	0.66	0.28	0.58	0.20
AB	0.65	0.30	0.69	0.34	0.71	0.35	0.56	0.15

Moreover, one patient shows no significant result. The second reason might be that strong inflammation disguises the carcinoma.

Table 21 shows the effect of mucus. It seems that a certain amount of mucus effects the classification results. However, due to the fact that areas with mucus are consequently labelled as healthy by the doctor, the classificator gets an easier classification for stronger mucus. Moreover, if the mucus leads to an over-saturation of the image, the over saturated parts are excluded from the analysis. Hence, the better classification with more mucus is most likely a pseudo correlation.

Table 21: Effect of mucus on the classification results.

Method	ACC2	MCC	ACC2	MCC	ACC2	MCC	ACC2	MCC
Mucus	no		a little		medium		a lot	
Patients	6		6		1		1	
RFW	0.70	0.38	0.67	0.35	0.78	0.28	0.66	0.17
RB	0.67	0.33	0.69	0.38	0.69	0.20	0.78	0.30
SVM (lin)	0.70	0.34	0.68	0.36	0.76	0.27	0.77	0.29
SVM (Gauss)	0.65	0.29	0.67	0.34	0.68	0.18	0.66	0.23
AB	0.66	0.32	0.67	0.33	0.65	0.16	0.77	0.28

In summary, the effects of inflammation, mucus and pre-treatment are fairly low. The dataset is to small too provide reliable results. However already in this data set, it might be possible that the clever Hans effect is present in the form of pseudo correlations used by the classifiers. This effect should be studied more in future studies and it should definitely be considered.

5.1.7 Analysis of carcinomas and pre-carcinomas in the oesophagus

Table 22: Classification results of carcinoma/no-carcinoma in the oesophagus of the tested classifiers for 12 patients with leave one out strategy. Four patients have no BE. The pre-processing is done with MNF, correction of the barrel distortion and usage of the spatial features. In total, 0.5 % of the data is used as training data. The PCA is done and 99 % of the variance of the PCA is used.

Method	ACC	ACC2	AUC	MCC
RFW	0.85	0.50	0.54	0.01
RB	0.83	0.50	0.48	0.02
SVM (lin)	0.86	0.50	0.59	0.00
SVM (Gauss)	0.81	0.50	0.46	0.00
AB	0.83	0.50	0.46	0.02
QDA	0.80	0.53	0.51	0.07
Naive Bayes	0.83	0.51	0.51	0.06
KNN	0.77	0.50	0.50	-0.01

Table 22 shows the result of the classification of carcinomas in the oesophagus. The carcinomas in the oesophagus cannot be detected. Most likely, the main reason for the bad results is the different geometry of the oesophagus. The geometry of the hollow tube like structure causes the images to differ even in a single image. For example, parts in the beginning are bright while parts farer away are darker. Moreover, the different angle of the tissue towards the camera might play an important role. Due to the strong absorbance of blood in the blue and green region, the reflection of the tissue is not a lambertian source [142]. Therefore, an image of the same sample with different angles towards the surface, will show different multi spectral images and, thus, different spectral information. Thus, the results from the stomach cannot be transferred to oesophagus.

Table 23 shows the rate of BE detection. The accuracy is comparable to rate of detection by the clinicians. Only nine out of 13 patients had BE. This leads to an accuracy of 69 % not including the BE which was not detected at all. In this study, the accuracy is up to 72 %. However, the closer analysis shows that nearly all pixels are seen as healthy in this case. For this reason, the MCC is used for the analysis. The results for the MCC are similar to the results for the analysis of the carcinoma in the stomach. Thus at the moment with the current set-up, BE might be detected with MSI and the results can be transferred from carcinomas in the stomach. The difference to the carcinomas

Table 23: Classification results of BE/no-BE of the tested classifiers for 13 patients with leave one out strategy. Four patients have no BE. The pre-processing is done with MNF, correction of the barrel distortion and usage of the spatial features. In total, 0.5 % of the data is used as training data. The PCA is done and 99 % of the variance of the PCA is used. For MCC and ACC2, only the patients where BE is present are used for the analysis.

Method	ACC	ACC2	AUC	MCC
RFW	0.69	0.53	0.68	0.07
RB	0.72	0.53	0.65	0.08
SVM (lin)	0.54	0.62	0.71	0.20
SVM (Gauss)	0.68	0.55	0.56	0.09
AB	0.68	0.56	0.63	0.10
QDA	0.64	0.58	0.70	0.13
Naive Bayes	0.67	0.57	0.70	0.13
KNN	0.66	0.56	0.60	0.11

in the oesophagus can be explained by the effect that BE always appears close the stomach. Therefore in all imaging cases, the angle of the image to the endoscope is similar. Thus, the spectral information keep constant. Furthermore, due to the fact that imaging is done close to the stomach, the whole image has a similar brightness. Hence, the problems from the hollow tube geometry play a minor role.

5.2 Spectral spatial variation

After the importance of features is shown, the usage of combined spatial and spectral features might generate additional benefit. To demonstrate the validity of the SSV, its effect is taken into account in more detail on the example image 31 from before. Figure 31 shows on the left side the SSV and on the right side the absolute SSV normalized by the intensity of the original image. The ellipse shows the main area of the carcinoma. The SSV is for most parts of the image constant except the upper right part. By dividing the SSV by the intensity of the image, the constant healthy tissue shows two different parts (figure 31 (right)). Thus, the SSV is at least partly independent of the intensity of the image. Thus, for the healthy part the SSV does not seem to depend on the intensity of the image. The upper right part is the area were the carcinoma is present and its SSV is clearly different (figure 31 (left)). The SSV is between -0.03 to 0.045 in the healthy area at the areas without specular reflection. The SSV of the cancerous area is around -0.18 to 0.02. Hence, there

is a difference between them. However, it should be noted that most of the central carcinoma is in the range between -0.18 to -0.13.

The quite constant value of the SSV for the most parts of the image can be explained by the noise of the endoscope system and the normal spectral variance of the tissue. On the one hand, the endoscope system generates a constant noise of 5 intensity values for the whole image, therefore the SSV detects this variation. On the other hand, the carcinoma should have a different spatial and spectral variance than the healthy tissue. The different SSV for the carcinoma can be explained with three main points. First, this part of the image is closer to the camera of the endoscope and, therefore, more gastric pits (GP) are visible, leading in combination with movement artefacts, to a higher SSV. Second, the movement artefacts are most likely caused by a stronger variance around the cancerous region when the movement artefacts alter the foreground with the background. Third and most important, the cancerous area itself might be the reason. At cancerous areas normally higher spatial and spectral variations are expected [14]. Thus, it indicates the presence of the cancerous tissue.

Table 24: Classification results of the tested classifiers for 13 patients with leave one out strategy after pre-processing with MNF and correction of the barrel distortion and usage of the MNF features for 0.25 % of the data being used as training data. The additional spatial features are not used. On the left side, the PCA is done and 99 % of the variance of the PCA is used and on the right side, RFW is used for feature selection and the six best features are used.

Method	ACC	ACC2	AUC	MCC	ACC	ACC2	AUC	MCC
Feature selection	PCA				RFW			
RFW	0.52	0.63	0.65	0.22	0.46	0.60	0.63	0.17
RB	0.48	0.61	0.60	0.17	0.43	0.58	0.57	0.13
SVM (lin)	0.50	0.63	0.62	0.23	0.52	0.65	0.59	0.25
SVM (Gauss)	0.49	0.58	0.57	0.14	0.49	0.57	0.56	0.13
AB	0.48	0.59	0.60	0.15	0.42	0.57	0.57	0.12
QDA	0.54	0.64	0.53	0.22	0.51	0.60	0.50	0.19
Naive Bayes	0.58	0.64	0.62	0.25	0.53	0.62	0.65	0.21
KNN	0.47	0.55	0.58	0.11	0.45	0.55	0.55	0.09

The results of the usage of the spatial-spectral feature, generated by the MNF, are shown in table 24. For both cases with PCA and RFW as feature selection tool, the results improve in comparison to the pure spatial features shown in table 15. The improvement will be especially high if RFW is used as tool for feature selection. In this case, the results are as good as for the case that

PCA is used for feature selection. For the case that PCA is used for feature reduction, the ACC does not change significantly except for Naive Bayes where it increases. The ACC2 is slightly better as well as the MCC. The AUC is much higher in comparison to pure spectral features. For RFW as tool for feature selection, the ACC increases slightly for the simple classifiers. ACC2, AUC and MCC increase significantly. Hence, the spatial-spectral features should be considered for the main analysis.

The reason that the spatial-spectral features provide such good results, might be explained again with help of figure 31. The noise level of the healthy area is dominated by the noise of the endoscope. Thus, homogeneous areas provide a nearly constant noise level independent of their intensity values. However, the cancerous area is less homogeneous in the spatial as well as the spectral dimension. Hence, the residuum most likely will have different values at the cancerous areas. Therefore, it can be used for classification.

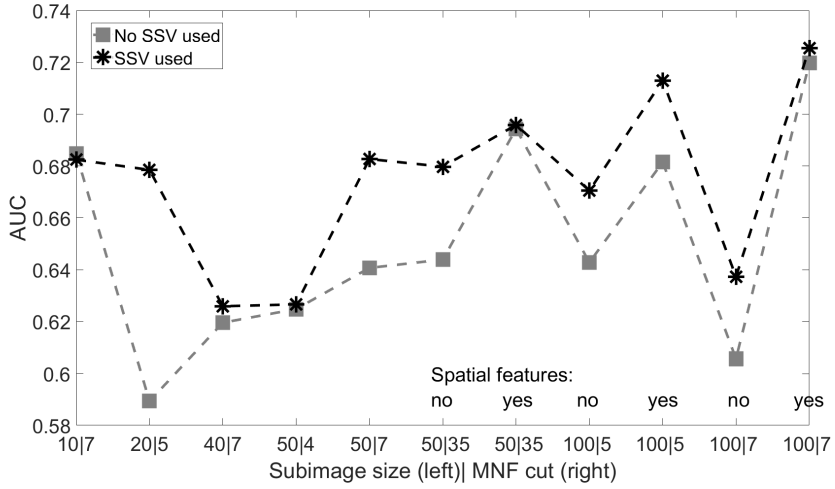

Figure 43: AUC as a function of the tested parameters: sub-image size, MNF cut, spatial features and the usage of the SSV.

After a basic improvement could be shown, the results of a wider parameter study is shown in figure 43. Figure 43 shows the mean result of the best classifier for comparison of the AUC of the parameter study for all parameters. There is an intersection of the two lines, representing the data with and without SSV, at only one specific data point (subimage size =10 and MNF cut=7). Thus, this main effect of the ANOVA should not be interpreted for SSV when this data point is included. However, it is only one point and a slight overlap and it is for the mean result of the best classifier.

Table 25: Anova for the AUC with the interaction as function of all tested parameters. The SSV shows a significant effect on the AUC. The MNF cut, the sub-image size and the usage of spatial features show also a significant effect and a significant interaction.

Source	Sum Sq.	d.f.	Mean Sq.	F	Prob>F
SSV	0.1211	1	0.12108	6.03	0.0142
MNF cut	0.2021	1	0.20213	10.1	0.0015
Sub-image size	0.2028	1	0.20282	10.1	0.0015
Spatial features	0.1733	1	0.17334	8.64	0.0033
Classifier	0.0214	4	0.00535	0.27	0.8996
SSV*MNF cut	0.0466	1	0.04663	2.32	0.1277
SSV*Sub-image size	0.0215	1	0.02152	1.07	0.3006
SSV*Spatial features	0.0094	1	0.00943	0.47	0.4933
SSV*Classifier	0.0137	4	0.00343	0.17	0.9533
MNF cut*Sub-image size	0.1536	1	0.15358	7.65	0.0057
MNF cut*Spatial features	0.1778	1	0.17784	8.86	0.003
MNF cut*Classifier	0.0956	4	0.0239	1.19	0.313
Sub-image size*Spatial features	0.1875	1	0.18747	9.34	0.0023
Sub-image size*Classifier	0.0144	4	0.0036	0.18	0.9492
Spatial features*Classifier	0.0432	4	0.01079	0.54	0.7082

The analysis of a complete dataset for the AUC is shown in table 25. The single parameters except for the classifier show a significant effect. The classifier does not seem to have a significant effect on the data set. This might be caused by the usage of strong filtering and spatial and spectral-spatial features. Due to this, the boundaries might smear out and, therefore, RB cannot shine. Furthermore, there is an interaction between the subimage size, the MNF cut and the spatial features. The interaction between the MNF cut and the subimage size is expected as both parameters are generated from the calculation of the MNF. Moreover, both are parameters which alter the noise filtering of the MNF. The interaction of both of them with the spatial features is expected to have the same origin, as the generation of the spatial features adds 72 features which are a weighted average and, therefore, also some kind of noise reduction. However, the usage of the SSV does not show any interaction and seems to improve nearly all results. Hence, the SSV seems to be statistically independent of spatial features and the noise reduction. Therefore, there is significantly different information collected from the SSV compared to the standard spatial features.

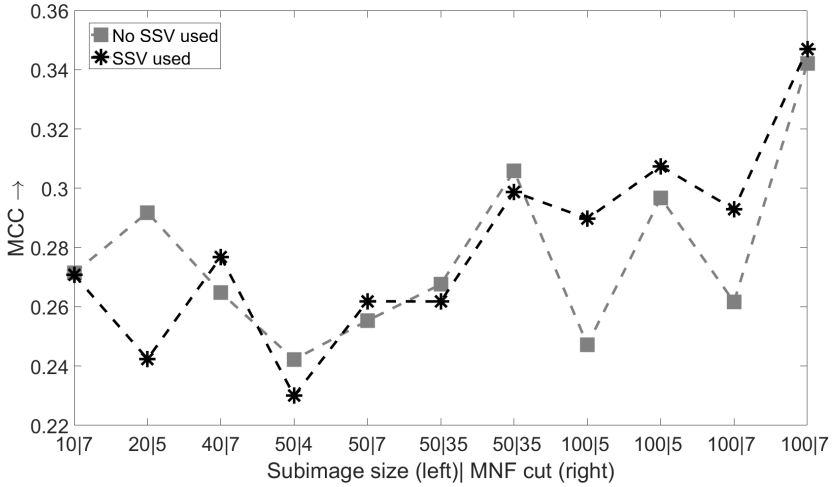

Figure 44: MCC as a function of the tested parameters: sub-image size, MNF cut, spatial features and the usage of the SSV.

Figure 43 shows the mean result of the best classifier for comparison of the MCC of the parameter study for all parameters. The strong interaction already shows that an ANOVA cannot be used. Thus, no detailed analysis is shown.

In summary the usage of the SSV, as a new feature seems to be a proper way for classification of carcinomas. The method seems to work despite the quite high noise generated by the endoscope used in this study. Moreover, the information provided by the SSV uses the strong variance of the carcinomas for detecting them, making an advantage out of an apparent hindrance. Even if it is possible to create a computer-aided method to identify images in the upper GI containing lesions with an accuracy of around 90 % for early carcinomas in the upper GI [101], Liu et al. [101] can only identify that there is a lesion in an image but they cannot localize it. Additionally, the required amount of features is 1500 to 10000 per image. Doing a similar analysis with a pixel by pixel analysis as done in this study is nearly impossible as the required memory of the computer would be far to high. Thus, strong features are needed which provide a lot of information. As it seems, the SSV is this kind of feature.

5.3 Monte-Carlo study of the effect of mislabelled carcinomas

Figure 45 shows the overview of the Monte-Carlo study. It is grouped into three sections. First, the validation of the MCS is shown. Afterwards, the some example images from patients and the average reflection are shown. As last part, the effects from mislabelling are studied.

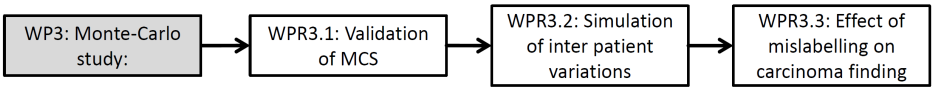

Figure 45: Overview of the first working package for the result section. Each box symbolized one sub chapter and corresponds to the headlines. The grey box symbolizes the generic topic/research question and italic font symbolizes that this part of the flow chart will be shown as generic topic later.

5.3.1 Validation of MCS

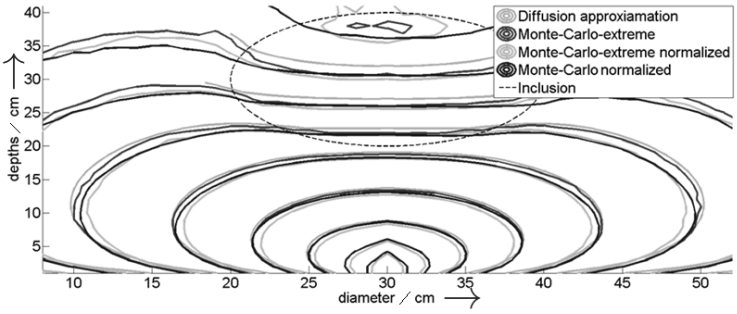

Figure 46: Cut through simulation volume: The light comes from the bottom. The lines are equipotential lines of the logarithmic intensity for the diffusion approximation, MCX, a normalized data set of MCX and a data set from the simulation software in this study.

First, the validation of the MCS is shown in figure 46. It can be seen that the normalized MCX and this simulation show similar results. However, there is a discrepancy close to the source to the diffusion approximation. This difference is, however, negligible due to the fact that the diffusion approximation is not valid close to the source. Moreover, it should be considered that the diffusion approximation is normalized to a different intensity. A second discrepancy is found deep inside the tissue directly on top of the source. The discrepancy is most likely caused by the low amount of photons in this depth from both MCSs, the one in this study and MCX. The effect due to the lack of photons can be seen by the non-smooth shape of the equipotential intensity lines of

both MCSs. However despite these two discrepancies, the rest of the image matches to a high degree. Thus, the used MCS can be regarded as validated and, therefore, it can be used for further calculations.

5.3.2 Simulation of inter patient variations

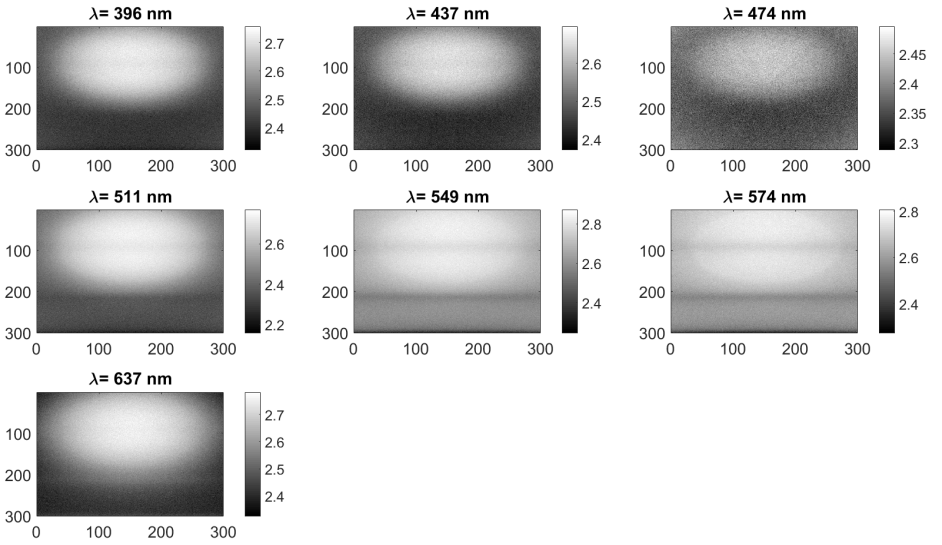

Figure 47: simulated multi spectral images for all wavelengths with logarithmic scale. On the top, the carcinoma is seen. For higher wavelengths the vessel below can also be seen. The scale represents the exponent a of the intensity (10^a). This scale is chosen as the human eye is a logarithmic detector as well.

From the validated MCS, the multi spectral images are calculated. Figure 47 shows an example for all seven wavelengths. The top brighter area shows the carcinoma. It can be seen that for longer wavelengths, the blood vessel below the carcinoma can be seen as darker lines. In the lower part, the second blood vessel can be seen. It should be noted that for red light the reflection of the blood vessel is higher than for the surrounding tissue. This is caused by the lower absorption of blood at this wavelength compared to the surrounding tissue. For 474 nm the image is the most noisy. This is caused by the high absorption at this spectral range shown in figure 48.

Figure 48 shows the optical properties used for the previous example calculation. It can be seen that the absorption of the healthy oesophagus is much higher than for the cancerous one. Due to this, the carcinoma appears brighter in the simulation compared to the healthy tissue. Additionally, the scattering coefficient is very similar for healthy and cancerous tissue. However,

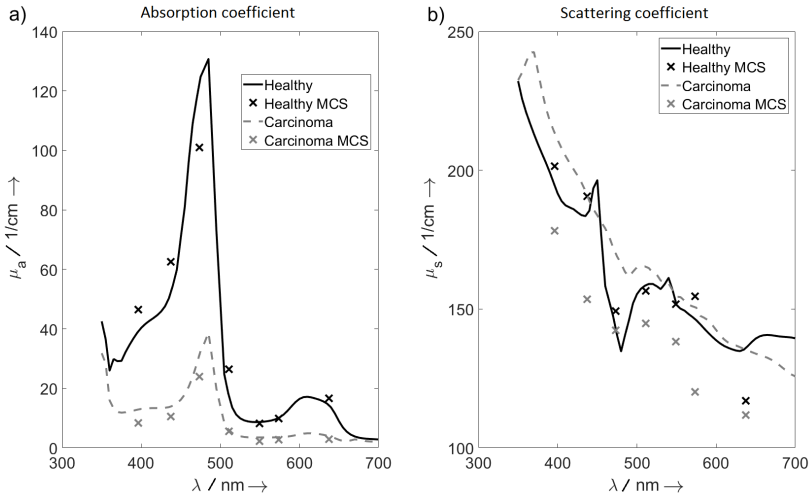

Figure 48: Absorption coefficient (a) and scattering coefficient (b) from Holmer et al. [130] (lines) and the absorption coefficient and scattering coefficient used for this simulation (x).

the parameters used for this example simulation vary from the ones from Holmer et al. [130] due to the variance which is introduced to simulate the inter patient variations.

The combination of inter patient variations for many patients leads to an averaged reflection of the carcinoma compared to the healthy tissue as shown in figure 49. The error bars show the standard deviation over all patients. It can be seen that the reflectance shows a high difference for 511 *nm*, 574 *nm* and 637 *nm*. Therefore, these wavelengths should allow the best classification. This result can be seen as hint that the idea and the way of simulating inter patient variations is promising as Kiyotoki et al. [14] could show that longer wavelength are better for classifications than the shorter wavelengths. In their study, the results improves with 570 *nm* and more while in this study the effect occurs already at 511 *nm*. However, this can be caused by the used optical properties from Holmer et al. [130] as they have some systematic errors.

However, the noise and the signal strength should be considered. The results for 474 *nm* show high noise as seen in figure 47. Moreover, the reflection has a high standard deviation due to the fact that small changes of the optical properties occur. Especially, fluctuations of the absorption might lead to big changes of the reflectance. Compared to figure 42, it can be seen that for the first three principal components, the weight of the intensity of 477 *nm* is low while there is at least an impact from the other colour channels. Therefore, the simulation is in agreement with the measured results.

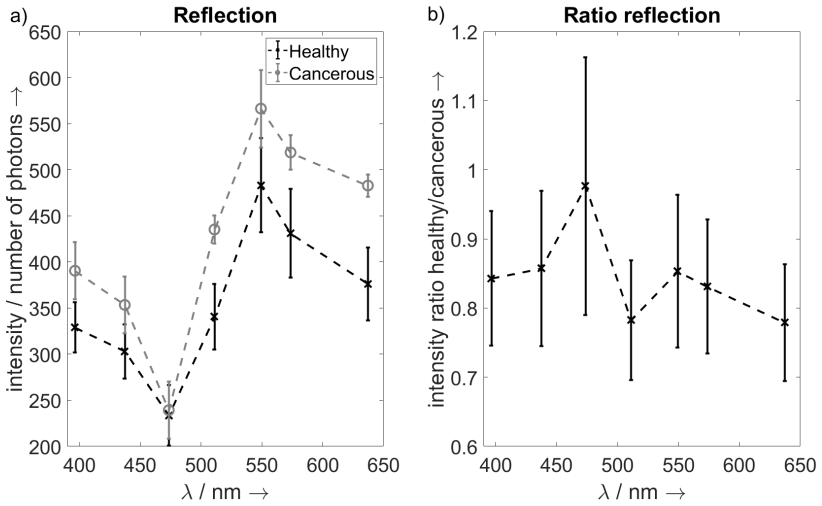

Figure 49: (a) Reflection spectrum for healthy and cancerous tissue. (b) ratio of healthy divided by cancerous tissue. The error bars represent the standard deviation.

5.3.3 Effect of mislabelling on carcinoma finding

First, the effect of 100 % to 50 % overlap of carcinoma is tested. Figure 50 shows the effect of the shift of the carcinoma used for training in comparison to the real one if the PCA is used for feature selection.

The results for zero shift are similar to the one with a low shift. For all cases, the ACC2 as well as the MCC drop for higher shifts. The ACC2 drops from around 85 % to 60-70 %, depending on the classifier. The MCC drops from 0.7 to 0.2-0.5 depending on the classifier. For both measures, the real carcinomas are detected worse than the ones used for training. Thus, it might happen in real scenarios that the classifier might be trained on the wrong data set. However, this effect is especially strong in this study due to the usage of small carcinomas for the simulation. For bigger carcinomas, the intermediate area between cancerous and healthy tissue in which the image is effected by both tissue types is relatively smaller. However for early stage carcinomas, it might still play a significant role.

Moreover, on RFW and SVM with a Gaussian kernel there is the lowest effect due to the mislabelling. However in the *in-vivo* study from Hohmann et al. [117], SVM with linear kernel and RB showed the best results. These results here only describe a constant shift which is not realistic. Despite this, RB seems to consistently find the real carcinoma better than the one used for training for high shifts. Thus, RB should definitely be considered further. Similar results

were shown in the study from Hohmann et al. [117] for carcinomas in the stomach.

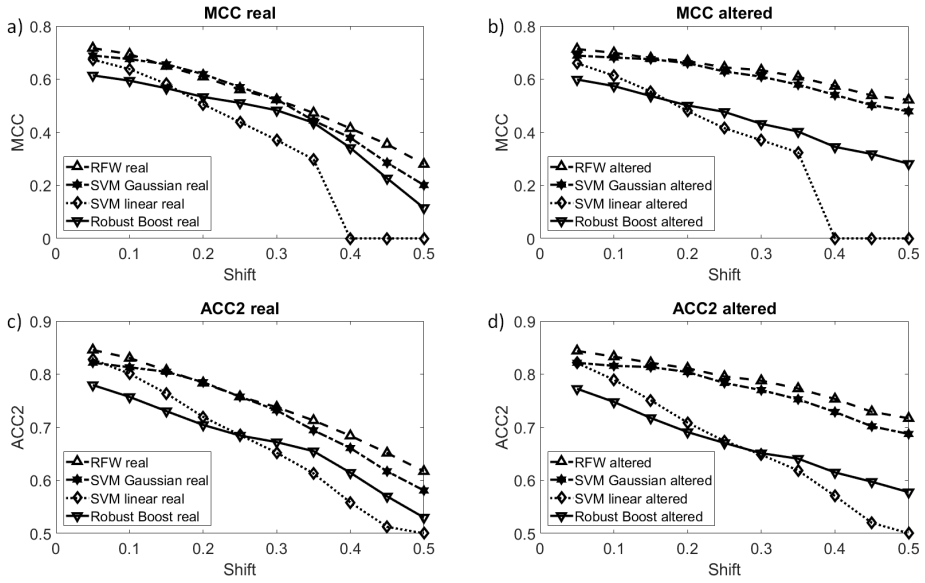

Figure 50: ACC2 (c,d) and MCC (a,b) as function of the shift between the real carcinoma (a,c) and the one used for training (b,d). PCA is used for feature selection.

Figure 51 shows the result for the case RFW is used for feature selection. The results for usage of RFW as feature selection tool are consistently lower as for the case when PCA is used for feature selection. However, RB is relatively slightly better. From both datasets, it can be concluded that the classifiers might train consistently for the altered carcinomas. This indicates that the measured ACC2 and MCC might show not correct results and the metric for evaluating the classifiers might adept to the wrong ground truth and, therefore, the results might be far off the actual ground truth. If the margin of the carcinoma is not known, it might lead to the effect that the measure for accuracy show quite good results even if the carcinomas are not found. However for RB, the real carcinoma is found as good as the shifted one. Up to now, only the shift of the carcinoma is varied and, therefore, the results might not be generalizable.

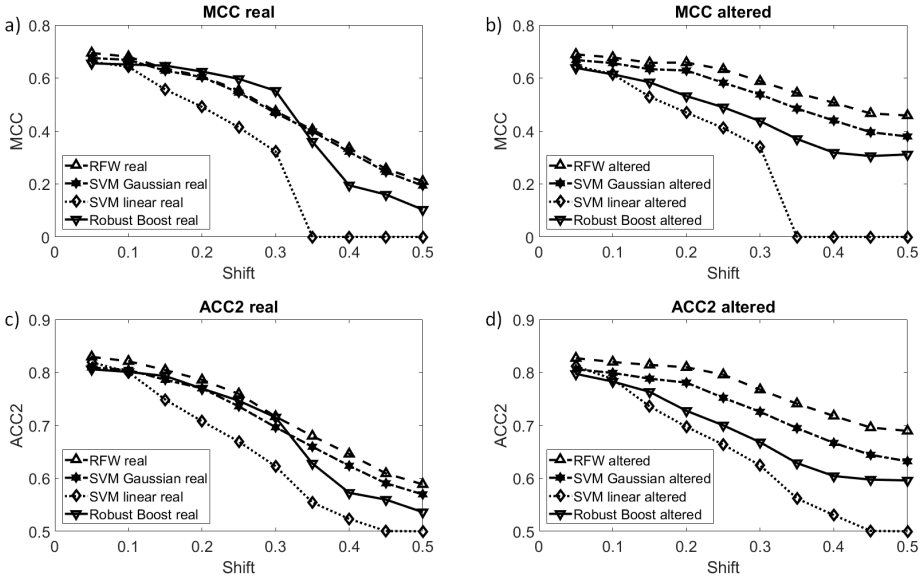

Figure 51: ACC2 (c,d) and MCC (a,b) as function of the shift between the real carcinoma (a,c) and the one used for training (b,d). RFW is used for feature selection.

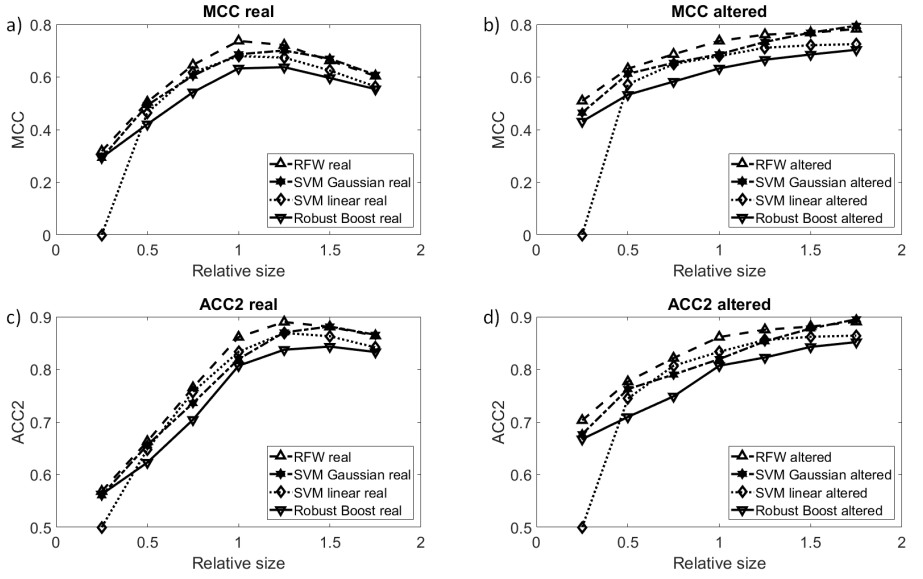

Figure 52: ACC2 (c,d) and MCC (a,b) as function of the relative size between the real carcinoma (a,c) and the one used for training (b,d). PCA is used for feature selection.

As next point, Figure 52 shows the effect of choosing a different size of the carcinoma used for training in comparison to the real one. The results are

shown in figure 52 and figure 53. Figure 52 shows the results for the case that the PCA is used for feature selection and figure 53 if RFW is used for feature selection. The ACC2 varies from around 0.57 to nearly 0.9 for the real carcinomas and varies from 0.65-0.7 to 0.9 for the altered carcinoma site. The MCC behaves similar. As for the results for the shift, the modified carcinomas are found better than the real ones. The more the size of the carcinoma used for training is different from the real one, the stronger this effect is.

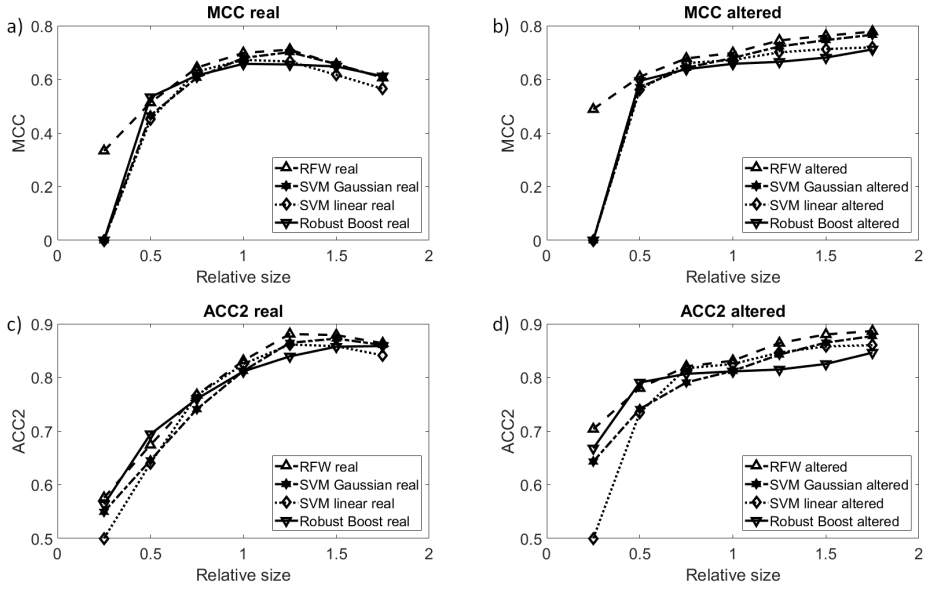

Figure 53: ACC2 (c,d) and MCC (a,b) as function of the relative size between the real carcinoma (a,c) and the one used for training (b,d). RFW is used for feature selection.

Independent of the usage of the PCA or RFW for feature selection, the real carcinoma is found best if the size used for training is chosen correctly or a little bit bigger. This effect happens because the back reflectance outside the carcinoma is still partly effected by the carcinoma due to the scattering of the tissue by the overlap area. As a conclusion for realistic scenarios, it seems to be beneficial to select a little bit larger margin of the carcinoma. Despite the fact that a too big margin might further improve the results of the ACC2 and MCC for the carcinoma used for training, the real carcinoma is found worse. Thus, the carcinoma margin should not be selected too big despite the improvement of the accuracy. For this case, all classifiers show a similar behaviour. RFW again shows the best results.

For too small carcinomas used for training, the accuracy decreases significantly. One reason is that there is to less data available for the carcinoma.

Moreover, only the data in the centre with the strongest effect is seen as carcinoma. Therefore, the accuracy has to decrease as this is less data for the carcinoma is available. Hence, there is less variability in the data which makes the classification more difficult.

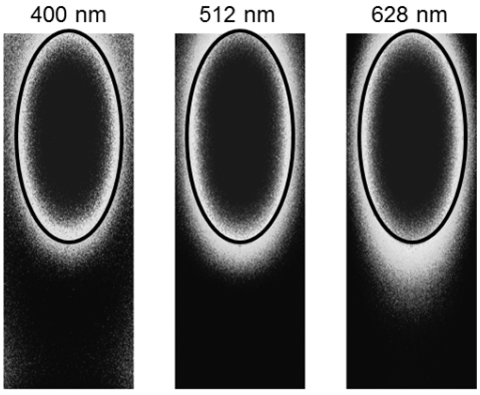

Figure 54: Simulative example of the reflection of a carcinoma for three wavelengths. Additionally, the carcinoma is labelled. The black circle shows the real carcinoma and the bright area the intermediate zone where the carcinoma and the healthy tissue both have a strong effect on the reflectance.

Furthermore, many of the effects can be accounted for by the intermediate zone between carcinoma and healthy tissue. In this zone the carcinoma as well as the healthy tissue effects the back reflectance. This can be seen in figure 54. Especially, for longer wavelengths this effect occurs. It can be seen that the carcinoma effects a wide surrounding around it. The longer wavelengths show a larger effect due to higher penetration depths of the light. Additionally, inside the carcinoma their is an intermediate zone. This effect might explain also why longer wavelength are in general better for finding carcinomas in the upper GI with hyper spectral imaging [14]. Due to the intermediate zone the results smear out and therefore act as a natural noise filter such as a Gaussian filter and irregularities of the tissue might be averaged out. In combination with the facts that blue light has a low penetration depths and tissue is no Lambertian reflector for blue light [142], the general low accuracy in this spectral region can be explained. This might pinpoint why NBI could not be successfully used. However for the case of altering the size of the carcinoma, RB cannot compensate the mislabelling.

The results for a randomly chosen overlap and shift are shown in figure 55 and figure 56. Both measures show a decrease of accuracy for stronger mislabelling. The ACC2 drops from 80-85 % to 65-70 % and the MCC drops from 0.6-0.7 to 0.3-0.4. The reason that in this case the real carcinomas are found better

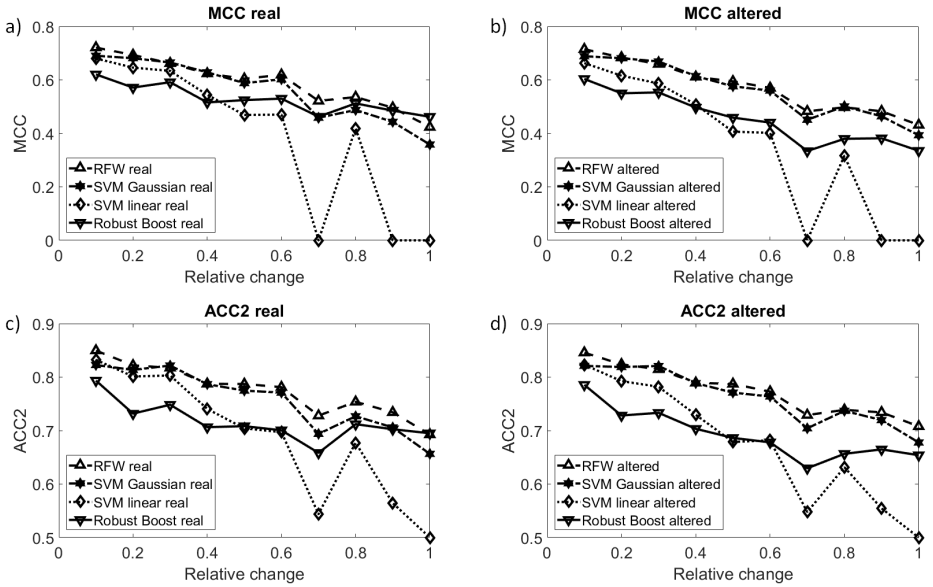

Figure 55: ACC2 (c,d) and MCC (a,b) as function of the relative size and shift change between the real carcinoma (a,c) and the one used for training (b,d). PCA is used for feature selection.

than the ones for training is most likely caused by the fact that the carcinomas for training are from all parts of the sample including the intermediate zone. Therefore, the training data gets more reliable. Furthermore, it can be concluded that for experimental multi spectral images, the real carcinoma is found better than the wrong one used for training. Thus, the effective ACC2 and MCC are most likely higher than the ones measured if carcinoma are only shifted.

For all three experiments, RFW seems to be the classifier which provides the best results. Thus, it seems to partly compensate for the mislabelling as RFW is not very dependent on noisy data and labelling noise [86]. The effect that SVM with linear kernel sometimes has an ACC2 of 0.5 and/or an MCC of zero is caused by the fact that all data is classified as one single class, resulting in these values.

For the highest potential mismatch between real carcinoma and the carcinoma used for training, the ACC2 and MCC are only a little bit better than for the clinical study. Without taking mucus or inflammation into account it is possible that the maximal accuracy which can be reached currently is around 70 %. Thus for further endoscopic *in-vivo* imaging, the margin has to be found more precise to allow better results. Up to now, there are two solutions: First, Goto et al. [15] used *ex-vivo* oesophagus and did regular biopsies across the

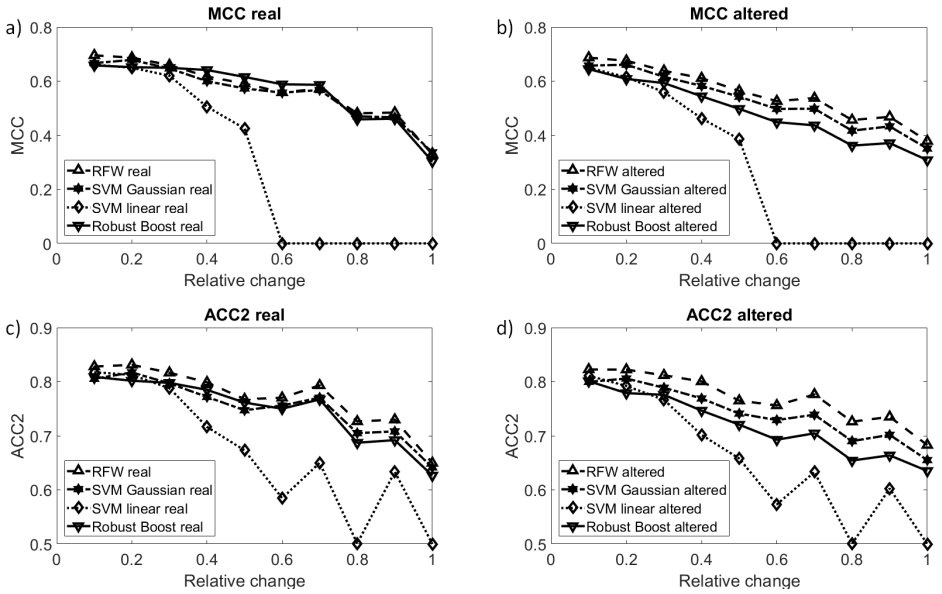

Figure 56: ACC2 (c,d) and MCC (a,b) as function of the relative size and shift change between the real carcinoma (a,c) and the one used for training (b,d). RFW is used for feature selection.

whole oesophagus. With this good classification results could be reached. Second, Liu et al. [101] used the complete endoscopic image and the classifier just decided if there is a carcinoma somewhere present in the image. However, they could not show where it is. Again RFW and SVM with Gaussian kernel show the best results. As for the examples before, RB shows better results for the real carcinoma than for the one used for training for the cases of high mismatch.

5.4 Murine multi/hyper spectral study

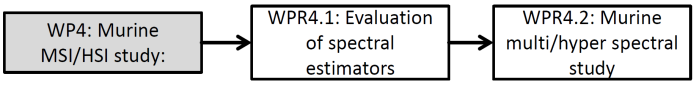

Figure 57: Overview of the first working package for the result section. Each box symbolized one sub chapter and corresponds to the headlines. The grey box symbolizes the generic topic/research question and italic font symbolizes that this part of the flow chart will be shown as generic topic later.

Figure 57 shows the overview of the murine multi/hyper spectral study. It consists out of two sections. First, the spectral estimation is evaluated and

in the second part, it is evaluated if spectral estimation is an alternative for direct hyper spectral imaging.

5.4.1 Evaluation of spectral estimators

To demonstrate the capability of the reconstruction of the spectral information from different tissue, an exemplary reconstructed spectra of human skin is shown in figure 58. For this example, the PI as well as the wPI method provide a good estimation. However, the wPI method provides the better estimation of the spectra and is much closer to the real spectrum. The most discrepancy can be found in the red and UV part of the spectrum. This is a typical behaviour for most reconstructed spectra and it is caused due to the lower amount of sample points in these two areas. The RMSE of the presented examples are 0.012 and 0.023 for the wPI method and the PI method, respectively.

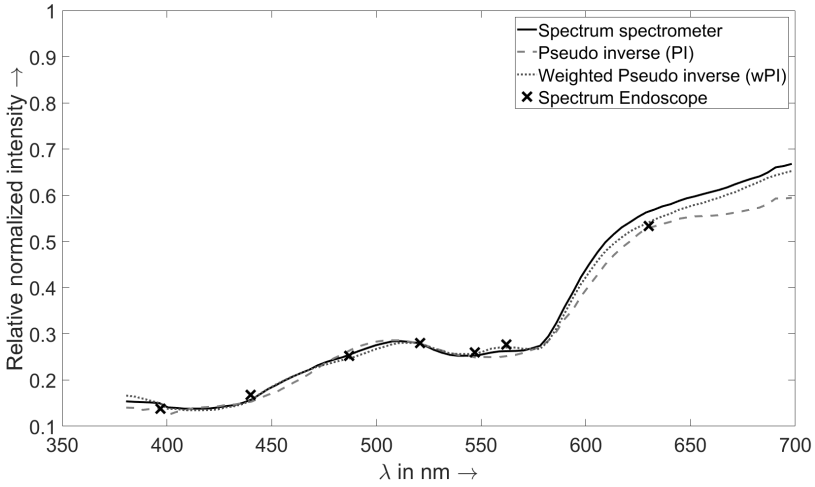

Figure 58: Measured and estimated of spectrum for a skin sample with the PI method and the wPI method. The black "x" and the solid black line represent the measured spectra from the endoscope and the spectrometer, respectively.

The mean of the RMSE for a leave-one-out method is shown in figure 59 as a function of the wavelength. As seen in the example in figure 58, the highest error can be found below 420 *nm*, from 580-620 *nm* and above 640 *nm*. While the behaviour below 420 *nm* and above 640 *nm* is expected by the low spectral resolution from the endoscope, the peak of uncertainty from 580-620 *nm* has to have a different reason. In this range, most of the reddish samples show a strong increase reflectivity towards longer wavelengths. The rising edge of the

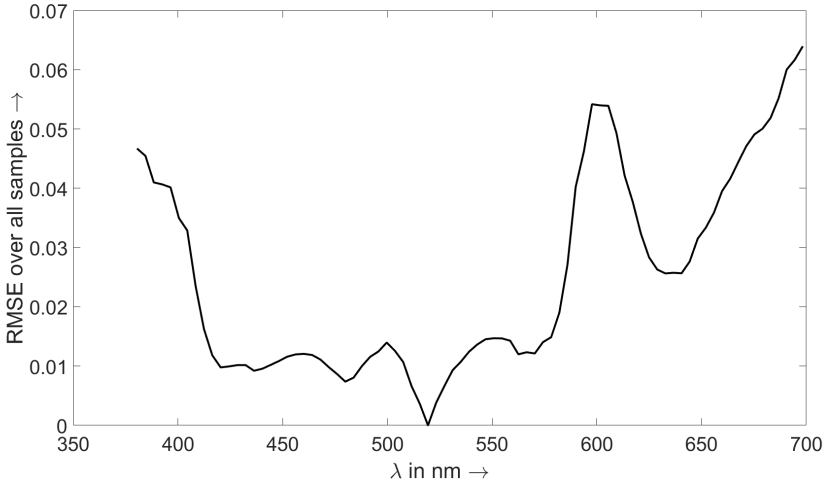

Figure 59: Mean RMSE as a function of the wavelength for all spectra used for estimation.

reflectivity is not and cannot perfectly be detected. Therefore, this fast rising edge leads to a strong increase of the local RMSE, despite the low difference seen by visual inspection in this spectral region. At the same time for this wavelength range, there is no narrow band available which can resolve this. This can also be seen in figure 58.

Figure 60 shows the effect, caused by the low spectral resolution around 600 *nm*, for two of the samples. On the left side, the spectra and its estimations are shown and on the right side the resulting error. It can be seen that both samples show a very large difference in the range of 585-630 *nm*. Due to the lack at similar spectra in the calibration charts, both spectra have a huge error as not enough calibration data is available. This leads to the peak of the error in the spectral region from 580-620 *nm*. However, it should be noted that the tissue samples do not show this increase of the RMSE in the region from 580-620 *nm*. The high RMSE starts from 630 *nm*. Thus, the RMSE is expected to be low for the mouse samples and the spectral region from 420 *nm* to 630 *nm*. Hence, the spectral estimation should be usable for the further analysis.

The total mean RMSE is shown in table 26 for all samples for the spectral estimation. In 21 out of 31 samples the wPI method shows better results than the PI method and on average the RMSE of the wPI method is smaller. Hence, the wPI method is preferable. Moreover, all the four tissue samples show a better estimation with the wPI method in comparison to the PI method. Therefore, it is expected that the estimation of the spectra of the mouse tissue

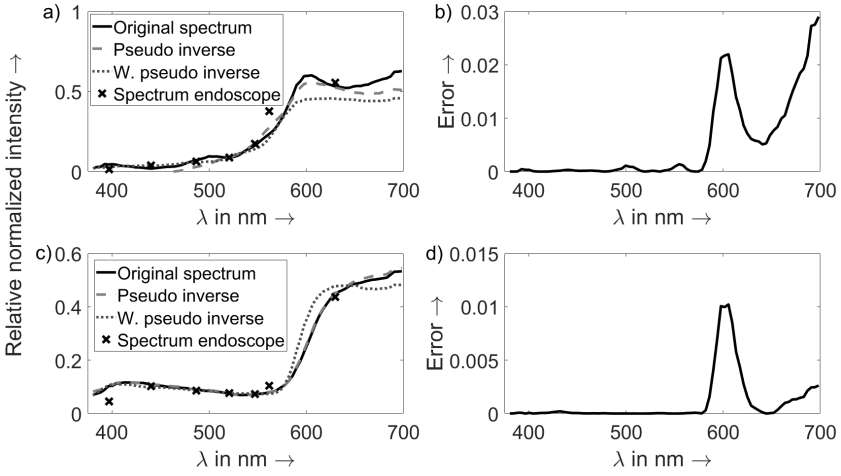

Figure 60: Spectral estimations (a,c) and the error (RMSE) for the weighted pseudo inverse (b,d) for two example spectra.

will also have better results with the wPI method. Therefore, only the wPI method will be used for the further analysis.

Table 26: The averaged root mean squared error of the test samples reconstructed with the PI method or the wPI method. Also the amount of spectra are shown in which one of the estimations provides better results.

Method	Average RMSE	Number of better estimations
Pseudo inverse	0.0275	10
Weighted pseudo inverse	0.0243	21

5.4.2 Murine multi/hyper spectral study

First, the averaged spectra reconstructed by the wPI method are shown in figure 61. On the left side, the spectra of the spontaneously developed neoplastic lesions and on the right side the spectra of the inflammation-driven carcinogenesis model are shown. For each mouse model, the left side shows the unnormalized spectra and the right side shows the normalized spectra. In general, the intensity of the carcinoma is higher because the whole imaging is focussed onto to cancerous area and, therefore, it is in the centre and the best illuminated part of the image. Moreover, larger tumours have partially grown into the lumen and, thus, they are placed more perpendicular

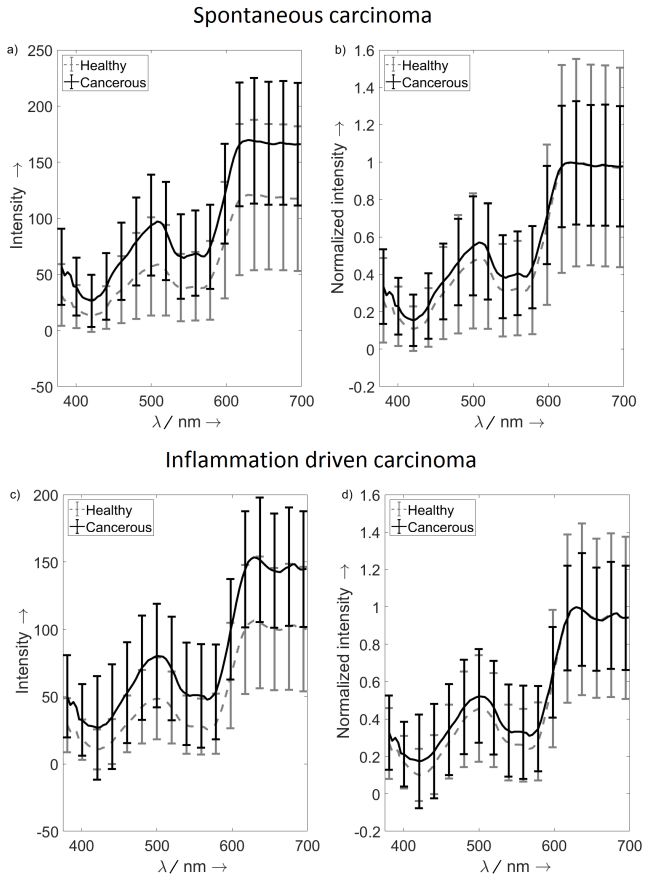

Figure 61: Average spectrum and its standard derivation for the unmodified (a,c) and normalized (b,d) spectra for the spontaneously developed neoplasms (a,b) and for the inflammation driven carcinogenesis (c,d).

to the endoscope. Thus, this effect might also be a reason for the higher back scattered intensity.

The normalized spectra show only a stronger variation of the haemoglobin peaks between 500 and 600 *nm*. Hence, there might either be higher scattering, a lower amount of haemoglobin present, a deep placement of the haemoglobin or a thin white scattering layer on the carcinoma. Due to the fact that haemoglobin is the dominant absorber in this spectral range, it can be assumed that the spectra should be more similar around 600 *nm* and, thus, the white mucus layer as reason for this behaviour is unlikely. However, whether the scattering is higher in the carcinoma, or whether the haemoglobin is in more shallow areas in healthy tissue or whether the haemoglobin

is decreased in the cancerous tissue cannot be concluded from the spectra alone. Due to the fact that neoplastic lesions are normally less homogeneous on the micro scale, it is likely that tumours have a higher scattering than the healthy tissue. Furthermore, neoplastic lesions have a higher overall reflectance which could also partly be explained by the higher scattering.

The findings regarding the optical properties from Holmer et al. [130] might provide a hint for the solution despite the fact that they are derived for oesophagus instead of colon. First, it is shown that healthy and cancerous tissue have a similar scattering coefficients. However, Holmer et al. [130] find less haemoglobin in the cancerous tissue. Therefore from the possible explanations, the reduced amount or density of haemoglobin in the neoplastic lesions is the most likely explanation.

From the average estimated spectra, it can be concluded that there is a difference of the spectrum which might lead to successful classification. The spectra show no significant difference for a single measurement. However, the standard error of the mean of the spectra is much lower and, thus, the difference of the mean spectra is significant. Furthermore, the unavoidable recording bias should be considered too, as the clinicians record the images focusing on the visible tumour, therefore putting the neoplastic lesion in the centre of the image. Thus, it might be that at least the overall intensity difference between the spectra might be caused by unconscious behaviour of the clinical expert recording the data. This point has to be investigated in the future for larger carcinomas as potential Clever-Hans-effect [141] for the classification process. Nevertheless, this effect should be reduced in very small tumours as the images are still focussed on the centre of the lesion, the surface to endoscope tilt is very similar for healthy and cancerous tissue in this case. Moreover, a pixel per pixel analysis is done and, in this case, the position of the carcinoma in the image is lost. For future experiments, tumour images should also be taken at the side of the image for compensation.

Furthermore, both subgroups of carcinogenesis (spontaneous versus inflammation-driven) from the multi spectral data set with spatial features are shown in table 27. It can be seen, that the classification of the spontaneous driven carcinomas (MCC=0.48) is similar as the inflammation tumour (MCC=0.46).

Figure 62 shows the comparison of the multi- and hyper spectral data set for the classifiers. It can be seen that the HSI data set equalizes the results for all classifiers. Especially, the results for the SVM with the linear kernel improve. In general, the classification between healthy and cancerous tissue in mice provides better results than the clinical study on humans.

Table 27: Classification results of the tested classifiers for the spontaneous cancer model (left) for 14 mice and the inflammation driven cancer model (right) for 11 mice.

Method	ACC	ACC2	AUC	MCC	ACC	ACC2	AUC	MCC
Cancer type	Spontaneous (n=14)				Inflammation driven (n=11)			
RFW	0.73	0.74	0.77	0.48	0.71	0.71	0.74	0.43
RB	0.72	0.74	0.77	0.48	0.72	0.72	0.76	0.45
SVM (lin)	0.65	0.64	0.65	0.30	0.68	0.66	0.68	0.32
SVM (Gauss)	0.62	0.63	0.66	0.27	0.64	0.67	0.70	0.36
AB	0.73	0.74	0.77	0.48	0.72	0.73	0.75	0.46

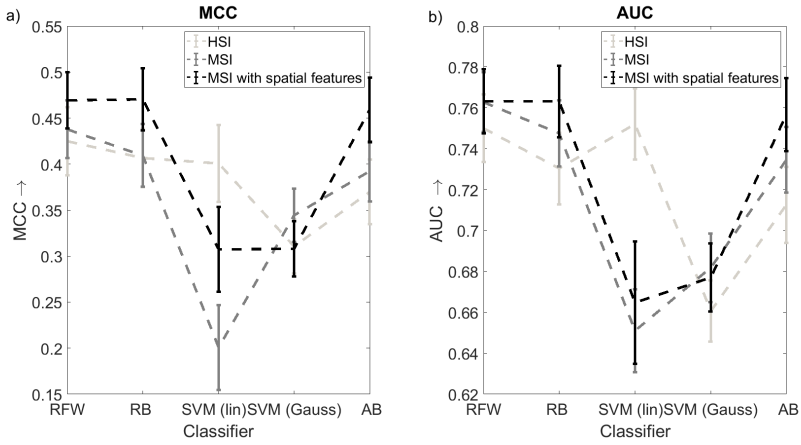

Figure 62: Comparison of the hyper and multi spectral data set for the different classifiers. The error bars show the uncertainty of the mean value.

Table 28 shows the results. In total, an MCC of 0.44 can be reached for the multi spectral data set without spatial features and an MCC of 0.43 can be reached for the hyper spectral data set. An ANOVA shows no significant difference between both data sets ($p > 0.3$) but a significant interaction between the classifier and the usage of the multi spectral or hyper spectral data set ($p < 0.01$). This is caused by the effect that the hyper spectral data set equalizes the results for all classifiers. In general, the results of the classification are better for all metrics in comparison to the human study. The best classifier is RB for all measures. Thus, it is likely that the training data has misclassified data. Therefore, some of the margin of the carcinoma was not correctly identified by the medical expert.

Table 28: Classification results of the tested classifiers for 25 mice with leave one out strategy for the multi spectral data set (left side) and hyper spectral data set (right side). The PCA is done and 99 % of the variance.

Method	ACC	ACC2	AUC	MCC	ACC	ACC2	AUC	MCC
Data set	Hyper spectral (HSI)				Multi spectral (MSI)			
RFW	0.67	0.69	0.71	0.37	0.67	0.64	0.73	0.39
RB	0.69	0.71	0.75	0.42	0.70	0.72	0.76	0.44
SVM (lin)	0.67	0.70	0.75	0.40	0.60	0.60	0.65	0.20
SVM (Gauss)	0.60	0.65	0.66	0.31	0.62	0.67	0.68	0.34
AB	0.68	0.70	0.73	0.41	0.68	0.70	0.75	0.41

Table 29 shows the results of the classification for the multi spectral data set with spatial features. The results are improved in comparison to the case without spatial features, shown in table 28. An ANOVA shows no significant improvement for the AUC ($p>0.4$) and for the MCC the ANOVA is significant ($p<0.05$).

However, it can be assumed that the results improve overall for two reasons: First, the parameters of the spatial features are not optimized for the mouse study. The same parameters as in the human study are used. Second at least for the MCC, the results are statistically significant. Hence, it is likely that the spatial features show an improvement. Moreover, an ANOVA shows no difference between the multi spectral data set with features and the hyper spectral data set ($p>0.3$). Hence, hyper spectral imaging by spectral estimation does not improve the results more than multi spectral imaging with the usage of spatial features.

Table 29: Classification results of the tested classifiers for 25 mice with leave one out strategy for the multi spectral data set with spatial features.

Method	ACC	ACC2	AUC	MCC
RFW	0.72	0.73	0.76	0.46
RB	0.72	0.73	0.76	0.47
SVM (lin)	0.66	0.65	0.66	0.31
SVM (Gauss)	0.63	0.65	0.68	0.31
AB	0.73	0.73	0.76	0.47

Moreover, an ANOVA shows no difference between the multi spectral data set with features and the hyper spectral data set ($p>0.3$). Hence, hyper spectral imaging by spectral estimation does not improve the results more than multi spectral imaging with the usage of spatial features. Thus for the future, the results from multi spectral imaging have to be transferred to real hyper spectral imaging.

Despite the expected advantage of real HSI (no spectral estimation) over MSI, HSI has two drawbacks. The first drawback is the curse of dimensionality. When the dimensionality increases, the volume of the space increases so fast that the available data become sparse, making classification problems much harder to solve. Second, the high correlation between continuous spectral bands [115] should be considered. This leads to the problem that in combination with the sparsity of the data, it is difficult to find the correlations between spectral bands. This might also be a reason that HSI does not improve the results as the amount of data is too less in this study. If this would be true, HSI will be very difficult to set up in future. A further issue is that for *in-vivo* endoscopy the margin of the carcinoma is not known [82].

The issue that not all spectral bands are required, is well known in remote sensing. Some spectral bands include already all significant information [143, 144]. This leads to two conclusions: First, huge amount of data sets is required for HSI. Second, it might make sense to switch back to MSI after the optimal spectral bands have been found by HSI as MSI set-ups are easier to build. Moreover, the results generated in this *in-vivo* study reach a similar ACC, AUC and MCC as the *ex-vivo* study from Baltusen et al. [145] in the visible range.

6 Summary and conclusion

As summary, automated finding of carcinomas *in-vivo* is possible. All results pinpoint that multi- and/or hyper spectral imaging might be used as a red flag technology in future.

WP1: Multi spectral *in-vivo* endoscopy allows the discrimination of healthy and cancerous tissue for a pixel by pixel analysis with an MCC of 0.89 (ACC2 0.96) for intra patient variations. For inter patient variations, the results drop to an MCC of 0.32 (ACC2 0.68). In comparison to the results from Hohmann et al. [117], this is a significant improvement (p=0.0034). This improvement can be realized by using Laguerre-Gaussian functions as spatial features and advanced noise removal techniques. However, two limitations remain. First, mislabelling of the training data set is a major issue. Second, the inter patient variations cannot be compensated well yet. It might even be that both effects have a synergistic reduction on the classification results.

WP2: To further improve the classification results the SSV is introduced as a new feature which significantly improves the AUC for all parameter sets (p=0.014). For the other measures such as ACC2 or MCC, a comparison is not feasible due to the intersection of the mean values for different parameter sets. The SSV cannot replace spatial features. Nevertheless, it is a significant support.

WP3: As mislabelled data is an issue, the MCS can be used to simulate inter patient variations. The effect of mislabelling significantly decreases the accuracy of the classification. For a realistic mislabelling of around 20 %, the ACC2 drops already to approximately 0.7-0.8 and the MCC drops from 0.8 to 0.5-0.65. Thus currently, there is a limit of the accuracy of around 70-80 % which has to be overcome by developing methods for correct data labelling. The upper limit of the MCC of the simulation corresponds to the result from the human *in-vivo* study. Therefore, MCS can explain the reason of the low MCC. In summary, the accuracy measures which are reached in this study might be already close to the maximum especially as in the human study the labelling of the carcinomas is very difficult. Thus for developing a red flag technique, a point technique will be required to pre label the data correctly.

WP4: In comparison to the human study, the results from the murine model show better classification results for two reasons: First, the carcinomas are better visible and, therefore, the labelling has less errors. This is especially caused by the lower intra mouse variations in comparison to the intra patients variations in the human study. Second, the imaging system is improved and, therefore, the noise is significantly less. Both factors allow a final ACC2 of

0.73, an AUC of 0.76 and a MCC of 0.47. Furthermore, multi spectral imaging with support of spatial features allows a better classification of neoplastic lesions in the colon than hyper spectral images derived by spectral estimation techniques. Therefore, assisted by the current findings, this thesis can support the statement from Swager et al. [7] that real hyper spectral imaging should be investigated instead of spectral estimation. The short cut to reach hyper spectral imaging by means of spectral estimation of multi spectral imaging is not expedient with automated classification. Despite this, the results of this MSI *in-vivo* study with spatial features are similar to HSI *ex-vivo* studies from Baltusen et al. [145].

MSI/HSI might work as red flag technique in future. However for overcoming the limitations, it is likely that a point spectroscopy technique is required to allow correct labelling of the data due to the fact that the insufficient labelling reduces the classification accuracy significantly. Moreover, it is expected that for HSI a huge amount of data is required for a successful classification due to the curse of dimensionality as the data becomes sparse with increasing dimensionality. Therefore, MSI will be part of future investigations.

7 Zusammenfassung und Schlussfolgerung

Zusammenfassend lässt sich sagen, dass ein automatisiertes Auffinden von Karzinomen*in-vivo* möglich ist. Alle Ergebnisse deuten darauf hin, dass die multi- und/oder hyper-spektrale Bildgebung in Zukunft als Red-Flag-Technologie eingesetzt werden könnte.

WP1: Multispektrale *in-vivo* Endoskopie ermöglicht die Unterscheidung von gesundem und karzinomatösem Gewebe für eine pixelweise Analyse mit einem MCC von 0,89 (ACC2 0,96) für Intra-Patientenvariationen. Bei Inter-Patientenvariationen sinken die Ergebnisse auf einen MCC von 0,32 (ACC2 0,68). Im Vergleich zu den Ergebnissen von Hohmann et al. [117] ist dies eine signifikante Verbesserung (p=0,0034). Diese Verbesserung kann durch die Verwendung von Laguerre-Gauß-Funktionen als räumliche Features und fortschrittliche Rauschunterdrückungstechniken erreicht werden. Es bleiben jedoch zwei Beschränkungen bestehen. Erstens ist die falsche Beschriftung des Trainingsdatensatzes ein großes Problem. Zweitens können die Variationen zwischen den einzelnen Patienten noch nicht gut kompensiert werden. Es könnte sogar sein, dass beide Effekte eine synergistische Reduktion auf die Klassifikationsergebnisse haben.

WP2: Um die Klassifikationsergebnisse weiter zu verbessern, wird die SSV als neues Merkmal eingeführt, das den AUC für alle Parametersätze signifikant verbessert (p=0,014). Für die anderen Maße wie ACC2 oder MCC ist ein Vergleich aufgrund der Überschneidung der Mittelwerte für verschiedene Parametersätze nicht möglich. Die SSV kann räumliche Merkmale nicht ersetzen. Dennoch ist sie eine deutliche Unterstützung.

WP3: Da falsch beschriftete Daten ein Problem darstellen, kann die MCS verwendet werden, um Inter-Patientenvariationen zu simulieren. Der Effekt von Falschlabelungen vermindert die Genauigkeit der Klassifikation erheblich. Für ein realistisches Mislabelling von etwa 20 % sinkt der ACC2 bereits auf etwa 0,7-0,8 und der MCC fällt von 0,8 auf 0,5-0,65. Somit gibt es derzeit eine Grenze der Genauigkeit von etwa 70-80 %, die durch die Entwicklung von Methoden zur korrekten Datenbeschriftung überwunden werden muss. Die obere Grenze der MCC der Simulation entspricht dem Ergebnis der menschlichen *in-vivo*-Studie. Daher können MCS den Grund für den niedrigen MCC erklären. Zusammenfassend lässt sich sagen, dass die in dieser Studie erreichten Genauigkeitsmaße bereits nahe am Maximum liegen könnten, zumal in der Humanstudie die Kennzeichnung der Karzinome sehr schwierig ist. Für die Entwicklung einer Red-Flag-Technik wird daher eine Punkttechnik zur korrekten Vorbeschriftung der Daten erforderlich sein.

WP4: Im Vergleich zur Humanstudie zeigen die Ergebnisse aus dem Mausmodell aus zwei Gründen bessere Klassifikationsergebnisse: Erstens sind die Karzinome besser sichtbar und daher ist die Kennzeichnung mit weniger Fehlern behaftet. Dies ist vor allem auf die geringeren Intra-Mausvariationen im Vergleich zu den Intra-Patientenvariationen in der Humanstudie zurückzuführen. Zweitens ist das Bildgebungssystem verbessert und damit das Rauschen deutlich geringer. Beide Faktoren ermöglichen einen endgültigen ACC2 von 0,73, einen AUC von 0,76 und einen MCC von 0,47. Darüber hinaus ermöglicht die multispektrale Bildgebung mit Unterstützung von räumlichen Merkmalen eine bessere Klassifikation von neoplastischen Läsionen im Dickdarm als hyper-spektrale Bilder, die durch spektrale Schätzverfahren abgeleitet werden. Daher kann diese Arbeit, unterstützt durch die aktuellen Ergebnisse, die Aussage von Swager et al. [7] unterstützen, dass echte hyper-spektrale Bildgebung anstelle von spektraler Schätzung untersucht werden sollte. Die Abkürzung zum Erreichen der hyper-spektralen Bildgebung mittels spektraler Schätzung der multispektralen Bildgebung ist bei automatisierter Klassifikation nicht sinnvoll. Trotzdem sind die Ergebnisse dieser MSI-Studie mit räumlichen Merkmalen ähnlich wie die HSI-Studien von Baltusen et al. [145].

MSI/HSI könnte in Zukunft als Red Flag-Technik funktionieren. Um die Einschränkungen zu überwinden, ist jedoch wahrscheinlich eine Punktspektroskopie-Technik erforderlich, die eine korrekte Kennzeichnung der Daten ermöglicht, da eine unzureichende Kennzeichnung die Klassifizierungsgenauigkeit deutlich verringert. Darüber hinaus wird erwartet, dass für HSI eine große Menge an Daten für eine erfolgreiche Klassifizierung aufgrund des Fluchs der Dimensionalität benötigt wird, da die Daten mit zunehmender Dimensionalität spärlicher werden. Daher wird MSI Teil zukünftiger Untersuchungen sein.

Bibliography

[1] Deutschland, Statistisches Bundesamt. 2016.

[2] Siegel, RL; Miller, KD and Jemal, A. 'Cancer statistics, 2015'. *CA: a cancer journal for clinicians* 65.1 (2015), pp. 5–29.

[3] Aida, K; Yoshikawa, H; Mochizuki, C; Mori, A; Muto, S; Fukuda, T and Otsuki, M. 'Clinicopathological features of gastric cancer detected by endoscopy as part of annual health checkup'. *Journal of gastroenterology and hepatology* 23.4 (2008), pp. 632–637.

[4] Wang, LV. 'Ultrasound-mediated biophotonic imaging: a review of acousto-optical tomography and photo-acoustic tomography'. *Disease markers* 19.2-3 (2004), pp. 123–138.

[5] Lee, MH; Buterbaugh, K; Richards-Kortum, R and Anandasabapathy, S. 'Advanced Endoscopic Imaging for Barrett's Esophagus: Current Options and Future Directions'. English. *Current Gastroenterology Reports* 14.3 (2012), pp. 216–225. http://dx.doi.org/10.1007/s11894-012-0259-3.

[6] Pohl, J; May, A; Rabenstein, T; Pech, O and Ell, C. 'Computed virtual chromoendoscopy: a new tool for enhancing tissue surface structures.' *Endoscopy* 39.1 (2007), pp. 80–83.

[7] Swager, A; Curvers, WL and Bergman, JJ. 'Diagnosis by endoscopy and advanced imaging'. *Best Practice & Research Clinical Gastroenterology* 29.1 (2015), pp. 97–111.

[8] Arnold, T; De Biasio, M and Leitner, R. 'High-sensitivity hyper-spectral video endoscopy system for intra-surgical tissue classification'. *Sensors, 2010 IEEE*. IEEE. 2010, pp. 2612–2615.

[9] Bearman, GH; Cabib, D and Levenson, RM. 'Spectral imaging: instrumentation, applications, and analysis'. *Spectral Imaging: Instrumentation, Applications, and Analysis*. Vol. 3920. 2000.

[10] Plaza, A; Benediktsson, JA; Boardman, JoW; Brazile, J; Bruzzone, L; Camps-Valls, G; Chanussot, J; Fauvel, M; Gamba, P; Gualtieri, A et al. 'Recent advances in techniques for hyperspectral image processing'. *Remote sensing of environment* 113 (2009), S110–S122.

[11] Kester, RT; Bedard, N; Gao, L and Tkaczyk, TS. 'Real-time snapshot hyperspectral imaging endoscope'. *Journal of Biomedical Optics* 16.5 (2011), pp. 056005-056005–12. +%20http://dx.doi.org/10.1117/1.3574756.

[12] Hohmann, M; Douplik, A; Varadhachari, J; Nasution, A; Mudter, J; Neurath, M and Schmidt, M. 'Preliminary results for hyperspectral videoendoscopy diagnostics on the phantoms of normal and abnormal tissues: towards gastrointestinal diagnostics'. *European Conference on Biomedical Optics*. Optical Society of America. 2011, 80872N.

[13] Lu, G and Fei, B. 'Medical hyperspectral imaging: a review'. *Journal of biomedical optics* 19.1 (2014), pp. 010901–010901.

[14] Kiyotoki, S; Nishikawa, J; Okamoto, T; Hamabe, K; Saito, M; Goto, A; Fujita, Y; Hamamoto, Y; Takeuchi, Y; Satori, S et al. 'New method for detection of gastric cancer by hyperspectral imaging: a pilot study'. *Journal of biomedical optics* 18.2 (2013), pp. 026010–026010.

[15] Goto, A; Nishikawa, J; Kiyotoki, S; Nakamura, M; Nishimura, J; Okamoto, T; Ogihara, H; Fujita, Y; Hamamoto, Y and Sakaida, I. 'Use of hyperspectral imaging technology to develop a diagnostic support system for gastric cancer'. *Journal of biomedical optics* 20.1 (2015), pp. 016017–016017.

[16] Lao-Sirieix, P; Caldas, C and Fitzgerald, RC. 'Genetic predisposition to gastro-oesophageal cancer'. *Current opinion in genetics & development* 20.3 (2010), pp. 210–217.

[17] Onmeda. 2010.

[18] Crew, KD and Neugut, AI. 'Epidemiology of gastric cancer'. *World Journal of Gastroenterology* 12.3 (2006), p. 354.

[19] Lauren, P. 'The two histological main types of gastric carcinoma: diffuse and so-called intestinal-type carcinoma: an attempt at a histo-clinical classification'. *Acta Pathologica Microbiologica Scandinavica* 64.1 (1965), pp. 31–49.

[20] Pennathur, A; Gibson, MK; Jobe, BA and Luketich, JD. 'Oesophageal carcinoma'. *The Lancet* 381.9864 (2013), pp. 400–412. http://www.sciencedirect.com/science/article/pii/S0140673612606436.

[21] Falk, GW; Rice, TW; Goldblum, JR and Richter, JE. 'Adenocarcinoma of the esophagus and Barrett's esophagus: a population-based study: DANISH ESOPHAGEAL CANCER STUDY'. *The American Journal of Gastroenterology* (1999), pp. 86–91.

[22] Johns Hopkins Pathology, http://pathology2.jhu.edu/beweb/Definition.cfm.

[23] Skinner, DB; Walther, BC; Riddell, RH; Schmidt, H; Iascone, C and TR, DeMeester. 'Barrett's esophagus. Comparison of benign and malignant cases.' *Annals of Surgery* 198.4 (1983), pp. 554–565.

[24] Skinner, D B; Dowlatshahi, KD; DeMeester, TR et al. 'Potentially curable cancer of the esophagus'. *Cancer* 50.11 Suppl (1982), pp. 2571–2575.

[25] Osawa, H; Yamamoto, H; Yamada, N; Yoshizawa, M; Sunada, K; Kita, H; Ajibe, H; Satoh, Kiichi and Sugano, K. 'Diagnosis of endoscopic Barrett's esophagus by transnasal flexible spectral imaging color enhancement'. *Journal of gastroenterology* 44.11 (2009), pp. 1125–1132.

[26] Kara, MA. 'High-resolution endoscopy plus chromoendoscopy or narrow-band imaging in Barrett's esophagus: a prospective randomized crossover study'. *Endoscopy* (2005), pp. 929–36.

[27] Sharma, P. 'Clinical practice. Barrett's esophagus.' *New England Journal of Medicine* 361.26 (2009), pp. 2548–2556. eprint: http://www.nejm.org/doi/pdf/10.1056/NEJMcp0902173. http://www.nejm.org/doi/full/10.1056/NEJMcp0902173.

[28] Torre, LA; Bray, F; Siegel, RL; Ferlay, J; Lortet-Tieulent, J and Jemal, A. 'Global cancer statistics, 2012'. *CA: a cancer journal for clinicians* 65.2 (2015), pp. 87–108.

[29] Quintero, E; Castells, A; Bujanda, L; Cubiella, J; Salas, D; Lanas, Á; Andreu, M; Carballo, F; Morillas, JD; Hernández, C et al. 'Colonoscopy versus fecal immunochemical testing in colorectal-cancer screening'. *New England Journal of Medicine* 366.8 (2012), pp. 697–706.

[30] Pan, J; Xin, L; Ma, YF; Hu, LH and Li, ZS. 'Colonoscopy reduces colorectal cancer incidence and mortality in patients with non-malignant findings: a meta-analysis'. *The American journal of gastroenterology* 111.3 (2016), p. 355.

[31] Heresbach, D; Barrioz, T; Lapalus, MG; Coumaros, D; Bauret, P; Potier, P; Sautereau, Denis; Boustière, C; Grimaud, JC; Barthélémy, C et al. 'Miss rate for colorectal neoplastic polyps: a prospective multicenter study of back-to-back video colonoscopies'. *Endoscopy* 40.04 (2008), pp. 284–290.

[32] Armstrong, D. 'Review article: towards consistency in the endoscopic diagnosis of Barrett's oesophagus and columnar metaplasia'. *Alimentary pharmacology & therapeutics* 20.s5 (2004), pp. 40–47.

[33] Vakoc, BJ; Fukumura, D; Jain, RK and Bouma, BE. 'Cancer imaging by optical coherence tomography: preclinical progress and clinical potential'. *Nature Reviews Cancer* 12.5 (2012), pp. 363–368.

[34] Hillman, EMC; Devor, A; Dunn, AK and Boas, DA. 'Laminar optical tomography: high-resolution 3D functional imaging of superficial tissues'. *Medical Imaging*. International Society for Optics and Photonics. 2006, pp. 61431M–61431M.

[35] Uno, K; Koike, T and Shimosegawa, T. 'Recent development of optical coherence tomography for preoperative diagnosis of esophageal malignancies'. *World journal of gastrointestinal endoscopy* 7.9 (2015), p. 872.

[36] Chen, Y; Aguirre, AD; Hsiung, PL; Desai, S; Herz, PR; Pedrosa, M; Huang, Q; Figueiredo, M; Huang, SW; Koski, A et al. 'Ultrahigh resolution optical coherence tomography of Barrett's esophagus: preliminary descriptive clinical study correlating images with histology.' *Endoscopy* 39.7 (2007), pp. 599–605.

[37] Wang, LV. 'Multiscale photoacoustic microscopy and computed tomography'. *Nature photonics* 3.9 (2009), pp. 503–509.

[38] Wang, LV and Hu, S. 'Photoacoustic tomography: in vivo imaging from organelles to organs'. *Science* 335.6075 (2012), pp. 1458–1462.

[39] Yang, JM; Favazza, CP; Yao, J; Chen, R; Zhou, Q; Shung, KK and Wang, LV. 'Three-dimensional photoacoustic and ultrasonic endoscopic imaging of two rabbit esophagi'. *SPIE BiOS*. International Society for Optics and Photonics. 2015, pp. 932334–932334.

[40] Kruger, RA; Kuzmiak, CM; Lam, RB; Reinecke, DR; Del Rio, SP and Steed, D. 'Dedicated 3D photoacoustic breast imaging'. *Medical physics* 40.11 (2013), p. 113301.

[41] Buehler, A; Deán-Ben, XL; Claussen, J; Ntziachristos, V and Razansky, D. 'Three-dimensional optoacoustic tomography at video rate'. *Optics express* 20.20 (2012), pp. 22712–22719.

[42] Dima, A and Ntziachristos, V. 'Non-invasive carotid imaging using optoacoustic tomography'. *Optics express* 20.22 (2012), pp. 25044–25057.

[43] Evans, JA and Nishioka, NS. 'Endoscopic confocal microscopy'. *Current opinion in gastroenterology* 21.5 (2005), pp. 578–584.

[44] Brown, WJ; JW Pyhtila, NG Terry; KJ Chalut, TA DAmico; TA Sporn, J. V. Obando and Wax, A. 'Review and Recent Development of Angle-Resolved Low-Coherence Interferometry for Detection of Precancerous Cells in Human Esophageal Epithelium'. *IEEE JOURNAL OF SELECTED TOPICS IN QUANTUM ELECTRONICS* 14.1 (2008), pp. 88–97.

[45] Curvers, WL; Broek, FJC van den; Reitsma, JB; Dekker, E and Bergman, JJGHM. 'Systematic review of narrow-band imaging for the detection and differentiation of abnormalities in the esophagus and stomach (with video)'. *Gastrointestinal Endoscopy* 69.2 (2009), pp. 307–317. http://www.sciencedirect.com/science/article/pii/S0016510708026321.

[46] Subramanian, V and Ragunath, K. 'Advanced endoscopic imaging: a review of commercially available technologies'. *Clinical Gastroenterology and Hepatology* 12.3 (2014), pp. 368–376.

[47] Curvers, WL; Singh, R; Song, LMWK; Wolfsen, HC; Ragunath, K; Wang, K; Wallace, MB; Fockens, P and Bergman, JJGHM. 'Endoscopic tri-modal imaging for detection of early neoplasia in Barrett's oesophagus: a multi-centre feasibility study using high-resolution endoscopy, autofluorescence imaging and narrow band imaging incorporated in one endoscopy system'. *Gut* 57.2 (2008), pp. 167–172.

[48] Olliver, JR; Wild, CP; Sahay, P; Dexter, S and Hardie, LJ. 'Chromoendoscopy with methylene blue and associated DNA damage in Barrett's oesophagus'. *The Lancet* 362.9381 (2003), pp. 373–374.

[49] Pohl, J; Lotterer, E; Balzer, C; Sackmann, M; Schmidt, KD; Gossner, L; Schaab, C; Frieling, T; Medve, M; Mayer, G et al. 'Computed virtual chromoendoscopy versus standard colonoscopy with targeted indigocarmine chromoscopy: a randomised multicentre trial'. *Gut* 58.1 (2009), pp. 73–78.

[50] Martin, R; Thies, B and Gerstner, AOH. 'Hyperspectral hybrid method classification for detecting altered mucosa of the human larynx'. *International journal of health geographics* 11.1 (2012), p. 21.

[51] Gerstner, AOH; Laffers, W; Bootz, F; Farkas, DL; Martin, R; Bendix, J and Thies, B. 'Hyperspectral imaging of mucosal surfaces in patients'. *Journal of Biophotonics* 5.3 (2012), pp. 255–262.

[52] Siddiqi, AM; Li, H; Faruque, F; Williams, W; Lai, K; Hughson, M; Bigler, S; Beach, J and Johnson, W. 'Use of hyperspectral imaging to distinguish normal, precancerous, and cancerous cells'. *Cancer Cytopathology* 114.1 (2008), pp. 13–21.

[53] Boucheron, LE; Bi, Z; Harvey, NR; Manjunath, BS and Rimm, DL. 'Utility of multispectral imaging for nuclear classification of routine clinical histopathology imagery'. *BMC cell biology* 8.Suppl 1 (2007), S8.

[54] Zuzak, KJ; Naik, SC; Alexandrakis, G; Hawkins, D; Behbehani, K and Livingston, EH. 'Characterization of a near-infrared laparoscopic hyperspectral imaging system for minimally invasive surgery'. *Analytical chemistry* 79.12 (2007), pp. 4709–4715.

[55] Masood, K and Rajpoot, NM. 'Spatial analysis for colon biopsy classification from hyperspectral imagery'. *The Annals of the BMVA* 2008.4 (2008), pp. 1–16.

[56] Masood, K and Rajpoot, NM. 'Classification of colon biopsy samples by spatial analysis of a single spectral band from its hyperspectral cube' (2007).

[57] Masood, K. 'Hyperspectral imaging with wavelet transform for classification of colon tissue biopsy samples'. *Optical Engineering+ Applications*. International Society for Optics and Photonics. 2008, pp. 707319–707319.

[58] Masood, K and Rajpoot, N. 'Texture based classification of hyperspectral colon biopsy samples using CLBP'. *Biomedical Imaging: From Nano to Macro, 2009. ISBI'09. IEEE International Symposium on*. IEEE. 2009, pp. 1011–1014.

[59] Maggioni, M; Davis, GL; Warner, FJ; Geshwind, FB; Coppi, AC; DeVerse, RA and Coifman, RR. 'Hyperspectral microscopic analysis of normal, benign and carcinoma microarray tissue sections'. *Biomedical Optics 2006*. International Society for Optics and Photonics. 2006, pp. 60910I–60910I.

[60] Nachabé, R; Hendriks, BHW; Voort, M van der; Desjardins, AE and Sterenborg, HJCM. 'Estimation of biological chromophores using diffuse optical spectroscopy: benefit of extending the UV-VIS wavelength range to include 1000 to 1600 nm'. *Biomedical optics express* 1.5 (2010), pp. 1432–1442.

[61] Nachabé, R; Hendriks, BHW; Desjardins, AE; Voort, M van der; Mark, MB van der and Sterenborg, HJCM. 'Estimation of lipid and water concentrations in scattering media with diffuse optical spectroscopy from 900to1600nm'. *Journal of biomedical optics* 15.3 (2010), pp. 037015–037015.

[62] Wang, Q; Le, D; Ramella-Roman, J and Pfefer, J. 'Visualization of mucosal vasculature with narrow band imaging: a theoretical study'. *SPIE BiOS*. International Society for Optics and Photonics. 2012, pp. 821505–821505.

[63] Gross, S; Trautwein, C; Behrens, A; Winograd, R; Palm, S; Lutz, HH; Schirin-Sokhan, R; Hecker, H; Aach, T and Tischendorf, JJW. 'Computer-based classification of small colorectal polyps by using narrow-band imaging with optical magnification'. *Gastrointestinal endoscopy* 74.6 (2011), pp. 1354–1359.

[64] Kwitt, R; Vasconcelos, N; Rasiwasia, N; Uhl, A; Davis, B; Häfner, M and Wrba, F. 'Endoscopic image analysis in semantic space'. *Medical image analysis* 16.7 (2012), pp. 1415–1422.

[65] Tischendorf, JJW; Gross, S; Winograd, R; Hecker, H; Auer, R; Behrens, A; Trautwein, C; Aach, T and Stehle, T. 'Computer-aided classification of colorectal polyps based on vascular patterns: a pilot study'. *Endoscopy* 42.03 (2010), pp. 203–207.

[66] Liedlgruber, M and Uhl, A. 'Computer-aided decision support systems for endoscopy in the gastrointestinal tract: a review'. *IEEE reviews in biomedical engineering* 4 (2011), pp. 73–88.

[67] Hagen, N and Kudenov, MW. 'Review of snapshot spectral imaging technologies'. *Optical Engineering* 52.9 (2013), pp. 090901–090901.

[68] Sinclair, MB; Haaland, DM; Timlin, JA and Jones, HDT. 'Hyperspectral confocal microscope'. *Applied optics* 45.24 (2006), pp. 6283–6291.

[69] Gao, L and Smith, RT. 'Optical hyperspectral imaging in microscopy and spectroscopy–a review of data acquisition'. *Journal of biophotonics* 8.6 (2015), pp. 441–456.

[70] Martin, ME; Wabuyele, MB; Chen, K; Kasili, P; Panjehpour, M; Phan, M; Overholt, B; Cunningham, G; Wilson, D; DeNovo, RC et al. 'Development of an advanced hyperspectral imaging (HSI) system with applications for cancer detection'. *Annals of biomedical engineering* 34.6 (2006), pp. 1061–1068.

[71] Stigell, P; Miyata, K and Hauta-Kasari, M. 'Wiener estimation method in estimating of spectral reflectance from RGB images'. *Pattern Recognition and Image Analysis* 17.2 (2007), pp. 233–242.

[72] Nishidate, I; Maeda, T; Niizeki, K and Aizu, Y. 'Estimation of melanin and hemoglobin using spectral reflectance images reconstructed from a digital RGB image by the Wiener estimation method'. *Sensors* 13.6 (2013), pp. 7902–7915.

[73] Shen, HL; Cai, PQ; Shao, SJ and Xin, JH. 'Reflectance reconstruction for multispectral imaging by adaptive Wiener estimation'. *Optics express* 15.23 (2007), pp. 15545–15554.

[74] Shimano, N; Terai, K and Hironaga, M. 'Recovery of spectral reflectances of objects being imaged by multispectral cameras'. *JOSA A* 24.10 (2007), pp. 3211–3219.

[75] Babaei, V; Amirshahi, SH and Agahian, F. 'Using weighted pseudo-inverse method for reconstruction of reflectance spectra and analyzing the dataset in terms of normality'. *Color Research & Application* 36.4 (2011), pp. 295–305.

[76] Cortes, C and Vapnik, V. 'Support-vector networks'. *Machine learning* 20.3 (1995), pp. 273–297.

[77] Lu, D and Weng, Q. 'A survey of image classification methods and techniques for improving classification performance'. *International journal of Remote sensing* 28.5 (2007), pp. 823–870.

[78] Ortega, S; Fabelo, H; Iakovidis, D; Koulaouzidis, A and Callico, G. 'Use of Hyperspectral/Multispectral Imaging in Gastroenterology. Shedding Some–Different–Light into the Dark'. *Journal of clinical medicine* 8.1 (2019), p. 36.

[79] Akbari, H; Uto, K; Kosugi, Y; Kojima, K and Tanaka, N. 'Cancer detection using infrared hyperspectral imaging'. *Cancer science* 102.4 (2011), pp. 852–857.

[80] Akbari, H; Halig, LV; Schuster, DM; Osunkoya, A; Master, V; Nieh, PT; Chen, GZ and Fei, B. 'Hyperspectral imaging and quantitative analysis for prostate cancer detection'. *Journal of biomedical optics* 17.7 (2012), pp. 0760051–07600510.

[81] Akbari, H; Halig, LV; Zhang, H; Wang, D; Chen, ZG and Fei, B. 'Detection of cancer metastasis using a novel macroscopic hyperspectral method'. *SPIE Medical Imaging*. International Society for Optics and Photonics. 2012, pp. 831711–831711.

[82] Yoshinaga, S; Oda, I; Abe, S; Nonaka, S; Suzuki, H; Takisawa, H; Taniguchi, H and Saito, Y. 'Evaluation of the margins of differentiated early gastric cancer by using conventional endoscopy'. *World journal of gastrointestinal endoscopy* 7.6 (2015), p. 659.

[83] Yamashina, T; Uedo, N; Matsui, F; Ishihara, R and Tomita, Y. 'Usefulness of chromoendoscopy and magnifying narrow band imaging endoscopy for diagnosis of demarcation of adenocarcinoma in Barrett's esophagus'. *Digestive Endoscopy* 25.S2 (2013), pp. 173–176.

[84] Freund, Y and Schapire, RE. 'A desicion-theoretic generalization of on-line learning and an application to boosting'. *Computational learning theory*. Springer. 1995, pp. 23–37.

[85] Freund, Y. 'A more robust boosting algorithm'. *arXiv preprint arXiv:0905.2138* (2009).

[86] Breiman, L. 'Random forests'. *Machine learning* 45.1 (2001), pp. 5–32.

[87] Kobetski, Mi and Sullivan, J. 'Improved Boosting Performance by Explicit Handling of Ambiguous Positive Examples'. *Pattern Recognition Applications and Methods*. Springer, 2015, pp. 17–37.

[88] Sabale, SP and Jadhav, CR. 'Hyperspectral Image Classification - Methods in Remote Sensing-A Review'. *Computing Communication Control and Automation (ICCUBEA), 2015 International Conference on*. IEEE. 2015, pp. 679–683.

[89] Coates, A; Carpenter, B; Case, C; Satheesh, S; Suresh, B; Wang, T; Wu, DJ and Ng, AY. 'Text detection and character recognition in scene images with unsupervised feature learning'. *2011 International Conference on Document Analysis and Recognition*. IEEE. 2011, pp. 440–445.

[90] Pearson, K. 'LIII. On lines and planes of closest fit to systems of points in space'. *The London, Edinburgh, and Dublin Philosophical Magazine and Journal of Science* 2.11 (1901), pp. 559–572.

[91] Malagón-Borja, L and Fuentes, O. 'Object detection using image reconstruction with PCA'. *Image and Vision Computing* 27.1 (2009), pp. 2–9.

[92] Green, AA; Berman, M; Switzer, P and Craig, MD. 'A transformation for ordering multispectral data in terms of image quality with implications for noise removal'. *IEEE Transactions on geoscience and remote sensing* 26.1 (1988), pp. 65–74.

[93] Regeling, B; Laffers, W; Gerstner, AOH; Westermann, Sn; Müller, NA; Schmidt, K; Bendix, J and Thies, B. 'Development of an image preprocessor for operational hyperspectral laryngeal cancer detection'. *Journal of biophotonics* (2015).

[94] Regeling, B; Thies, B; Gerstner, AOH; Westermann, S; Müller, NA; Bendix, J and Laffers, W. 'Hyperspectral Imaging Using Flexible Endoscopy for Laryngeal Cancer Detection'. *Sensors* 16.8 (2016), p. 1288.

[95] Roger, RE and Arnold, JF. 'Reliably estimating the noise in AVIRIS hyperspectral images'. *International Journal of Remote Sensing* 17.10 (1996), pp. 1951–1962.

[96] Gao, L; Du, Q; Zhang, B; Yang, W and Wu, Y. 'A comparative study on linear regression-based noise estimation for hyperspectral imagery'. *IEEE Journal of Selected Topics in Applied Earth Observations and Remote Sensing* 6.2 (2013), pp. 488–498.

[97] Peng, H; Long, F and Ding, C. 'Feature selection based on mutual information criteria of max-dependency, max-relevance, and min-redundancy'. *IEEE Transactions on pattern analysis and machine intelligence* 27.8 (2005), pp. 1226–1238.

[98] Gabrilovich, E and Markovitch, S. 'Feature generation for text categorization using world knowledge'. *IJCAI*. Vol. 5. 2005, pp. 1048–1053.

[99] Kim, Y; Lee, H and Provost, EM. 'Deep learning for robust feature generation in audiovisual emotion recognition'. *Acoustics, Speech and Signal Processing (ICASSP), 2013 IEEE International Conference on*. IEEE. 2013, pp. 3687–3691.

[100] Liedlgruber, M and Uhl, A. 'Computer-aided decision support systems for endoscopy in the gastrointestinal tract: a review'. *IEEE reviews in biomedical engineering* 4 (2011), pp. 73–88.

[101] Liu, DY; Gan, T; Rao, NN; Xing, YW; Zheng, J; Li, S; Luo, CS; Zhou, ZJ and Wan, YL. 'Identification of lesion images from gastrointestinal endoscope based on feature extraction of combinational methods with and without learning process'. *Medical image analysis* 32 (2016), pp. 281–294.

[102] Sun, Z; Bebis, G and Miller, R. 'Monocular precrash vehicle detection: Features and classifiers'. *IEEE transactions on image processing* 15.7 (2006), pp. 2019–2034.

[103] Arróspide, J and Salgado, L. 'A study of feature combination for vehicle detection based on image processing'. *The Scientific World Journal* 2014 (2014).

[104] Zhang, Q; Tian, Y; Yang, Y and Pan, C. 'Automatic spatial–spectral feature selection for hyperspectral image via discriminative sparse multimodal learning'. *IEEE Transactions on Geoscience and Remote Sensing* 53.1 (2015), pp. 261–279.

[105] Fauvel, M; Chanussot, J and Benediktsson, JA. 'A spatial–spectral kernel-based approach for the classification of remote-sensing images'. *Pattern Recognition* 45.1 (2012), pp. 381–392.

[106] Zhang, L; Zhang, L; Tao, D and Huang, X. 'Tensor discriminative locality alignment for hyperspectral image spectral–spatial feature extraction'. *IEEE Transactions on Geoscience and Remote Sensing* 51.1 (2013), pp. 242–256.

[107] Zhu, C and Liu, Q. 'Review of Monte Carlo modeling of light transport in tissues'. *Journal of biomedical optics* 18.5 (2013), p. 050902.

[108] Lu, Q; Gan, X; Gu, M and Luo, Q. 'Monte Carlo modeling of optical coherence tomography imaging through turbid media'. *Applied optics* 43.8 (2004), pp. 1628–1637.

[109] Bigio, IJ and Mourant, JR. 'Ultraviolet and visible spectroscopies for tissue diagnostics: fluorescence spectroscopy and elastic-scattering spectroscopy'. *Physics in Medicine & Biology* 42.5 (1997), p. 803.

[110] Binzoni, T; Seelamantula, CS and Van De Ville, D. 'A fast time-domain algorithm for the assessment of tissue blood flow in laser-Doppler flowmetry'. *Physics in Medicine & Biology* 55.13 (2010), N383.

[111] Hidovic-Rowe, D and Claridge, E. 'Modelling and validation of spectral reflectance for the colon'. *Physics in Medicine and Biology* 50.6 (2005), p. 1071. http://stacks.iop.org/0031-9155/50/i=6/a=003.

[112] Lisenko, SA; Kugeiko, MM; Firago, VA and Sobchuk, AN. 'Analytical model of diffuse reflectance spectrum of skin tissue'. *Quantum Electronics* 44.1 (2014), p. 69.

[113] Lee, KS; Cohen, WB; Kennedy, RE; Maiersperger, TK and Gower, ST. 'Hyperspectral versus multispectral data for estimating leaf area index in four different biomes'. *Remote Sensing of Environment* 91.3 (2004), pp. 508–520.

[114] Taghizadeh, M; Gowen, AA and O'Donnell, CP. 'Comparison of hyperspectral imaging with conventional RGB imaging for quality evaluation of Agaricus bisporus mushrooms'. *Biosystems engineering* 108.2 (2011), pp. 191–194.

[115] Medjahed, SA; Saadi, TA; Benyettou, A and Ouali, M. 'Gray wolf optimizer for hyperspectral band selection'. *Applied Soft Computing* 40 (2016), pp. 178–186.

[116] Begley, CG and Ellis, LM. 'Drug development: Raise standards for preclinical cancer research'. *Nature* 483.7391 (2012), pp. 531–533.

[117] Hohmann, M; Kanawade, R; Klämpfl, F; Douplik, A; Mudter, J; Neurath, MF and Albrecht, H. 'In-vivo multispectral video endoscopy towards in-vivo hyperspectral video endoscopy'. *Journal of Biophotonics* (2016).

[118] Hagen, N; Kester, RT; Gao, L and Tkaczyk, TS. 'Snapshot advantage: a review of the light collection improvement for parallel high-dimensional measurement systems'. *Optical Engineering* 51.11 (2012), pp. 111702–1.

[119] Yokoya, N; Miyamura, N and Iwasaki, A. 'Preprocessing of hyperspectral imagery with consideration of smile and keystone properties'. *SPIE Asia-Pacific Remote Sensing*. International Society for Optics and Photonics. 2010, 78570B–78570B.

[120] Hohmann, M; Albrecht, H; Mudter, J; Nagulin, KY; Klämpfl, F and Schmidt, M. 'spectral spatial Variation'. *Scientific reports* 9.1 (2019), p. 7512.

[121] Chen, C; Klämpfl, F; Kanawade, R; MRiemann; Knipfer, C; Stelzle, F and Schmidt, M. 'Recovering the superficial microvascular pattern via diffuse reflection imaging: phantom validation'. *Biomedical engineering online* 14.1 (2015), p. 87.

[122] Vécsei, A; Fuhrmann, T; Liedlgruber, M; Brunauer, L; Payer, H and Uhl, A. 'Automated classification of duodenal imagery in celiac disease using evolved Fourier feature vectors'. *Computer methods and programs in biomedicine* 95.2 (2009), S68–S78.

[123] Schiele, B and Crowley, JL. 'Recognition without correspondence using multidimensional receptive field histograms'. *International Journal of Computer Vision* 36.1 (2000), pp. 31–50.

[124] Statnikov, Ar; Wang, L and Aliferis, CF. 'A comprehensive comparison of random forests and support vector machines for microarray-based cancer classification'. *BMC bioinformatics* 9.1 (2008), p. 319.

[125] Pal, M. 'Random forest classifier for remote sensing classification'. *International Journal of Remote Sensing* 26.1 (2005), pp. 217–222.

[126] Matthews, BW. 'Comparison of the predicted and observed secondary structure of T4 phage lysozyme'. *Biochimica et Biophysica Acta (BBA)-Protein Structure* 405.2 (1975), pp. 442–451.

[127] Powers, DMW. *Evaluation: From Precision, Recall and F-Factor to ROC, Informedness, Markedness & Correlation'(SPIE-07-001)*. Tech. rep. School of Informatics and Engineering, Flinders University, Adelaide, Australia, 2007.

[128] Malagón-Borja, L and Fuentes, O. 'Object detection using image reconstruction with PCA'. *Image and Vision Computing* 27.1 (2009), pp. 2–9.

[129] Fang, Q and Boas, DA. 'Monte Carlo simulation of photon migration in 3D turbid media accelerated by graphics processing units'. *Optics express* 17.22 (2009), p. 20178.

[130] Holmer, C; Lehmann, KS; Wanken, J; Reissfelder, C; Roggan, A; Mueller, G; Buhr, HJ and Ritz, JP. 'Optical properties of adenocarcinoma and squamous cell carcinoma of the gastroesophageal junction'. *Journal of Biomedical Optics* 12.1 (2007), pp. 014025-014025–8. +%20http://dx.doi.org/10.1117/1.2564793.

[131] Hohmann, M; Lengenfelder, B; Kanawade, R; Klämpfl, F; Douplik, A and Albrecht, H. 'Measurement of optical properties of pig esophagus by using a modified spectrometer set-up'. *Journal of Biophotonics* (2017).

[132] Roggan, A; Schädel, D; Netz, U; Ritz, J-P; Germer, C-T and Müller, G. 'The effect of preparation technique on the optical parameters of biological tissue'. *Applied Physics B* 69.5-6 (1999), pp. 445–453.

[133] Jacques, SL. 'Optical properties of biological tissues: a review'. *Physics in medicine and biology* 58.11 (2013), R37.

[134] Kreiss, L; Hohmann, M; Klaempfl, F; Schuermann, S; Dehghani, F; Schmidt, M; Friedrich, O and Buechler, L. 'Diffuse reflectance spectroscopy and Raman spectroscopy for label-free molecular characterization and automated detection of human cartilage and subchondral bone'. *Sensors and Actuators B: Chemical* 301 (2019), p. 127121.

[135] Neufert, C; Becker, C and Neurath, MF. 'An inducible mouse model of colon carcinogenesis for the analysis of sporadic and inflammation-driven tumor progression'. *Nature protocols* 2.8 (2007), p. 1998.

[136] Becker, C; Fantini, MC; Wirtz, S; Nikolaev, A; Kiesslich, R; Lehr, HA; Galle, PR and Neurath, MF. 'In vivo imaging of colitis and colon cancer development in mice using high resolution chromoendoscopy'. *Gut* 54.7 (2005), pp. 950–954.

[137] Neurath, MF; Wittkopf, N; Wlodarski, A; Waldner, M; Neufert, C; Wirtz, S; Günther, C and Becker, C. 'Assessment of tumor development and wound healing using endoscopic techniques in mice'. *Gastroenterology* 139.6 (2010), pp. 1837–1843.

[138] Szczęsny, G; Veihelmann, A; Massberg, S; Nolte, D and Messmer, K. 'Long-term anaesthesia using inhalatory isoflurane in different strains of mice the haemodynamic effects'. *Laboratory animals* 38.1 (2004), pp. 64–69.

[139] Nowland, MH. *Guidelines on Anesthesia and Analgesia in Mice*. 2016 (accessed May 28th, 2018).

[140] Lin, Y and Jeon, Y. 'Random forests and adaptive nearest neighbors'. *Journal of the American Statistical Association* 101.474 (2006), pp. 578–590.

[141] Lapuschkin, S; Wäldchen, S; Binder, A; Montavon, G; Samek, W and Müller, KR. 'Unmasking Clever Hans predictors and assessing what machines really learn'. *Nature communications* 10.1 (2019), p. 1096.

[142] Fukutomi, D; Ishii, K and Awazu, K. 'Highly accurate scattering spectra of strongly absorbing samples obtained using an integrating sphere system by considering the angular distribution of diffusely reflected light'. *Lasers in medical science* 30.4 (2015), pp. 1335–1340.

[143] Du, H; Qi, H; Wang, X; Ramanath, R and Snyder, WE. 'Band selection using independent component analysis for hyperspectral image processing'. *32nd Applied Imagery Pattern Recognition Workshop, 2003. Proceedings.* IEEE. 2003, pp. 93–98.

[144] Sarhrouni, E; Hammouch, A and Aboutajdine, D. 'Dimensionality reduction and classification feature using mutual information applied to hyperspectral images: a filter strategy based algorithm'. *arXiv preprint arXiv:1210.0052* (2012).

[145] Baltussen, EJM; Kok, END; Koning, SGB de; Sanders, J; Aalbers, AGJ; Kok, NFM; Beets, GL; Flohil, CC; Bruin, SC; Kuhlmann, KFD et al. 'Hyperspectral imaging for tissue classification, a way toward smart laparoscopic colorectal surgery'. *Journal of biomedical optics* 24.1 (2019), p. 016002.

Own publications referring to this work

1. Hohmann, M; Kanawade, R; Klämpfl, F; Douplik, A; Mudter, J; Neurath, M, and Albrecht H. 'In-vivo multispectral video endoscopy towards in-vivo hyperspectral video endoscopy' in Journal of Biophotonics 10 (2017), S. 553-564
2. Hohmann, M; Albrecht, H; Mudter, J; Nagulin, K; Klämpfl, F, and Schmidt, M. 'Spectral spatial variation' in Scientific Reports 9, 7512 (2019)
3. Hohmann, M; Albrecht, Lengenfelder, L; Klämpfl, F, and Schmidt, M. 'Factors influencing the accuracy for tissue classification in multi spectral in-vivo endoscopy for the upper gastro-internal tract.' in Scientific reports 10, 3546 (2020)
4. **In preparation:** 'In-vivo multi spectral colonoscopy in mice'

Related student thesis

1. Peterhansl, D. 'Design und Aufbau eines kombinierten Fluoreszenz/Weißlichtendoskopes', Bacherlor thesis (2015)
2. Grünberg, A. 'Multi- and hyperspectral endoscopy for the detection of carcinomas in the colon', Master thesis (2017)
3. Glas, R. 'Spectral estimation of hyper spectral images for hyper spectral endoscopy', Bachelor thesis (2020)

Reihenübersicht

Koordination der Reihe (Stand 2021):
Geschäftsstelle Maschinenbau, Dr.-Ing. Oliver Kreis, www.mb.fau.de/diss/

Im Rahmen der Reihe sind bisher die nachfolgenden Bände erschienen.

Band 1 – 52
Fertigungstechnik – Erlangen
ISSN 1431-6226
Carl Hanser Verlag, München

Band 53 – 307
Fertigungstechnik – Erlangen
ISSN 1431-6226
Meisenbach Verlag, Bamberg

ab Band 308
FAU Studien aus dem Maschinenbau
ISSN 2625-9974
FAU University Press, Erlangen

Die Zugehörigkeit zu den jeweiligen Lehrstühlen ist wie folgt gekennzeichnet:

Lehrstühle:

FAPS	Lehrstuhl für Fertigungsautomatisierung und Produktionssystematik
FMT	Lehrstuhl für Fertigungsmesstechnik
KTmfk	Lehrstuhl für Konstruktionstechnik
LFT	Lehrstuhl für Fertigungstechnologie
LPT	Lehrstuhl für Photonische Technologien
REP	Lehrstuhl für Ressourcen- und Energieeffiziente Produktionsmaschinen

Band 1: Andreas Hemberger
Innovationspotentiale in der rechnerintegrierten Produktion durch wissensbasierte Systeme
FAPS, 208 Seiten, 107 Bilder. 1988.
ISBN 3-446-15234-2.

Band 2: Detlef Classe
Beitrag zur Steigerung der Flexibilität automatisierter Montagesysteme durch Sensorintegration und erweiterte Steuerungskonzepte
FAPS, 194 Seiten, 70 Bilder. 1988.
ISBN 3-446-15529-5.

Band 3: Friedrich-Wilhelm Nolting
Projektierung von Montagesystemen
FAPS, 201 Seiten, 107 Bilder, 1 Tab. 1989.
ISBN 3-446-15541-4.

Band 4: Karsten Schlüter
Nutzungsgradsteigerung von Montagesystemen durch den Einsatz der Simulationstechnik
FAPS, 177 Seiten, 97 Bilder. 1989.
ISBN 3-446-15542-2.

Band 5: Shir-Kuan Lin
Aufbau von Modellen zur Lageregelung von Industrierobotern
FAPS, 168 Seiten, 46 Bilder. 1989.
ISBN 3-446-15546-5.

Band 6: Rudolf Nuss
Untersuchungen zur Bearbeitungsqualität im Fertigungssystem Laserstrahlschneiden
LFT, 206 Seiten, 115 Bilder, 6 Tab. 1989.
ISBN 3-446-15783-2.

Band 7: Wolfgang Scholz
Modell zur datenbankgestützten Planung automatisierter Montageanlagen
FAPS, 194 Seiten, 89 Bilder. 1989.
ISBN 3-446-15825-1.

Band 8: Hans-Jürgen Wißmeier
Beitrag zur Beurteilung des Bruchverhaltens von Hartmetall-Fließpreßmatrizen
LFT, 179 Seiten, 99 Bilder, 9 Tab. 1989.
ISBN 3-446-15921-5.

Band 9: Rainer Eisele
Konzeption und Wirtschaftlichkeit von Planungssystemen in der Produktion
FAPS, 183 Seiten, 86 Bilder. 1990.
ISBN 3-446-16107-4.

Band 10: Rolf Pfeiffer
Technologisch orientierte Montageplanung am Beispiel der Schraubtechnik
FAPS, 216 Seiten, 102 Bilder, 16 Tab. 1990.
ISBN 3-446-16161-9.

Band 11: Herbert Fischer
Verteilte Planungssysteme zur Flexibilitätssteigerung der rechnerintegrierten Teilefertigung
FAPS, 201 Seiten, 82 Bilder. 1990.
ISBN 3-446-16105-8.

Band 12: Gerhard Kleineidam
CAD/CAP: Rechnergestützte Montagefeinplanung
FAPS, 203 Seiten, 107 Bilder. 1990.
ISBN 3-446-16112-0.

Band 13: Frank Vollertsen
Pulvermetallurgische Verarbeitung eines übereutektoiden verschleißfesten Stahls
LFT, XIII u. 217 Seiten, 67 Bilder, 34 Tab. 1990. ISBN 3-446-16133-3.

Band 14: Stephan Biermann
Untersuchungen zur Anlagen- und Prozeßdiagnostik für das Schneiden mit CO_2-Hochleistungslasern
LFT, VIII u. 170 Seiten, 93 Bilder, 4 Tab. 1991. ISBN 3-446-16269-0.

Band 15: Uwe Geißler
Material- und Datenfluß in einer flexiblen Blechbearbeitungszelle
LFT, 124 Seiten, 41 Bilder, 7 Tab. 1991.
ISBN 3-446-16358-1.

Band 16: Frank Oswald Hake
Entwicklung eines rechnergestützten Diagnosesystems für automatisierte Montagezellen
FAPS, XIV u. 166 Seiten, 77 Bilder. 1991.
ISBN 3-446-16428-6.

Band 17: Herbert Reichel
Optimierung der Werkzeugbereitstellung durch rechnergestützte Arbeitsfolgenbestimmung
FAPS, 198 Seiten, 73 Bilder, 2 Tab. 1991.
ISBN 3-446-16453-7.

Band 18: Josef Scheller
Modellierung und Einsatz von Softwaresystemen für rechnergeführte Montagezellen
FAPS, 198 Seiten, 65 Bilder. 1991.
ISBN 3-446-16454-5.

Band 19: Arnold vom Ende
Untersuchungen zum Biegeumforme mit elastischer Matrize
LFT, 166 Seiten, 55 Bilder, 13 Tab. 1991.
ISBN 3-446-16493-6.

Band 20: Joachim Schmid
Beitrag zum automatisierten Bearbeiten von Keramikguß mit Industrierobotern
FAPS, XIV u. 176 Seiten, 111 Bilder, 6 Tab. 1991. ISBN 3-446-16560-6.

Band 21: Egon Sommer
Multiprozessorsteuerung für kooperierende Industrieroboter in Montagezellen
FAPS, 188 Seiten, 102 Bilder. 1991.
ISBN 3-446-17062-6.

Band 22: Georg Geyer
Entwicklung problemspezifischer Verfahrensketten in der Montage
FAPS, 192 Seiten, 112 Bilder. 1991.
ISBN 3-446-16552-5.

Band 23: Rainer Flohr
Beitrag zur optimalen Verbindungstechnik in der Oberflächenmontage (SMT)
FAPS, 186 Seiten, 79 Bilder. 1991.
ISBN 3-446-16568-1.

Band 24: Alfons Rief
Untersuchungen zur Verfahrensfolge Laserstrahlschneiden und -schweißen in der Rohkarosseriefertigung
LFT, VI u. 145 Seiten, 58 Bilder, 5 Tab. 1991. ISBN 3-446-16593-2.

Band 25: Christoph Thim
Rechnerunterstützte Optimierung von Materialflußstrukturen in der Elektronikmontage durch Simulation
FAPS, 188 Seiten, 74 Bilder. 1992.
ISBN 3-446-17118-5.

Band 26: Roland Müller
CO_2 -Laserstrahlschneiden von kurzglasverstärkten Verbundwerkstoffen
LFT, 141 Seiten, 107 Bilder, 4 Tab. 1992.
ISBN 3-446-17104-5.

Band 27: Günther Schäfer
Integrierte Informationsverarbeitung bei der Montageplanung
FAPS, 195 Seiten, 76 Bilder. 1992.
ISBN 3-446-17117-7.

Band 28: Martin Hoffmann
Entwicklung einer CAD/CAM-Prozeßkette für die Herstellung von Blechbiegeteilen
LFT, 149 Seiten, 89 Bilder. 1992.
ISBN 3-446-17154-1.

Band 29: Peter Hoffmann
Verfahrensfolge Laserstrahlschneiden und –schweißen: Prozeßführung und Systemtechnik in der 3D-Laserstrahlbearbeitung von Blechformteilen
LFT, 186 Seiten, 92 Bilder, 10 Tab. 1992.
ISBN 3-446-17153-3.

Band 30: Olaf Schrödel
Flexible Werkstattsteuerung mit objektorientierten Softwarestrukturen
FAPS, 180 Seiten, 84 Bilder. 1992.
ISBN 3-446-17242-4.

Band 31: Hubert Reinisch
Planungs- und Steuerungswerkzeuge zur impliziten Geräteprogrammierung in Roboterzellen
FAPS, XI u. 212 Seiten, 112 Bilder. 1992.
ISBN 3-446-17380-3.

Band 32: Brigitte Bärnreuther
Ein Beitrag zur Bewertung des Kommunikationsverhaltens von Automatisierungsgeräten in flexiblen Produktionszellen
FAPS, XI u. 179 Seiten, 71 Bilder. 1992.
ISBN 3-446-17451-6.

Band 33: Joachim Hutfless
Laserstrahlregelung und Optikdiagnostik in der Strahlführung einer CO_2-Hochleistungslaseranlage
LFT, 175 Seiten, 70 Bilder, 17 Tab. 1993.
ISBN 3-446-17532-6.

Band 34: Uwe Günzel
Entwicklung und Einsatz eines Simulationsverfahrens für operative und strategische Probleme der Produktionsplanung und –steuerung
FAPS, XIV u. 170 Seiten, 66 Bilder, 5 Tab. 1993. ISBN 3-446-17604-7.

Band 35: Bertram Ehmann
Operatives Fertigungscontrolling durch Optimierung auftragsbezogener Bearbeitungsabläufe in der Elektronikfertigung
FAPS, XV u. 167 Seiten, 114 Bilder. 1993.
ISBN 3-446-17658-6.

Band 36: Harald Kolléra
Entwicklung eines benutzerorientierten Werkstattprogrammiersystems für das Laserstrahlschneiden
LFT, 129 Seiten, 66 Bilder, 1 Tab. 1993.
ISBN 3-446-17719-1.

Band 37: Stephanie Abels
Modellierung und Optimierung von Montageanlagen in einem integrierten Simulationssystem
FAPS, 188 Seiten, 88 Bilder. 1993.
ISBN 3-446-17731-0.

Band 38: Robert Schmidt-Hebbel
Laserstrahlbohren durchflußbestimmender Durchgangslöcher
LFT, 145 Seiten, 63 Bilder, 11 Tab. 1993.
ISBN 3-446-17778-7.

Band 39: Norbert Lutz
Oberflächenfeinbearbeitung keramischer Werkstoffe mit XeCl-Excimerlaserstrahlung
LFT, 187 Seiten, 98 Bilder, 29 Tab. 1994.
ISBN 3-446-17970-4.

Band 40: Konrad Grampp
Rechnerunterstützung bei Test und Schulung an Steuerungssoftware von SMD-Bestücklinien
FAPS, 178 Seiten, 88 Bilder. 1995.
ISBN 3-446-18173-3.

Band 41: Martin Koch
Wissensbasierte Unterstützung der Angebotsbearbeitung in der Investitionsgüterindustrie
FAPS, 169 Seiten, 68 Bilder. 1995.
ISBN 3-446-18174-1.

Band 42: Armin Gropp
Anlagen- und Prozeßdiagnostik beim Schneiden mit einem gepulsten Nd:YAG-Laser
LFT, 160 Seiten, 88 Bilder, 7 Tab. 1995.
ISBN 3-446-18241-1.

Band 43: Werner Heckel
Optische 3D-Konturerfassung und on-line Biegewinkelmessung mit dem Lichtschnittverfahren
LFT, 149 Seiten, 43 Bilder, 11 Tab. 1995.
ISBN 3-446-18243-8.

Band 44: Armin Rothhaupt
Modulares Planungssystem zur Optimierung der Elektronikfertigung
FAPS, 180 Seiten, 101 Bilder. 1995.
ISBN 3-446-18307-8.

Band 45: Bernd Zöllner
Adaptive Diagnose in der Elektronikproduktion
FAPS, 195 Seiten, 74 Bilder, 3 Tab. 1995.
ISBN 3-446-18308-6.

Band 46: Bodo Vormann
Beitrag zur automatisierten Handhabungsplanung komplexer Blechbiegeteile
LFT, 126 Seiten, 89 Bilder, 3 Tab. 1995.
ISBN 3-446-18345-0.

Band 47: Peter Schnepf
Zielkostenorientierte Montageplanung
FAPS, 144 Seiten, 75 Bilder. 1995.
ISBN 3-446-18397-3.

Band 48: Rainer Klotzbücher
Konzept zur rechnerintegrierten Materialversorgung in flexiblen Fertigungssystemen
FAPS, 156 Seiten, 62 Bilder. 1995.
ISBN 3-446-18412-0.

Band 49: Wolfgang Greska
Wissensbasierte Analyse und Klassifizierung von Blechteilen
LFT, 144 Seiten, 96 Bilder. 1995.
ISBN 3-446-18462-7.

Band 50: Jörg Franke
Integrierte Entwicklung neuer Produkt- und Produktionstechnologien für räumliche spritzgegossene Schaltungsträger (3-D MID)
FAPS, 196 Seiten, 86 Bilder, 4 Tab. 1995.
ISBN 3-446-18448-1.

Band 51: Franz-Josef Zeller
Sensorplanung und schnelle Sensorregelung für Industrieroboter
FAPS, 190 Seiten, 102 Bilder, 9 Tab. 1995.
ISBN 3-446-18601-8.

Band 52: Michael Solvie
Zeitbehandlung und Multimedia-Unterstützung in Feldkommunikationssystemen
FAPS, 200 Seiten, 87 Bilder, 35 Tab. 1996.
ISBN 3-446-18607-7.

Band 53: Robert Hopperdietzel
Reengineering in der Elektro- und Elektronikindustrie
FAPS, 180 Seiten, 109 Bilder, 1 Tab. 1996.
ISBN 3-87525-070-2.

Band 54: Thomas Rebhahn
Beitrag zur Mikromaterialbearbeitung mit Excimerlasern - Systemkomponenten und Verfahrensoptimierungen
LFT, 148 Seiten, 61 Bilder, 10 Tab. 1996.
ISBN 3-87525-075-3.

Band 55: Henning Hanebuth
Laserstrahlhartlöten mit Zweistrahltechnik
LFT, 157 Seiten, 58 Bilder, 11 Tab. 1996.
ISBN 3-87525-074-5.

Band 56: Uwe Schönherr
Steuerung und Sensordatenintegration für flexible Fertigungszellen mit kooperierenden Robotern
FAPS, 188 Seiten, 116 Bilder, 3 Tab. 1996.
ISBN 3-87525-076-1.

Band 57: Stefan Holzer
Berührungslose Formgebung mit Laserstrahlung
LFT, 162 Seiten, 69 Bilder, 11 Tab. 1996.
ISBN 3-87525-079-6.

Band 58: Markus Schultz
Fertigungsqualität beim 3D-Laserstrahlschweißen von Blechformteilen
LFT, 165 Seiten, 88 Bilder, 9 Tab. 1997.
ISBN 3-87525-080-X.

Band 59: Thomas Krebs
Integration elektromechanischer CA-Anwendungen über einem STEP-Produktmodell
FAPS, 198 Seiten, 58 Bilder, 8 Tab. 1997.
ISBN 3-87525-081-8.

Band 60: Jürgen Sturm
Prozeßintegrierte Qualitätssicherung in der Elektronikproduktion
FAPS, 167 Seiten, 112 Bilder, 5 Tab. 1997.
ISBN 3-87525-082-6.

Band 61: Andreas Brand
Prozesse und Systeme zur Bestückung räumlicher elektronischer Baugruppen (3D-MID)
FAPS, 182 Seiten, 100 Bilder. 1997.
ISBN 3-87525-087-7.

Band 62: Michael Kauf
Regelung der Laserstrahlleistung und der Fokusparameter einer CO_2-Hochleistungslaseranlage
LFT, 140 Seiten, 70 Bilder, 5 Tab. 1997.
ISBN 3-87525-083-4.

Band 63: Peter Steinwasser
Modulares Informationsmanagement in der integrierten Produkt- und Prozeßplanung
FAPS, 190 Seiten, 87 Bilder. 1997.
ISBN 3-87525-084-2.

Band 64: Georg Liedl
Integriertes Automatisierungskonzept für den flexiblen Materialfluß in der Elektronikproduktion
FAPS, 196 Seiten, 96 Bilder, 3 Tab. 1997.
ISBN 3-87525-086-9.

Band 65: Andreas Otto
Transiente Prozesse beim Laserstrahlschweißen
LFT, 132 Seiten, 62 Bilder, 1 Tab. 1997.
ISBN 3-87525-089-3.

Band 66: Wolfgang Blöchl
Erweiterte Informationsbereitstellung an offenen CNC-Steuerungen zur Prozeß- und Programmoptimierung
FAPS, 168 Seiten, 96 Bilder. 1997.
ISBN 3-87525-091-5.

Band 67: Klaus-Uwe Wolf
Verbesserte Prozeßführung und Prozeßplanung zur Leistungs- und Qualitätssteigerung beim Spulenwickeln
FAPS, 186 Seiten, 125 Bilder. 1997.
ISBN 3-87525-092-3.

Band 68: Frank Backes
Technologieorientierte Bahnplanung für die 3D-Laserstrahlbearbeitung
LFT, 138 Seiten, 71 Bilder, 2 Tab. 1997.
ISBN 3-87525-093-1.

Band 69: Jürgen Kraus
Laserstrahlumformen von Profilen
LFT, 137 Seiten, 72 Bilder, 8 Tab. 1997.
ISBN 3-87525-094-X.

Band 70: Norbert Neubauer
Adaptive Strahlführungen für CO_2-Laseranlagen
LFT, 120 Seiten, 50 Bilder, 3 Tab. 1997.
ISBN 3-87525-095-8.

Band 71: Michael Steber
Prozeßoptimierter Betrieb flexibler Schraubstationen in der automatisierten Montage
FAPS, 168 Seiten, 78 Bilder, 3 Tab. 1997.
ISBN 3-87525-096-6.

Band 72: Markus Pfestorf
Funktionale 3D-Oberflächenkenngrößen in der Umformtechnik
LFT, 162 Seiten, 84 Bilder, 15 Tab. 1997.
ISBN 3-87525-097-4.

Band 73: Volker Franke
Integrierte Planung und Konstruktion von Werkzeugen für die Biegebearbeitung
LFT, 143 Seiten, 81 Bilder. 1998.
ISBN 3-87525-098-2.

Band 74: Herbert Scheller
Automatisierte Demontagesysteme und recyclinggerechte Produktgestaltung elektronischer Baugruppen
FAPS, 184 Seiten, 104 Bilder, 17 Tab. 1998.
ISBN 3-87525-099-0.

Band 75: Arthur Meßner
Kaltmassivumformung metallischer Kleinstteile – Werkstoffverhalten, Wirkflächenreibung, Prozeßauslegung
LFT, 164 Seiten, 92 Bilder, 14 Tab. 1998.
ISBN 3-87525-100-8.

Band 76: Mathias Glasmacher
Prozeß- und Systemtechnik zum Laserstrahl-Mikroschweißen
LFT, 184 Seiten, 104 Bilder, 12 Tab. 1998.
ISBN 3-87525-101-6.

Band 77: Michael Schwind
Zerstörungsfreie Ermittlung mechanischer Eigenschaften von Feinblechen mit dem Wirbelstromverfahren
LFT, 124 Seiten, 68 Bilder, 8 Tab. 1998.
ISBN 3-87525-102-4.

Band 78: Manfred Gerhard
Qualitätssteigerung in der Elektronikproduktion durch Optimierung der Prozeßführung beim Löten komplexer Baugruppen
FAPS, 179 Seiten, 113 Bilder, 7 Tab. 1998.
ISBN 3-87525-103-2.

Band 79: Elke Rauh
Methodische Einbindung der Simulation in die betrieblichen Planungs- und Entscheidungsabläufe
FAPS, 192 Seiten, 114 Bilder, 4 Tab. 1998.
ISBN 3-87525-104-0.

Band 80: Sorin Niederkorn
Meßeinrichtung zur Untersuchung der Wirkflächenreibung bei umformtechnischen Prozessen
LFT, 99 Seiten, 46 Bilder, 6 Tab. 1998.
ISBN 3-87525-105-9.

Band 81: Stefan Schuberth
Regelung der Fokuslage beim Schweißen mit CO_2-Hochleistungslasern unter Einsatz von adaptiven Optiken
LFT, 140 Seiten, 64 Bilder, 3 Tab. 1998.
ISBN 3-87525-106-7.

Band 82: Armando Walter Colombo
Development and Implementation of Hierarchical Control Structures of Flexible Production Systems Using High Level Petri Nets
FAPS, 216 Seiten, 86 Bilder. 1998.
ISBN 3-87525-109-1.

Band 83: Otto Meedt
Effizienzsteigerung bei Demontage und Recycling durch flexible Demontagetechnologien und optimierte Produktgestaltung
FAPS, 186 Seiten, 103 Bilder. 1998.
ISBN 3-87525-108-3.

Band 84: Knuth Götz
Modelle und effiziente Modellbildung zur Qualitätssicherung in der Elektronikproduktion
FAPS, 212 Seiten, 129 Bilder, 24 Tab. 1998.
ISBN 3-87525-112-1.

Band 85: Ralf Luchs
Einsatzmöglichkeiten leitender Klebstoffe zur zuverlässigen Kontaktierung elektronischer Bauelemente in der SMT
FAPS, 176 Seiten, 126 Bilder, 30 Tab. 1998.
ISBN 3-87525-113-7.

Band 86: Frank Pöhlau
Entscheidungsgrundlagen zur Einführung räumlicher spritzgegossener Schaltungsträger (3-D MID)
FAPS, 144 Seiten, 99 Bilder. 1999.
ISBN 3-87525-114-8.

Band 87: Roland T. A. Kals
Fundamentals on the miniaturization of sheet metal working processes
LFT, 128 Seiten, 58 Bilder, 11 Tab. 1999.
ISBN 3-87525-115-6.

Band 88: Gerhard Luhn
Implizites Wissen und technisches Handeln am Beispiel der Elektronikproduktion
FAPS, 252 Seiten, 61 Bilder, 1 Tab. 1999.
ISBN 3-87525-116-4.

Band 89: Axel Sprenger
Adaptives Streckbiegen von Aluminium-Strangpreßprofilen
LFT, 114 Seiten, 63 Bilder, 4 Tab. 1999.
ISBN 3-87525-117-2.

Band 90: Hans-Jörg Pucher
Untersuchungen zur Prozeßfolge Umformen, Bestücken und Laserstrahllöten von Mikrokontakten
LFT, 158 Seiten, 69 Bilder, 9 Tab. 1999.
ISBN 3-87525-119-9.

Band 91: Horst Arnet
Profilbiegen mit kinematischer Gestalterzeugung
LFT, 128 Seiten, 67 Bilder, 7 Tab. 1999.
ISBN 3-87525-120-2.

Band 92: Doris Schubart
Prozeßmodellierung und Technologieentwicklung beim Abtragen mit CO_2-Laserstrahlung
LFT, 133 Seiten, 57 Bilder, 13 Tab. 1999.
ISBN 3-87525-122-9.

Band 93: Adrianus L. P. Coremans
Laserstrahlsintern von Metallpulver - Prozeßmodellierung, Systemtechnik, Eigenschaften laserstrahlgesinterter Metallkörper
LFT, 184 Seiten, 108 Bilder, 12 Tab. 1999.
ISBN 3-87525-124-5.

Band 94: Hans-Martin Biehler
Optimierungskonzepte für Qualitätsdatenverarbeitung und Informationsbereitstellung in der Elektronikfertigung
FAPS, 194 Seiten, 105 Bilder. 1999.
ISBN 3-87525-126-1.

Band 95: Wolfgang Becker
Oberflächenausbildung und tribologische Eigenschaften excimerlaserstrahlbearbeiteter Hochleistungskeramiken
LFT, 175 Seiten, 71 Bilder, 3 Tab. 1999.
ISBN 3-87525-127-X.

Band 96: Philipp Hein
Innenhochdruck-Umformen von Blechpaaren: Modellierung, Prozeßauslegung und Prozeßführung
LFT, 129 Seiten, 57 Bilder, 7 Tab. 1999.
ISBN 3-87525-128-8.

Band 97: Gunter Beitinger
Herstellungs- und Prüfverfahren für thermoplastische Schaltungsträger
FAPS, 169 Seiten, 92 Bilder, 20 Tab. 1999.
ISBN 3-87525-129-6.

Band 98: Jürgen Knoblach
Beitrag zur rechnerunterstützten verursachungsgerechten Angebotskalkulation von Blechteilen mit Hilfe wissensbasierter Methoden
LFT, 155 Seiten, 53 Bilder, 26 Tab. 1999.
ISBN 3-87525-130-X.

Band 99: Frank Breitenbach
Bildverarbeitungssystem zur Erfassung der Anschlußgeometrie elektronischer SMT-Bauelemente
LFT, 147 Seiten, 92 Bilder, 12 Tab. 2000.
ISBN 3-87525-131-8.

Band 100: Bernd Falk
Simulationsbasierte Lebensdauervorhersage für Werkzeuge der Kaltmassivumformung
LFT, 134 Seiten, 44 Bilder, 15 Tab. 2000.
ISBN 3-87525-136-9.

Band 101: Wolfgang Schlögl
Integriertes Simulationsdaten-Management für Maschinenentwicklung und Anlagenplanung
FAPS, 169 Seiten, 101 Bilder, 20 Tab. 2000.
ISBN 3-87525-137-7.

Band 102: Christian Hinsel
Ermüdungsbruchversagen hartstoffbeschichteter Werkzeugstähle in der Kaltmassivumformung
LFT, 130 Seiten, 80 Bilder, 14 Tab. 2000.
ISBN 3-87525-138-5.

Band 103: Stefan Bobbert
Simulationsgestützte Prozessauslegung für das Innenhochdruck-Umformen von Blechpaaren
LFT, 123 Seiten, 77 Bilder. 2000.
ISBN 3-87525-145-8.

Band 104: Harald Rottbauer
Modulares Planungswerkzeug zum Produktionsmanagement in der Elektronikproduktion
FAPS, 166 Seiten, 106 Bilder. 2001.
ISBN 3-87525-139-3.

Band 105: Thomas Hennige
Flexible Formgebung von Blechen durch Laserstrahlumformen
LFT, 119 Seiten, 50 Bilder. 2001.
ISBN 3-87525-140-7.

Band 106: Thomas Menzel
Wissensbasierte Methoden für die rechnergestützte Charakterisierung und Bewertung innovativer Fertigungsprozesse
LFT, 152 Seiten, 71 Bilder. 2001.
ISBN 3-87525-142-3.

Band 107: Thomas Stöckel
Kommunikationstechnische Integration der Prozeßebene in Produktionssysteme durch Middleware-Frameworks
FAPS, 147 Seiten, 65 Bilder, 5 Tab. 2001.
ISBN 3-87525-143-1.

Band 108: Frank Pitter
Verfügbarkeitssteigerung von Werkzeugmaschinen durch Einsatz mechatronischer Sensorlösungen
FAPS, 158 Seiten, 131 Bilder, 8 Tab. 2001.
ISBN 3-87525-144-X.

Band 109: Markus Korneli
Integration lokaler CAP-Systeme in einen globalen Fertigungsdatenverbund
FAPS, 121 Seiten, 53 Bilder, 11 Tab. 2001.
ISBN 3-87525-146-6.

Band 110: Burkhard Müller
Laserstrahljustieren mit Excimer-Lasern - Prozeßparameter und Modelle zur Aktorkonstruktion
LFT, 128 Seiten, 36 Bilder, 9 Tab. 2001.
ISBN 3-87525-159-8.

Band 111: Jürgen Göhringer
Integrierte Telediagnose via Internet zum effizienten Service von Produktionssystemen
FAPS, 178 Seiten, 98 Bilder, 5 Tab. 2001.
ISBN 3-87525-147-4.

Band 112: Robert Feuerstein
Qualitäts- und kosteneffiziente Integration neuer Bauelementetechnologien in die Flachbaugruppenfertigung
FAPS, 161 Seiten, 99 Bilder, 10 Tab. 2001.
ISBN 3-87525-151-2.

Band 113: Marcus Reichenberger
Eigenschaften und Einsatzmöglichkeiten alternativer Elektroniklote in der Oberflächenmontage (SMT)
FAPS, 165 Seiten, 97 Bilder, 18 Tab. 2001.
ISBN 3-87525-152-0.

Band 114: Alexander Huber
Justieren vormontierter Systeme mit dem Nd:YAG-Laser unter Einsatz von Aktoren
LFT, 122 Seiten, 58 Bilder, 5 Tab. 2001.
ISBN 3-87525-153-9.

Band 115: Sami Krimi
Analyse und Optimierung von Montagesystemen in der Elektronikproduktion
FAPS, 155 Seiten, 88 Bilder, 3 Tab. 2001.
ISBN 3-87525-157-1.

Band 116: Marion Merklein
Laserstrahlumformen von Aluminiumwerkstoffen - Beeinflussung der Mikrostruktur und der mechanischen Eigenschaften
LFT, 122 Seiten, 65 Bilder, 15 Tab. 2001.
ISBN 3-87525-156-3.

Band 117: Thomas Collisi
Ein informationslogistisches Architekturkonzept zur Akquisition simulationsrelevanter Daten
FAPS, 181 Seiten, 105 Bilder, 7 Tab. 2002.
ISBN 3-87525-164-4.

Band 118: Markus Koch
Rationalisierung und ergonomische Optimierung im Innenausbau durch den Einsatz moderner Automatisierungstechnik
FAPS, 176 Seiten, 98 Bilder, 9 Tab. 2002.
ISBN 3-87525-165-2.

Band 119: Michael Schmidt
Prozeßregelung für das Laserstrahl-Punktschweißen in der Elektronikproduktion
LFT, 152 Seiten, 71 Bilder, 3 Tab. 2002.
ISBN 3-87525-166-0.

Band 120: Nicolas Tiesler
Grundlegende Untersuchungen zum Fließpressen metallischer Kleinstteile
LFT, 126 Seiten, 78 Bilder, 12 Tab. 2002.
ISBN 3-87525-175-X.

Band 121: Lars Pursche
Methoden zur technologieorientierten Programmierung für die 3D-Lasermikrobearbeitung
LFT, 111 Seiten, 39 Bilder, 0 Tab. 2002.
ISBN 3-87525-183-0.

Band 122: Jan-Oliver Brassel
Prozeßkontrolle beim Laserstrahl-Mikroschweißen
LFT, 148 Seiten, 72 Bilder, 12 Tab. 2002.
ISBN 3-87525-181-4.

Band 123: Mark Geisel
Prozeßkontrolle und -steuerung beim Laserstrahlschweißen mit den Methoden der nichtlinearen Dynamik
LFT, 135 Seiten, 46 Bilder, 2 Tab. 2002.
ISBN 3-87525-180-6.

Band 124: Gerd Eßer
Laserstrahlunterstützte Erzeugung metallischer Leiterstrukturen auf Thermoplastsubstraten für die MID-Technik
LFT, 148 Seiten, 60 Bilder, 6 Tab. 2002.
ISBN 3-87525-171-7.

Band 125: Marc Fleckenstein
Qualität laserstrahl-gefügter Mikroverbindungen elektronischer Kontakte
LFT, 159 Seiten, 77 Bilder, 7 Tab. 2002.
ISBN 3-87525-170-9.

Band 126: Stefan Kaufmann
Grundlegende Untersuchungen zum Nd:YAG- Laserstrahlfügen von Silizium für Komponenten der Optoelektronik
LFT, 159 Seiten, 100 Bilder, 6 Tab. 2002.
ISBN 3-87525-172-5.

Band 127: Thomas Fröhlich
Simultanes Löten von Anschlußkontakten elektronischer Bauelemente mit Diodenlaserstrahlung
LFT, 143 Seiten, 75 Bilder, 6 Tab. 2002.
ISBN 3-87525-186-5.

Band 128: Achim Hofmann
Erweiterung der Formgebungsgrenzen beim Umformen von Aluminiumwerkstoffen durch den Einsatz prozessangepasster Platinen
LFT, 113 Seiten, 58 Bilder, 4 Tab. 2002.
ISBN 3-87525-182-2.

Band 129: Ingo Kriebitzsch
3 - D MID Technologie in der Automobilelektronik
FAPS, 129 Seiten, 102 Bilder, 10 Tab. 2002.
ISBN 3-87525-169-5.

Band 130: Thomas Pohl
Fertigungsqualität und Umformbarkeit laserstrahlgeschweißter Formplatinen aus Aluminiumlegierungen
LFT, 133 Seiten, 93 Bilder, 12 Tab. 2002.
ISBN 3-87525-173-3.

Band 131: Matthias Wenk
Entwicklung eines konfigurierbaren Steuerungssystems für die flexible Sensorführung von Industrierobotern
FAPS, 167 Seiten, 85 Bilder, 1 Tab. 2002.
ISBN 3-87525-174-1.

Band 132: Matthias Negendanck
Neue Sensorik und Aktorik für Bearbeitungsköpfe zum Laserstrahlschweißen
LFT, 116 Seiten, 60 Bilder, 14 Tab. 2002.
ISBN 3-87525-184-9.

Band 133: Oliver Kreis
Integrierte Fertigung - Verfahrensintegration durch Innenhochdruck-Umformen, Trennen und Laserstrahlschweißen in einem Werkzeug sowie ihre tele- und multimediale Präsentation
LFT, 167 Seiten, 90 Bilder, 43 Tab. 2002.
ISBN 3-87525-176-8.

Band 134: Stefan Trautner
Technische Umsetzung produktbezogener Instrumente der Umweltpolitik bei Elektro- und Elektronikgeräten
FAPS, 179 Seiten, 92 Bilder, 11 Tab. 2002.
ISBN 3-87525-177-6.

Band 135: Roland Meier
Strategien für einen produktorientierten Einsatz räumlicher spritzgegossener Schaltungsträger (3-D MID)
FAPS, 155 Seiten, 88 Bilder, 14 Tab. 2002.
ISBN 3-87525-178-4.

Band 136: Jürgen Wunderlich
Kostensimulation - Simulationsbasierte Wirtschaftlichkeitsregelung komplexer Produktionssysteme
FAPS, 202 Seiten, 119 Bilder, 17 Tab. 2002.
ISBN 3-87525-179-2.

Band 137: Stefan Novotny
Innenhochdruck-Umformen von Blechen aus Aluminium- und Magnesiumlegierungen bei erhöhter Temperatur
LFT, 132 Seiten, 82 Bilder, 6 Tab. 2002.
ISBN 3-87525-185-7.

Band 138: Andreas Licha
Flexible Montageautomatisierung zur Komplettmontage flächenhafter Produktstrukturen durch kooperierende Industrieroboter
FAPS, 158 Seiten, 87 Bilder, 8 Tab. 2003.
ISBN 3-87525-189-X.

Band 139: Michael Eisenbarth
Beitrag zur Optimierung der Aufbau- und Verbindungstechnik für mechatronische Baugruppen
FAPS, 207 Seiten, 141 Bilder, 9 Tab. 2003.
ISBN 3-87525-190-3.

Band 140: Frank Christoph
Durchgängige simulationsgestützte Planung von Fertigungseinrichtungen der Elektronikproduktion
FAPS, 187 Seiten, 107 Bilder, 9 Tab. 2003.
ISBN 3-87525-191-1.

Band 141: Hinnerk Hagenah
Simulationsbasierte Bestimmung der zu erwartenden Maßhaltigkeit für das Blechbiegen
LFT, 131 Seiten, 36 Bilder, 26 Tab. 2003.
ISBN 3-87525-192-X.

Band 142: Ralf Eckstein
Scherschneiden und Biegen metallischer Kleinstteile - Materialeinfluss und Materialverhalten
LFT, 148 Seiten, 71 Bilder, 19 Tab. 2003.
ISBN 3-87525-193-8.

Band 143: Frank H. Meyer-Pittroff
Excimerlaserstrahlbiegen dünner metallischer Folien mit homogener Lichtlinie
LFT, 138 Seiten, 60 Bilder, 16 Tab. 2003.
ISBN 3-87525-196-2.

Band 144: Andreas Kach
Rechnergestützte Anpassung von Laserstrahlschneidbahnen an Bauteilabweichungen
LFT, 139 Seiten, 69 Bilder, 11 Tab. 2004.
ISBN 3-87525-197-0.

Band 145: Stefan Hierl
System- und Prozeßtechnik für das simultane Löten mit Diodenlaserstrahlung von elektronischen Bauelementen
LFT, 124 Seiten, 66 Bilder, 4 Tab. 2004.
ISBN 3-87525-198-9.

Band 146: Thomas Neudecker
Tribologische Eigenschaften keramischer Blechumformwerkzeuge- Einfluss einer Oberflächenendbearbeitung mittels Excimerlaserstrahlung
LFT, 166 Seiten, 75 Bilder, 26 Tab. 2004.
ISBN 3-87525-200-4.

Band 147: Ulrich Wenger
Prozessoptimierung in der Wickeltechnik durch innovative maschinenbauliche und regelungstechnische Ansätze
FAPS, 132 Seiten, 88 Bilder, 0 Tab. 2004.
ISBN 3-87525-203-9.

Band 148: Stefan Slama
Effizienzsteigerung in der Montage durch marktorientierte Montagestrukturen und erweiterte Mitarbeiterkompetenz
FAPS, 188 Seiten, 125 Bilder, 0 Tab. 2004.
ISBN 3-87525-204-7.

Band 149: Thomas Wurm
Laserstrahljustieren mittels Aktoren-Entwicklung von Konzepten und Methoden für die rechnerunterstützte Modellierung und Optimierung von komplexen Aktorsystemen in der Mikrotechnik
LFT, 122 Seiten, 51 Bilder, 9 Tab. 2004.
ISBN 3-87525-206-3.

Band 150: Martino Celeghini
Wirkmedienbasierte Blechumformung: Grundlagenuntersuchungen zum Einfluss von Werkstoff und Bauteilgeometrie
LFT, 146 Seiten, 77 Bilder, 6 Tab. 2004.
ISBN 3-87525-207-1.

Band 151: Ralph Hohenstein
Entwurf hochdynamischer Sensor- und Regelsysteme für die adaptive Laserbearbeitung
LFT, 282 Seiten, 63 Bilder, 16 Tab. 2004.
ISBN 3-87525-210-1.

Band 152: Angelika Hutterer
Entwicklung prozessüberwachender Regelkreise für flexible Formgebungsprozesse
LFT, 149 Seiten, 57 Bilder, 2 Tab. 2005.
ISBN 3-87525-212-8.

Band 153: Emil Egerer
Massivumformen metallischer Kleinstteile bei erhöhter Prozesstemperatur
LFT, 158 Seiten, 87 Bilder, 10 Tab. 2005.
ISBN 3-87525-213-6.

Band 154: Rüdiger Holzmann
Strategien zur nachhaltigen Optimierung von Qualität und Zuverlässigkeit in der Fertigung hochintegrierter Flachbaugruppen
FAPS, 186 Seiten, 99 Bilder, 19 Tab. 2005.
ISBN 3-87525-217-9.

Band 155: Marco Nock
Biegeumformen mit Elastomerwerkzeugen Modellierung, Prozessauslegung und Abgrenzung des Verfahrens am Beispiel des Rohrbiegens
LFT, 164 Seiten, 85 Bilder, 13 Tab. 2005.
ISBN 3-87525-218-7.

Band 156: Frank Niebling
Qualifizierung einer Prozesskette zum Laserstrahlsintern metallischer Bauteile
LFT, 148 Seiten, 89 Bilder, 3 Tab. 2005.
ISBN 3-87525-219-5.

Band 157: Markus Meiler
Großserientauglichkeit trockenschmierstoffbeschichteter Aluminiumbleche im Presswerk Grundlegende Untersuchungen zur Tribologie, zum Umformverhalten und Bauteilversuche
LFT, 104 Seiten, 57 Bilder, 21 Tab. 2005.
ISBN 3-87525-221-7.

Band 158: Agus Sutanto
Solution Approaches for Planning of Assembly Systems in Three-Dimensional Virtual Environments
FAPS, 169 Seiten, 98 Bilder, 3 Tab. 2005.
ISBN 3-87525-220-9.

Band 159: Matthias Boiger
Hochleistungssysteme für die Fertigung elektronischer Baugruppen auf der Basis flexibler Schaltungsträger
FAPS, 175 Seiten, 111 Bilder, 8 Tab. 2005.
ISBN 3-87525-222-5.

Band 160: Matthias Pitz
Laserunterstütztes Biegen höchstfester Mehrphasenstähle
LFT, 120 Seiten, 73 Bilder, 11 Tab. 2005.
ISBN 3-87525-223-3.

Band 161: Meik Vahl
Beitrag zur gezielten Beeinflussung des Werkstoffflusses beim Innenhochdruck-Umformen von Blechen
LFT, 165 Seiten, 94 Bilder, 15 Tab. 2005.
ISBN 3-87525-224-1.

Band 162: Peter K. Kraus
Plattformstrategien - Realisierung einer varianz- und kostenoptimierten Wertschöpfung
FAPS, 181 Seiten, 95 Bilder, 0 Tab. 2005.
ISBN 3-87525-226-8.

Band 163: Adrienn Cser
Laserstrahlschmelzabtrag - Prozessanalyse und -modellierung
LFT, 146 Seiten, 79 Bilder, 3 Tab. 2005.
ISBN 3-87525-227-6.

Band 164: Markus C. Hahn
Grundlegende Untersuchungen zur Herstellung von Leichtbauverbundstrukturen mit Aluminiumschaumkern
LFT, 143 Seiten, 60 Bilder, 16 Tab. 2005.
ISBN 3-87525-228-4.

Band 165: Gordana Michos
Mechatronische Ansätze zur Optimierung von Vorschubachsen
FAPS, 146 Seiten, 87 Bilder, 17 Tab. 2005.
ISBN 3-87525-230-6.

Band 166: Markus Stark
Auslegung und Fertigung hochpräziser Faser-Kollimator-Arrays
LFT, 158 Seiten, 115 Bilder, 11 Tab. 2005.
ISBN 3-87525-231-4.

Band 167: Yurong Zhou
Kollaboratives Engineering Management in der integrierten virtuellen Entwicklung der Anlagen für die Elektronikproduktion
FAPS, 156 Seiten, 84 Bilder, 6 Tab. 2005.
ISBN 3-87525-232-2.

Band 168: Werner Enser
Neue Formen permanenter und lösbarer elektrischer Kontaktierungen für mechatronische Baugruppen
FAPS, 190 Seiten, 112 Bilder, 5 Tab. 2005.
ISBN 3-87525-233-0.

Band 169: Katrin Melzer
Integrierte Produktpolitik bei elektrischen und elektronischen Geräten zur Optimierung des Product-Life-Cycle
FAPS, 155 Seiten, 91 Bilder, 17 Tab. 2005.
ISBN 3-87525-234-9.

Band 170: Alexander Putz
Grundlegende Untersuchungen zur Erfassung der realen Vorspannung von armierten Kaltfließpresswerkzeugen mittels Ultraschall
LFT, 137 Seiten, 71 Bilder, 15 Tab. 2006.
ISBN 3-87525-237-3.

Band 171: Martin Prechtl
Automatisiertes Schichtverfahren für metallische Folien - System- und Prozesstechnik
LFT, 154 Seiten, 45 Bilder, 7 Tab. 2006.
ISBN 3-87525-238-1.

Band 172: Markus Meidert
Beitrag zur deterministischen Lebensdauerabschätzung von Werkzeugen der Kaltmassivumformung
LFT, 131 Seiten, 78 Bilder, 9 Tab. 2006.
ISBN 3-87525-239-X.

Band 173: Bernd Müller
Robuste, automatisierte Montagesysteme durch adaptive Prozessführung und montageübergreifende Fehlerprävention am Beispiel flächiger Leichtbauteile
FAPS, 147 Seiten, 77 Bilder, 0 Tab. 2006.
ISBN 3-87525-240-3.

Band 174: Alexander Hofmann
Hybrides Laserdurchstrahlschweißen von Kunststoffen
LFT, 136 Seiten, 72 Bilder, 4 Tab. 2006.
ISBN 978-3-87525-243-9.

Band 175: Peter Wölflick
Innovative Substrate und Prozesse mit feinsten Strukturen für bleifreie Mechatronik-Anwendungen
FAPS, 177 Seiten, 148 Bilder, 24 Tab. 2006.
ISBN 978-3-87525-246-0.

Band 176: Attila Komlodi
Detection and Prevention of Hot Cracks during Laser Welding of Aluminium Alloys Using Advanced Simulation Methods
LFT, 155 Seiten, 89 Bilder, 14 Tab. 2006.
ISBN 978-3-87525-248-4.

Band 177: Uwe Popp
Grundlegende Untersuchungen zum Laserstrahlstrukturieren von Kaltmassivumformwerkzeugen
LFT, 140 Seiten, 67 Bilder, 16 Tab. 2006.
ISBN 978-3-87525-249-1.

Band 178: Veit Rückel
Rechnergestützte Ablaufplanung und Bahngenerierung Für kooperierende Industrieroboter
FAPS, 148 Seiten, 75 Bilder, 7 Tab. 2006.
ISBN 978-3-87525-250-7.

Band 179: Manfred Dirscherl
Nicht-thermische Mikrojustiertechnik mittels ultrakurzer Laserpulse
LFT, 154 Seiten, 69 Bilder, 10 Tab. 2007.
ISBN 978-3-87525-251-4.

Band 180: Yong Zhuo
Entwurf eines rechnergestützten integrierten Systems für Konstruktion und Fertigungsplanung räumlicher spritzgegossener Schaltungsträger (3D-MID)
FAPS, 181 Seiten, 95 Bilder, 5 Tab. 2007.
ISBN 978-3-87525-253-8.

Band 181: Stefan Lang
Durchgängige Mitarbeiterinformation zur Steigerung von Effizienz und Prozesssicherheit in der Produktion
FAPS, 172 Seiten, 93 Bilder. 2007.
ISBN 978-3-87525-257-6.

Band 182: Hans-Joachim Krauß
Laserstrahlinduzierte Pyrolyse präkeramischer Polymere
LFT, 171 Seiten, 100 Bilder. 2007.
ISBN 978-3-87525-258-3.

Band 183: Stefan Junker
Technologien und Systemlösungen für die flexibel automatisierte Bestückung permanent erregter Läufer mit oberflächenmontierten Dauermagneten
FAPS, 173 Seiten, 75 Bilder. 2007.
ISBN 978-3-87525-259-0.

Band 184: Rainer Kohlbauer
Wissensbasierte Methoden für die simulationsgestützte Auslegung wirkmedienbasierter Blechumformprozesse
LFT, 135 Seiten, 50 Bilder. 2007.
ISBN 978-3-87525-260-6.

Band 185: Klaus Lamprecht
Wirkmedienbasierte Umformung tiefgezogener Vorformen unter besonderer Berücksichtigung maßgeschneiderter Halbzeuge
LFT, 137 Seiten, 81 Bilder. 2007.
ISBN 978-3-87525-265-1.

Band 186: Bernd Zolleiß
Optimierte Prozesse und Systeme für die Bestückung mechatronischer Baugruppen
FAPS, 180 Seiten, 117 Bilder. 2007.
ISBN 978-3-87525-266-8.

Band 187: Michael Kerausch
Simulationsgestützte Prozessauslegung für das Umformen lokal wärmebehandelter Aluminiumplatinen
LFT, 146 Seiten, 76 Bilder, 7 Tab. 2007.
ISBN 978-3-87525-267-5.

Band 188: Matthias Weber
Unterstützung der Wandlungsfähigkeit von Produktionsanlagen durch innovative Softwaresysteme
FAPS, 183 Seiten, 122 Bilder, 3 Tab. 2007.
ISBN 978-3-87525-269-9.

Band 189: Thomas Frick
Untersuchung der prozessbestimmenden Strahl-Stoff-Wechselwirkungen beim Laserstrahlschweißen von Kunststoffen
LFT, 104 Seiten, 62 Bilder, 8 Tab. 2007.
ISBN 978-3-87525-268-2.

Band 190: Joachim Hecht
Werkstoffcharakterisierung und Prozessauslegung für die wirkmedienbasierte Doppelblech-Umformung von Magnesiumlegierungen
LFT, 107 Seiten, 91 Bilder, 2 Tab. 2007.
ISBN 978-3-87525-270-5.

Band 191: Ralf Völkl
Stochastische Simulation zur Werkzeuglebensdaueroptimierung und Präzisionsfertigung in der Kaltmassivumformung
LFT, 178 Seiten, 75 Bilder, 12 Tab. 2008.
ISBN 978-3-87525-272-9.

Band 192: Massimo Tolazzi
Innenhochdruck-Umformen verstärkter Blech-Rahmenstrukturen
LFT, 164 Seiten, 85 Bilder, 7 Tab. 2008.
ISBN 978-3-87525-273-6.

Band 193: Cornelia Hoff
Untersuchung der Prozesseinflussgrößen beim Presshärten des höchstfesten Vergütungsstahls 22MnB5
LFT, 133 Seiten, 92 Bilder, 5 Tab. 2008.
ISBN 978-3-87525-275-0.

Band 194: Christian Alvarez
Simulationsgestützte Methoden zur effizienten Gestaltung von Lötprozessen in der Elektronikproduktion
FAPS, 149 Seiten, 86 Bilder, 8 Tab. 2008.
ISBN 978-3-87525-277-4.

Band 195: Andreas Kunze
Automatisierte Montage von makromechatronischen Modulen zur flexiblen Integration in hybride Pkw-Bordnetzsysteme
FAPS, 160 Seiten, 90 Bilder, 14 Tab. 2008.
ISBN 978-3-87525-278-1.

Band 196: Wolfgang Hußnätter
Grundlegende Untersuchungen zur experimentellen Ermittlung und zur Modellierung von Fließortkurven bei erhöhten Temperaturen
LFT, 152 Seiten, 73 Bilder, 21 Tab. 2008.
ISBN 978-3-87525-279-8.

Band 197: Thomas Bigl
Entwicklung, angepasste Herstellungsverfahren und erweiterte Qualitätssicherung von einsatzgerechten elektronischen Baugruppen
FAPS, 175 Seiten, 107 Bilder, 14 Tab. 2008.
ISBN 978-3-87525-280-4.

Band 198: Stephan Roth
Grundlegende Untersuchungen zum Excimerlaserstrahl-Abtragen unter Flüssigkeitsfilmen
LFT, 113 Seiten, 47 Bilder, 14 Tab. 2008.
ISBN 978-3-87525-281-1.

Band 199: Artur Giera
Prozesstechnische Untersuchungen zum Rührreibschweißen metallischer Werkstoffe
LFT, 179 Seiten, 104 Bilder, 36 Tab. 2008.
ISBN 978-3-87525-282-8.

Band 200: Jürgen Lechler
Beschreibung und Modellierung des Werkstoffverhaltens von presshärtbaren Bor-Manganstählen
LFT, 154 Seiten, 75 Bilder, 12 Tab. 2009.
ISBN 978-3-87525-286-6.

Band 201: Andreas Blankl
Untersuchungen zur Erhöhung der Prozessrobustheit bei der Innenhochdruck-Umformung von flächigen Halbzeugen mit vor- bzw. nachgeschalteten Laserstrahlfügeoperationen
LFT, 120 Seiten, 68 Bilder, 9 Tab. 2009.
ISBN 978-3-87525-287-3.

Band 202: Andreas Schaller
Modellierung eines nachfrageorientierten Produktionskonzeptes für mobile Telekommunikationsgeräte
FAPS, 120 Seiten, 79 Bilder, 0 Tab. 2009.
ISBN 978-3-87525-289-7.

Band 203: Claudius Schimpf
Optimierung von Zuverlässigkeitsuntersuchungen, Prüfabläufen und Nacharbeitsprozessen in der Elektronikproduktion
FAPS, 162 Seiten, 90 Bilder, 14 Tab. 2009.
ISBN 978-3-87525-290-3.

Band 204: Simon Dietrich
Sensoriken zur Schwerpunktslagebestimmung der optischen Prozessemissionen beim Laserstrahltiefschweißen
LFT, 138 Seiten, 70 Bilder, 5 Tab. 2009.
ISBN 978-3-87525-292-7.

Band 205: Wolfgang Wolf
Entwicklung eines agentenbasierten Steuerungssystems zur Materialflussorganisation im wandelbaren Produktionsumfeld
FAPS, 167 Seiten, 98 Bilder. 2009.
ISBN 978-3-87525-293-4.

Band 206: Steffen Polster
Laserdurchstrahlschweißen transparenter Polymerbauteile
LFT, 160 Seiten, 92 Bilder, 13 Tab. 2009.
ISBN 978-3-87525-294-1.

Band 207: Stephan Manuel Dörfler
Rührreibschweißen von walzplattiertem Halbzeug und Aluminiumblech zur Herstellung flächiger Aluminiumschaum-Sandwich-Verbundstrukturen
LFT, 190 Seiten, 98 Bilder, 5 Tab. 2009.
ISBN 978-3-87525-295-8.

Band 208: Uwe Vogt
Seriennahe Auslegung von Aluminium Tailored Heat Treated Blanks
LFT, 151 Seiten, 68 Bilder, 26 Tab. 2009.
ISBN 978-3-87525-296-5.

Band 209: Till Laumann
Qualitative und quantitative Bewertung der Crashtauglichkeit von höchstfesten Stählen
LFT, 117 Seiten, 69 Bilder, 7 Tab. 2009.
ISBN 978-3-87525-299-6.

Band 210: Alexander Diehl
Größeneffekte bei Biegeprozessen- Entwicklung einer Methodik zur Identifikation und Quantifizierung
LFT, 180 Seiten, 92 Bilder, 12 Tab. 2010.
ISBN 978-3-87525-302-3.

Band 211: Detlev Staud
Effiziente Prozesskettenauslegung für das Umformen lokal wärmebehandelter und geschweißter Aluminiumbleche
LFT, 164 Seiten, 72 Bilder, 12 Tab. 2010.
ISBN 978-3-87525-303-0.

Band 212: Jens Ackermann
Prozesssicherung beim Laserdurchstrahlschweißen thermoplastischer Kunststoffe
LPT, 129 Seiten, 74 Bilder, 13 Tab. 2010.
ISBN 978-3-87525-305-4.

Band 213: Stephan Weidel
Grundlegende Untersuchungen zum Kontaktzustand zwischen Werkstück und Werkzeug bei umformtechnischen Prozessen unter tribologischen Gesichtspunkten
LFT, 144 Seiten, 67 Bilder, 11 Tab. 2010.
ISBN 978-3-87525-307-8.

Band 214: Stefan Geißdörfer
Entwicklung eines mesoskopischen Modells zur Abbildung von Größeneffekten in der Kaltmassivumformung mit Methoden der FE-Simulation
LFT, 133 Seiten, 83 Bilder, 11 Tab. 2010.
ISBN 978-3-87525-308-5.

Band 215: Christian Matzner
Konzeption produktspezifischer Lösungen zur Robustheitssteigerung elektronischer Systeme gegen die Einwirkung von Betauung im Automobil
FAPS, 165 Seiten, 93 Bilder, 14 Tab. 2010.
ISBN 978-3-87525-309-2.

Band 216: Florian Schüßler
Verbindungs- und Systemtechnik für thermisch hochbeanspruchte und miniaturisierte elektronische Baugruppen
FAPS, 184 Seiten, 93 Bilder, 18 Tab. 2010.
ISBN 978-3-87525-310-8.

Band 217: Massimo Cojutti
Strategien zur Erweiterung der Prozessgrenzen bei der Innhochdruck-Umformung von Rohren und Blechpaaren
LFT, 125 Seiten, 56 Bilder, 9 Tab. 2010.
ISBN 978-3-87525-312-2.

Band 218: Raoul Plettke
Mehrkriterielle Optimierung komplexer Aktorsysteme für das Laserstrahljustieren
LFT, 152 Seiten, 25 Bilder, 3 Tab. 2010.
ISBN 978-3-87525-315-3.

Band 219: Andreas Dobroschke
Flexible Automatisierungslösungen für die Fertigung wickeltechnischer Produkte
FAPS, 184 Seiten, 109 Bilder, 18 Tab. 2011.
ISBN 978-3-87525-317-7.

Band 220: Azhar Zam
Optical Tissue Differentiation for Sensor-Controlled Tissue-Specific Laser Surgery
LPT, 99 Seiten, 45 Bilder, 8 Tab. 2011.
ISBN 978-3-87525-318-4.

Band 221: Michael Rösch
Potenziale und Strategien zur Optimierung des Schablonendruckprozesses in der Elektronikproduktion
FAPS, 192 Seiten, 127 Bilder, 19 Tab. 2011.
ISBN 978-3-87525-319-1.

Band 222: Thomas Rechtenwald
Quasi-isothermes Laserstrahlsintern von Hochtemperatur-Thermoplasten - Eine Betrachtung werkstoff-prozessspezifischer Aspekte am Beispiel PEEK
LPT, 150 Seiten, 62 Bilder, 8 Tab. 2011.
ISBN 978-3-87525-320-7.

Band 223: Daniel Craiovan
Prozesse und Systemlösungen für die SMT-Montage optischer Bauelemente auf Substrate mit integrierten Lichtwellenleitern
FAPS, 165 Seiten, 85 Bilder, 8 Tab. 2011.
ISBN 978-3-87525-324-5.

Band 224: Kay Wagner
Beanspruchungsangepasste Kaltmassivumformwerkzeuge durch lokal optimierte Werkzeugoberflächen
LFT, 147 Seiten, 103 Bilder, 17 Tab. 2011.
ISBN 978-3-87525-325-2.

Band 225: Martin Brandhuber
Verbesserung der Prognosegüte des Versagens von Punktschweißverbindungen bei höchstfesten Stahlgüten
LFT, 155 Seiten, 91 Bilder, 19 Tab. 2011.
ISBN 978-3-87525-327-6.

Band 226: Peter Sebastian Feuser
Ein Ansatz zur Herstellung von pressgehärteten Karosseriekomponenten mit maßgeschneiderten mechanischen Eigenschaften: Temperierte Umformwerkzeuge. Prozessfenster, Prozesssimuation und funktionale Untersuchung
LFT, 195 Seiten, 97 Bilder, 60 Tab. 2012.
ISBN 978-3-87525-328-3.

Band 227: Murat Arbak
Material Adapted Design of Cold Forging Tools Exemplified by Powder Metallurgical Tool Steels and Ceramics
LFT, 109 Seiten, 56 Bilder, 8 Tab. 2012.
ISBN 978-3-87525-330-6.

Band 228: Indra Pitz
Beschleunigte Simulation des Laserstrahlumformens von Aluminiumblechen
LPT, 137 Seiten, 45 Bilder, 27 Tab. 2012.
ISBN 978-3-87525-333-7.

Band 229: Alexander Grimm
Prozessanalyse und -überwachung des Laserstrahlhartlötens mittels optischer Sensorik
LPT, 125 Seiten, 61 Bilder, 5 Tab. 2012.
ISBN 978-3-87525-334-4.

Band 230: Markus Kaupper
Biegen von höhenfesten Stahlblechwerkstoffen - Umformverhalten und Grenzen der Biegbarkeit
LFT, 160 Seiten, 57 Bilder, 10 Tab. 2012.
ISBN 978-3-87525-339-9.

Band 231: Thomas Kroiß
Modellbasierte Prozessauslegung für die Kaltmassivumformung unter Brücksichtigung der Werkzeug- und Pressenauffederung
LFT, 169 Seiten, 50 Bilder, 19 Tab. 2012.
ISBN 978-3-87525-341-2.

Band 232: Christian Goth
Analyse und Optimierung der Entwicklung und Zuverlässigkeit räumlicher Schaltungsträger (3D-MID)
FAPS, 176 Seiten, 102 Bilder, 22 Tab. 2012.
ISBN 978-3-87525-340-5.

Band 233: Christian Ziegler
Ganzheitliche Automatisierung mechatronischer Systeme in der Medizin am Beispiel Strahlentherapie
FAPS, 170 Seiten, 71 Bilder, 19 Tab. 2012.
ISBN 978-3-87525-342-9.

Band 234: Florian Albert
Automatisiertes Laserstrahllöten und -reparaturlöten elektronischer Baugruppen
LPT, 127 Seiten, 78 Bilder, 11 Tab. 2012.
ISBN 978-3-87525-344-3.

Band 235: Thomas Stöhr
Analyse und Beschreibung des mechanischen Werkstoffverhaltens von presshärtbaren Bor-Manganstählen
LFT, 118 Seiten, 74 Bilder, 18 Tab. 2013.
ISBN 978-3-87525-346-7.

Band 236: Christian Kägeler
Prozessdynamik beim Laserstrahlschweißen verzinkter Stahlbleche im Überlappstoß
LPT, 145 Seiten, 80 Bilder, 3 Tab. 2013.
ISBN 978-3-87525-347-4.

Band 237: Andreas Sulzberger
Seriennahe Auslegung der Prozesskette zur wärmeunterstützten Umformung von Aluminiumblechwerkstoffen
LFT, 153 Seiten, 87 Bilder, 17 Tab. 2013.
ISBN 978-3-87525-349-8.

Band 238: Simon Opel
Herstellung prozessangepasster Halbzeuge mit variabler Blechdicke durch die Anwendung von Verfahren der Blechmassivumformung
LFT, 165 Seiten, 108 Bilder, 27 Tab. 2013.
ISBN 978-3-87525-350-4.

Band 239: Rajesh Kanawade
In-vivo Monitoring of Epithelium Vessel and Capillary Density for the Application of Detection of Clinical Shock and Early Signs of Cancer Development
LPT, 124 Seiten, 58 Bilder, 15 Tab. 2013.
ISBN 978-3-87525-351-1.

Band 240: Stephan Busse
Entwicklung und Qualifizierung eines Schneidclinchverfahrens
LFT, 119 Seiten, 86 Bilder, 20 Tab. 2013.
ISBN 978-3-87525-352-8.

Band 241: Karl-Heinz Leitz
Mikro- und Nanostrukturierung mit kurz und ultrakurz gepulster Laserstrahlung
LPT, 154 Seiten, 71 Bilder, 9 Tab. 2013.
ISBN 978-3-87525-355-9.

Band 242: Markus Michl
Webbasierte Ansätze zur ganzheitlichen technischen Diagnose
FAPS, 182 Seiten, 62 Bilder, 20 Tab. 2013.
ISBN 978-3-87525-356-6.

Band 243: Vera Sturm
Einfluss von Chargenschwankungen auf die Verarbeitungsgrenzen von Stahlwerkstoffen
LFT, 113 Seiten, 58 Bilder, 9 Tab. 2013.
ISBN 978-3-87525-357-3.

Band 244: Christian Neudel
Mikrostrukturelle und mechanisch-technologische Eigenschaften widerstandspunktgeschweißter Aluminium-Stahl-Verbindungen für den Fahrzeugbau
LFT, 178 Seiten, 171 Bilder, 31 Tab. 2014.
ISBN 978-3-87525-358-0.

Band 245: Anja Neumann
Konzept zur Beherrschung der Prozessschwankungen im Presswerk
LFT, 162 Seiten, 68 Bilder, 15 Tab. 2014.
ISBN 978-3-87525-360-3.

Band 246: Ulf-Hermann Quentin
Laserbasierte Nanostrukturierung mit optisch positionierten Mikrolinsen
LPT, 137 Seiten, 89 Bilder, 6 Tab. 2014.
ISBN 978-3-87525-361-0.

Band 247: Erik Lamprecht
Der Einfluss der Fertigungsverfahren auf die Wirbelstromverluste von Stator-Einzelzahnblechpaketen für den Einsatz in Hybrid- und Elektrofahrzeugen
FAPS, 148 Seiten, 138 Bilder, 4 Tab. 2014.
ISBN 978-3-87525-362-7.

Band 248: Sebastian Rösel
Wirkmedienbasierte Umformung von Blechhalbzeugen unter Anwendung magnetorheologischer Flüssigkeiten als kombiniertes Wirk- und Dichtmedium
LFT, 148 Seiten, 61 Bilder, 12 Tab. 2014.
ISBN 978-3-87525-363-4.

Band 249: Paul Hippchen
Simulative Prognose der Geometrie indirekt pressgehärteter Karosseriebauteile für die industrielle Anwendung
LFT, 163 Seiten, 89 Bilder, 12 Tab. 2014.
ISBN 978-3-87525-364-1.

Band 250: Martin Zubeil
Versagensprognose bei der Prozess simulation von Biegeumform- und Falzverfahren
LFT, 171 Seiten, 90 Bilder, 5 Tab. 2014.
ISBN 978-3-87525-365-8.

Band 251: Alexander Kühl
Flexible Automatisierung der Statorenmontage mit Hilfe einer universellen ambidexteren Kinematik
FAPS, 142 Seiten, 60 Bilder, 26 Tab. 2014.
ISBN 978-3-87525-367-2.

Band 252: Thomas Albrecht
Optimierte Fertigungstechnologien für Rotoren getriebeintegrierter PM-Synchronmotoren von Hybridfahrzeugen
FAPS, 198 Seiten, 130 Bilder, 38 Tab. 2014.
ISBN 978-3-87525-368-9.

Band 253: Florian Risch
Planning and Production Concepts for Contactless Power Transfer Systems for Electric Vehicles
FAPS, 185 Seiten, 125 Bilder, 13 Tab. 2014.
ISBN 978-3-87525-369-6.

Band 254: Markus Weigl
Laserstrahlschweißen von Mischverbindungen aus austenitischen und ferritischen korrosionsbeständigen Stahlwerkstoffen
LPT, 184 Seiten, 110 Bilder, 6 Tab. 2014.
ISBN 978-3-87525-370-2.

Band 255: Johannes Noneder
Beanspruchungserfassung für die Validierung von FE-Modellen zur Auslegung von Massivumformwerkzeugen
LFT, 161 Seiten, 65 Bilder, 14 Tab. 2014.
ISBN 978-3-87525-371-9.

Band 256: Andreas Reinhardt
Ressourceneffiziente Prozess- und Produktionstechnologie für flexible Schaltungsträger
FAPS, 123 Seiten, 69 Bilder, 19 Tab. 2014.
ISBN 978-3-87525-373-3.

Band 257: Tobias Schmuck
Ein Beitrag zur effizienten Gestaltung globaler Produktions- und Logistiknetzwerke mittels Simulation
FAPS, 151 Seiten, 74 Bilder. 2014.
ISBN 978-3-87525-374-0.

Band 258: Bernd Eichenhüller
Untersuchungen der Effekte und Wechselwirkungen charakteristischer Einflussgrößen auf das Umformverhalten bei Mikroumformprozessen
LFT, 127 Seiten, 29 Bilder, 9 Tab. 2014.
ISBN 978-3-87525-375-7.

Band 259: Felix Lütteke
Vielseitiges autonomes Transportsystem basierend auf Weltmodellerstellung mittels Datenfusion von Deckenkameras und Fahrzeugsensoren
FAPS, 152 Seiten, 54 Bilder, 20 Tab. 2014.
ISBN 978-3-87525-376-4.

Band 260: Martin Grüner
Hochdruck-Blechumformung mit formlos festen Stoffen als Wirkmedium
LFT, 144 Seiten, 66 Bilder, 29 Tab. 2014.
ISBN 978-3-87525-379-5.

Band 261: Christian Brock
Analyse und Regelung des Laserstrahltiefschweißprozesses durch Detektion der Metalldampffackelposition
LPT, 126 Seiten, 65 Bilder, 3 Tab. 2015.
ISBN 978-3-87525-380-1.

Band 262: Peter Vatter
Sensitivitätsanalyse des 3-Rollen-Schubbiegens auf Basis der Finite Elemente Methode
LFT, 145 Seiten, 57 Bilder, 26 Tab. 2015.
ISBN 978-3-87525-381-8.

Band 263: Florian Klämpfl
Planung von Laserbestrahlungen durch simulationsbasierte Optimierung
LPT, 169 Seiten, 78 Bilder, 32 Tab. 2015.
ISBN 978-3-87525-384-9.

Band 264: Matthias Domke
Transiente physikalische Mechanismen bei der Laserablation von dünnen Metallschichten
LPT, 133 Seiten, 43 Bilder, 3 Tab. 2015.
ISBN 978-3-87525-385-6.

Band 265: Johannes Götz
Community-basierte Optimierung des Anlagenengineerings
FAPS, 177 Seiten, 80 Bilder, 30 Tab. 2015.
ISBN 978-3-87525-386-3.

Band 266: Hung Nguyen
Qualifizierung des Potentials von Verfestigungseffekten zur Erweiterung des Umformvermögens aushärtbarer Aluminiumlegierungen
LFT, 137 Seiten, 57 Bilder, 16 Tab. 2015.
ISBN 978-3-87525-387-0.

Band 267: Andreas Kuppert
Erweiterung und Verbesserung von Versuchs- und Auswertetechniken für die Bestimmung von Grenzformänderungskurven
LFT, 138 Seiten, 82 Bilder, 2 Tab. 2015.
ISBN 978-3-87525-388-7.

Band 268: Kathleen Klaus
Erstellung eines Werkstofforientierten Fertigungsprozessfensters zur Steigerung des Formgebungsvermögens von Aluminiumlegierungen unter Anwendung einer zwischengeschalteten Wärmebehandlung
LFT, 154 Seiten, 70 Bilder, 8 Tab. 2015.
ISBN 978-3-87525-391-7.

Band 269: Thomas Svec
Untersuchungen zur Herstellung von funktionsoptimierten Bauteilen im partiellen Presshärtprozess mittels lokal unterschiedlich temperierter Werkzeuge
LFT, 166 Seiten, 87 Bilder, 15 Tab. 2015.
ISBN 978-3-87525-392-4.

Band 270: Tobias Schrader
Grundlegende Untersuchungen zur Verschleißcharakterisierung beschichteter Kaltmassivumformwerkzeuge
LFT, 164 Seiten, 55 Bilder, 11 Tab. 2015.
ISBN 978-3-87525-393-1.

Band 271: Matthäus Brela
Untersuchung von Magnetfeld-Messmethoden zur ganzheitlichen Wertschöpfungsoptimierung und Fehlerdetektion an magnetischen Aktoren
FAPS, 170 Seiten, 97 Bilder, 4 Tab. 2015.
ISBN 978-3-87525-394-8.

Band 272: Michael Wieland
Entwicklung einer Methode zur Prognose adhäsiven Verschleißes an Werkzeugen für das direkte Presshärten
LFT, 156 Seiten, 84 Bilder, 9 Tab. 2015.
ISBN 978-3-87525-395-5.

Band 273: René Schramm
Strukturierte additive Metallisierung durch kaltaktives Atmosphärendruckplasma
FAPS, 136 Seiten, 62 Bilder, 15 Tab. 2015.
ISBN 978-3-87525-396-2.

Band 274: Michael Lechner
Herstellung beanspruchungsangepasster Aluminiumblechhalbzeuge durch eine maßgeschneiderte Variation der Abkühlgeschwindigkeit nach Lösungsglühen
LFT, 136 Seiten, 62 Bilder, 15 Tab. 2015.
ISBN 978-3-87525-397-9.

Band 275: Kolja Andreas
Einfluss der Oberflächenbeschaffenheit auf das Werkzeugeinsatzverhalten beim Kaltfließpressen
LFT, 169 Seiten, 76 Bilder, 4 Tab. 2015.
ISBN 978-3-87525-398-6.

Band 276: Marcus Baum
Laser Consolidation of ITO Nanoparticles for the Generation of Thin Conductive Layers on Transparent Substrates
LPT, 158 Seiten, 75 Bilder, 3 Tab. 2015.
ISBN 978-3-87525-399-3.

Band 277: Thomas Schneider
Umformtechnische Herstellung dünnwandiger Funktionsbauteile aus Feinblech durch Verfahren der Blechmassivumformung
LFT, 188 Seiten, 95 Bilder, 7 Tab. 2015.
ISBN 978-3-87525-401-3.

Band 278: Jochen Merhof
Sematische Modellierung automatisierter Produktionssysteme zur Verbesserung der IT-Integration zwischen Anlagen-Engineering und Steuerungsebene
FAPS, 157 Seiten, 88 Bilder, 8 Tab. 2015.
ISBN 978-3-87525-402-0.

Band 279: Fabian Zöller
Erarbeitung von Grundlagen zur Abbildung des tribologischen Systems in der Umformsimulation
LFT, 126 Seiten, 51 Bilder, 3 Tab. 2016.
ISBN 978-3-87525-403-7.

Band 280: Christian Hezler
Einsatz technologischer Versuche zur Erweiterung der Versagensvorhersage bei Karosseriebauteilen aus höchstfesten Stählen
LFT, 147 Seiten, 63 Bilder, 44 Tab. 2016.
ISBN 978-3-87525-404-4.

Band 281: Jochen Bönig
Integration des Systemverhaltens von Automobil-Hochvoltleitungen in die virtuelle Absicherung durch strukturmechanische Simulation
FAPS, 177 Seiten, 107 Bilder, 17 Tab. 2016.
ISBN 978-3-87525-405-1.

Band 282: Johannes Kohl
Automatisierte Datenerfassung für diskret ereignisorientierte Simulationen in der energieflexibelen Fabrik
FAPS, 160 Seiten, 80 Bilder, 27 Tab. 2016.
ISBN 978-3-87525-406-8.

Band 283: Peter Bechtold
Mikroschockwellenumformung mittels ultrakurzer Laserpulse
LPT, 155 Seiten, 59 Bilder, 10 Tab. 2016.
ISBN 978-3-87525-407-5.

Band 284: Stefan Berger
Laserstrahlschweißen thermoplastischer Kohlenstofffaserverbundwerkstoffe mit spezifischem Zusatzdraht
LPT, 118 Seiten, 68 Bilder, 9 Tab. 2016.
ISBN 978-3-87525-408-2.

Band 285: Martin Bornschlegl
Methods-Energy Measurement - Eine Methode zur Energieplanung für Fügeverfahren im Karosseriebau
FAPS, 136 Seiten, 72 Bilder, 46 Tab. 2016.
ISBN 978-3-87525-409-9.

Band 286: Tobias Rackow
Erweiterung des Unternehmenscontrollings um die Dimension Energie
FAPS, 164 Seiten, 82 Bilder, 29 Tab. 2016.
ISBN 978-3-87525-410-5.

Band 287: Johannes Koch
Grundlegende Untersuchungen zur Herstellung zyklisch-symmetrischer Bauteile mit Nebenformelementen durch Blechmassivumformung
LFT, 125 Seiten, 49 Bilder, 17 Tab. 2016.
ISBN 978-3-87525-411-2.

Band 288: Hans Ulrich Vierzigmann
Beitrag zur Untersuchung der tribologischen Bedingungen in der Blechmassivumformung - Bereitstellung von tribologischen Modellversuchen und Realisierung von Tailored Surfaces
LFT, 174 Seiten, 102 Bilder, 34 Tab. 2016.
ISBN 978-3-87525-412-9.

Band 289: Thomas Senner
Methodik zur virtuellen Absicherung der formgebenden Operation des Nasspressprozesses von Gelege-Mehrschichtverbunden
LFT, 156 Seiten, 96 Bilder, 21 Tab. 2016.
ISBN 978-3-87525-414-3.

Band 290: Sven Kreitlein
Der grundoperationsspezifische Mindestenergiebedarf als Referenzwert zur Bewertung der Energieeffizienz in der Produktion
FAPS, 185 Seiten, 64 Bilder, 30 Tab. 2016.
ISBN 978-3-87525-415-0.

Band 291: Christian Roos
Remote-Laserstrahlschweißen verzinkter Stahlbleche in Kehlnahtgeometrie
LPT, 123 Seiten, 52 Bilder, 0 Tab. 2016.
ISBN 978-3-87525-416-7.

Band 292: Alexander Kahrimanidis
Thermisch unterstützte Umformung von Aluminiumblechen
LFT, 165 Seiten, 103 Bilder, 18 Tab. 2016.
ISBN 978-3-87525-417-4.

Band 293: Jan Tremel
Flexible Systems for Permanent Magnet Assembly and Magnetic Rotor Measurement / Flexible Systeme zur Montage von Permanentmagneten und zur Messung magnetischer Rotoren
FAPS, 152 Seiten, 91 Bilder, 12 Tab. 2016.
ISBN 978-3-87525-419-8.

Band 294: Ioannis Tsoupis
Schädigungs- und Versagensverhalten hochfester Leichtbauwerkstoffe unter Biegebeanspruchung
LFT, 176 Seiten, 51 Bilder, 6 Tab. 2017.
ISBN 978-3-87525-420-4.

Band 295: Sven Hildering
Grundlegende Untersuchungen zum Prozessverhalten von Silizium als Werkzeugwerkstoff für das Mikroscherschneiden metallischer Folien
LFT, 177 Seiten, 74 Bilder, 17 Tab. 2017.
ISBN 978-3-87525-422-8.

Band 296: Sasia Mareike Hertweck
Zeitliche Pulsformung in der Lasermikromaterialbearbeitung – Grundlegende Untersuchungen und Anwendungen
LPT, 146 Seiten, 67 Bilder, 5 Tab. 2017.
ISBN 978-3-87525-423-5.

Band 297: Paryanto
Mechatronic Simulation Approach for the Process Planning of Energy-Efficient Handling Systems
FAPS, 162 Seiten, 86 Bilder, 13 Tab. 2017.
ISBN 978-3-87525-424-2.

Band 298: Peer Stenzel
Großserientaugliche Nadelwickeltechnik für verteilte Wicklungen im Anwendungsfall der E-Traktionsantriebe
FAPS, 239 Seiten, 147 Bilder, 20 Tab. 2017.
ISBN 978-3-87525-425-9.

Band 299: Mario Lušić
Ein Vorgehensmodell zur Erstellung montageführender Werkerinformationssysteme simultan zum Produktentstehungsprozess
FAPS, 174 Seiten, 79 Bilder, 22 Tab. 2017.
ISBN 978-3-87525-426-6.

Band 300: Arnd Buschhaus
Hochpräzise adaptive Steuerung und Regelung robotergeführter Prozesse
FAPS, 202 Seiten, 96 Bilder, 4 Tab. 2017.
ISBN 978-3-87525-427-3.

Band 301: Tobias Laumer
Erzeugung von thermoplastischen Werkstoffverbunden mittels simultanem, intensitätsselektivem Laserstrahlschmelzen
LPT, 140 Seiten, 82 Bilder, 0 Tab. 2017.
ISBN 978-3-87525-428-0.

Band 302: Nora Unger
Untersuchung einer thermisch unterstützten Fertigungskette zur Herstellung umgeformter Bauteile aus der höherfesten Aluminiumlegierung EN AW-7020
LFT, 142 Seiten, 53 Bilder, 8 Tab. 2017.
ISBN 978-3-87525-429-7.

Band 303: Tommaso Stellin
Design of Manufacturing Processes for the Cold Bulk Forming of Small Metal Components from Metal Strip
LFT, 146 Seiten, 67 Bilder, 7 Tab. 2017.
ISBN 978-3-87525-430-3.

Band 304: Bassim Bachy

Experimental Investigation, Modeling, Simulation and Optimization of Molded Interconnect Devices (MID) Based on Laser Direct Structuring (LDS) / Experimentelle Untersuchung, Modellierung, Simulation und Optimierung von Molded Interconnect Devices (MID) basierend auf Laser Direktstrukturierung (LDS)

FAPS, 168 Seiten, 120 Bilder, 26 Tab. 2017.

ISBN 978-3-87525-431-0.

Band 305: Michael Spahr

Automatisierte Kontaktierungsverfahren für flachleiterbasierte Pkw-Bordnetzsysteme

FAPS, 197 Seiten, 98 Bilder, 17 Tab. 2017.

ISBN 978-3-87525-432-7.

Band 306: Sebastian Suttner

Charakterisierung und Modellierung des spannungszustandsabhängigen Werkstoffverhaltens der Magnesiumlegierung AZ31B für die numerische Prozessauslegung

LFT, 150 Seiten, 84 Bilder, 19 Tab. 2017.

ISBN 978-3-87525-433-4.

Band 307: Bhargav Potdar

A reliable methodology to deduce thermo-mechanical flow behaviour of hot stamping steels

LFT, 203 Seiten, 98 Bilder, 27 Tab. 2017.

ISBN 978-3-87525-436-5.

Band 308: Maria Löffler

Steuerung von Blechmassivumformprozessen durch maßgeschneiderte tribologische Systeme

LFT, viii u. 166 Seiten, 90 Bilder, 5 Tab. 2018. ISBN 978-3-96147-133-1.

Band 309: Martin Müller

Untersuchung des kombinierten Trenn- und Umformprozesses beim Fügen artungleicher Werkstoffe mittels Schneidclinchverfahren

LFT, xi u. 149 Seiten, 89 Bilder, 6 Tab. 2018. ISBN: 978-3-96147-135-5.

Band 310: Christopher Kästle

Qualifizierung der Kupfer-Drahtbondtechnologie für integrierte Leistungsmodule in harschen Umgebungsbedingungen

FAPS, xii u. 167 Seiten, 70 Bilder, 18 Tab. 2018. ISBN 978-3-96147-145-4.

Band 311: Daniel Vipavc

Eine Simulationsmethode für das 3-Rollen-Schubbiegen

LFT, xiii u. 121 Seiten, 56 Bilder, 17 Tab. 2018. ISBN 978-3-96147-147-8.

Band 312: Christina Ramer

Arbeitsraumüberwachung und autonome Bahnplanung für ein sicheres und flexibles Roboter-Assistenzsystem in der Fertigung

FAPS, xiv u. 188 Seiten, 57 Bilder, 9 Tab. 2018. ISBN 978-3-96147-153-9.

Band 313: Miriam Rauer

Der Einfluss von Poren auf die Zuverlässigkeit der Lötverbindungen von Hochleistungs-Leuchtdioden

FAPS, xii u. 209 Seiten, 108 Bilder, 21 Tab. 2018. ISBN 978-3-96147-157-7.

Band 314: Felix Tenner

Kamerabasierte Untersuchungen der Schmelze und Gasströmungen beim Laserstrahlschweißen verzinkter Stahlbleche

LPT, xxiii u. 184 Seiten, 94 Bilder, 7 Tab.
2018. ISBN 978-3-96147-160-7.

Band 315: Aarief Syed-Khaja

Diffusion Soldering for High-temperature Packaging of Power Electronics

FAPS, x u. 202 Seiten, 144 Bilder, 32 Tab.
2018. ISBN 978-3-87525-162-1.

Band 316: Adam Schaub

Grundlagenwissenschaftliche Untersuchung der kombinierten Prozesskette aus Umformen und Additive Fertigung

LFT, xi u. 192 Seiten, 72 Bilder, 27 Tab.
2019. ISBN 978-3-96147-166-9.

Band 317: Daniel Gröbel

Herstellung von Nebenformelementen unterschiedlicher Geometrie an Blechen mittels Fließpressverfahren der Blechmassivumformung

LFT, x u. 165 Seiten, 96 Bilder, 13 Tab.
2019. ISBN 978-3-96147-168-3.

Band 318: Philipp Hildenbrand

Entwicklung einer Methodik zur Herstellung von Tailored Blanks mit definierten Halbzeugeigenschaften durch einen Taumelprozess

LFT, ix u. 153 Seiten, 77 Bilder, 4 Tab.
2019. ISBN 978-3-96147-174-4.

Band 319: Tobias Konrad

Simulative Auslegung der Spann- und Fixierkonzepte im Karosserierohbau: Bewertung der Baugruppenmaßhaltigkeit unter Berücksichtigung schwankender Einflussgrößen

LFT, x u. 203 Seiten, 134 Bilder, 32 Tab.
2019. ISBN 978-3-96147-176-8.

Band 320: David Meinel

Architektur applikationsspezifischer Multi-Physics-Simulationskonfiguratoren am Beispiel modularer Triebzüge

FAPS, xii u. 166 Seiten, 82 Bilder, 25 Tab.
2019. ISBN 978-3-96147-184-3.

Band 321: Andrea Zimmermann

Grundlegende Untersuchungen zum Einfluss fertigungsbedingter Eigenschaften auf die Ermüdungsfestigkeit kaltmassivumgeformter Bauteile

LFT, ix u. 160 Seiten, 66 Bilder, 5 Tab.
2019. ISBN 978-3-96147-190-4.

Band 322: Christoph Amann

Simulative Prognose der Geometrie nassgepresster Karosseriebauteile aus Gelege-Mehrschichtverbunden

LFT, xvi u. 169 Seiten, 80 Bilder, 13 Tab.
2019. ISBN 978-3-96147-194-2.

Band 323: Jennifer Tenner

Realisierung schmierstofffreier Tiefziehprozesse durch maßgeschneiderte Werkzeugoberflächen

LFT, x u. 187 Seiten, 68 Bilder, 13 Tab.
2019. ISBN 978-3-96147-196-6.

Band 324: Susan Zöller

Mapping Individual Subjective Values to Product Design

KTmfk, xi u. 223 Seiten, 81 Bilder, 25 Tab.
2019. ISBN 978-3-96147-202-4.

Band 325: Stefan Lutz
Erarbeitung einer Methodik zur semiempirischen Ermittlung der Umwandlungskinetik durchhärtender Wälzlagerstähle für die Wärmebehandlungssimulation
LFT, xiv u. 189 Seiten, 75 Bilder, 32 Tab.
2019. ISBN 978-3-96147-209-3.

Band 326: Tobias Gnibl
Modellbasierte Prozesskettenabbildung rührreibgeschweißter Aluminiumhalbzeuge zur umformtechnischen Herstellung höchstfester Leichtbaustrukturteile
LFT, xii u. 167 Seiten, 68 Bilder, 17 Tab.
2019. ISBN 978-3-96147-217-8.

Band 327: Johannes Bürner
Technisch-wirtschaftliche Optionen zur Lastflexibilisierung durch intelligente elektrische Wärmespeicher
FAPS, xiv u. 233 Seiten, 89 Bilder, 27 Tab.
2019. ISBN 978-3-96147-219-2.

Band 328: Wolfgang Böhm
Verbesserung des Umformverhaltens von mehrlagigen Aluminiumblechwerkstoffen mit ultrafeinkörnigem Gefüge
LFT, ix u. 160 Seiten, 88 Bilder, 14 Tab.
2019. ISBN 978-3-96147-227-7.

Band 329: Stefan Landkammer
Grundsatzuntersuchungen, mathematische Modellierung und Ableitung einer Auslegungsmethodik für Gelenkantriebe nach dem Spinnenbeinprinzip
LFT, xii u. 200 Seiten, 83 Bilder, 13 Tab.
2019. ISBN 978-3-96147-229-1.

Band 330: Stephan Rapp
Pump-Probe-Ellipsometrie zur Messung transienter optischer Materialeigenschaften bei der Ultrakurzpuls-Lasermaterialbearbeitung
LPT, xi u. 143 Seiten, 49 Bilder, 2 Tab.
2019. ISBN 978-3-96147-235-2.

Band 331: Michael Scholz
Intralogistics Execution System mit integrierten autonomen, servicebasierten Transportentitäten
FAPS, xi u. 195 Seiten, 55 Bilder, 11 Tab.
2019. ISBN 978-3-96147-237-6.

Band 332: Eva Bogner
Strategien der Produktindividualisierung in der produzierenden Industrie im Kontext der Digitalisierung
FAPS, ix u. 201 Seiten, 55 Bilder, 28 Tab.
2019. ISBN 978-3-96147-246-8.

Band 333: Daniel Benjamin Krüger
Ein Ansatz zur CAD-integrierten muskuloskelettalen Analyse der Mensch-Maschine-Interaktion
KTmfk, x u. 217 Seiten, 102 Bilder, 7 Tab.
2019. ISBN 978-3-96147-250-5.

Band 334: Thomas Kuhn
Qualität und Zuverlässigkeit laserdirektstrukturierter mechatronisch integrierter Baugruppen (LDS-MID)
FAPS, ix u. 152 Seiten, 69 Bilder, 12 Tab.
2019. ISBN: 978-3-96147-252-9.

Band 335: Hans Fleischmann
Modellbasierte Zustands- und Prozessüberwachung auf Basis sozio-cyber-physischer Systeme
FAPS, xi u. 214 Seiten, 111 Bilder, 18 Tab.
2019. ISBN: 978-3-96147-256-7.

Band 336: Markus Michalski
Grundlegende Untersuchungen zum Prozess- und Werkstoffverhalten bei schwingungsüberlagerter Umformung
LFT, xii u. 197 Seiten, 93 Bilder, 11 Tab.
2019. ISBN: 978-3-96147-270-3.

Band 337: Markus Brandmeier
Ganzheitliches ontologiebasiertes Wissensmanagement im Umfeld der industriellen Produktion
FAPS, xi u. 255 Seiten, 77 Bilder, 33 Tab.
2020. ISBN: 978-3-96147-275-8.

Band 338: Stephan Purr
Datenerfassung für die Anwendung lernender Algorithmen bei der Herstellung von Blechformteilen
LFT, ix u. 165 Seiten, 48 Bilder, 4 Tab.
2020. ISBN: 978-3-96147-281-9.

Band 339: Christoph Kiener
Kaltfließpressen von gerad- und schrägverzahnten Zahnrädern
LFT, viii u. 151 Seiten, 81 Bilder, 3 Tab.
2020. ISBN 978-3-96147-287-1.

Band 340: Simon Spreng
Numerische, analytische und empirische Modellierung des Heißcrimpprozesses
FAPS, xix u. 204 Seiten, 91 Bilder, 27 Tab.
2020. ISBN 978-3-96147-293-2.

Band 341: Patrik Schwingenschlögl
Erarbeitung eines Prozessverständnisses zur Verbesserung der tribologischen Bedingungen beim Presshärten
LFT, x u. 177 Seiten, 81 Bilder, 8 Tab.
2020. ISBN 978-3-96147-297-0.

Band 342: Emanuela Affronti
Evaluation of failure behaviour of sheet metals
LFT, ix u. 136 Seiten, 57 Bilder, 20 Tab.
2020. ISBN 978-3-96147-303-8.

Band 343: Julia Degner
Grundlegende Untersuchungen zur Herstellung hochfester Aluminiumblechbauteile in einem kombinierten Umform- und Abschreckprozess
LFT, x u. 172 Seiten, 61 Bilder, 9 Tab.
2020. ISBN 978-3-96147-307-6.

Band 344: Maximilian Wagner
Automatische Bahnplanung für die Aufteilung von Prozessbewegungen in synchrone Werkstück- und Werkzeugbewegungen mittels Multi-Roboter-Systemen
FAPS, xxi u. 181 Seiten, 111 Bilder, 15 Tab.
2020. ISBN 978-3-96147-309-0.

Band 345: Stefan Härter
Qualifizierung des Montageprozesses hochminiaturisierter elektronischer Bauelemente
FAPS, ix u. 194 Seiten, 97 Bilder, 28 Tab.
2020. ISBN 978-3-96147-314-4.

Band 346: Toni Donhauser
Ressourcenorientierte Auftragsregelung in einer hybriden Produktion mittels betriebsbegleitender Simulation
FAPS, xix u. 242 Seiten, 97 Bilder, 17 Tab.
2020. ISBN 978-3-96147-316-8.

Band 347: Philipp Amend
Laserbasiertes Schmelzkleben von Thermoplasten mit Metallen
LPT, xv u. 154 Seiten, 67 Bilder.
2020. ISBN 978-3-96147-326-7.

Band 348: Matthias Ehlert
Simulationsunterstützte funktionale Grenzlagenabsicherung
KTmfk, xvi u. 300 Seiten, 101 Bilder,
73 Tab. 2020. ISBN 978-3-96147-328-1.

Band 349: Thomas Sander
Ein Beitrag zur Charakterisierung und Auslegung des Verbundes von Kunststoffsubstraten mit harten Dünnschichten
KTmfk, xiv u. 178 Seiten, 88 Bilder, 21 Tab. 2020. ISBN 978-3-96147-330-4.

Band 350: Florian Pilz
Fließpressen von Verzahnungselementen an Blechen
LFT, x u. 170 Seiten, 103Bilder, 4 Tab.
2020. ISBN 978-3-96147-332-8.

Band 351: Sebastian Josef Katona
Evaluation und Aufbereitung von Produktsimulationen mittels abweichungsbehafteter Geometriemodelle
KTmfk, ix u. 147 Seiten, 73 Bilder, 11 Tab.
2020. ISBN 978-3-96147-336-6.

Band 352: Jürgen Herrmann
Kumulatives Walzplattieren. Bewertung der Umformeigenschaften mehrlagiger Blechwerkstoffe der ausscheidungshärtbaren Legierung AA6014
LFT, x u. 157 Seiten, 64 Bilder, 5 Tab.
2020. ISBN 978-3-96147-344-1.

Band 353: Christof Küstner
Assistenzsystem zur Unterstützung der datengetriebenen Produktentwicklung
KTmfk, xii u. 219 Seiten, 63 Bilder, 14 Tab.
2020. ISBN 978-3-96147-348-9.

Band 354: Tobias Gläßel
Prozessketten zum Laserstrahlschweißen von flachleiterbasierten Formspulenwicklungen für automobile Traktionsantriebe
FAPS, xiv u. 206 Seiten, 89 Bilder, 11 Tab.
2020. ISBN 978-3-96147-356-4.

Band 355: Andreas Meinel
Experimentelle Untersuchung der Auswirkungen von Axialschwingungen auf Reibung und Verschleiß in Zylinderrollenlagern
KTmfk, xii u. 162 Seiten, 56 Bilder, 7 Tab.
2020. ISBN 978-3-96147-358-8.

Band 356: Hannah Riedle
Haptische, generische Modelle weicher anatomischer Strukturen für die chirurgische Simulation
FAPS, xxx u. 179 Seiten, 82 Bilder, 35 Tab.
2020. ISBN 978-3-96147-367-0.

Band 357: Maximilian Landgraf
Leistungselektronik für den Einsatz dielektrischer Elastomere in aktorischen, sensorischen und integrierten sensomotorischen Systemen
FAPS, xxiii u. 166 Seiten, 71 Bilder, 10 Tab.
2020. ISBN 978-3-96147-380-9.

Band 358: Alireza Esfandyari
Multi-Objective Process Optimization for Overpressure Reflow Soldering in Electronics Production
FAPS, xviii u. 175 Seiten, 57 Bilder, 23 Tab.
2020. ISBN 978-3-96147-382-3.

Band 359: Christian Sand
Prozessübergreifende Analyse komplexer Montageprozessketten mittels Data Mining
FAPS, XV u. 168 Seiten, 61 Bilder, 12 Tab. 2021. ISBN 978-3-96147-398-4.

Band 360: Ralf Merkl
Closed-Loop Control of a Storage-Supported Hybrid Compensation System for Improving the Power Quality in Medium Voltage Networks
FAPS, xxvii u. 200 Seiten, 102 Bilder, 2 Tab. 2021. ISBN 978-3-96147-402-8.

Band 361: Thomas Reitberger
Additive Fertigung polymerer optischer Wellenleiter im Aerosol-Jet-Verfahren
FAPS, xix u. 141 Seiten, 65 Bilder, 11 Tab. 2021. ISBN 978-3-96147-400-4.

Band 362: Marius Christian Fechter
Modellierung von Vorentwürfen in der virtuellen Realität mit natürlicher Fingerinteraktion
KTmfk, x u. 188 Seiten, 67 Bilder, 19 Tab. 2021. ISBN 978-3-96147-404-2.

Band 363: Franziska Neubauer
Oberflächenmodifizierung und Entwicklung einer Auswertemethodik zur Verschleißcharakterisierung im Presshärteprozess
LFT, ix u. 177 Seiten, 42 Bilder, 6 Tab. 2021. ISBN 978-3-96147-406-6.

Band 364: Eike Wolfram Schäffer
Web- und wissensbasierter Engineering-Konfigurator für roboterzentrierte Automatisierungslösungen
FAPS, xxiv u. 195 Seiten, 108 Bilder, 25 Tab. 2021. ISBN 978-3-96147-410-3.

Band 365: Daniel Gross
Untersuchungen zur kohlenstoffdioxidbasierten kryogenen Minimalmengenschmierung
REP, xii u. 184 Seiten, 56 Bilder, 18 Tab. 2021. ISBN 978-3-96147-412-7.

Band 366: Daniel Junker
Qualifizierung laser-additiv gefertigter Komponenten für den Einsatz im Werkzeugbau der Massivumformung
LFT, vii u. 142 Seiten, 62 Bilder, 5 Tab. 2021. ISBN 978-3-96147-416-5.

Band 367: Tallal Javied
Totally Integrated Ecology Management for Resource Efficient and Eco-Friendly Production
FAPS, xv u. 160 Seiten, 60 Bilder, 13 Tab. 2021. ISBN 978-3-96147-418-9.

Band 368: David Marco Hochrein
Wälzlager im Beschleunigungsfeld – Eine Analysestrategie zur Bestimmung des Reibungs-, Axialschub- und Temperaturverhaltens von Nadelkränzen –
KTmfk, xiii u. 279 Seiten, 108 Bilder, 39 Tab. 2021. ISBN 978-3-96147-420-2.

Band 369: Daniel Gräf

Funktionalisierung technischer Oberflächen mittels prozessüberwachter aerosolbasierter Drucktechnologie

FAPS, xxii u. 175 Seiten, 97 Bilder, 6 Tab.

2021. ISBN 978-3-96147-433-2.

Band 370: Andreas Gröschl

Hochfrequent fokusabstandsmodulierte Konfokalsensoren für die Nanokoordinatenmesstechnik

FMT, x u. 144 Seiten, 98 Bilder, 6 Tab.

2021. ISBN 978-3-96147-435-6.

Band 371: Johann Tüchsen

Konzeption, Entwicklung und Einführung des Assistenzsystems D-DAS für die Produktentwicklung elektrischer Motoren

KTmfk, xii u. 178 Seiten, 92 Bilder, 12 Tab.

2021. ISBN 978-3-96147-437-0.

Band 372: Max Marian

Numerische Auslegung von Oberflächenmikrotexturen für geschmierte tribologische Kontakte

KTmfk, xviii u. 276 Seiten, 85 Bilder, 45 Tab.

2021. ISBN 978-3-96147-439-4.

Band 373: Johannes Strauß

Die akustooptische Strahlformung in der Lasermaterialbearbeitung

LPT, xvi u. 113 Seiten, 48 Bilder.

2021. ISBN 978-3-96147-441-7.

Band 374: Martin Hohmann

Machine learning and hyper spectral imaging: multi spectral endoscopy in the gastro intestinal tract towards hyper spectral endoscopy

LPT, x u. 137 Seiten, 62 Bilder, 29 Tab.

2021. ISBN 978-3-96147-445-5.

Abstract

Weltweit stehen Karzinome an zweiter Stelle der Todesursachen nach Herz-Kreislauf-Erkrankungen. Von diesen werden mehr als 25 % durch Krebs im Magen-Darm-Trakt verursacht. Beim Screening werden jedoch immer noch etwa 20 % der Karzinome übersehen. Eine optimale Lösung wäre eine Red-Flag-Technologie zur Lokalisierung des verdächtigen Bereichs. Trotz des Einsatzes vieler optischer Technologien und Weiterentwicklungen traditioneller endoskopischer Technologien konnten die meisten Methoden bisher nicht zu einer signifikanten Verbesserung der Erkennbarkeit von Karzinomen im GI führen. Daher wurde in der Literatur vorgeschlagen, spektroskopische quantitative Messungen zu verwenden, welche durch hyperspektrale Bildgebung erreicht wird. In dieser Arbeit wird jedoch ein multispektrales Endoskopsystem für den in-vivo-Einsatz für Studien am Menschen (Magen) und an Mäusen (Dickdarm) verwendet. Bei der Humanstudie konnten mit den Standardverfahren die Tumoure nur bedingt gefunden werden (MCC = 0,32; ACC2=0,68). Dennoch ist dies eine deutliche Verbesserung im Vergleich zu früheren Ergebnissen. Durch die Einführung der spektralen räumlichen Variation als räumlich-spektrales Merkmal verbessern sich die Ergebnisse nochmals deutlich. Im Vergleich zur Humanstudie zeigen die Ergebnisse aus dem Mausmodell bessere Klassifikationsergebnisse: ACC2 = 0,73 und MCC = 0,47. Für die Entwicklung einer endoskopischen Red-Flag-Technik wird also eine Punkttechnik zur korrekten Voretikettierung der Daten benötigt. Darüber hinaus sind die Ergebnisse dieser MSI-*in-vivo*-Studie mit räumlichen Merkmalen ähnlich wie die jüngsten HSI-*ex-vivo*-Studien. Daher ist es wahrscheinlich, dass MSI Teil zukünftiger Forschungen bleiben wird.

Worldwide, carcinomas are the second leading cause of death after cardiovascular diseases. Of these, more than 25 % are caused by cancer in the gastrointestinal tract. However, screening still misses about 20 % of carcinomas. An optimal solution would be a red flag technology to locate the suspicious area. Despite the use of many optical technologies and advancements in traditional endoscopic technologies, most methods have failed to significantly improve the detectability of carcinomas in the GI. Therefore, it has been suggested in the literature to use spectroscopic quantitative measurements, which is achieved by hyperspectral imaging. However, in this work, a multispectral endoscope system for in vivo use is used for human (stomach) and mouse (colon) studies. In the human study, the tumours could only be found to a limited extent with the standard methods (MCC = 0.32; ACC2=0.68). Nevertheless, this is a significant improvement compared to previous results. The introduction of spectral spatial variation as a spatialspectral feature improves the results significantly again. Compared to the human study, the results from the mouse model show better classification results: ACC2 = 0.73 and MCC = 0.47. Thus, for the development of an endoscopic red flag technique, a point technique for correct pre-labelling of the data is needed. Moreover, the results of this MSI-in vivo study with spatial features are similar to the recent HSI-ex vivo studies. Therefore, it is likely that MSI will remain part of future research.

ISBN 978-3-96147-445-5

FAU UNIVERSITY PRESS 2021